High-Resolution Imaging of Relativistic Jets and Supermassive Black Holes

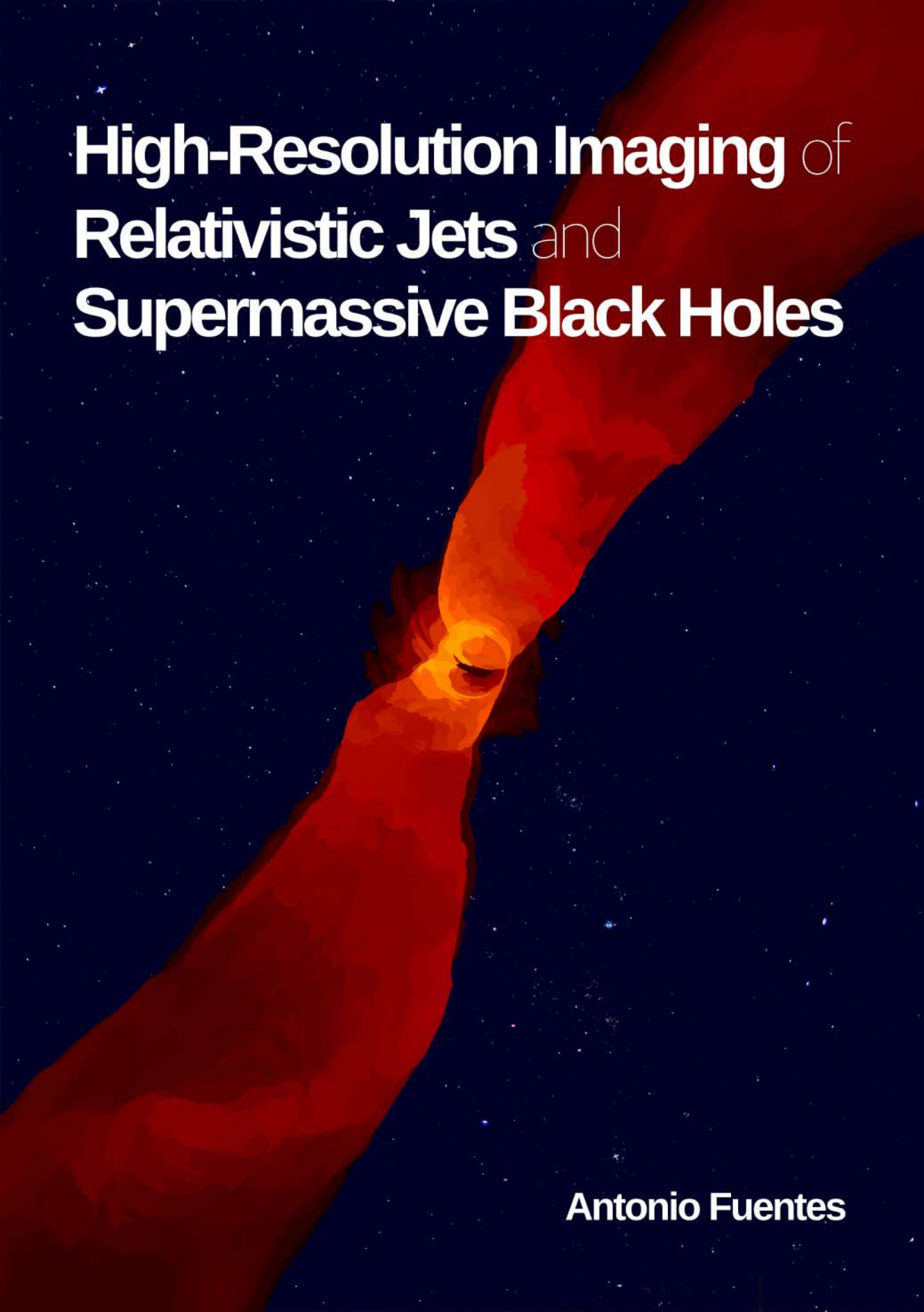

Antonio Fuentes

UNIVERSIDAD DE GRANADA

INSTITUTO DE ASTROFÍSICA DE ANDALUCÍA

High-Resolution Imaging of Relativistic Jets and Supermassive Black Holes

by
Antonio Fuentes Fernández

Supervised by
Dr. José L. Gómez

A dissertation submitted in partial fulfillment
of the requirements for the degree of
Doctor of Philosophy in Physics

Doctoral Programme in Physics and Space Sciences

October 2022

Editor: Universidad de Granada. Tesis Doctorales
Autor: Antonio Fuentes Fernández
ISBN: 978-84-1117-650-7
URI: https://hdl.handle.net/10481/79637

A mis padres y a mi hermana.
Y a todas las personas que me han apoyado
durante el camino.

Gracias.

Abstract

This thesis focuses on the observational signatures encoded in the radio emission produced by accretion processes onto supermassive black holes (SMBH), located at the core of active galactic nuclei (AGN), and the highly collimated relativistic jets that emanate from their surroundings. Theoretical models predict that AGN jets are launched from the vicinity of these extreme, compact objects through energy extraction via large-scale helical magnetic fields (Blandford & Znajek, 1977; Blandford & Payne, 1982). We tackle this scenario by direct imaging of the main actors through high-angular-resolution very long baseline interferometric (VLBI) observations at millimeter and centimeter wavelengths (e.g., Event Horizon Telescope Collaboration *et al.,* 2019a; Gómez *et al.,* 2022). In addition to VLBI observations, we also study the properties of AGN jets at the parsec scale through relativistic magnetohydrodynamical (RMHD) simulations and their corresponding synchrotron emission (e.g., Gómez *et al.,* 1997). Therefore, the work developed in this thesis covers a wide range of spatial (and temporal) scales, from the polarimetric properties and microarcsecond internal structure of AGN jets to the dynamic, event-horizon-scale radiation produced by the hot plasma accreting onto SMBHs.

In Chapters 2 and 3, corresponding to the publications Fuentes *et al.* (2018, 2021), we study the influence of the helical magnetic field in the jet dynamics and emission at the parsec scale. To this aim, we analyze the polarimetric synchrotron radiation expected from several RMHD simulations of stationary overpressured magnetized relativistic jet models. These models are characterized by their dominant type of energy, namely, internal, kinetic, or magnetic. We find that the properties of *recollimation shocks*, formed by the pressure mismatch between the jet and the ambient medium, are mainly governed by the magnetosonic Mach number and the specific internal energy. Associated to these shocks, the radio maps obtained from the RMHD jet models feature a series of bright "knots", typically reported in VLBI observations of AGN jets and particularly strong in the case of models dominated by the internal energy. We test several configurations of the threaded helical magnetic field and study the linearly polarized emission from the jet models. We recover a bimodal distribution of the polarization angle, especially for small viewing angles and magnetic fields dominated by their toroidal component. For larger viewing angles and poloidal magnetic field components, the polarization angle remains perpendicular to the jet propagation direction. Nonetheless, we find small rotations near the bright knots, a signature that can be used to identify recollimation shocks in VLBI observations of blazar jets.

In Chapter 4, corresponding to the publication Fuentes *et al.* (submitted 2022), we focus on the internal and innermost structure of relativistic jets by extending the global VLBI network to space. Thus, we observe the archetypal blazar 3C 279 at 22 GHz (or 1.3 cm) with *RadioAstron*, a space-ground interferometer capable of providing microarcsecond angular resolutions at centimeter wavelengths. Supported by 23 radio telescopes on Earth, we report *fringe* detections of the source up to a projected baseline distance of 8 Earth diameters. Aided by novel image reconstruction algorithms, the highly eccentric orbit of the spacecraft allows us to resolve the transversal structure of the jet and reveal several filaments forming a helical shape. The origin of these filaments is likely related to the triggering of Kelvin-Helmholtz plasma instabilities in a kinetically dominated flow. Taking into account the image properties reconstructed, we estimate a flow Lorentz factor of ~ 13 in a jet threaded by a helical magnetic field rotating clockwise, as seen in the direction of flow motion. Moreover, the brighter regions found in the jet, originated by a differential Doppler boosting within the filaments, should propagate down the jet with a pattern speed equal to the velocity of the instability. Based on this, we propose a novel model in which the jet variability observed in 3C 279, and possibly in other blazar sources, results from the propagation of plasma instabilities, as opposed to the standard shock-in-jet model usually invoked (Marscher & Gear, 1985).

Finally, in Chapter 5, corresponding to the publication Event Horizon Telescope Collaboration *et al.* (2022c), we present the first movie reconstructions and dynamic characterization of a supermassive black hole accreting matter, the mechanism responsible for the formation of relativistic jets. Specifically, we employ dynamic imaging and modeling techniques to analyze the spatially-resolved intraday variability of Sagittarius A*, the SMBH located at the Galactic Center. To this aim, we explore the data collected with the Event Horizon Telescope during the 2017 campaign, focusing on a small time window with the best (u, v)-coverage on April 6 and 7. We train our methods on a suite of synthetic data sets, including state-of-the-art black hole simulations. To quantify our ability to successfully reconstruct the dynamics of a given model, we compute the average position angle (PA). We find that we are able to recover the ground-truth PA in some cases, but we fail in others. On April 6, most dynamic imaging and modeling results agree on a quasi-static PA over the time window. On April 7, dynamic imaging and modeling results align when using strong spatial priors and show an evolution in the PA of $\sim$140°. However, we also see several other PA trends in the dynamic imaging results, including a PA evolution in the opposite direction and *modes* where the PA is static on both days. While this analysis supposes a promising starting point, the sparse coverage of the 2017 EHT array limits our ability to conclusively determine the PA evolution of Sagittarius A* and our results should be interpreted with caution.

Resumen

Esta tesis se centra en las trazas observacionales y la emisión radio producida por procesos de acreción en agujeros negros supermasivos (SMBH), situados en el centro de los núcleos activos de galaxias (AGN), y los *jets* relativistas que se forman a su alrededor. Los modelos teóricos predicen que los jets en AGNs se lanzan desde las proximidades de estos objetos tan compactos mediante la extracción de energía a través de campos magnéticos helicoidales a gran escala (Blandford & Znajek, 1977; Blandford & Payne, 1982). Una forma de abordar esta hipótesis es mediante la obtención directa de imágenes de los actores principales a través de observaciones interferométricas de muy larga línea de base (VLBI) de alta resolución angular en longitudes de onda centimétricas y milimétricas (e.g., Event Horizon Telescope Collaboration *et al.,* 2019a; Gómez *et al.,* 2022). En paralelo a dichas observaciones, también se pueden estudiar las propiedades de los jets en AGNs a escalas del pársec mediante simulaciones magnetohidrodinámicas relativistas (RMHD) y su correspondiente emisión sincrotrón (e.g., Gómez *et al.,* 1997). Por tanto, el trabajo desarrollado en esta tesis cubre un amplio rango de escalas espaciales (y temporales), desde las propiedades polarimétricas y la estructura interna de jets en AGNs, hasta la dinámica y la radiación a escalas del horizonte de sucesos del plasma caliente que acretan los SMBHs.

En los Capítulos 2 y 3, que corresponden a las publicaciones Fuentes *et al.* (2018, 2021), estudiamos la influencia del campo magnético helicoidal en la dinámica y la emisión del jet en escalas del pársec. Para ello, analizamos la radiación sincrotrón producida por varias simulaciones de jets relativistas estacionarios, sobrepresionados y confinados por un campo magnético helicoidal. Estos modelos se caracterizan por el tipo de energía dominante, a saber, interna, cinética o magnética. Las propiedades de los *choques de recolimación*, formados por el desequilibrio de presión entre el jet y el medio externo, están determinadas principalmente por el número de Mach magnetosónico y la energía interna. Asociadas a dichos choques, los mapas de emisión radio calculados a partir de los modelos RMHD muestran una serie de "compontes" brillantes, comúnmente observadas en jets en AGNs y particularmente intensas en modelos dominados por la energía interna. Probamos varias configuraciones del campo magnético helicoidal y estudiamos la emisión linealmente polarizada radiada por nuestras simulaciones. Recuperamos una distribución bimodal del ángulo de polarización, especialmente para ángulos de visión pequeños y campos magnéticos dominados por su componente toroidal. Para ángulos de visión y componentes poloidales del campo magnético mayores, el ángulo de polarización permanece perpendicular a la dirección

de propagación del jet. No obstante, podemos apreciar pequeñas rotaciones alrededor de las componentes brillantes, hecho que puede usarse para identificar choques de recolimación en observaciones VLBI de jets en blázares.

En el Capítulo 4, correspondiente a la publicación Fuentes *et al.* (submitted 2022), nos centramos en la estructura interna más cercana a la base del jet extendiendo la red global de VLBI al espacio. Así, observamos el blazar 3C 279 con *RadioAstron*, un interferómetro espacio-tierra capaz de ofrecer resoluciones angulares de microsegundos de arco en longitudes de onda centimétricas. Junto a 23 radiotelescopios en tierra, detectamos franjas de inteferencia de la fuente hasta una distancia, en proyección, de 8 diámetros terrestres. Con la ayuda de nuevos algoritmos de reconstrucción de imagen, la órbita extremadamente elíptica de *RadioAstron* nos permite resolver la estructura transversal del jet y revelar varios filamentos entrelazados de forma helicoidal. El origen de estos filamentos está probablemente relacionado con el desarrollo de inestabilidades Kelvin-Helmholtz en un plasma dominado por la energía cinética. Teniendo en cuenta las propiedades de las imágenes reconstruidas, estimamos un factor de Lorentz del flujo de ~ 13 en un jet confinado por un campo magnético helicoidal que gira en el sentido de las agujas del reloj. Además, las regiones brillantes que encontramos en el jet, originadas por un reforzamiento Doppler diferencial a lo largo de los filamentos, deberían propagarse con una velocidad igual a la de las propias inestabilidades. Con esto, proponemos un modelo que explica la variabilidad observada en el jet de 3C 279, y posiblemente en otras fuentes, como resultado de la propagación de inestabilidades en el plasma, en contraposición al modelo estándar de choques en jets que se suele invocar (Marscher & Gear, 1985).

Finalmente, en el Capítulo 5, correspondiente a la publicación Event Horizon Telescope Collaboration *et al.* (2022c), presentamos las primeras películas y la caracterización dinámica de un agujero negro super masivo acretando materia, el mecanismo responsable de la formación de jets relativistas. En concreto, empleamos técnicas de reconstrucción de imagen y modelado dinámicas para analizar la rápida variabilidad de Sagitario A*, el SMBH que alberga el centro de la Vía Láctea. Con este objetivo, exploramos los datos obtenidos por el Event Horizon Telescope en 2017, centrándonos en una pequeña ventana temporal con el mejor cubrimiento (u, v) el 6 y 7 de abril. Entrenamos nuestros métodos con una amplia variedad de datos sintéticos, incluyendo simulaciones vanguardistas de agujeros negros. Para cuantificar nuestra habilidad para reconstruir con éxito la dinámica real de los modelos, empleamos el ángulo de posición medio (PA). Vemos que somos capaces de recuperar el PA real en algunos casos, pero fallamos en otros. El 6 de abril, la mayoría de los resultados de imagen dinámica y modelado muestran un PA casi estático durante la ventana temporal. El 7 de abril, ambos resultados coinciden de nuevo cuando restringimos la estructura espacial, mostrando una evolución del PA de $\sim 140^\circ$. Sin embargo, también recuperamos otras tendencias del PA usando imagen dinámica, que incluyen "modos" estáticos o evolución en la dirección contraria. Aunque el análisis aquí descrito supone un punto de partida prometedor, el escaso cubrimiento del EHT en 2017 limita nuestra capacidad para determinar de forma concluyente la evolución de Sagitario A* y nuestros resultados deben interpretarse con precaución.

Contents

List of Figures

List of Tables

Chapter 1 | Introduction

1.1 Active Galactic Nuclei

We call Active Galactic Nuclei (AGNs) to the inner, central region of galaxies displaying an enormous nuclear luminosity, up to $L_{\rm bol} \approx 10^{48}\,{\rm erg\,s^{-1}}$, and whose origin is not related to stellar emission processes. Instead, the radiation produced by AGNs is driven by active accretion of gas and dust onto a central supermassive black hole (SMBH). This mechanism makes AGNs the brighter, non-explosive sources of the Universe (e.g., Zensus, 1997).

The detection of the first AGNs can be attributed to C. K. Seyfert, when he reported on a paper in 1943 the presence of broad and strong emission lines in the nuclei of seven spiral nebulae, and suggested a correlation between the width of the lines and the nucleus luminosity (Seyfert, 1943). His work went unnoticed until 1954, when W. Badee and R. Minkowsky mentioned in their work the similarities between the spectrum of the galaxies studied by Seyfert and the spectrum of the galaxy they had associated with the radio source Cygnus A (Baade & Minkowski, 1954), which today is one of the most remarkable examples of an active galaxy. In the coming years, several radio sources were associated to an optical counterpart and in 1963, the first *quasar*, 3C 273, was detected (Hazard *et al.,* 1963; Schmidt, 1963). A quasar is an AGN that outshines its host galaxy and has a star-like appearance. With a luminosity even greater than that of Cygnus A, 3C 273 displayed a linear jet of around 20 arcsec visible even at optical wavelengths. Multi-frequency observations of AGNs continued during the second half of the 20 th century and several types of AGNs were proposed to explain the differences found in their spectra: Seyfert I and Seyfert II galaxies, FR I and FR II radio galaxies (Fanaroff & Riley, 1974), quasars, blazars, etc. (e.g., see Padovani *et al.,* 2017, and references therein). It was not until the 1990s when the *unified model* of AGNs is proposed (Antonucci, 1993; Urry & Padovani, 1995). This model reconciles all AGNs subclasses into a standard model in which the intrinsic power of the nucleus is the only physical parameter that changes among AGNs. The remaining differences come solely from the angle at which the observer sees the source. Throughout this thesis, we primarily study blazars, that is, AGNs which are capable of forming a pair of relativistic jets and one of them is pointing towards us with a very small inclination angle.

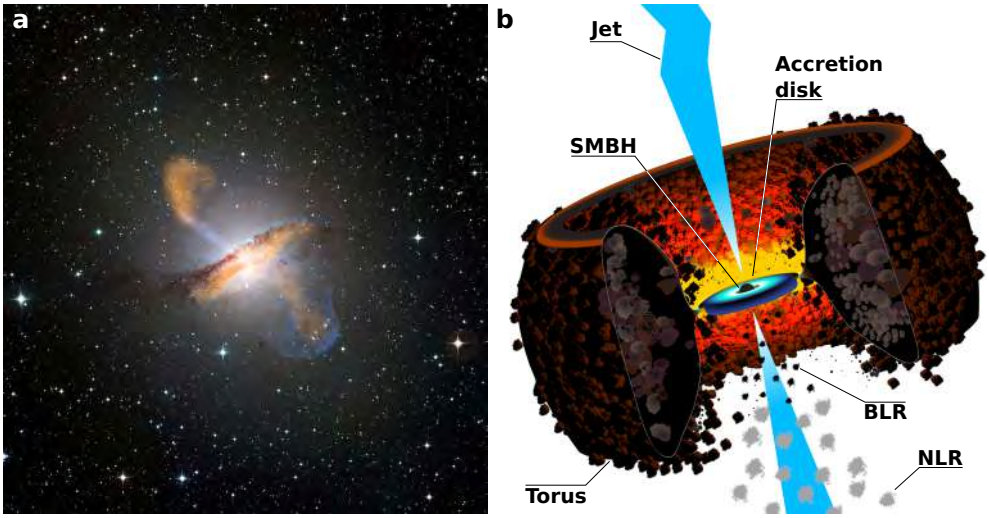

Figure 1.1: The multi-wavelength view of Centaurus A and a sketch of an AGN. a, Colour composite image of the radio galaxy Centaurus A, revealing the lobes and jets (colored in blue and orange, corresponding to radio and X-ray emission, respectively) emanating perpendicularly to the galactic plane (“true color", corresponding to optical emission) from the central SMBH. Credit: ESO/WFI (Optical); MPIfR/ESO/APEX/Weiß *et al.,* 2008 (Submillimetre); NASA/CXC/CfA/Kraft *et al.,* 2002 (X-ray). **b,** Sketch showing the inner region of an AGN, adapted from Bill Saxton, NRAO/AUI/NSF. Note that the scales shown in **a** and **b** are vastly different.

The current AGN paradigm consists mainly of a central SMBH, with typical masses larger than $10^6\ M_\odot$ (e.g., Kormendy & Richstone, 1995), encircled by an accretion disk glowing at ultraviolet and X-ray wavelengths. In addition, clouds of line-emitting gas surround the system, usually classified into broad-line (which are located closer to the central engine) or narrow-line (located further away) region clouds, depending on the width of the measured emission lines. Encompassing all the previous components, we find an axisymmetric dusty torus which, depending on the inclination angle, can obscure some of the features mentioned. Under some circumstances, a pair of perpendicular and highly collimated outflows of plasma can be launched from the vicinity of the SMBH at relativistic speeds. These jets shine strongly at radio wavelengths and AGNs can be further categorized into radio loud and radio quiet, if jets are formed and can be detected or not, respectively. A multi-wavelength image composition of one of the archetypal AGNs, Centaurus A, is shown in Figure 1.1 along with a sketch of the inner region of an AGN.

1.1.1 Supermassive Black Holes

With the publication of A. Einstein’s general theory of relativity (GR) in 1915 (Einstein, 1916), came the first non-trivial exact solution to the equations of GR by K. Schwarzschild in 1916 (Schwarzschild, 1916). Schwarzschild’s metric describes the

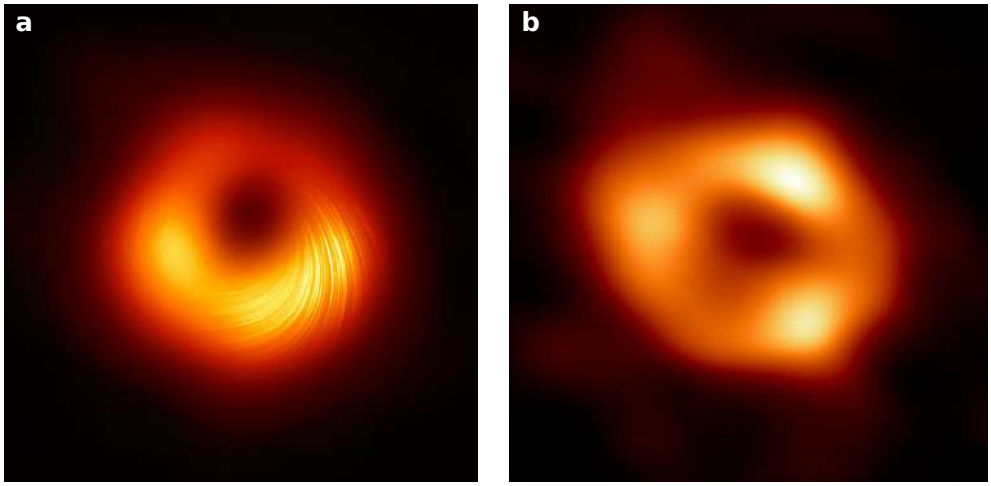

Figure 1.2: The black hole shadow of M 87* and Sgr A*. a, The 1.3 mm polarimetric image of M 87*, the SMBH at the center of the radio galaxy M 87. Linear polarization information is added on top of total intensity as sweeping lines. **b,** The 1.3 mm image of Sgr A*, the SMBH at the center of the Milky Way. Both images were obtained by the EHT Collaboration (Event Horizon Telescope Collaboration *et al.,* 2019a; b; c; d; e; f; 2021a; b; 2022a; b; c; d; e; f).

spacetime around a spherically symmetric point mass M with no electric charge or angular momentum, that is, a static black hole. Two singularities can be derived from this solution: a point of infinite curvature at a radius $r = 0$ and a surface enclosing it at a radius

$$r_S = \frac{2GM}{c^2}, \tag{1.1}$$

where G is Newton's constant and c is the speed of light. This quantity is called *Schwarzschild radius* and defines the distance from the black hole center at which the *event horizon* (Finkelstein, 1958) is formed, a boundary surface causally disconnecting the interior of the black hole from the outside. Later in the century, R. P. Kerr (Kerr, 1963) generalized this solution to point masses with nonzero angular momentum, and a few years later Newman *et al.* (1965) further extended it to point masses with electric charge.

From the astronomical point of view, S. Chandrasekhar postulated in 1931 (Chandrasekhar, 1931) the maximum mass for a star to collapse into a white dwarf at the end of its lifetime ($\sim 1.44\,M_\odot$). Some years later, J. R. Oppenheimer and G. M. Volkoff published an article (Oppenheimer & Volkoff, 1939), following the work of R. C. Tolman (Tolman, 1939), in which they established the mass limit beyond which a neutron star will collapse into a black hole. This type of stellar black holes are thought to populate galaxies (Remillard & McClintock, 2006) and are commonly observed accreting material from a companion star, a system referred to as *X-ray binary* because of its X-ray emission (e.g., Cygnus X-1; Webster & Murdin, 1972). The LIGO/VIRGO collaboration recently reported (Abbott *et al.,* 2019) on the detection of

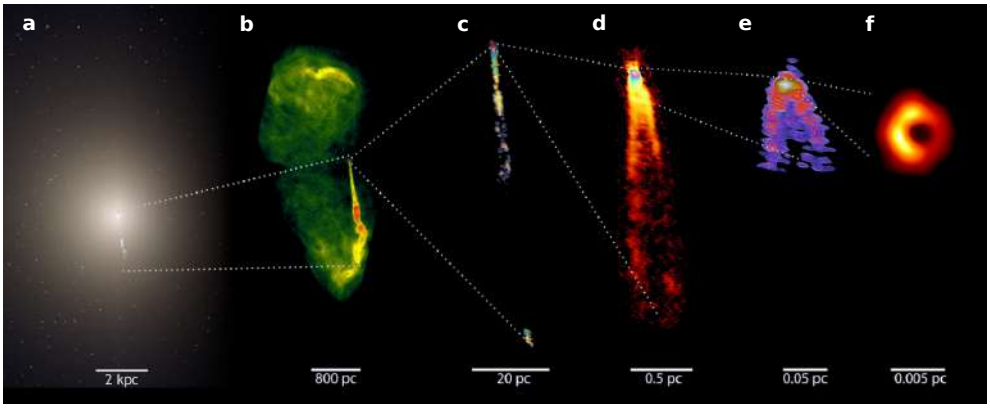

Figure 1.3: The multi-scale and multi-wavelength view of the radio galaxy M 87. a, The nuclear emission as seen by the Hubble Space Telescope in the optical band. **b,** The radio jet and inner lobes as seen by the Very Large Array (VLA) at 20 cm. **c,** The innermost jet as seen by the Very Long Baseline Array (VLBA) at 20 cm (Cheung *et al.,* 2007). **d,** The limb-brightened jet closer to the central engine as seen by the VLBA at 7 mm (Walker *et al.,* 2018). **e,** The jet launching region as seen by the Global millimeter VLBI array (GMVA) at 3 mm (Kim *et al.,* 2018). **f,** The inner accretion disk and black hole shadow as seen by the Event Horizon Telescope at 1.3 mm (Event Horizon Telescope Collaboration *et al.,* 2019a). Adapted from Blandford *et al.* (2019). Images are rotated $\sim 90°$.

gravitational waves produced by merging black holes more massive than typical stellar types ($\sim 10 - 100\,M_\odot$). Much further away in the mass scale, we find SMBH. The high luminosity and the rapid variability observed in AGNs quickly led astronomers to believe that accretion of matter onto SMBH, or extraction of its rotational energy, could be the mechanism responsible for the radiation of such large amount of energies (Salpeter, 1964; Lynden-Bell, 1969; Rees, 1984). Nowadays, nearly all galaxies are thought to harbor a SMBH at their center, and whose activity is a key ingredient in the evolution of the host galaxy (King, 2003; Kormendy & Ho, 2013; King & Pounds, 2015).

J.-P. Luminet began the quest to directly image a black hole, such as the one located at the center of M 87, with the first simulated image of how a black hole surrounded by a thin accretion disk and bending the spacetime around it should look like (Luminet, 1979). In a similar manner, Falcke *et al.* (2000) showed some years later what would be the appearance of Sagittarius A* (Sgr A*), the radio source at the center of our galaxy, assuming the central compact object is a SMBH. Both M 87* and Sgr A* had a predicted *shadow* size, that is, the dark region encompassing the black hole which manifests as light rays bend near the event horizon, that could be, in principle, directly imaged trough very long baseline interferometry (VLBI) observations at 1.3 mm. Thus, the Event Horizon Telescope (EHT) Collaboration was born with that aim. In 2019 and 2022, the EHT collaboration published the first images (see Figure 1.2) of the supermassive black holes living at the heart of the giant elliptical galaxy M 87 and the Milky Way (Event Horizon Telescope Collaboration *et al.,* 2019a; b; c; d; e; f; 2021a;

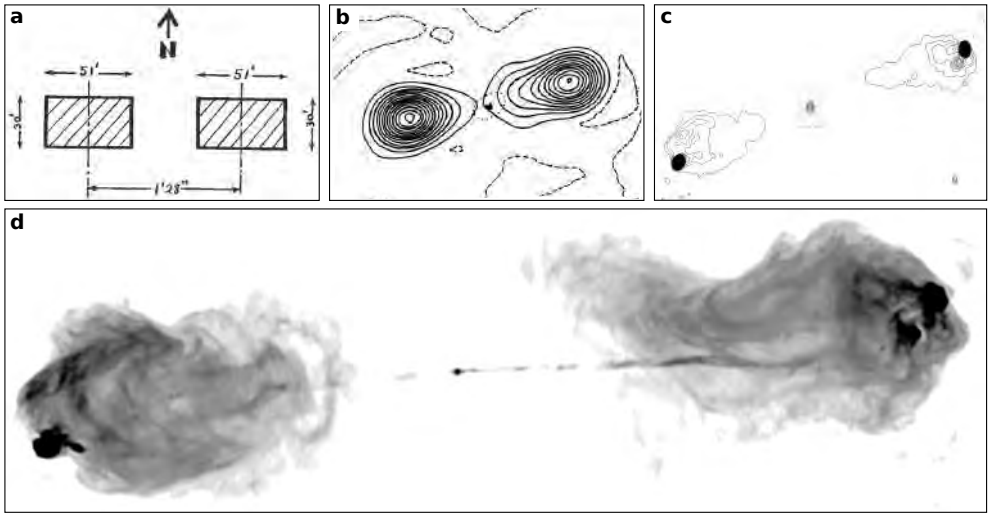

Figure 1.4: Cygnus A and the results of three decades of technical advances. **a,** The approximate intensity distribution inferred by Jennison & Das Gupta (1953) using an *intensity interferometer* at Jodrell Bank. **b,** Contour image obtained by Ryle *et al.* (1965) using the Cambridge One-Mile Telescope and Earth rotation synthesis at 1.4 GHz. **c,** Contour image obtained by Hargrave & Ryle (1974) using the Cambridge Five-Kilometre Radio Telescope at 5 GHz. **d,** Image of Cygnus A obtained by Perley *et al.* (1984) using the VLA at 4.9 GHz.

b; 2022a; b; c; d; e; f).

1.1.2 Relativistic Jets

The giant elliptical galaxy M 87 does not only host the first imaged black hole, but also the first relativistic jet detected. The discovery is attributed to H. D. Curtis, who in 1918 described it as “a curious straight ray apparently connected with the nucleus by a thin line of matter" (Curtis, 1918). The relative closeness of M 87 makes it one of the best laboratories to study relativistic jets at very different scales: from a few tens of Schwarzschild radii and horizon scales (Kim *et al.,* 2018; Event Horizon Telescope Collaboration *et al.,* 2019a) to kiloparsec scales (e.g., Pasetto *et al.,* 2021), as shown in the multi-wavelength image composition in Figure 1.3.

With the start of radio astronomy (Jansky, 1933; Reber, 1940) began the understanding of the nature of AGN jets. Nonetheless, the development of radio interferometry and aperture synthesis (see Section 1.3; Ryle & Vonberg, 1946; Ryle, 1962), and subsequent technological advances, truly opened the possibility to study and resolve AGN jets. An early and significant advance came with the realization that the bright radio source Cygnus A had a double component (two jet lobes) structure (Jennison & Das Gupta, 1953). Highly sensitive connected interferometers began operating in the 1970s and early 1980s, e.g., the Five-Kilometre Radio Telescope at Cambridge, England (Ryle, 1972), or the Very Large Array in New Mexico (VLA; Thompson *et al.,* 1980). A beautiful example of the capabilities offered by interferometry and these

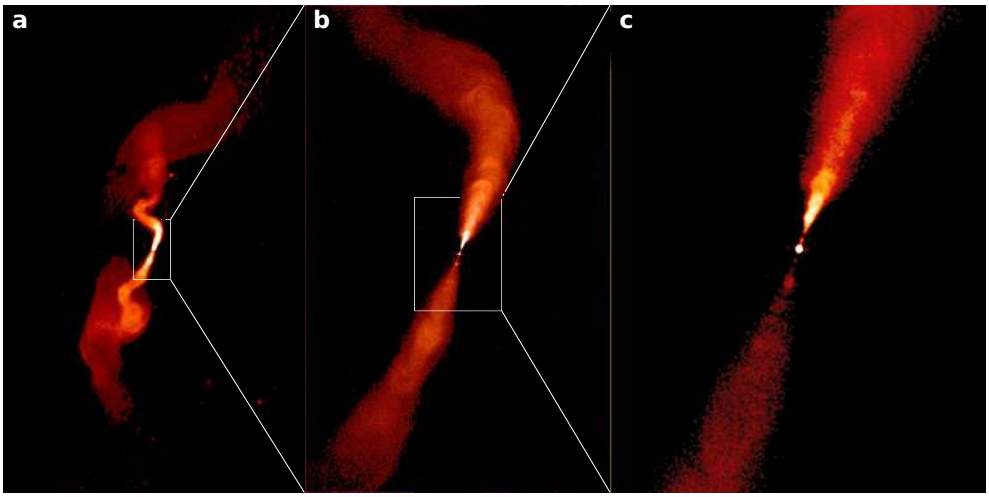

Figure 1.5: The multi-scale jet in 3C 31. a, VLA 20 cm image of the FR I plumed radio galaxy 3C 31. **b,** VLA 3.6 cm image of the conical jets. **c,** VLA 3.6 cm image of the inner jet and counter jet. Credit: NRAO, Laing & Bridle (2002) and Laing *et al.* (2008).

dedicated arrays is shown in Figure 1.4, where we see the evolution of the image quality achieved over three decades of technical advances and observations of the FR II radio galaxy Cygnus A. In Figure 1.5, we see as well the pair of powerful and highly collimated conical jets being ejected from the core of the FR I radio galaxy 3C 31.

Blazar jets, on the contrary, remained elusive until Very Long Baseline Interferometry (VLBI) observations succeeded (see Section 1.3.3). Because of their extremely small inclination angle, images of blazars were typically dominated by a very bright, Gaussian-like core. Nonetheless, important discoveries such as apparent superluminal motions were soon reported (see Section 1.2; Cohen *et al.,* 1971; Whitney *et al.,* 1971). VLBI surveys and kinematic studies of parsec-scale jets started to arise late in the 20th century (Wilkinson, 1995; Zensus, 1997). More recently, very extensive multi-wavelength VLBI surveys of a wide sample of AGN jets came trough thanks to new dedicated VLBI facilities such as the Very Long Baseline Array (VLBA; Napier *et al.,* 1994). For instance, the MOJAVE program (Lister *et al.,* 2016) or the VLBA-BU-BLAZAR (Marscher *et al.,* 2011; Jorstad *et al.,* 2017). Although these new VLBI arrays provided a boost in angular resolution, the detailed internal structure and jet launching region near the SMBH still remained hidden. The usual morphologies reported in blazar jets were funnel like with little cross section information. Advances in this direction came from space VLBI experiments operating at centimeter wavelengths, such as *RadioAstron* (Kardashev *et al.,* 2013; Gómez *et al.,* 2016; Giovannini *et al.,* 2018; Bruni *et al.,* 2021; Gómez *et al.,* 2022), and from highly sensitive millimeter wave VLBI experiments, such as the EHT at 1.3 mm (Kim *et al.,* 2020; Janssen *et al.,* 2021) and the joint observations of the Global Millimeter VLBI Array (GMVA) and the Atacama Large Millimeter Array (ALMA) at 3 mm (e.g., G.-Y. Zhao *et al.,* 2022). In Figure 1.6 we show state-of-the-art results from *RadioAstron* and GMVA+ALMA

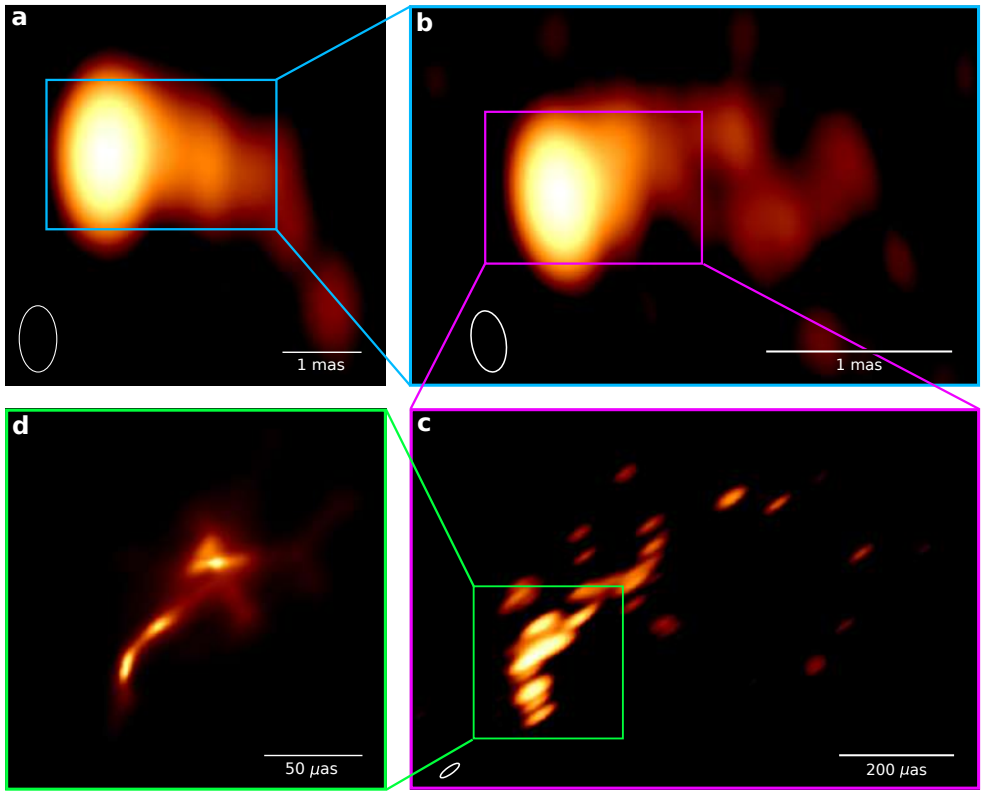

Figure 1.6: The innermost jet regions of the blazar OJ 287, VLBA image at 2 cm obtained on 5 May 2014 (MOJAVE program). **b,** VLBA image at 7 mm obtained on 3 May 2014 (VLBA-BU-BLAZAR program). **c,** *RadioAstron* image at 1 cm obtained on 4 April 2014 (Gómez *et al.,* 2022). **d,** GMVA+ALMA image at 3 mm obtained three years later, on 2 April 2017 (G.-Y. Zhao *et al.,* 2022).

observations of the archetypal blazar OJ 287, which exemplify the capabilities of these new instruments to unveil the internal structure and innermost regions of blazars (e.g., Gómez *et al.,* 2022; G.-Y. Zhao *et al.,* 2022).

Relativistic jets in AGNs are launched from the vicinity of the central SMBH. The astrophysical mechanism responsible for the formation an ejection of these jets is still subject of debate, but the two main models ususally invoked were formulated already in the late 1970s (BZ: Blandford & Znajek, 1977) and early 1980s (BP: Blandford & Payne, 1982). The BZ model proposes extraction of rotational energy from a Kerr black hole by strong, threaded magnetic fields as a mechanism capable of developing a pair of highly collimated plasma outflows emanating perpendicularly to the equatorial plane of the SMBH. In contrast, the BP model proposes that extraction of angular momentum from the accretion disk itself by strong poloidal magnetic field lines could be sufficient to trigger the ejection of a pair of relativistic jets. Although different, the BZ and BP models are not mutually exclusive and could coexist, leading to the

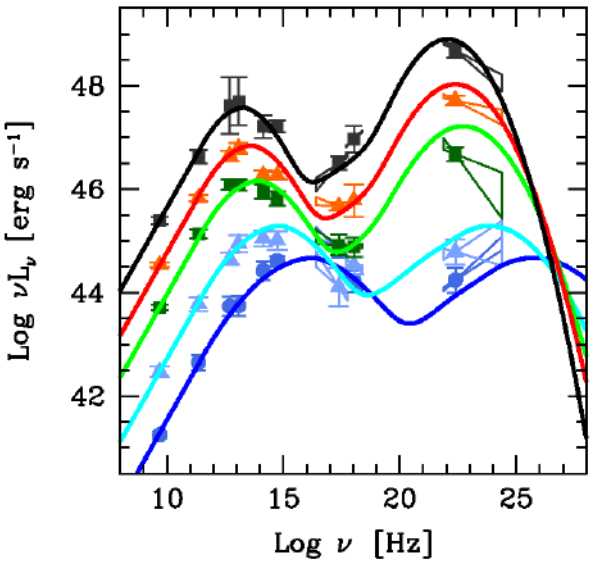

Figure 1.7: The blazar sequence. Average spectral energy distribution of a variety of blazar subclasses as described in Fossati *et al.* (1998) and Ghisellini *et al.* (1998)

formation of stratified jets with an external, slower sheath and an internal, faster spine (e.g., Hardee *et al.,* 2007). In any case, the presence of strong (helical) magnetic fields (e.g., McKinney & Blandford, 2009; Porth *et al.,* 2011; Tchekhovskoy *et al.,* 2011), along which particles will radiate (polarized) synchrotron emission (e.g., Blandford & Königl, 1979), are a fundamental ingredient of jet formation. This large initial magnetic energy will be converted gradually into kinetic energy, accelerating and propelling the jet away from the central engine (e.g., McKinney, 2006; Komissarov *et al.,* 2007; Lyubarsky, 2009; Mościbrodzka *et al.,* 2016).

1.2 Physics of AGN Jets

1.2.1 Radiative Processes

Synchrotron and inverse Compton radiation are the two main mechanism responsible for the observed nonthermal continuum emission in AGN jets. The spectral energy distribution (SED) of blazars, for instance, follow a two-hump Bactrian form as seen in Figure 1.7, where the low- and high-energy humps correspond to Synchrotron and inverse Compton emission, respectively. Simple one-zone models assume both humps originate at the same location of the jet, usually at the SMBH gravitational influence boundary (or Bondi radius, Bondi, 1952), where a *recollimation shock* may form (see Chapter 2 and Chapter 3), although more complex models involving variations along the jet are invoked as well in some occasions (e.g., Baloković *et al.,* 2016). In the following pages we focus on the basic physics of synchrotron radiation, responsible for the radio emission that we observe and analyze in the results presented in the next chapters. The content of this section is mainly based on Pacholczyk (1970), Rybicki & Lightman (1979), and Ghisellini (2013).

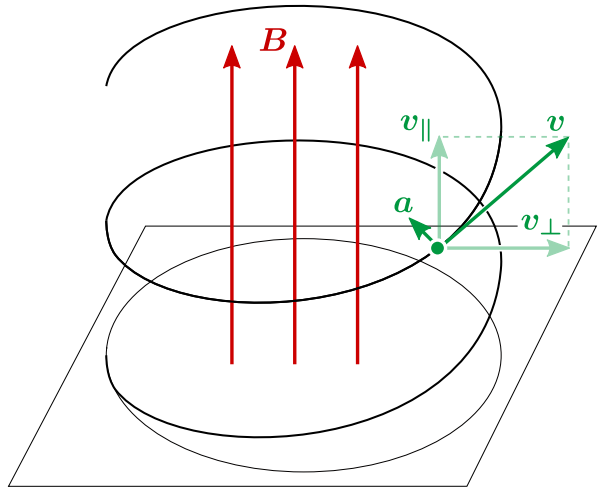

Figure 1.8: Synchrotron radiation. Helical motion of a particle in a uniform magnetic field.

1.2.1.1 Synchrotron Emission

Most of the radio emission radiated by AGN jets and supermassive blackholes comes from synchrotron radiation, that is, the radiation produced by charged particles moving at relativistic speeds and spiraling around magnetic field lines, see the sketch presented in Figure 1.8. Particles and magnetic field interact with each other trough the Lorentz force, which is defined as

$$F = \frac{d}{dt}(\Gamma m \boldsymbol{v}) = \Gamma m \frac{d\boldsymbol{v}}{dt} = \frac{q}{c}\boldsymbol{v} \times \boldsymbol{B} = \frac{q}{c} v B \sin\phi, \tag{1.2}$$

where $\Gamma = 1/\sqrt{1 - v^2/c^2}$ is the Lorentz factor, m, q, and $\boldsymbol{v}$ are the particle's mass, charge, and velocity, respectively, $\boldsymbol{B}$ is the magnetic field, and ϕ is the pitch angle, that is, the angle between the particle's velocity and the magnetic field. Decomposing the Lorentz force into its parallel and perpendicular components, we get

$$F_\parallel = \Gamma m \frac{dv_\parallel}{dt} = 0, \tag{1.3}$$

$$F_\perp = \Gamma m \frac{dv_\perp}{dt} = \frac{q}{c} v_\perp B, \tag{1.4}$$

and therefore

$$a_\parallel = 0 \qquad \text{and} \qquad a_\perp = \frac{qvB\sin\phi}{\Gamma m c}, \tag{1.5}$$

i.e., $v_\parallel$ is constant and, in the absence of an electric field, $|\boldsymbol{v}|$ will be constant, which then makes $|v_\perp|$ also constant. Since the acceleration is normal to the velocity, we obtain a helical motion of the particle along the magnetic field (see Figure 1.8).

The radiation emitted by such relativistic particles is Lorentz invariant and is given by the Larmor formula, that is

$$P = P' = \frac{2q^2}{3c^3}|\boldsymbol{a'}|^2 = \frac{2q^2}{3c^3}\left(a_\parallel'^2 + a_\perp'^2\right) = \frac{2q^2}{3c^3}\Gamma^4\left(a_\parallel^2 + \Gamma^2 a_\perp^2\right), \tag{1.6}$$

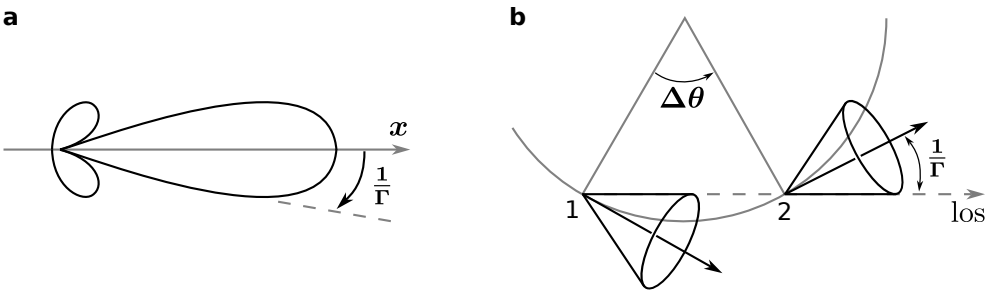

Figure 1.9: a, Angular distribution of radiation emitted by a relativistic particle with perpendicular acceleration and velocity. **b,** Emission cones at various points of a relativistic particle gyrating along a magnetic field line. An external observer will only measure the radiation emitted by the particle between points 1 and 2 due to aberration.

for an observer's and particle's rest frames K and K', respectively, where the particle's acceleration Lorentz-transforms from K' to K as

$$a'_{\parallel} = \Gamma^3 a_{\parallel} \qquad \text{and} \qquad a'_{\perp} = \Gamma^2 a_{\perp}. \tag{1.7}$$

Then, for a particle gyrating around magnetic field lines, we can use the acceleration terms derived before and obtain the synchrotron power emitted for a given pitch angle, that is, the angle between the magnetic field and the particle velocity, as

$$P(\phi) = \frac{2q^4}{3m^2c^3} B^2 \Gamma^2 \beta^2 \sin^2 \phi, \tag{1.8}$$

where $\beta = v/c$. We can further simplify this expression by taking into account that $U_B = B^2/8\pi$ is the magnetic energy density, $r_0 = q^2/mc^2$ is the particle radius, and $\sigma_T = 8\pi r_0^2/3$ is the Thomson scattering cross section. For an isotropic velocity distribution we can average the term $\sin^2 \phi$ over all angles, finally obtaining

$$P = \frac{4}{3} \sigma_T c \Gamma^2 \beta^2 U_B. \tag{1.9}$$

As the relativistic particle orbits magnetic field lines, its velocity and acceleration are perpendicular. Due to light aberration (see Section 1.2.2), the angular distribution of the radiation emitted by the particle takes the form of the left diagram in Figure 1.9, with most of its power being emitted in the forward direction within a cone of semiangle $1/\Gamma$. Because of this effect, an external observer will only see "pulses" of radiation when the line of sight falls within the particle's emission cone, that is, when the particle travels from point 1 to point 2 in Figure 1.9 (right panel). The effective duration of this pulse is then given by

$$\tau \approx \frac{\Delta\theta}{\omega_B \sin\phi}(1-\beta) = \frac{2mc}{qB\sin\phi}(1-\beta) \approx \frac{mc}{qB\Gamma^2 \sin\phi}, \tag{1.10}$$

where $\Delta\theta = 2/\Gamma$, $\omega_B = qB/\Gamma mc$ is the frequency of rotation, and $1 - \beta \approx 1/2\Gamma^2$ since $\Gamma \gg 1$. Finally, the critical frequency ν_c, around which most of the particle's power

will be emitted, is related to τ trough the expression

$$\nu_c = \frac{3}{4\pi}\frac{1}{\tau} = \frac{3}{4\pi}\frac{qB\Gamma^2 \sin\phi}{mc}. \tag{1.11}$$

Thus, the power emitted per frequency interval can be approximated as

$$P(\nu) \simeq \frac{12\pi B \sin\phi}{\Gamma mc^2}\left(\frac{\nu}{2\nu_c}\right)^{1/3} q^{(-\nu/\nu_c)+3}. \tag{1.12}$$

Instead of just one particle, we now consider an ensemble of relativistic particles gyrating around magnetic field lines. In AGN jets, it is typically assumed that particles follow a power law distribution of the form

$$N(E)dE = N_0 E^{-p} dE, \qquad E_{\min} \leq E \leq E_{\max}, \tag{1.13}$$

where $N(E)dE$ is the particle density between energies E and $E + dE$, p is the particle population spectral index, and the quantity N_0 depends on the internal energy density and rest-mass density of the particles (see Chapter 2). Then, assuming isotropic emission, the specific synchrotron *emissivity* is obtained as

$$j_\nu = \frac{1}{4\pi}\int N(E)P(\nu, E)dE, \tag{1.14}$$

and the specific intensity I_ν, or power radiated per unit area, frequency interval, and steradian, by an ensemble of non-thermal particles is obtained trough the radiative transfer equation

$$dI_\nu = j_\nu ds - \kappa_\nu I_\nu ds, \tag{1.15}$$

where the values of j_ν and κ_ν, the total emission and absorption coefficients, respectively, are given by the expressions (Pacholczyk, 1970)

$$j_\nu = c_5(p) N_0 (B\sin\vartheta)^{(p+1)/2}\left(\frac{\nu}{2c_1}\right)^{(1-p)/2}, \tag{1.16}$$

$$\kappa_\nu = c_6(p) N_0 (B\sin\vartheta)^{(p+2)/2}\left(\frac{\nu}{2c_1}\right)^{-(p+4)/2}, \tag{1.17}$$

where $c_1 = 3q/4\pi m^3 c^5$, c_5 and c_6 are dimensionless functions of p defined and tabulated in Pacholczyk (1970), and ϑ is the angle between the magnetic field, B, and the line of sight. The optical depth, τ_ν, is related to the absorption coefficient trough

$$d\tau_\nu = \kappa_\nu ds. \tag{1.18}$$

When $\tau_\nu < 1$, we would say that the medium trough which the photons emitted by our particles pass is optically thin, that is, photons are not absorbed by the medium. On the contrary, when $\tau_\nu > 1$ the medium turns optically thick. If we define the source function S_ν as the ratio j_ν/κ_ν, we obtain the following expression for the specific intensity by integrating Equation 1.15 assuming an homogeneous emitting source

$$I_\nu = S_\nu(1 - e^{-\tau_\nu}). \tag{1.19}$$

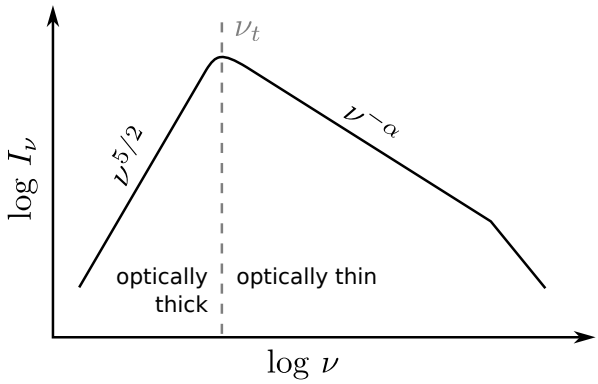

Figure 1.10: Synchrotron spectrum of a partially self-absorbed emitting source.

Then, in the optically thick regime we have that $I_\nu \propto \nu^{5/2}$, while in the optically thin regime $I_\nu \propto \nu^{-\alpha}$, where $\alpha = (p-1)/2$ is the synchrotron radiation spectral index. The transition from one regime to the other takes place at the turnover frequency ν_t. The typical synchrotron spectrum is illustrated in Figure 1.10.

1.2.1.2 Polarization

Because electrons are accelerated perpendicularly to the magnetic field, synchrotron emission is naturally polarized, and thus investigating the properties of the linearly (and even circularly) polarized emission from AGNs allow us to study the configuration of the magnetic field threaded to the relativistic jets and the magnetized plasma surrounding SMBHs. Ideally, for an optically thin homogeneus source with a particle energy distribution as that of Equation 1.13, the degree of linear polarization is given by the ratio (Pacholczyk, 1970)

$$\Pi = \frac{3p+3}{3p+7} = \frac{3\alpha+3}{3\alpha+5}. \tag{1.20}$$

The theoretical maximum degree of linear polarization for optically thin emission is $\Pi_{\rm max} = 0.75$, found when $\alpha \to 1$, which makes synchrotron emission highly polarized. In reality, any disordering of the magnetic field or Faraday depolarization (e.g., Pasetto *et al.*, 2018) will reduce the degree of polarization. On the contrary, if the emitting source is optically thick, Π usually peaks around 10% and takes the form

$$\Pi = \frac{3}{6p+13} = \frac{3}{12\alpha+19}. \tag{1.21}$$

An usual way to characterize the polarization of incoming electromagnetic waves is to decompose them into their Stokes parameters (Stokes, 1851): $\boldsymbol{I}$, which describes total intensity; $\boldsymbol{Q}$ and $\boldsymbol{U}$, which describe linearly polarized intensity; and $\boldsymbol{V}$, which describes circularly polarized intensity. Typical measured values of circular polarization in blazars are below 1%, thus we assume throughout this thesis that $V = 0$. By combining these different quantities, we obtain the following important polarization

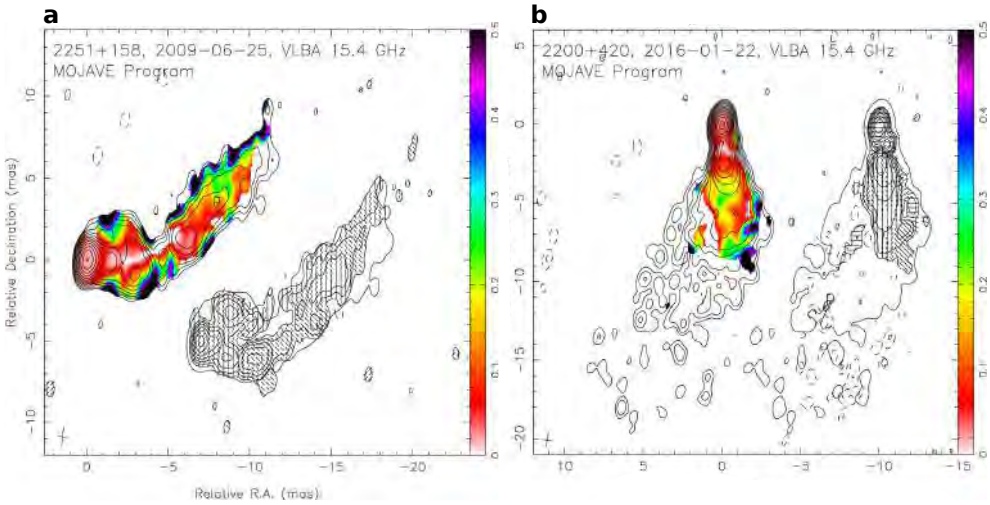

Figure 1.11: The parsec-scale polarization of blazar jets. a, Linear polarization of the jet in 3C 454.3. **b,** Same for BL Lac. Color indicates degree of linear polarization and bars the polarization angle vector or EVPAs. Credit: Lister *et al.* (2018).

products

$$P = \sqrt{Q^2 + U^2}, \qquad \Pi = \frac{P}{I}, \qquad \chi = \frac{1}{2}\arctan\left(\frac{U}{Q}\right), \tag{1.22}$$

where P is the linearly polarized intensity and χ is the polarization angle, commonly referred to as the electric vector position angle (EVPA). The latter indicates the electric field oscillation plane, which is perpendicular to the oscillation plane of the magnetic field. This quantity allow us to infer, for instance, the main component of the helical magnetic field. In Figure 1.11 we show two examples of blazar jets and the measured linear polarization. The jet in 3C 454.3 has EVPAs predominantly perpendicular to the propagation direction, which indicates a magnetic field dominated by its poloidal component. In contrast, the extended jet in BL Lac shows a polarization angle oriented in the same direction of the jet, thus indicating a helical magnetic field dominated by its toroidal component. Nonetheless, the core presents a more complex polarization pattern with sudden changes in the EVPAs in both cases, as expected as we move closer to the jet launching region where recollimation shocks or other phenomena may be present.

1.2.2 Relativistic Effects

Because particles forming the ejected plasma in AGN jets move at velocities close to the speed of light, special relativity effects transform some of the measured properties of these objects in our reference frame. Below we summarize them.

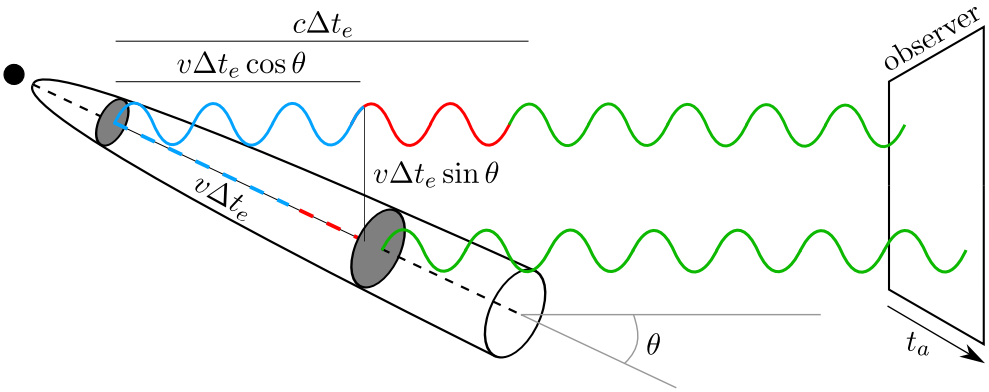

Figure 1.12: Schematic figure of a superluminal component traveling down the jet. This component emits a photon and then travels a distance $v\Delta t_e$, finally emitting another photon. If the jet is oriented close to the line of sight, the time interval measured between the two pulses will be significantly smaller than the real interval $\Delta t_a < \Delta t_e$. Depending on the component velocity and orientation, this effect can lead to apparent superluminal motions.

1.2.2.1 Light Aberration

When particles move at relativistic speeds, the angle formed between the line of sight and their velocity vector, or viewing angle θ, is subject as well to a Lorentz transformation between the observer's and particles' reference frames (K and K', respectively). Specifically, the transformation is given by the light aberration equations (Rybicki & Lightman, 1979)

$$\sin\theta' = \frac{\sin\theta}{\Gamma(1-\beta\cos\theta)}, \quad \cos\theta' = \frac{\cos\theta - \beta}{1-\beta\cos\theta}, \tag{1.23}$$

where Γ is the Lorentz factor, which let us remind, is just a function of the particles' velocity β (normalized by the speed of light c)

$$\Gamma = \frac{1}{\sqrt{1-v^2/c^2}} = \frac{1}{\sqrt{1-\beta^2}}. \tag{1.24}$$

Let us note that $\sin\theta = 1/\Gamma$ when $\theta' = \pi/2$ and then $\theta \approx 1/\Gamma$ since $\Gamma \gg 1$. Then, a particle radiating isotropically in a comoving reference frame will appear to radiate half of its power in a cone of semiangle $1/\Gamma$ in the observer's frame, as we discussed in the previous section.

1.2.2.2 Superluminal Motions

With the birth of VLBI (see Section 1.3.3) and the ability to resolve milliarcsecond features in AGN jets, radio astronomores discovered that jets are not continuous streams of plasma but formed by "knotty" structures (e.g. Biretta *et al.,* 1991; Ghisellini *et al.,* 1993; Jorstad *et al.,* 2005). By continuously observing these sources, it was clear that some of these features were traveling down the jet and, in some cases, with

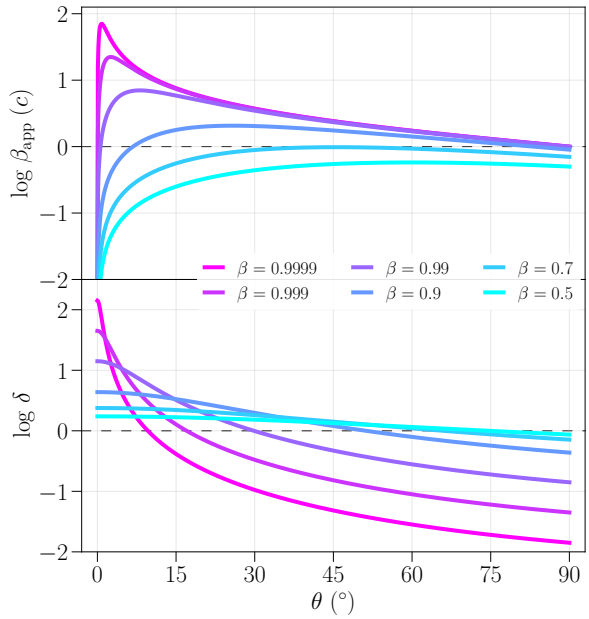

Figure 1.13: Apparent velocity, $\beta_{\rm app}$, and Doppler factor, δ, as a function of the jet orientation, θ, for different intrinsic fluid velocities, β.

apparent velocities exceeding the speed of light (e.g. Cohen *et al.,* 1971; Whitney *et al.,* 1971; Gómez *et al.,* 2000).

In the schematic Figure 1.12, we show a jet oriented with an angle θ with respect to the observer line of sight. One of these commonly observed bright features, or *components*, emit a photon and then travels down the jet a distance $v\Delta t_e$, finally emitting another photon. During the emitting time interval Δt_e, the difference in the path lengths between the first photon emitted and the component is $c\Delta t_e - v\Delta t_e \cos\theta$, thus the observer will measure a time interval $\Delta t_a = \Delta t_e(1 - \beta\cos\theta)$, and therefore $\Delta t_a \leq \Delta t_e$. Then, the apparent velocity of the component projected on the sky plane is

$$v_{\rm app} = \frac{v\Delta t_e \sin\theta}{\Delta t_a}, \qquad \text{or,} \qquad \beta_{\rm app} = \frac{\beta\sin\theta}{1-\beta\cos\theta}. \tag{1.25}$$

If $\theta \ll \pi/2$ and $\beta \to 1$, that is, the jet is oriented close to the line of sight and the component is traveling at relativistic speeds, $\beta_{\rm app}$ can reach much larger values than the speed of light, see Figure 1.13.

1.2.2.3 Doppler Boosting

Let's consider again Figure 1.12. Because of relativistic time dilation, the emitting time interval in the comoving ($\Delta t'_e$) and observer's (Δt_e) frames are related as $\Delta t_e = \Gamma\Delta t'_e$. Then, following the previous expressions

$$\Delta t_a = \Delta t_e(1 - \beta\cos\theta) \tag{1.26}$$
$$\Delta t_a = \Gamma\Delta t'_e(1 - \beta\cos\theta) \tag{1.27}$$
$$\Delta t_a = \Delta t'_e/\delta, \tag{1.28}$$

and therefore frequency transforms as

$$\nu = \delta \nu', \tag{1.29}$$

where

$$\delta = \frac{1}{\Gamma(1 - \beta \cos\theta)} \tag{1.30}$$

is the relativistic Doppler factor. This quantity accounts for the relativistic motion of the particles, trough the Lorentz factor Γ, and the classical Doppler shift of their frequency as they move towards (or away from) the observer.

If we write the specific intensity as the power radiated by an ensemble of particles per unit of time, frequency, area, and solid angle, then

$$I_\nu = \frac{h\nu dN}{dt d\nu dA d\Omega} = \frac{h\delta\nu' dN'}{(dt'/\delta)\delta d\nu' dA' (d\Omega'/\delta^2)} = \delta^3 I'_{\nu'}, \tag{1.31}$$

where dN and dA are Lorentz invariant, and $d\Omega = d\Omega'/\delta^2$. The bolometric intensity, which is obtained by integrating over all frequencies, transforms as $I = \delta^4 I'$. It is easily seen then from Figure 1.13 that for $\theta \to 0°$ and $\beta \to 1$, as in the case of blazar jets, the measured intensity is boosted by a large factor, which allow radio astronomers to observe intrinsically fainter sources. At the same time, this effect makes counter jets almost impossible to observe, since their emission is being deboosted by the same factor as particles move away from the observer.

1.3 Radio Interferometry

The resolving power of a telescope is determined by the observing wavelength λ and the diameter of its collecting surface D as

$$\theta \approx \frac{\lambda}{D}. \tag{1.32}$$

We call this relation the diffraction limit of the telescope. With a few exceptions, like the nearby sources M 87 or 3C 273, optical band observations lack the resolving power to image relativistic jets in AGNs due to the extreme angular compactness they subtend on the sky plane. For instance, an 8-meter ground optical telescope using adaptive optics can achieve a maximum angular resolution of about 15 mas. Although operating at radio frequencies allow single-dish radio telescopes to have collecting surfaces up to $\sim$100 m in diameter, their longer observing wavelength limits them to an angular resolution of around 17 as, for $\lambda = 7$ mm and $D = 100$ m. However, the development and application of interferometry techniques to radio observations (also known as aperture synthesis; Ryle & Hewish, 1960) open the possibility to actually image and resolve the structure of relativistic jets and other radio sources (see Figure 1.4). In the following sections we give an overview of the fundamentals of radio interferometry, primarily based on the contents of Thompson *et al.* (2017).

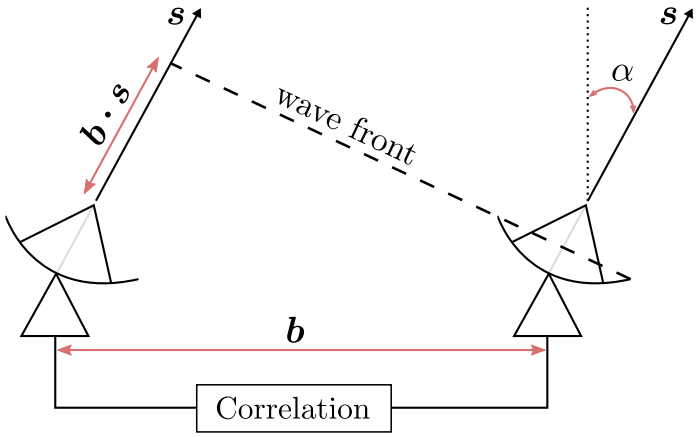

Figure 1.14: Simplified two-element interferometer

1.3.1 Basic interferometer

To illustrate and gain some intuition on how radio interferometry works, let us consider a simple and idealized one-dimensional, two-element radio interferometer observing a point source sufficiently distant (that is, the incident wave front can be considered a plane) at a monochromatic frequency ν, with spatial separation between the two antennas, or baseline $\boldsymbol{b}$, and the angle at which the wave front arrives to the telescopes α. This is summarized in Fig Figure 1.14. The *geometric delay* between the arrival times of the wave front at the two antennas is given by

$$\tau_g = \frac{\boldsymbol{b} \cdot \boldsymbol{s}}{c}, \tag{1.33}$$

where c is the velocity of light. Each antenna measures a voltage $V_i(t)$ which, taking into account the geometric delay, takes the form

$$V_1(t) = A\cos[2\pi\nu t], \tag{1.34}$$
$$V_2(t) = A\cos[2\pi\nu(t-\tau_g)]. \tag{1.35}$$

These voltages are then multiplied and time-averaged, a process commonly known as *correlation*. In this idealized case, the interferometer *cosine* response R_c or *fringe function* is

$$R_c := \langle V_1(t)V_2(t)\rangle = \frac{A^2}{2}\cos(2\pi\nu\tau_g) \tag{1.36}$$
$$= I\cos\left(2\pi\frac{\boldsymbol{b}\cdot\boldsymbol{s}}{\lambda}\right) = I\cos\left(2\pi\frac{b}{\lambda}\sin\alpha\right) = I\cos(2\pi ux), \tag{1.37}$$

where $I = A^2/2$ is the received power, $u = b/\lambda$ is the baseline length in wavelength units, and $x = \sin\alpha = \cos(\pi/2 - \alpha)$ is the direction cosine. As we see, this expression is just a function of the distance between the two telescopes and the location of the source on the sky.

Instead of a point source, let us now consider an extended source whose emission is spatially incoherent. The voltages measured by each antenna, as well as the geometric delay between them, are a function of the incident wave front vector $\boldsymbol{s}$ and are obtained by summing the voltages measured over the solid angle subtended by the source $d\Omega$. As before, the voltages are multiplied and time-averaged during correlation and the cosine response of the interferometer reduces to

$$R_c = \left\langle \iint V_1(\boldsymbol{s}) d\Omega_1 \iint V_2(\boldsymbol{s}) d\Omega_2 \right\rangle = \iint I(\boldsymbol{s}) \cos\left(2\pi \frac{\boldsymbol{b}\cdot\boldsymbol{s}}{\lambda}\right) d\Omega, \tag{1.38}$$

where $I(\boldsymbol{s})$ is the brightness distribution of the observed extended source. Since the cosine function is an even function, that is $\cos(x) = \cos(-x)$ for $x \in \mathbb{R}$, and any real-valued function can be decomposed into the sum of an even and real function, i.e. $I(\boldsymbol{s}) = I_E(\boldsymbol{s}) + I_O(\boldsymbol{s})$, we obtain

$$\iint I(\boldsymbol{s}) \cos\left(2\pi \frac{\boldsymbol{b}\cdot\boldsymbol{s}}{\lambda}\right) d\Omega = \iint (I_E(\boldsymbol{s}) + I_O(\boldsymbol{s})) \cos\left(2\pi \frac{\boldsymbol{b}\cdot\boldsymbol{s}}{\lambda}\right) d\Omega \tag{1.39}$$

$$= \iint I_E(\boldsymbol{s}) \cos\left(2\pi \frac{\boldsymbol{b}\cdot\boldsymbol{s}}{\lambda}\right) d\Omega, \tag{1.40}$$

since the product of an odd and an even function is an odd function and the integral of an odd function is zero. Thus, our interferometer is blind to odd symmetries in the source brightness distribution. In order to recover all the information, a *sine* response term is generated by introducing a 90 degree phase shift in the measurements of one telescope during correlation of the signal, which results in

$$R_s = \iint I(\boldsymbol{s}) \sin\left(2\pi \frac{\boldsymbol{b}\cdot\boldsymbol{s}}{\lambda}\right) d\Omega = \iint I_O(\boldsymbol{s}) \sin\left(2\pi \frac{\boldsymbol{b}\cdot\boldsymbol{s}}{\lambda}\right) d\Omega. \tag{1.41}$$

With this, we define the *complex visibility* measured by the pair of antennas forming our interferometer as the complex function

$$\mathcal{V}(\boldsymbol{b}) = R_c - iR_s \tag{1.42}$$

$$= \iint I(\boldsymbol{s}) \cos\left(2\pi \frac{\boldsymbol{b}\cdot\boldsymbol{s}}{\lambda}\right) d\Omega - i \iint I(\boldsymbol{s}) \sin\left(2\pi \frac{\boldsymbol{b}\cdot\boldsymbol{s}}{\lambda}\right) d\Omega \tag{1.43}$$

$$= \iint I(\boldsymbol{s}) e^{-2\pi i \boldsymbol{b}\boldsymbol{s}/\lambda} d\Omega, \tag{1.44}$$

where the visibility amplitude and phase are, respectively,

$$A = \sqrt{R_c^2 + R_s^2} \quad \text{and} \quad \phi = \tan^{-1}\left(\frac{R_s}{R_c}\right). \tag{1.45}$$

Thus, the previous formulation has led us to the van-Cittert-Zernike theorem (van Cittert, 1934; Zernike, 1938), which states that the interferometer fringe or visibility function is the Fourier transform of the source image or brightness distribution, and therefore we can recover the image of the observed source by simply performing an inverse Fourier transform of the measured visibilities. By defining appropriate angular

coordinates on the sky (x, y) and baseline coordinates orthogonal to the line of sight on Earth (u, v), we obtain the following, more general expressions

$$\mathcal{V}(u,v) = \iint I(x,y) e^{-2\pi i(ux+vy)} dxdy \quad \text{and} \quad I(x,y) = \iint \mathcal{V}(u,v) e^{2\pi i(ux+vy)} dudv. \tag{1.46}$$

1.3.2 Earth Rotation Synthesis

The previous relations make several assumptions; among them, an infinite sampling of the visibility distribution. In reality, each pair of antennas composing our radio interferometer samples only a spatial frequency, or (u, v) point, at a given time. As we keep adding telescopes to our interferometer, the number of spatial frequencies sampled grow as $n(n-1)/2$ for n telescopes. This, however, might not be sufficient to accurately constraint the underlying source image, especially for sparse interferometers like the EHT. The reliability of the final reconstructed image is directly related to a good sampling of the Fourier components. As Earth rotates, the baseline vector (u, v) changes and samples additional visibilities, thus increasing the filling fraction of the so-called (u, v) plane. Figure 1.15 illustrate how Earth rotation synthesis works with real data from the Sagittarius A* EHT observations on 10 April 2017. For the development and application of this technique, Martin Ryle won the Nobel Prize in Physics in 1974.

1.3.3 Very Long Baseline Interferometry

When we introduced radio interferometry in the previous sections, we were implicitly assuming that the telescopes forming the interferometer are physically connected. While this is a valid approach, we have examples like the Atacama Large Millimeter Array (ALMA), the search for higher angular resolution forced radio astronomers to consider interferometers with physically disconnected elements scattered around the globe. This technique, known as *Very Long Baseline Interferometry* (VLBI), is conceptually equal to radio interferometry, with the exception of data being recorded and stored independently at each antenna participating in the VLBI observations, and then delivered to a common central station for correlation. This procedure is only possible thanks to the accuracy of the hydrogen maser clocks located at each telescope, which time-stamp the data collected in order to successfully correlate the measured signals later on.

There are several VLBI networks operating currently, among them: the Very Long Baseline Array (VLBA), formed by 10 equal radio telescopes located across the United States; the European VLBI Network (EVN), formed by 22 radio telescopes across Europe and Asia; the East Asian VLBI Network (EAVN), formed by 21 radio telescope across Asia; the Global Millimeter VLBI Array (GMVA), formed by 15 radio telescopes across Europe and the United States; or the Event Horizon Telescope (EHT), formed by 11 radio telescopes (as of today) across the globe. Some of these facilities enable VLBI observations spanning baseline distances up to a whole Earth diameter, which for a wavelength of 1.3 mm implies a maximum angular resolution of around 20

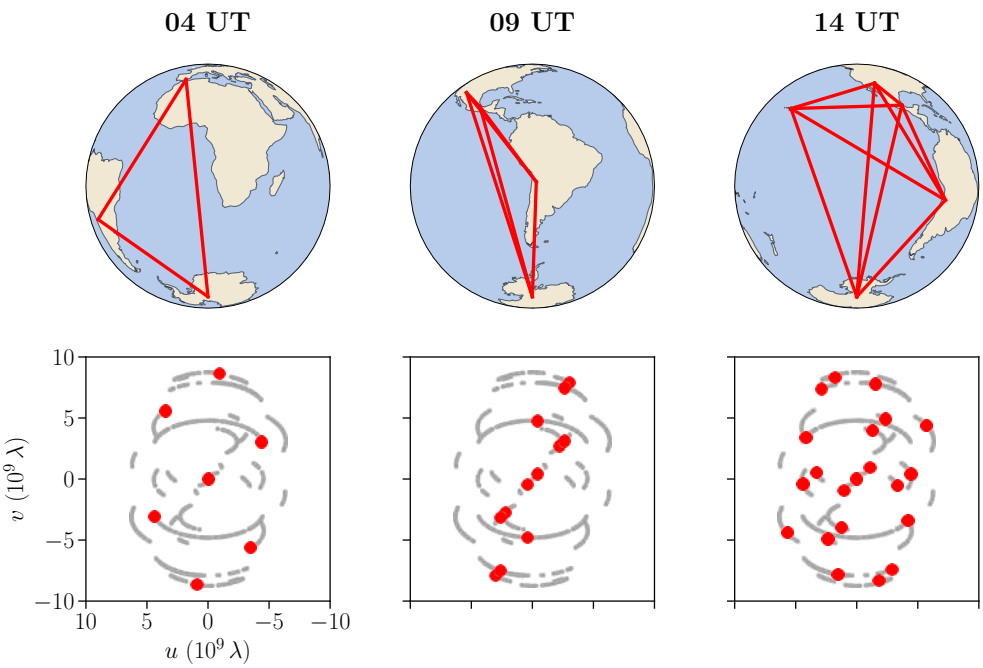

Figure 1.15: Earth rotation synthesis. Illustrated with the 2017 EHT observations of Sgr A* (Event Horizon Telescope Collaboration *et al.,* 2022a; b; c; d; e; f).

micro-arcseconds. Nonetheless, larger baselines can still be achieved by extending the VLBI network to space. In particular, the *RadioAstron* space VLBI mission (Kardashev *et al.,* 2013) made possible to observe radio sources at centimeter wavelengths with angular resolutions of tens of micro-arcseconds (see Chapter 4).

1.3.3.1 Data Calibration

The precise time-stamps assigned to the data collected on each station enables the cross-correlation of the measured signals. However, the telescopes forming the interferometer were in many cases not designed for VLBI purposes, and frequency offsets in the standards can induce fringe frequency and timing errors of the order of tenths of a microsecond over the course of an observation. It is therefore necessary to consider a two-dimensional search over a range of delay and fringe frequency (delay-rate) values in order to find the relationships that maximize the correlation function, a process known as fringe finding. Nonetheless, amplitude and residual phase errors will still be present in the complex visibilities produced after correlation due to inaccuracies in the array model, and therefore processes like time and frequency averaging to increase the signal-to-noise ratio, or image reconstruction, are not recommended. A measured visibility V_{ij}, that is, the output from the correlator, on a baseline between antennas i

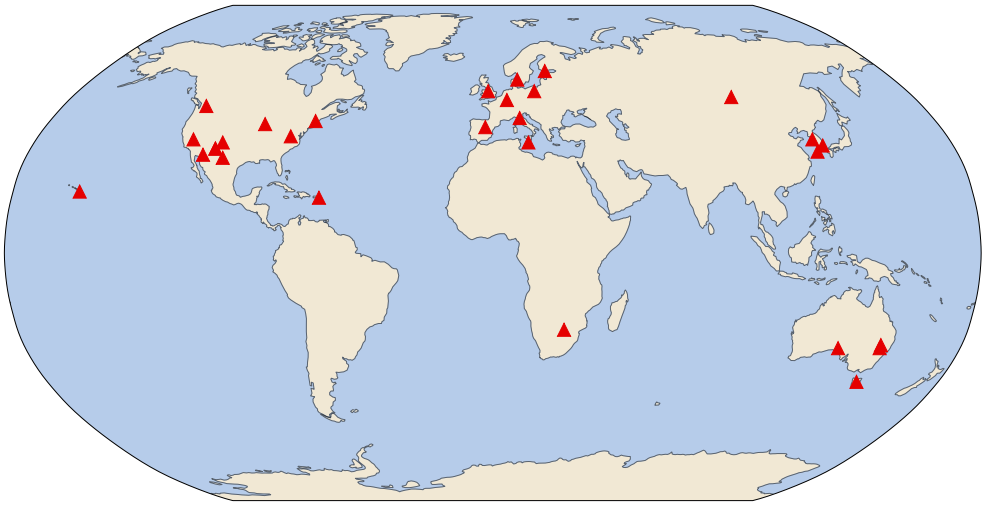

Figure 1.16: The global VLBI network. Geographycal distribution of the ground-based antennas participating in the *RadioAstron* observations of 3C 454.3 in March 2016.

and j is related to the true visibility $\mathcal{V}_{ij}$ on that same baseline as

$$V_{ij} = g_i g_j^* \mathcal{V}_{ij} + \epsilon_{ij} \tag{1.47}$$

$$= |g_i||g_j| e^{i(\varphi_i - \varphi_j)} \mathcal{V}_{ij} + \epsilon_{ij}, \tag{1.48}$$

where g_i and g_j are complex station gains, $|g_i|$ and φ_i are the gain amplitude and phase of station i, and ϵ_{ij} is thermal noise. Given a time interval and a frequency channel over which the correlator output is integrated, the measured ($^{\rm me}$) and true ($^{\rm tr}$) visibility phases are related as

$$\phi_{ij}^{\rm me} = \phi_{ij}^{\rm tr} + \varphi_i - \varphi_j, \tag{1.49}$$

and will change as a function of time and frequency as

$$r_{ij} = \frac{\delta \phi_{ij}^{\rm me}}{\delta t} \qquad \text{and} \qquad \tau_{ij} = \frac{\delta \phi_{ij}^{\rm me}}{\delta \nu}, \tag{1.50}$$

where r_{ij} is known as the fringe rate, delay rate, or simply rate, and τ_{ij} as the delay. Then, the process of data reduction after correlation reduces to solving for the stations gain amplitude, the gain phase, the rate, and the delay. In the following I briefly describe the standard procedure followed by VLBI users to correct for these complex station gains and approximate true visibilities from measured visibilities.

A priori amplitude calibration Calibrated visibility amplitudes $|\mathcal{V}_{ij}|$, measured in Jy, are related to the measured visibility amplitudes $|V_{ij}|$ as

$$|\mathcal{V}_{ij}| = |g_i|^{-1}|g_j|^{-1}|V_{ij}| \tag{1.51}$$

$$= \sqrt{\text{SEFD}_i}\sqrt{\text{SEFD}_j}|V_{ij}| \tag{1.52}$$

$$= \sqrt{\frac{T_{\text{sys},i}}{\text{DPFU} \times \eta_{\text{el},i}}}\sqrt{\frac{T_{\text{sys},j}}{\text{DPFU} \times \eta_{\text{el},j}}}|V_{ij}|, \tag{1.53}$$

for a baseline $i-j$, where SEFD is the telescope's System Equivalent Flux Density, or the flux density (in Jy) of a point source that would double the total system noise; T_{sys} is the antenna system temperature corrected for the atmosphere opacity; DPFU is the Degrees Per Flux Unit, which provides the conversion from temperature (K) to intensity (Jy) accounting for the antenna's aperture efficiency; and η_{el} is the antenna gain curve, which further models the aperture efficiency as a function of its elevation. These values are usually delivered by the telescopes participating in the VLBI observations, although it is not uncommon to face a situation in which the system temperatures of several stations are missing. This could complicate enormously the process of image reconstruction. As will be described in the next subsection, regularized maximum likelihood methods can naturally deal with this problem by incorporating full closure quantities during imaging.

There are three main software packages used by the VLBI community for data calibration: `AIPS` (Greisen, 2003), `CASA` (McMullin *et al.*, 2007), and `HOPS` (Blackburn *et al.*, 2019). Among the three, `AIPS` is the most used for centimeter VLBI experiments. For the *a priori* amplitude calibration described above, the tasks ANTAB and APCAL are frequently used, which generate a set of corrections subsequently applied to the data with the task CLCAL.

Fringe fitting The process of correcting for the residual rates and delays, as well as the station gain phases, is known as fringe fitting. In particular, the *global fringe fitting* algorithm (Schwab & Cotton, 1983) is widely used for this purpose. Visibility phases are referenced to a common antenna, usually the most sensitive one, for which the delay, rate, and phase are assumed to be zero. Since visibility amplitudes are calibrated separately, the number of parameters to solve for is $3(N-1)$, where N is the number of antennas participating in the observations. The true complex visibility to be determined is assumed to be that of a simple source model, usually a point source, as a "first guess". Even if the true source structure is significantly more complex than a point source, this method has been demonstrated extensively to be a sufficiently good approximation in order to correct the measured visibility phases. Then, the global fringe solution is found by performing a least-mean-square fit of the unknown parameters. In particular, for space VLBI observations, it has proven very useful in order to determine the visibility phase parameters of the space radio telescope (SRT) to first perform a fringe fitting of the ground stations only, apply the found solutions, and then search for the delay, rate, and phase of the SRT by *baseline stacking* the ground array. The most common `AIPS` task used for fringe fitting the data is FRING.

1.3.3.2 Image Reconstruction

As mentioned in subsection 1.3.1, the van-Cittert-Zernike theorem allows us to obtain the observed source intensity distribution, or simply the source image, from the ideal interferometric visibilities. Through the data calibration methods described above, we have approximated our measured complex visibilities to those invoked in Equation 1.46, and therefore we can attempt image reconstruction. Although many novel algorithms are being developed and used currently (e.g. full Bayesian posterior exploration methods, variational neural networks, etc. Broderick *et al.,* 2020; Sun & Bouman, 2021; Arras *et al.,* 2022), especially in the context of EHT observations, I will focus on two of them: traditional CLEAN (Högbom, 1974) and novel regularized maximum likelihood (RML) methods (Narayan & Nityananda, 1986).

Before briefly discussing these two techniques, let first introduce the concept of *closure quantities*. Apart from visibility amplitudes and phases, other *data products* can be derived from interferometric visibilities. In particular, *closure phases* and *closure amplitudes* are especially important, since these are naturally insensitive to station-based complex gain errors, e.g., phase corruption due to bad weather conditions in a particular geographical location. A closure phase is defined as the sum of three visibility phases forming a closed triangle $i-j-k$, and then from Equation 1.49 we get

$$\begin{aligned}\phi_{\mathrm{C},ijk} &= \phi_{ij}^{\mathrm{me}} + \phi_{jk}^{\mathrm{me}} + \phi_{ki}^{\mathrm{me}} && (1.54)\\ &= \phi_{ij}^{\mathrm{tr}} + \varphi_i - \varphi_j + \phi_{jk}^{\mathrm{tr}} + \varphi_j - \varphi_k + \phi_{ki}^{\mathrm{tr}} + \varphi_k - \varphi_i && (1.55)\\ &= \phi_{ij}^{\mathrm{tr}} + \phi_{jk}^{\mathrm{tr}} + \phi_{ki}^{\mathrm{tr}}. && (1.56)\end{aligned}$$

Given N antennas forming the interferometer, the total number of independent closure phases is $(N-1)(N-2)/2$. Likewise, a closure amplitude is defined as the product of four visibility amplitudes forming a quadrangle $i-j-k-l$, and from Equation 1.51 we get

$$|\mathcal{V}_{\mathrm{C},ijkl}| = \left|\frac{V_{ij}\,V_{kl}}{V_{ik}\,V_{jl}}\right| = \left|\frac{g_i g_j \mathcal{V}_{ij}\;\; g_k g_l \mathcal{V}_{kl}}{g_i g_k \mathcal{V}_{ik}\;\; g_j g_l \mathcal{V}_{jl}}\right| = \left|\frac{\mathcal{V}_{ij}\,\mathcal{V}_{kl}}{\mathcal{V}_{ik}\,\mathcal{V}_{jl}}\right|, \tag{1.57}$$

being the total number of independent closure amplitudes $N(N-3)/2$. Closure quantities are more difficult to interpret physically than complex visibilities because they mix different Fourier components. Nonetheless, closure phases deviating from 0 or 180 degrees imply asymmetry in the source brightness distribution.

CLEAN Integrated in several software packages (e.g. `DIFMAP`, Shepherd, 1997; `CASA`), the CLEAN algorithm family is the most extensively used method for VLBI image reconstruction. CLEAN directly applies an inverse Fourier transform to the visibility data, thus obtaining what is called the *dirty image*, the source intensity distribution convolved with the *dirty beam*, that is, the interferometer point source response or point spread function. Assuming the image brightness distribution can be accurately represented by a collection of point sources, the algorithm iteratively deconvolves from the dirty image the brightest features, often guided by an experienced user, which

makes CLEAN a subjective procedure. A source model is formed with all the delta component subtracted from the dirty image. Under ideal circumstances, the image obtained by convolving the previous model with the interferometer *nominal beam*, that is, a two-dimensional Gaussian fitted to the dirty beam, is a satisfactory representation of the true source image. Nonetheless, a sufficiently good data calibration is not always possible and the visibility data employed during imaging could contain large errors, leading to a bad image reconstruction. Therefore, it is usual to combine rounds of CLEAN-ing and *self-calibration*, a procedure in which complex station gains are tuned according to the image model created and the closure relationship derived from the complex visibilities. Typically, phase self-calibration is performed early in the imaging process and amplitude self-calibration at the end, when the image model is mature enough. Finally, the delta components are blurred to the nominal array resolution and the image residuals are added as a measure of the image noise level.

RML Bayesian-inspired RML methods are conceptually very different from CLEAN. They don't involve inverse Fourier transforming the visibility data, but instead they attempt to minimize the objective function

$$J(I) = \sum_{\text{data terms}} \alpha_D \chi^2_D(I, V_D) - \sum_{\text{reg. terms}} \beta_R S_R(I), \tag{1.58}$$

where the first term corresponds to a measure of the reconstructed image likelihood χ^2_D (for each data product D) and the second term to prior assumptions S_R (for each image regularizer R) on how this image should be. Contrary to CLEAN, RML methods can naturally incorporate full complex visibilities and closure quantities in the imaging process, thus constraining even more the space of possible solutions. In particular, when visibility amplitudes and/or phases suffer from a poor calibration, imaging with only closure information can provide an accurate description of the true image without the need to self-calibrate to a simplistic source model. Several *regularizations* can be imposed to the proposed image solution. For instance, the software package `eht-imaging` (Chael *et al.,* 2016; 2018) includes, among others, maximum entropy regularization, which favors images to be similar to a prior image; total (squared) variation, which encourages smoothness in the intensity between adjacent pixels; and ℓ_1-norm, which favors sparsity in the source brightness distribution. Another software package which also implements RML methods for image reconstruction is `SMILI` (Akiyama *et al.,* 2017a; b). Because of the ability of RML methods to work directly with closure data products, self-calibration is not as important as it is for CLEAN, although it is also possible and recommended to perform cycles of imaging and self-calibration until convergence to an image that best minimizes Equation 1.58. `eht-imaging` accomplishes this by means of gradient descent algorithms. To avoid getting stuck in local minima during optimization, each imaging iteration is initialized with a blurred version of the image solution found in the previous step. Supplementary information about the imaging process with RML methods can be found in Chapter 4.

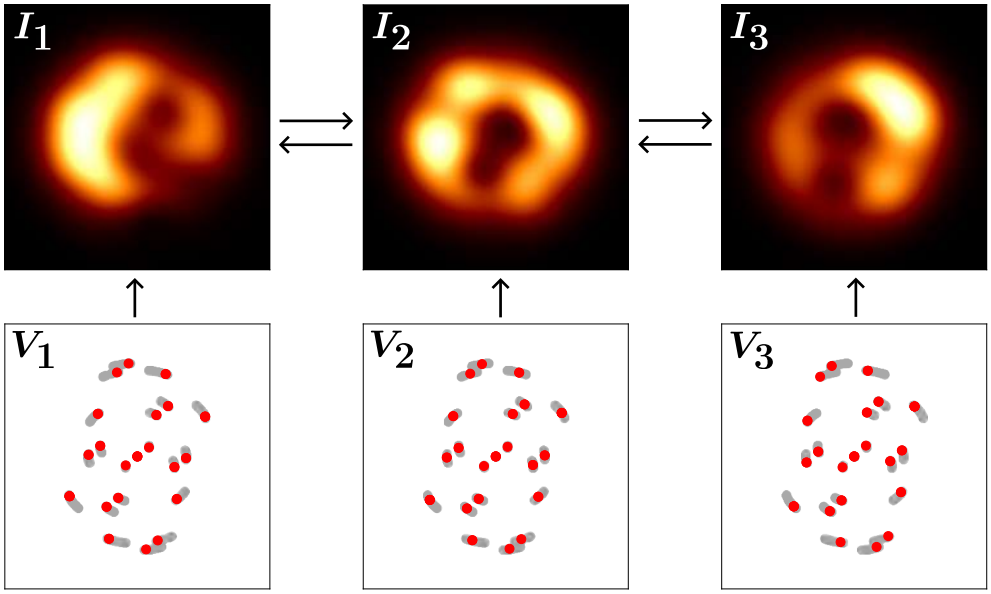

Figure 1.17: Movie reconstruction using StarWarps. Each individual frame, I_k, is reconstructed from its corresponding data segment, V_k, which is illustrated with the associated instantaneous (u, v)-coverage. Images and data are taken from real observations of Sgr A* (see Chapter 5).

1.3.3.3 Dynamic Imaging

Earth rotation synthesis works under the fundamental assumption that the astronomical object being observed will not change its brightness distribution during the course of an observation. While this is true for the immense majority of VLBI targets, there are a few types of sources that violate this assumption. The most remarkable example is Sagittarius A*, with a variability timescale of minutes. There are two main approaches for imaging visibility data affected by this intrinsic variability: inflate the error budget of the data so the variability is absorbed and then reconstruct a "mean" static image, or reconstruct a "movie" formed by several image frames describing the instantaneous brightness distribution of the source (see Event Horizon Telescope Collaboration *et al.,* 2022c). Within the latter approach, the recently developed RML dynamic imaging (Johnson *et al.,* 2017) and `StarWarps` (Bouman *et al.,* 2018) methods are capable of reconstructing movies of the source evolution during the observing window. RML dynamic imaging extends the objective function in Equation 1.58 to account for time regularization as well. `StarWarps` on the contrary adopts a probabilistic approach. Assuming that the latent images conforming the target movie reconstruction follow a multivariate Gaussian distribution, `StarWarps` can propagate information trough adjacent frames, thus alleviating the extremely sparse measurements corresponding to small segments of the visibility data where intrinsic source variability is negligible. By tuning up or down the temporal regularization parameter, different amounts of frame-to-frame variability are allowed to be reconstructed, similarly to RML dynamic

imaging. These features are encoded in the following potential functions defining the `StarWarps` dynamic imaging model:

$$\psi_{V_k|I_k} = \mathcal{N}_{V_k}(f_k(I_k),\, \sigma_k^2), \tag{1.59}$$

$$\psi_{I_k} = \mathcal{N}_{I_k}(\mu,\, \Lambda), \tag{1.60}$$

$$\psi_{I_k|I_{k-1}} = \mathcal{N}_{I_k}(I_{k-1},\, \beta_Q^{-1}\mathbb{1}), \tag{1.61}$$

where $\mathcal{N}(m, C)$ is a normal distribution with mean m and covariance matrix C. At each time k, a video frame I_k is related to the corresponding data segment V_k trough the measurement model $f_k(I_k)$. This frame is sampled from a multivariate Gaussian distribution with mean μ and covariance Λ, and adjacent frames are related to each other trough the temporal regularization parameter β_Q^{-1}. We illustrate this approach for movie reconstruction in Figure 1.17. In Chapter 5, the `StarWarps` algorithm is employed to recover, for the first time, the temporal evolution of the compact structure surrounding Sagittarius A*.

Chapter 2 | Polarimetric Emission from RMHD Jets. I.

A. Fuentes, J. L. Gómez, J. M. Martí, and M. Perucho

Total and Linearly Polarized Synchrotron Emission from Overpressured Magnetized Relativistic Jets
The Astrophysical Journal, **860**, 121 (2018)

Abstract

We present relativistic magnetohydrodynamic (RMHD) simulations of stationary overpressured magnetized relativistic jets which are characterized by their dominant type of energy, namely internal, kinetic, or magnetic. Each model is threaded by a helical magnetic field with a pitch angle of 45° and features a series of recollimation shocks produced by the initial pressure mismatch, whose strength and number varies as a function of the dominant type of energy. We perform a study of the polarization signatures from these models by integrating the radiative transfer equations for synchrotron radiation using as inputs the RMHD solutions. These simulations show a top-down emission asymmetry produced by the helical magnetic field and a progressive confinement of the emission into a jet spine as the magnetization increases and the internal energy of the non-thermal population is considered to be a constant fraction of the thermal one. Bright stationary components associated with the recollimation shocks appear presenting a relative intensity modulated by the Doppler boosting ratio between the pre-shock and post-shock states. Small viewing angles show a roughly bimodal distribution in the polarization angle due to the helical structure of the magnetic field, which is also responsible for the highly stratified degree of linear polarization across the jet width. In addition, small variations of the order of 26° are observed in the polarization angle of the stationary components, which can be used to identify recollimation shocks in astrophysical jets.

2.1 Introduction

Extragalactic, relativistic jets are associated to radio-emitting active galactic nuclei (AGN). They form in the environment of accreting supermassive black holes (SMBH) at the centre of the AGN. According to general relativistic magnetohydrodynamic (GRMHD) simulations (e.g., McKinney & Blandford, 2009; Tchekhovskoy *et al.,* 2011; Porth, 2013), relativistic jets originate from the extraction of rotational energy from the SMBH by magnetic field lines, via the Blandford-Znajek model (Blandford & Znajek, 1977). Following this model, the magnetic field carried to the black hole by the accreting plasma anchors to the black hole's ergosphere and is able to extract rotational energy from it due to the resistance of the magnetic lines to being rotated. The twisted magnetic lines generate an outwards Poynting flux that pushes particles out along the rotation axis. Recent observational results show that the magnetic field close the the galactic nucleus is of the expected order to trigger the formation of jets (Zamaninasab *et al.,* 2014; Baczko *et al.,* 2016).

The ejected particles are accelerated from sub-slow magnetosonic speeds to relativistic, super-fast magnetosonic speeds as the internal and magnetic energies of the field are converted into kinetic energy (Vlahakis & Königl, 2004; Komissarov *et al.,* 2007). The magnetic field, which is twisted at the formation site becomes predominantly toroidal. Jet expansion also favors the dominance of toroidal field, because the conservation of the magnetic flux makes this component to fall linearly with the jet radius, whereas the poloidal component falls with the square of the jet radius. Nevertheless, there are hints of helical field structure at parsec scales (e.g., Gabuzda *et al.,* 2015; Gómez *et al.,* 2016). Although it is unclear why the poloidal field is still relevant at those scales, this could be due to, e.g., shearing within the jet (Huarte-Espinosa *et al.,* 2011; Beuchert *et al.,* 2018). In summary, evidence brought by detailed polarimetric VLBI observations of parsec and sub-parsec-scale jets points towards the magnetic field having a structured helical morphology, probably modulated by a turbulent component.

The dynamics of relativistic jets have been studied through numerical simulations for more than twenty years now (e.g., Duncan & Hughes, 1994; Martí *et al.,* 1994; 1995; Koide *et al.,* 1996; Koide, 1997; Martí *et al.,* 1997; Nishikawa *et al.,* 1997; Komissarov & Falle, 1998; Nishikawa *et al.,* 1998). The difficulties to consistently compute the radiative output from jets taking into account relativistic and projection effects (e.g., Gómez *et al.,* 1993; 1994a; b) has translated in a smaller number of works devoted to the calculation of this output and the qualitative comparison with VLBI jets. The first papers were published early after the appearance of RHD numerical codes. Gómez *et al.* (1995, 1997), Mioduszewski *et al.* (1997), and Komissarov & Falle (1997) were able to reproduce the basic synchrotron structure of a stationary jet. In those cases, the emissivity was computed from purely RHD simulations, so magnetic field was added a posteriori, considering a dominant turbulent distribution, and the energetic losses of the particles in these calculations were purely adiabatic. Aloy *et al.* (2000) studied the asymmetric observed distribution of flux for the case of jets in which the magnetic field lines present helical structure. Agudo *et al.* (2001)

computed the dynamic changes produced in the observed jet when a perturbation is injected, and predicted the generation of the so-called 'trailing components'. These features represent the coupling of the oscillation in the jet cross section induced by the perturbation, with a Kelvin-Helmholtz pinching mode. Aloy *et al.* (2003) extended this study to 3D, confirming the aforementioned results and the possible changes in observed brightness of perturbations propagating following a helical trajectory. Mimica *et al.* (2009) introduced the self consistent evolution of the non-thermal particles along with the flow via the SPEV code, and included synchrotron losses to the picture. More recently Porth *et al.* (2011) has studied the synchrotron emission from jets through the acceleration region and obtained Faraday rotation measure at those scales. The authors were able to reproduce the frequency dependent core-shift as produced by opacity. Fromm *et al.* (2016) have studied the effect of the interaction of a traveling perturbation with a standing, recollimation shock, on the spectral evolution of the system in relativistic hydrodynamical simulations. RMHD simulations performed with the RAISHIN code (Mizuno *et al.,* 2006; 2011) were used in Gómez *et al.* (2016) to successfully reproduce the strength and spacing of stationary features observed in space-VLBI observations of BL Lacertae as produced by recollimation shocks. More recently, Fromm *et al.* (2018) have studied the influence of an obscuring torus on the asymmetries found between jet and counter-jet in misaligned sources following RHD simulations.

In two recent papers, Martí (2015b) and Martí *et al.* (2016) describe jet transversal equilibrium for super-fast magnetosonic jets for some particular configurations of the magnetic field. In the first of these papers, analytical solutions for the radial structure of jets in transversal equilibrium were obtained for given profiles of the jet's rest-mass density, flow velocity and helical magnetic field. In the second paper, numerical simulations (using a multidimensional RMHD code presented in Martí, 2015a; b) aimed to study the steady state of overpressured jets were presented. The overpressure of the jet at injection causes periodic expansions and recollimations via standing shocks, with distinct properties depending on the jet parameters. The paper covers a broad range of parameters including jets in the internal, magnetic or kinetic energy dominated regimes in an attempt to characterize their distinctive internal structure (transversal profiles, internal shocks). The next natural step is to continue this line of work by means of relating the magnetohydrodynamical structure of jets from numerical simulations with VLBI observations of actual extragalactic relativistic jets. In particular, in Jorstad *et al.* (2017) the authors have found that one fifth of the observed components at 43 GHz are quasi-stationary. With the aim of performing that comparison, we present here radiative simulations from RMHD simulations. The RMHD simulations have been performed with the same code as in Martí *et al.* (2016) using the one-dimensional approximation presented in Komissarov *et al.* (2015). As explained below, this approximation alleviates some of the difficulties in reaching steady jet solutions hence allowing to study in depth wider regions of the parameter space. The radiative simulations are performed using the code presented in Gómez *et al.* (1995, 1997). In order to make a better comparison, polarization of light is crucial, as it provides us with hints of the magnetic field structure. With this aim we

present here the first simulations of the polarized emission in the stationary features observed in the synthetic images associated with recollimation shocks.

The paper is organized as follows. In Section 2.2, we define the parameter space and the transversal structure of the RMHD jet models. The properties of the recollimation shocks produced by the pressure mismatch are analyzed attending to the jets dominant type of energy. In Section 2.3, we describe the code used to compute the synchrotron radiation emitted by the previous models, as well as the radio properties and polarization signatures derived from the internal structure of the jets and the presence of a helical magnetic field. Finally, we summarize our main conclusions in Section 2.4.

2.2 Stationary Overpressured Magnetized Relativistic Jet Models

2.2.1 Stationary relativistic jets in the quasi-one-dimensional approximation

Magnetohydrodynamical models have been computed following the approach developed by Komissarov *et al.* (2015) that allows to study the structure of steady, axisymmetric relativistic (magnetized) flows using one-dimensional time-dependent simulations. The approach is based on the fact that for narrow jets (*quasi-one-dimensional approach*) with axial velocities close to the light speed the steady-state equations of relativistic magnetohydrodynamics can be accurately approximated by the one-dimensional time-dependent equations with the axial coordinate acting as the *temporal* coordinate. Hence, our models are time-independent, two-dimensional (radial-, axial-dependent) models but are computed as time-dependent, one-dimensional (radial-dependent) models. Once the model has been computed, the axial dependence is recovered from the time dependence taking into account that for highly relativistic jets, $z \approx ct$, where t and z are the time and the axial coordinate, and c is the speed of light. Section 2.A.1 summarizes the main characteristics of Komissarov *et al.* (2015) approach.

Despite its approximate nature, using the quasi-one-dimensional approach to generate the axisymmetric steady jet models has many advantages for the present study. The most obvious one is that since the models are computed at the cost of one-dimensional calculations, the space of parameters can be swept densely. Moreover, the quasi-one-dimensional approach circumvents the inherent difficulties found by two-dimensional time-dependent codes to reach steady state solutions. In the case of the results presented by Martí *et al.* (2016) (MPG16, from now on) these difficulties led to i) limit the length of the steady models (to, e.g., 40 jet radii in low Mach number models), and ii) introduce a wide shear layer to damp the growth of instabilities in the transient phase in both magnetically-dominated and kinetically-dominated jet models. Using the quasi-one-dimensional approach allowed us to compute long enough jet models (specifically, 100 jet radii long) and avoid the use of wide shear layers.

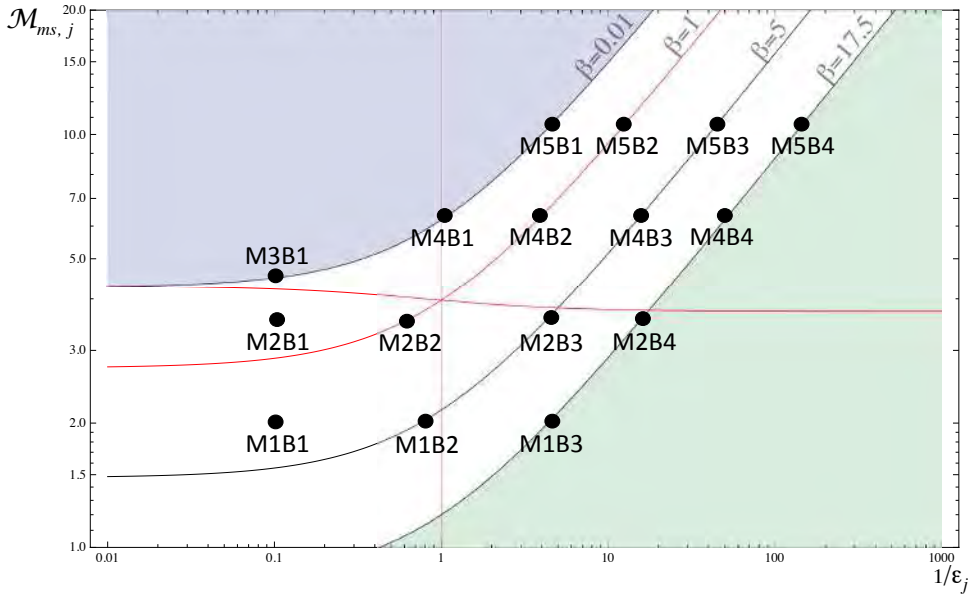

Figure 2.1: Distribution of the models considered in this paper on the $\mathcal{M}_{ms,j} - 1/\varepsilon_j$ diagram. Drawn are lines of constant magnetization (0, 1, 5 and 17.5). Kinetically dominated jets, magnetically dominated jets and hot jets occupy different zones separated by three (red) lines corresponding to models with $\varepsilon_j = c^2$, $\beta_j = 1$ and $\varepsilon_j \beta_j = c^2$. Hot jets are those with $\varepsilon_j > c^2$, $\beta_j < 1$; magnetically dominated jets occupy the zone with $\beta > 1$, $\varepsilon_j \beta_j > c^2$; kinetically dominated jets have $\varepsilon_j \beta_j < c^2$, $\varepsilon_j < c^2$. Pure hydrodynamic models are placed on the $\beta_j = 0$ line which bounds a forbidden region (in violet) corresponding to unphysical models with negative magnetic energies. Models in the green region beyond $\beta_j = 17.5$ would have negative gas pressures and are also forbidden.

On the other hand, among the main drawbacks of using the quasi-one-dimensional approximation is that it can not describe properly the flow dynamics at the jet/ambient medium interface as this interface is handled artificially to fix the boundary conditions every integration step.

2.2.2 Parameter space and transversal structure of the injected jet models

The stationary models have been generated according to the procedure described in MPG16 (see also Martí, 2015b). Axially symmetric, non-rotating, steady jet models are characterized by five functions, namely the jet density and pressure ($\rho(r)$, $p(r)$, respectively), the jet axial velocity, $v(r)$, and the toroidal and axial components of the jet magnetic field ($B^\phi(r)$, $B^z(r)$, respectively), whereas the static unmagnetized ambient medium is characterized by a constant pressure, p_a and a constant density, ρ_a. As discussed in the previous references, the equation of transversal equilibrium allows one to find the equilibrium profile for any of the functions, in particular the jet pressure, in terms of the others. As in these references, we have chosen top-hat

Table 2.1: Parameters defining the overpressured jet models.

Model	$\mathcal{M}_{ms,j}$	β_j	$\varepsilon_j\,[c^2]$	$\beta_j\varepsilon_j\,[c^2]$	K_1	$p_a\,[\rho_a c^2]$
M1B1	2.0	2.77	10.0	27.7	1.87	3.31×10^{-2}
M1B2	2.0	5.0	1.34	6.7	1.85	6.72×10^{-3}
M1B3	2.0	17.5	0.230	4.03	1.83	3.55×10^{-3}
M2B1	3.5	0.45	10.0	4.5	1.94	1.21×10^{-2}
M2B2	3.5	1.0	1.72	1.72	1.91	2.87×10^{-3}
M2B3	3.5	5.0	0.243	1.22	1.85	1.22×10^{-3}
M2B4	3.5	17.5	0.0661	1.16	1.83	1.02×10^{-3}
M3B1	4.505	0.01	10.0	0.1	2.00	8.42×10^{-3}
M4B1	6.0	0.01	1.16	0.0116	2.00	9.72×10^{-4}
M4B2	6.0	1.0	0.291	0.291	1.91	4.86×10^{-4}
M4B3	6.0	5.0	0.0724	0.362	1.85	3.62×10^{-4}
M4B4	6.0	17.5	0.0216	0.378	1.83	3.33×10^{-4}
M5B1	10.0	0.01	0.251	0.00251	2.00	2.11×10^{-4}
M5B2	10.0	1.0	0.0900	0.0900	1.91	1.50×10^{-4}
M5B3	10.0	5.0	0.0250	0.125	1.85	1.25×10^{-4}
M5B4	10.0	17.5	0.00770	0.135	1.83	1.19×10^{-4}

Note. Tabulated data denote jet model, (relativistic) magnetosonic Mach number, magnetization, specific internal energy, specific magnetic energy, overpressure factor at the jet surface, and ambient medium pressure, in this order.

profiles for the density, axial flow velocity and axial magnetic field and considered a particular profile for the toroidal component of the magnetic field. With all this into account, once fixed the equation of state (that we assume as the one corresponding to a perfect gas with constant adiabatic index $4/3$), the jet models are characterized by six parameters, namely the constant values of the jet density (ρ_j) and axial flow velocity (v_j), and the averaged values of the jet overpressure factor, K, the internal (relativistic) magnetosonic Mach number, $\mathcal{M}_{\mathrm{ms},j}$, the jet magnetization, β_j, and the magnetic pitch

angle, ϕ_j. The selection of the parameters defining the jet models is justified by their role in the characterization of the jet internal structure. Appendix B summarizes the procedure to build the jet models from the chosen set of parameters. Parameters ρ_j, v_j, K and ϕ_j have the same fixed values as in MPG16 ($0.005\rho_a$, $0.95c$, 2, 45°, respectively). Table 2.1 lists the values of the remaining parameters defining the models which are also displayed on the magnetosonic Mach number-specific internal energy diagram shown in Figure 2.1. The magnetosonic Mach number covers the same range of variation (2.0 to 10.0) as in MPG16 whereas the interval of the jet magnetization has been expanded to cover models with passive magnetic fields ($\beta_j = 0.01$) as well as models with the maximum allowed magnetizations (compatible with a positive gas pressure at the jet surface; $\beta_j \approx 17.5$ for the current choice of jet parameters). Hot jets, magnetically dominated jets and kinetically dominated jets occupy different regions in the Mach number-specific internal energy diagram (see the caption of Figure 2.1). According to this, models M2B1 and M3B1 are hot; M1B1, M1B2 and M1B3 are magnetically dominated; and M4B2, M4B3, M4B4, M5B1, M5B2, M5B3 and M5B4 are kinetically dominated. The remaining models are hybrid: M2B2, between hot and magnetically dominated jets; M2B3 and M2B4, between magnetically dominated and kinetically dominated jets; M4B1, between hot and kinetically dominated jets. As in MPG16, the transition between the jet and the ambient medium is smoothed by means of a shear layer of width Δr_{sl} by convolving the sharp jumps at the jet surface with the function $\mathrm{sech}(r^m)$ for some integer m. However, unlike in that paper, where uncomfortably wide shear layers had to be enforced to stabilize the jets against pinch instabilities, a thin shear layer ($m = 16$, $\Delta r_{sl} \approx 0.12$) has been imposed in all the present models.

It is important to note that since all the models have identical jet rest-mass density and axial flow velocity, all the models have the same kinetic energy flux in the limit of zero internal energy (cold jets) and zero magnetization. This means that the jets' total energy flux is different from model to model and increases for models with increasing internal and magnetic energy densities (in practice, increasing ε_j and increasing $\varepsilon_j\beta_j$). The ambient pressure follows the same trend. Since it sets the condition for the jet transversal equilibrium (for fixed jet average overpressure factor), the ambient pressure increases for increasing jet total pressure (or, again, for increasing ε_j and increasing $\varepsilon_j\beta_j$).

Finally, two out of the sixteen models analyzed in the present paper coincide with those in MPG16, namely M1B1 (PH02) and M2B1 (HP03). The comparison of the original two-dimensional models with the corresponding quasi-one-dimensional models helps us to gauge the quality of the approximation considered in the present paper (see Section 2.A).

2.2.3 Internal structure

In all the models, the equilibrium of the jet against the underpressured ambient medium is established by a series of standing oblique shocks (recollimation shocks) and gentle expansions and compressions of the jet flow. On the other hand, a jet

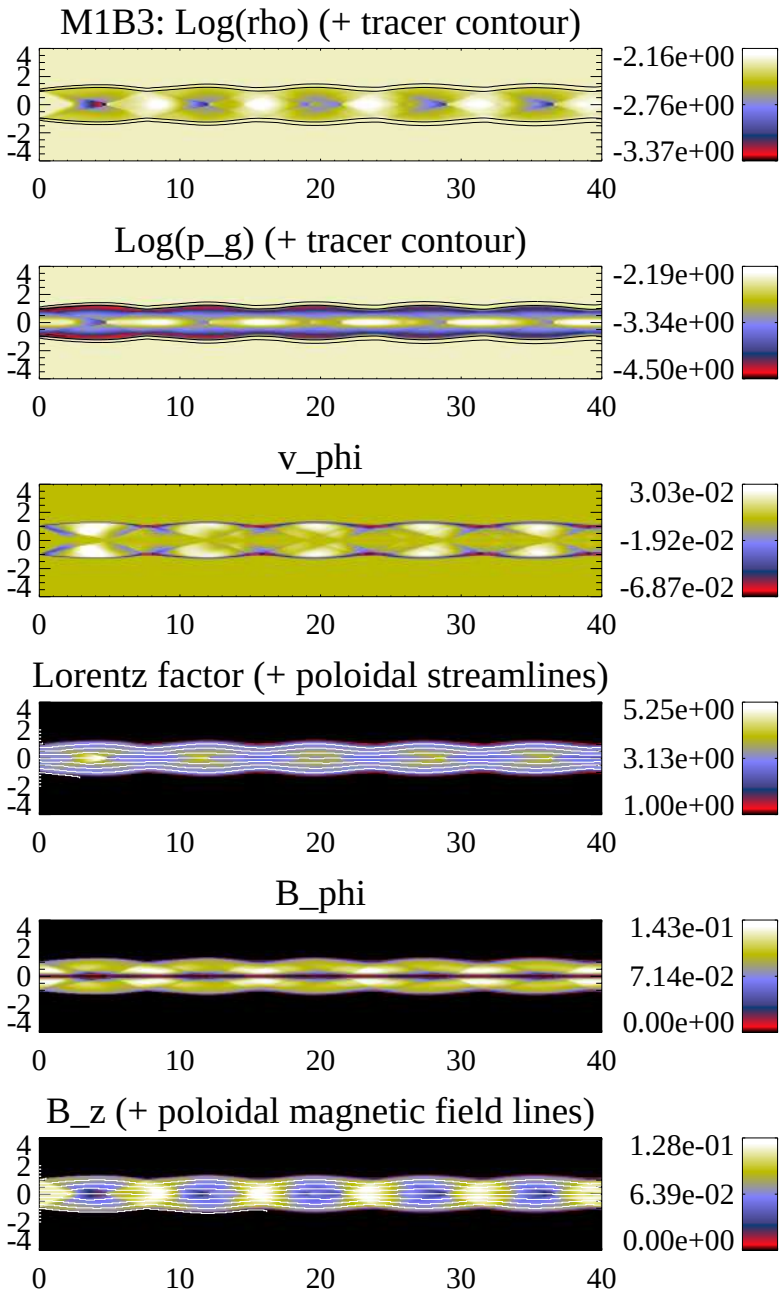

Figure 2.2: Steady structure of the magnetically dominated jet model M1B3. From top to bottom, distributions of rest-mass density, gas pressure, toroidal flow velocity, flow Lorentz factor, and toroidal and axial magnetic field components. Poloidal flow and magnetic field lines are overimposed onto the Lorentz factor and axial magnetic field panels, respectively. Two contour lines for jet mass fraction values 0.005 and 0.995 are overplotted on the rest-mass density panel.

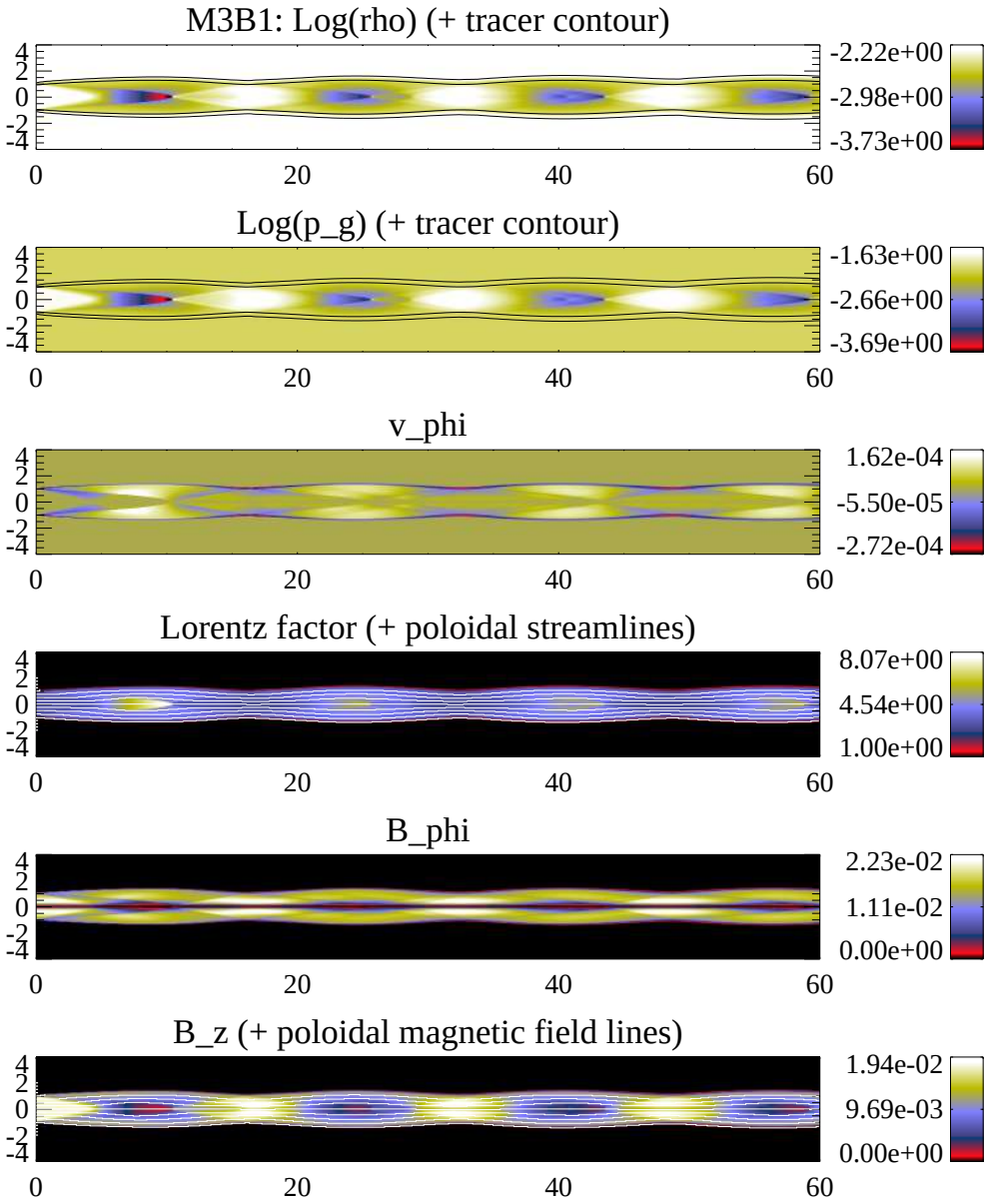

Figure 2.3: Steady structure of the hot jet model M3B1. Panel distribution as in Figure 2.2.

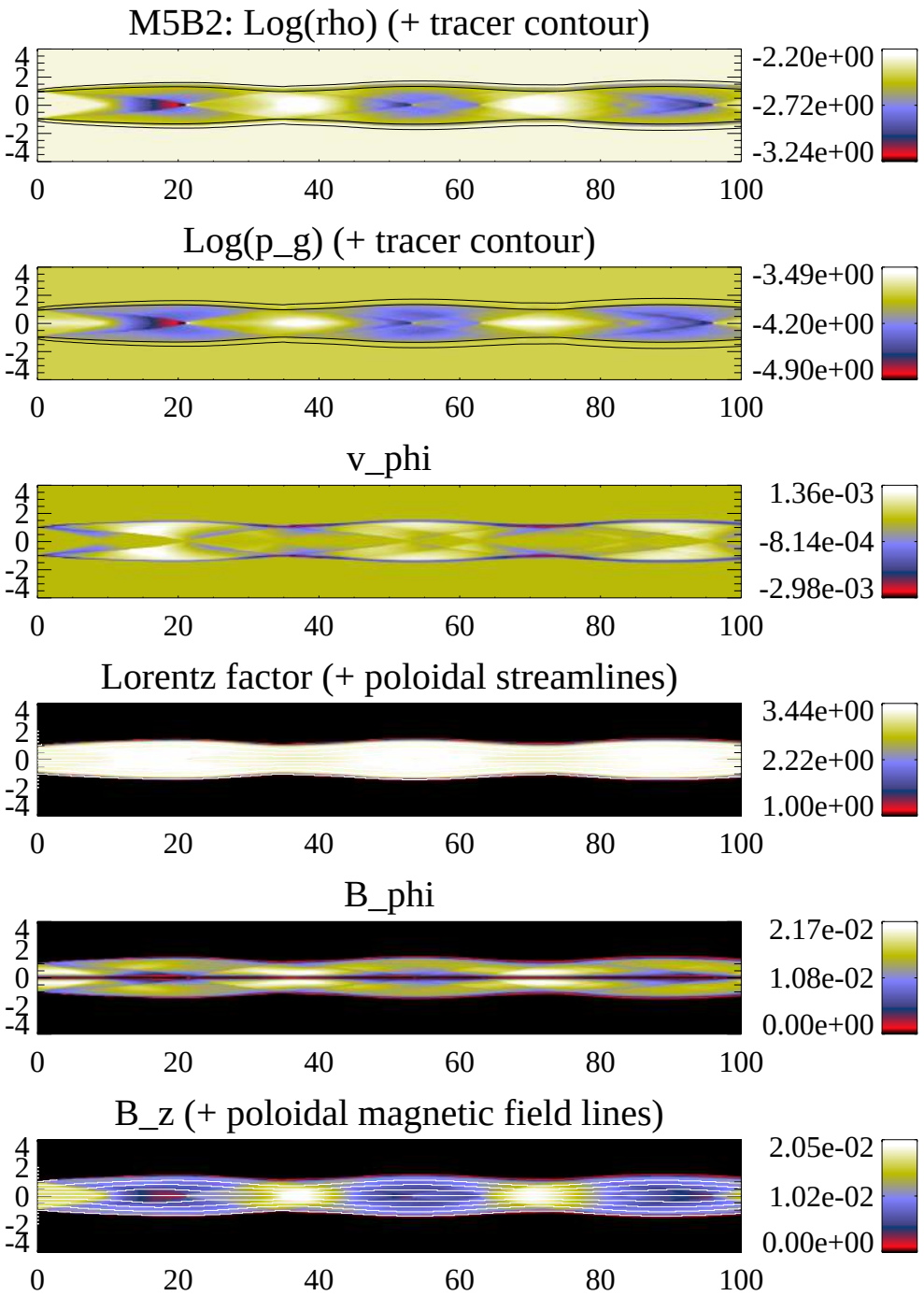

Figure 2.4: Steady structure of the kinetically dominated jet model M5B2.Panel distribution as in Figure 2.2. Note that the axial scale has been compressed by a factor of 2 with respect to the radial one.

propagating through a pressure-decreasing atmosphere with a steep enough gradient would lose the internal shock structure after few periods due to the sideways jet expansion and the corresponding decrease in energy flux per unit area (e.g., Gómez *et al.,* 1995). However, the fact that in our models the ambient medium is homogeneous helps to keep this internal structure periodic. The expansions and compressions produce a net toroidal component of the Lorentz force that causes the growth of nonzero toroidal flow speeds (of the order of a few percent[1]). Superimposed to these periodical structures, as a result of both the magnetic pinch exerted by the toroidal magnetic field and the gradient of the magnetic pressure, models with large magnetizations tend to concentrate most of their internal energy in a thin, hot spine around the axis.

For fixed overpressure factor, the properties of the recollimation shocks (i.e., strength, obliquity) and those of the radial oscillations (amplitude, wavelength) are governed by the magnetosonic Mach number, that controls the angle at which waves penetrate into the jet (Mach angle) whose steepening forms the recollimation shocks, and the specific internal energy, that establishes the amount of energy that can be exchanged into kinetic energy at shocks/radial oscillations. Figures 2.2 to 2.4 correspond to models M1B3, M3B1 and M5B2 which have been chosen as representative of magnetically dominated, hot, and kinetically dominated models, respectively. The figures include panels of the rest-mass density and pressure (in logarithmic scale), azimuthal flow velocity and Lorentz factor, and toroidal and axial components of the magnetic field. Both recollimation shocks and radial oscillations are clearly seen in all the panels[2].

In the following paragraphs we describe in a more quantitative way the properties of recollimation shocks and radial oscillations, and the jet transversal structure, as functions of three scalar quantities defining the jet models, namely the magnetosonic (relativistic) Mach number, the specific internal energy in units of the specific rest-mass energy and the magnetization.

In contrast to the results shown in MPG16, the use of a thin shear layer in the present calculations allows the formation of recollimation shocks in all the models. Crossing a shock is an irreversible process. The irreversibility manifests in the increase in specific entropy of the fluid parcels going through the shock. Since the specific entropy of the fluid parcels can never decrease along the evolution, the pre-shock flow conditions can not be recovered downstream and the sequence of recollimation shocks in the overpressured jet models can not be exactly periodic. However, the fact that shocks appear so alike is an evidence that the change in entropy across them is small and that the shocks are weak. Besides this (small) difference between shocks due to the net increase of specific entropy along the streamlines, the imposed boundary conditions at the jet's inlet sets an additional difference between the first shock and the rest (see Figures 2.2 to 2.4).

[1] Besides having a physical origin, the smallness of these toroidal velocities validates the self-consistency of the approximation used in our simulations.

[2] A series of figures as Figures 2.2 to 2.4 for all the models discussed in the paper can be found at Extended Data Figures 2.20 to 2.22.

Table 2.2: Properties of the recollimation shocks.

Model	$\bar{p}_s\,[\rho_a c^2]$	Δp_s	$\bar{p}_{m,s}\,[\rho_a c^2]$	$\Delta p_{m,s}$	$\bar{\Gamma}_s$	$\Delta\Gamma_s$	$\phi_s\,[^\circ]$
M1B1	1.9×10^{-2}	21 ± 11	9.5×10^{-3}	20 ± 9	3.6	2.2 ± 0.4	13.0
M1B2	4.3×10^{-3}	18 ± 10	3.1×10^{-3}	20 ± 10	3.4	1.9 ± 0.2	12.0
M1B3	2.3×10^{-3}	10 ± 5	2.2×10^{-3}	18 ± 11	3.2	1.5 ± 0.1	12.5
M2B1	6.7×10^{-3}	23 ± 11	1.2×10^{-3}	22 ± 10	3.9	2.1 ± 0.3	7.0
M2B2	1.8×10^{-3}	17 ± 7	6.5×10^{-4}	23 ± 10	3.7	1.6 ± 0.1	8.5
M2B3	6.9×10^{-4}	11 ± 3	6.5×10^{-4}	18 ± 6	3.4	1.3 ± 0.1	8.5
M2B4	5.9×10^{-4}	9 ± 2	7.0×10^{-4}	17 ± 5	3.3	1.3 ± 0.1	9.5
M3B1	5.6×10^{-3}	28 ± 15	2.8×10^{-4}	31 ± 15	4.3	2.2 ± 0.3	5.5
M4B1	7.7×10^{-4}	22 ± 11	3.5×10^{-5}	40 ± 20	3.6	1.5 ± 0.1	4.0
M4B2	2.4×10^{-4}	12 ± 4	1.3×10^{-4}	26 ± 11	3.3	1.2 ± 0.1	5.0
M4B3	2.0×10^{-4}	7 ± 2	2.1×10^{-4}	15 ± 5	3.2	1.1 ± 0.1	5.5
M4B4	1.8×10^{-4}	7 ± 2	2.5×10^{-4}	13 ± 4	3.2	1.1 ± 0.1	5.5
M5B1	1.6×10^{-4}	21 ± 10	7.5×10^{-7}	60 ± 40	3.2	1.2 ± 0.1	3.0
M5B2	9.1×10^{-5}	10 ± 3	4.4×10^{-5}	30 ± 11	3.2	1.1 ± 0.1	3.0
M5B3	6.7×10^{-5}	6 ± 2	1.5×10^{-4}	11 ± 5	3.2	1.1 ± 0.1	3.5
M5B4	6.2×10^{-5}	5 ± 2	1.8×10^{-4}	10 ± 4	3.2	1.1 ± 0.1	3.5

Note. Tabulated data denote jet model, averages ($\bar{x}$) and jumps (Δx) of gas pressure, magnetic pressure, and Lorentz factor across shocks (see text for definitions), and shock angle.

The energy involved in the shocks can be estimated through the averages of gas pressure and magnetic pressure[3] across the shock, respectively, $\bar{p}_s = (p_1 + p_2)/2$, $\bar{p}_{m,s} = (p_{m,1} + p_{m,2})/2$. In these expressions, subindex 1 (2) refers to pre-(post-)shock quantities. A criterion to determine the shock strength is the magnitude of the jumps of gas pressure, $\Delta p_s = p_2/p_1$, and magnetic pressure, $\Delta p_{m,s} = p_{m,2}/p_{m,1}$,

[3]Let us remind the reader that the gas pressure is one third of the internal energy density (for a perfect gas with adiabatic exponent $4/3$), whereas the magnetic pressure is one half of the magnetic energy density.

equal, respectively, to the jumps of internal and magnetic energy densities. Finally, connected to the jump in gas pressure is the jump in the flow Lorentz factor. Quantities $\Delta\Gamma = \Gamma_1/\Gamma_2$ (note the change in the definition with respect to Δp_s and $\Delta p_{m,s}$) and $\bar{\Gamma}_s = (\Gamma_1 + \Gamma_2)/2$ define the jump in Lorentz factor and the average between the pre- and post-shock values, respectively.

Table 2.2 collects the values of all these quantities calculated at some particular radius close to the axis for the shocks of the models in Table 2.1[4]. As seen from the table and the top panel of Figure 2.5, there is a correlation between both the average gas pressure and the average magnetic pressure involved at the shocks, and the ambient pressure. In the case of the average gas pressure, it is always an almost fixed fraction ($50-60\%$ for high-magnetization models; close to 80% for low-magnetization ones) of the ambient pressure of the corresponding model. In the case of the average magnetic pressure it is almost zero in the lowest magnetized models and increases up to 75% of the ambient pressure in the models with the largest magnetizations[5].

The jumps presented in Table 2.2 are calculated at a particular radius close to the jet axis where the shocks can be more planar and hence stronger than at larger radii. The large values of the gas pressure jumps (in the range $\approx 5-30$) and the magnetic pressure jumps (in the range $\approx 10-60$) indicate that the shocks are strong close to the axis, however, as said in a previous paragraph, the small deviation of the shock sequence from periodicity is an indication of the shocks' overall weakness. From the data shown in the table and also in the bottom panel of Figure 2.5, it can be concluded that the jump in gas pressure decreases for decreasing ε_j (i.e., colder models). This tendency holds for fixed Mach number (and increasing magnetization) as well as for increasing Mach number and constant magnetization. This means that the strength of the shocks in terms of the internal energy density jumps is smaller for colder jets or, alternatively, for kinetically dominated / magnetically dominated jets. The jump in the flow Lorentz factor follows the same tendency. Larger jumps are found in low magnetization, low Mach number jets (i.e., hot jets).Also deduced from the bottom panel of Figure 2.5 is the trend of the gas pressure jump to increase for fixed internal energy and increasing Mach number (decreasing magnetization). The magnitude of the jumps of magnetic pressure (or, equivalently, magnetic energy density), $\Delta p_{m,s}$, for kinetically dominated jets (models M4Bx and M5Bx) show a remarkable tendency to decrease with increasing magnetization for constant Mach number. However this trend is less solid in the case of hot / magnetically dominated jets (models M1Bx and M2Bx). For increasing Mach number and constant magnetization, $\Delta p_{m,s}$ increases for low magnetization models and decreases for highly magnetized ones. As in the case of the gas pressure, the jumps of magnetic pressure tend to increase for fixed internal energy and increasing Mach number (decreasing magnetization). All these trends are consistent with the the fact that the strength of the shocks depends on the internal

[4]The analysis of the recollimation shocks of a given model relies on a small number of jumps -3 to 5- evaluated at some particular radius -next to the axis- and with some dispersion in their properties as reflected by the large relative errors of the jumps of gas pressure and magnetic pressure shown in the table.

[5]An ambient medium at pressure p_a can only compress the jet up to a maximum pressure of the same order. The fact that the sum of $\bar{p}_s$ and $\bar{p}_{m,s}$ matches p_a within a factor of two confirms this claim and makes p_a a good estimator of the jet total pressure at shocks.

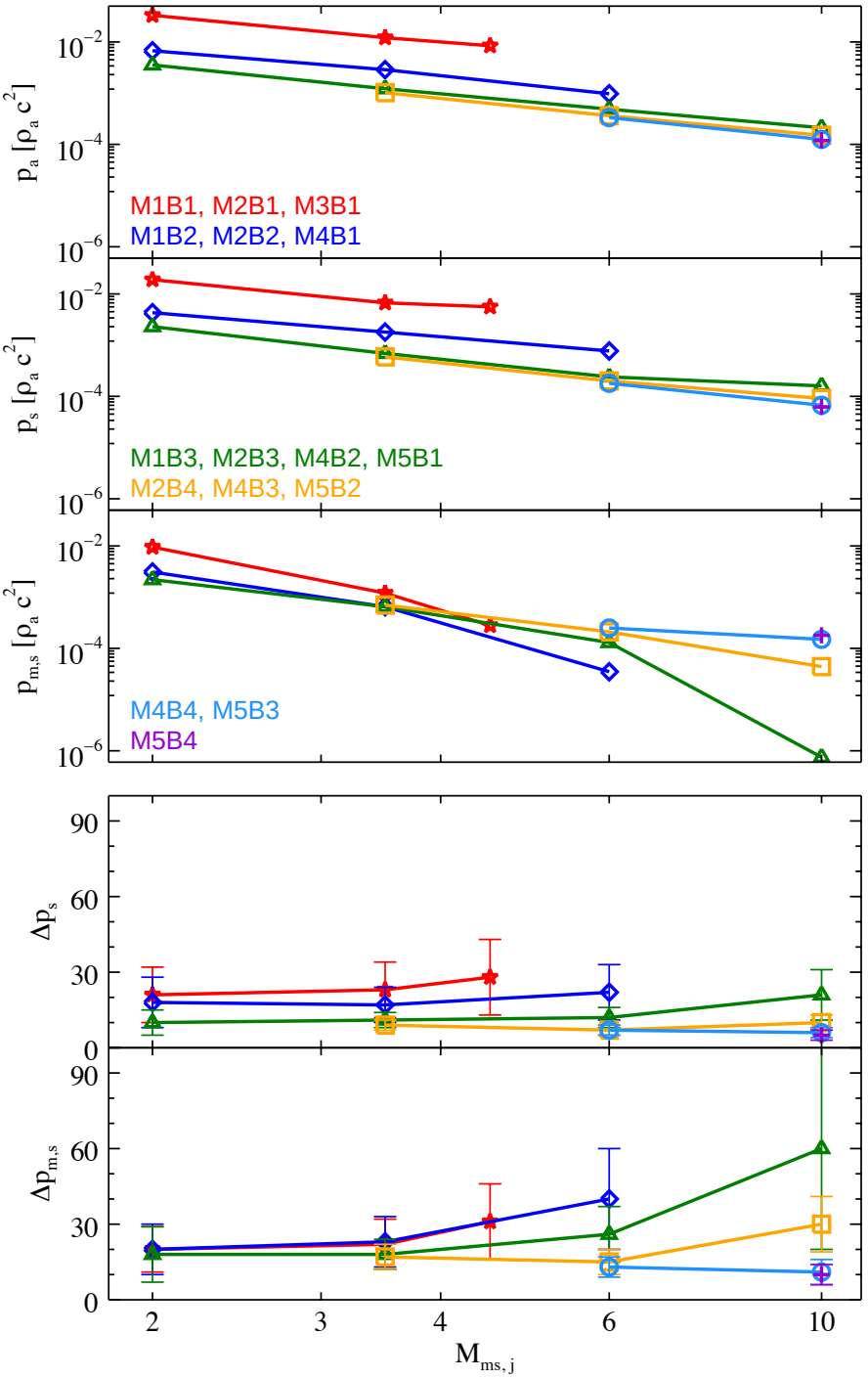

Figure 2.5: Top panel: Ambient pressure and averages of gas and magnetic pressures across shocks as a function of the magnetosonic Mach number. **Bottom panel:** As in the top panel but for the jumps of gas and magnetic pressures. Lines connect models with a *similar* internal energy. Labels correspond to both plots.

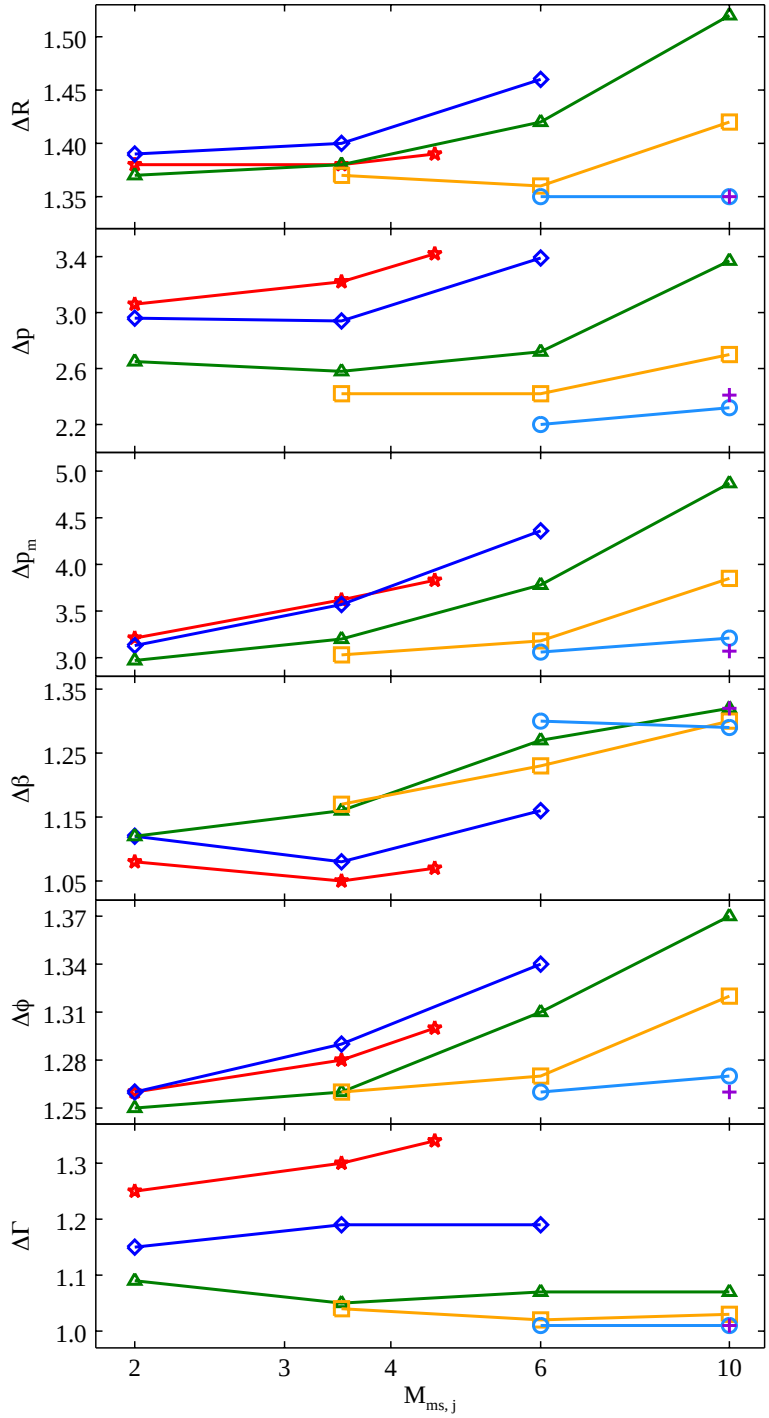

Figure 2.6: From top to bottom: Relative average variations of jet radius, gas and magnetic pressures, magnetization, magnetic pitch angle and flow Lorentz factor as a function of the jet magnetosonic Mach number. Lines connect models with a *similar* internal energy. Color labeling is as in Figure 2.5.

Table 2.3: Relative variations along the jet of the quantities defining the steady models.

Model	ΔR	Δp	Δp_m	$\Delta\beta$	$\Delta\phi$	$\Delta\Gamma$	$D\,[R_j]$
M1B1	1.38	3.06	3.21	1.08	1.26	1.25	8.64
M1B2	1.39	2.96	3.13	1.12	1.26	1.15	8.33
M1B3	1.37	2.65	2.97	1.12	1.25	1.09	7.92
M2B1	1.38	3.22	3.62	1.05	1.28	1.30	13.29
M2B2	1.40	2.94	3.57	1.08	1.29	1.19	13.28
M2B3	1.38	2.58	3.20	1.16	1.26	1.05	12.86
M2B4	1.37	2.42	3.03	1.17	1.26	1.04	12.50
M3B1	1.39	3.42	3.83	1.07	1.30	1.34	16.00
M4B1	1.46	3.39	4.36	1.16	1.34	1.19	21.25
M4B2	1.42	2.72	3.78	1.27	1.31	1.07	21.75
M4B3	1.36	2.42	3.18	1.23	1.27	1.02	21.25
M4B4	1.35	2.20	3.06	1.30	1.26	1.01	20.75
M5B1	1.52	3.37	4.87	1.32	1.37	1.07	36.00
M5B2	1.42	2.70	3.85	1.30	1.32	1.03	36.00
M5B3	1.35	2.32	3.21	1.29	1.27	1.01	36.00
M5B4	1.35	2.41	3.07	1.32	1.26	1.01	35.00

Note. Tabulated data denote jet model, relative average variations of jet radius, gas and magnetic pressures, magnetization, pitch angle and Lorentz factor, and wavelength of the jet oscillation along the jet axis.

energy of the jet, which establishes the amount of energy that can be exchanged into kinetic energy at shocks (as advanced earlier in this section), and is in general reduced for increasing jet magnetizations (probably as a consequence of the magnetic tension). The shock obliquity (as determined by ϕ_s, the angle between the shock and the jet axis; see last column in Table 2.2) and the shock separation follows a remarkable correlation with the relativistic (magnetosonic) Mach number.

Together with the sequence of recollimation shocks, the jets exhibit a series of radial

oscillations with the same periodicity. Table 2.3 lists the relative average variation of several relevant jet quantities along the jet as a result of the radial expansions and compressions. The same quantities are shown in Figure 2.6 as a function of the magnetosonic Mach number of the jet and for models with similar internal energy. The jet radii change by $\approx 35 - 50\%$, with a slight tendency of the oscillation amplitud to increase with the Mach number for constant internal energy (decreasing magnetization), and to decrease with increasing magnetization (decreasing internal energy) for constant Mach number. The pressure follows the changes dictated by the adiabatic expansions/compressions of the flow (as a consequence of the variations in jet radius) plus the jumps at internal shocks and display variations of a few (≈ 3) units. A similar behaviour is found in the magnetic pressure, dominated by the axial component of the magnetic field, which also experiences changes by a factor of $3 - 4$. Since both magnetic and gas pressures behave similarly at compressions/expansions and shocks, the changes in magnetization are more limited (below $\approx 30\%$). Associated with the changes in the axial and toroidal magnetic field components is also a change in the magnetic pitch angle, which changes as little as a $\approx 37\%$ (i.e., between 45^o and 60^o). The changes in the Lorentz factor reflects the potential of the jet flow to exchange internal and kinetic energies and is larger in the hotter models, and becomes negligible in cold, kinetically dominated jets in spite of the large radial oscillations. It is interesting to highlight the trend of the variations of the jet radius, gas pressure, magnetic pressure and magnetic pitch angle to decrease with increasing magnetization and constant internal energy, which is a consequence of the increasing magnetic pinch of the jet for higher magnetization models.

The last column in Table 2.3 records the axial wavelength of the oscillations in the different models. It shows the expected correlation with the Mach number. For fixed Mach number, only hot (low Mach number) jets display a slight variation of the oscillation wavelength with the internal energy, whereas it is almost constant for kinetically dominated jets despite the broad spread of magnetization.

As a consequence of the profile of the magnetic pressure across the jet and the pinch exerted by the toroidal component of the magnetic field, the thermal pressure is not constant across the jet. For a given Mach number, models with increasing magnetization tend to concentrate most of their internal energy in a thin hot spine around the axis. (Compare the thermal pressure panels of Figure 2.2 corresponding to model M1B3, a highly magnetized jet, with those of Figure 2.3, a purely hydrodynamic jet with a passive magnetic field, and Figure 2.4, a jet in equipartition.)

2.3 Emission Calculations and Results

To compute the synchrotron emission from the magnetohydrodynamical jet models described in Section 2 we used the same numerical code described in Gómez *et al.* (1993, 1994a,b, 1995, 1997), and references therein. In this Section we provide a summary of the model and its assumptions, followed by a study of the radio emission properties derived from these calculations.

2.3.1 Emission Code

In order to calculate the synchrotron emission from the previous RMHD jet models we need to establish some assumptions. While the radio continuum emission we are interested in is being produced by a population of non-thermal electrons (and maybe positrons), the RMHD simulations discussed previously account only for the evolution of the thermal electrons present in the jet. Establishing a relationship between the thermal and non-thermal populations requires a detailed prescription for the particle acceleration processes that connect both populations, presumably taking place in strong shocks or in magnetic reconnection events (see e.g., Sironi *et al.,* 2015). A proper treatment of particle acceleration/injection in shocks (e.g., Kirk *et al.,* 2000) or magnetic reconnection (e.g., Lyubarsky, 2005) requires a microscopic description of the fluid, such as in particle-in-cell (PIC) simulations (e.g., Nishikawa *et al.,* 2016), and its implementation in macroscopic RMHD models, such as the one used here, still falls outside current computing capabilities given the vastly different scales involved. Nevertheless, as a first-order approximation we consider that the internal energy of the non-thermal population is a constant fraction of the thermal electrons considered in the RMHD simulations (e.g., Gómez *et al.,* 1995; 1997; Komissarov & Falle, 1997; Broderick & McKinney, 2010; Porth *et al.,* 2011). Alternatively, the non-thermal population can also be considered to be proportional to the magnetic energy density (e.g., Porth *et al.,* 2011), which determines the particle acceleration efficiency in shocks and magnetic reconnection events. No significant differences are found in our emission calculations when considering the latter approach for particle acceleration, given the similarities between the gas pressure and magnetic energy density distributions in our RMHD simulations, except for the particular case of jet spine brightening discussed in more detail in section 3.3. On the other hand, we note that particle acceleration at shock fronts is probably the most important ingredient for computing the expected non-thermal emission from our RMHD simulations. Our results should therefore be considered in these cases as a first-order approximation, which could be used as a base model to test different prescriptions for in-situ particle acceleration in future modeling.

We consider the usual power law for distributing the total energy computed by the RMHD simulations among the relativistic non-thermal electrons using $N(E)\mathrm{d}E = N_0 E^{-\gamma}\mathrm{d}E$, where $E_{min} \leq E \leq E_{max}$. Neglecting radiative losses, the ratio $C_E = E_{max}/E_{min}$ will remain constant throughout the jet, and can be treated as a parameter in our model. In this case, assuming that the internal energy of the non-thermal population is a constant fraction of the thermal one, the power law for the electron energy distribution is fully determined by the equations (Gómez *et al.,* 1995)

$$N_0 = \left[\frac{U(\gamma-2)}{1-C_E^{2-\gamma}}\right]^{\gamma-1}\left[\frac{1-C_E^{1-\gamma}}{N(\gamma-1)}\right]^{\gamma-2}, \tag{2.1}$$

$$E_{min} = \frac{U}{N}\frac{\gamma-2}{\gamma-1}\frac{1-C_E^{1-\gamma}}{1-C_E^{2-\gamma}}, \tag{2.2}$$

where U and N are a constant fraction of the internal energy density and rest-mass

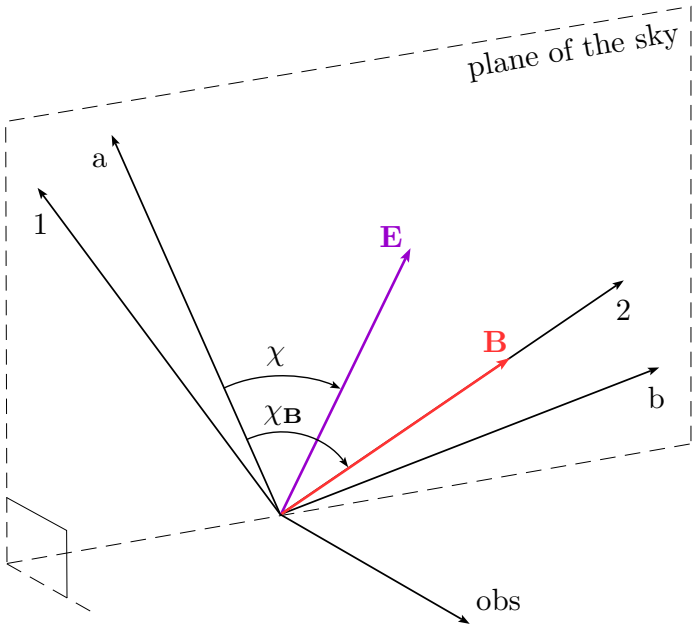

Figure 2.7: Geometry of the coordinate systems used to compute the radiation coefficients and to solve the transfer equations. $(1, 2)$ corresponds to the fluid's frame and (a, b) to the observer's frame.

density calculated by the RMHD code. Note that the fraction between the thermal and non-thermal populations provides a scale factor for the emission in our models (expressed in arbitrary units), but otherwise our simulations are not affected by the particular value chosen.

To compute the emission and absorption coefficients for the synchrotron radiation is convenient to establish two different reference frames, the observer's and emitting fluid frames (see Figure 2.7). The radiation coefficients are computed in the fluid's frame $(1, 2)$, where the direction of the magnetic field in the plane of the sky defines the axis 2, which together with the axis 1 and the direction toward the observer form a right-handed orthogonal system. For the case of our assumed power law energy distribution the emission and absorption coefficients, for a given polarization (i), are given by

$$\varepsilon^{(i)} = \frac{1}{2} c_5(\gamma) N_0 (B' \sin\vartheta')^{(\gamma+1)/2} \left(\frac{\nu}{2c_1}\right)^{(1-\gamma)/2} \left[(-1)^{i+1} \frac{\gamma+1}{\gamma+7/3} + 1\right], \qquad (2.3)$$

$$\kappa^{(i)} = c_6(\gamma) N_0 (B' \sin\vartheta')^{(\gamma+2)/2} \left(\frac{\nu}{2c_1}\right)^{-(\gamma+4)/2} \left[(-1)^{i+1} \frac{\gamma+2}{\gamma+10/3} + 1\right], \qquad (2.4)$$

being $i = 1, 2$; B' the modulus of the magnetic field calculated by the RMHD code in the lab frame and transformed to the fluid frame; ϑ' the angle between the magnetic

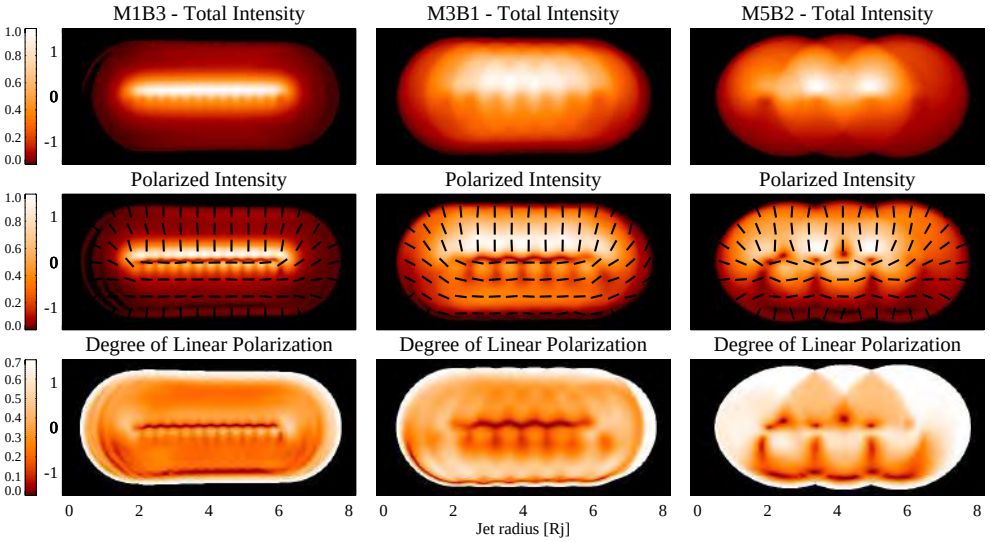

Figure 2.8: Total intensity, linearly polarized intensity, with electric vector position angle (EVPA) overplotted as black bars, and degree of polarization for the representative magnetically dominated, hot and kinetically dominated jet models M1B3, M3B1 and M5B2, respectively, computed for a viewing angle of 2°. Total intensity values are normalized to unity. Axes units represent distance in jet radius units.

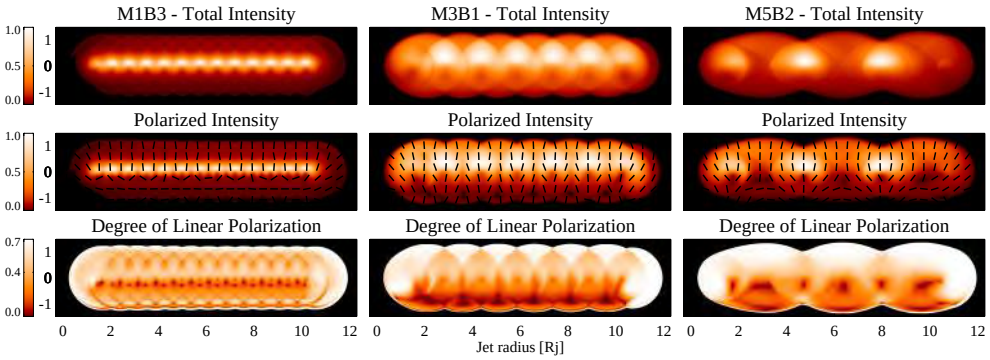

Figure 2.9: Same as Figure 2.8 for a viewing angle of 5°.

field and the line of sight; ν the observing frequency; $c_1 = (3e)/(4\pi m^3 c^5)$; and c_5, c_6 dimensionless functions of γ which are defined and tabulated by Pacholczyk (1970).

If the orientation of the magnetic field is not uniform within the jet the fluid frame will change from computational cell to computational cell. Thus, the integration of the of transfer equations is more conveniently formulated in the observer's frame (a, b), with χ_B defining the angle between the axis 2 (for each particular computational cell) and a. The radiation field is characterized by the four Stokes parameters I, Q, U, and V, or alternatively $I^{(a)}$, $I^{(b)}$, U, and V, where $I = I^{(a)} + I^{(b)}$ and $Q = I^{(a)} - I^{(b)}$. Given the small amount of circular polarization observed in blazar jets we consider

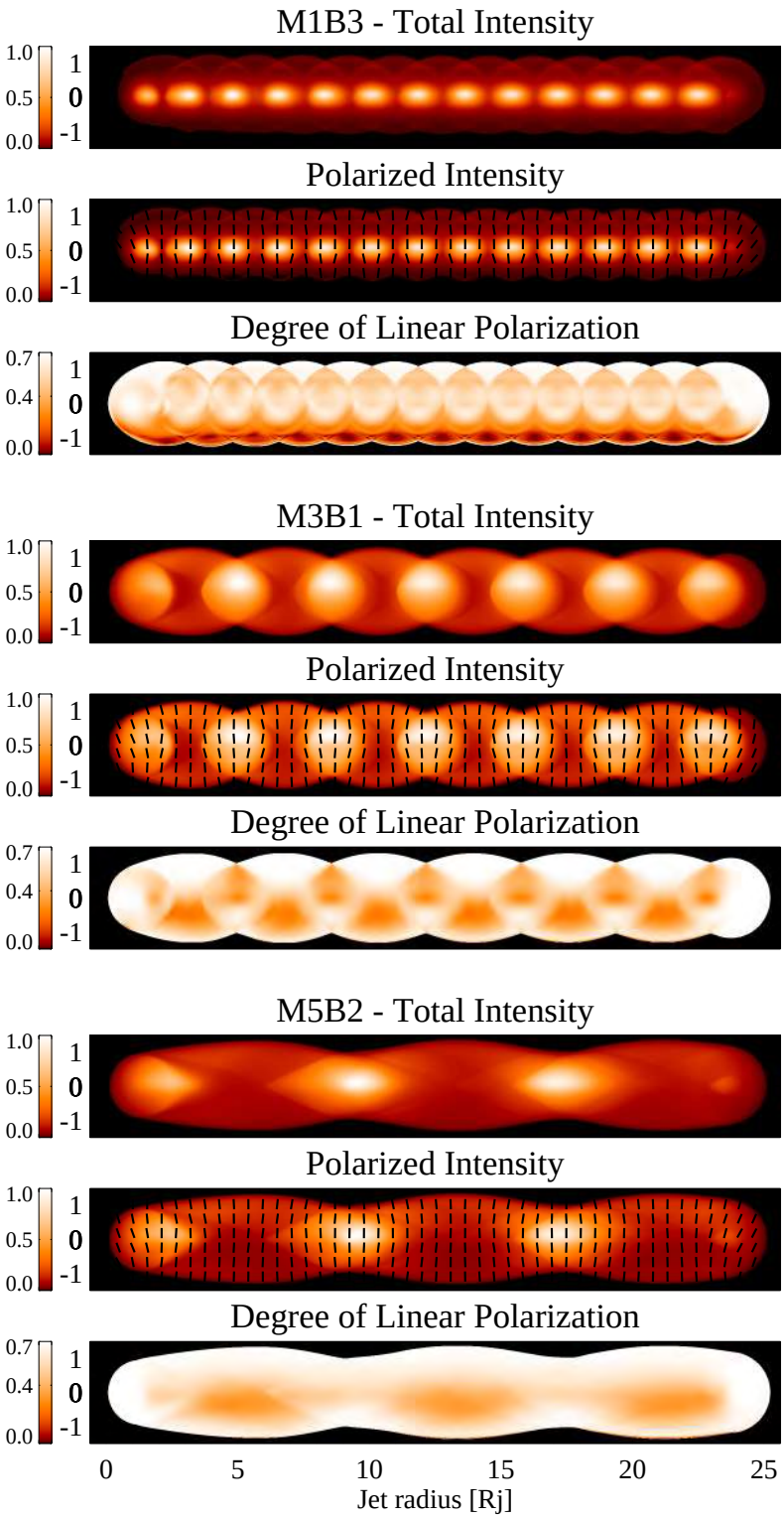

Figure 2.10: Same as Figure 2.8 for a viewing angle of 10°.

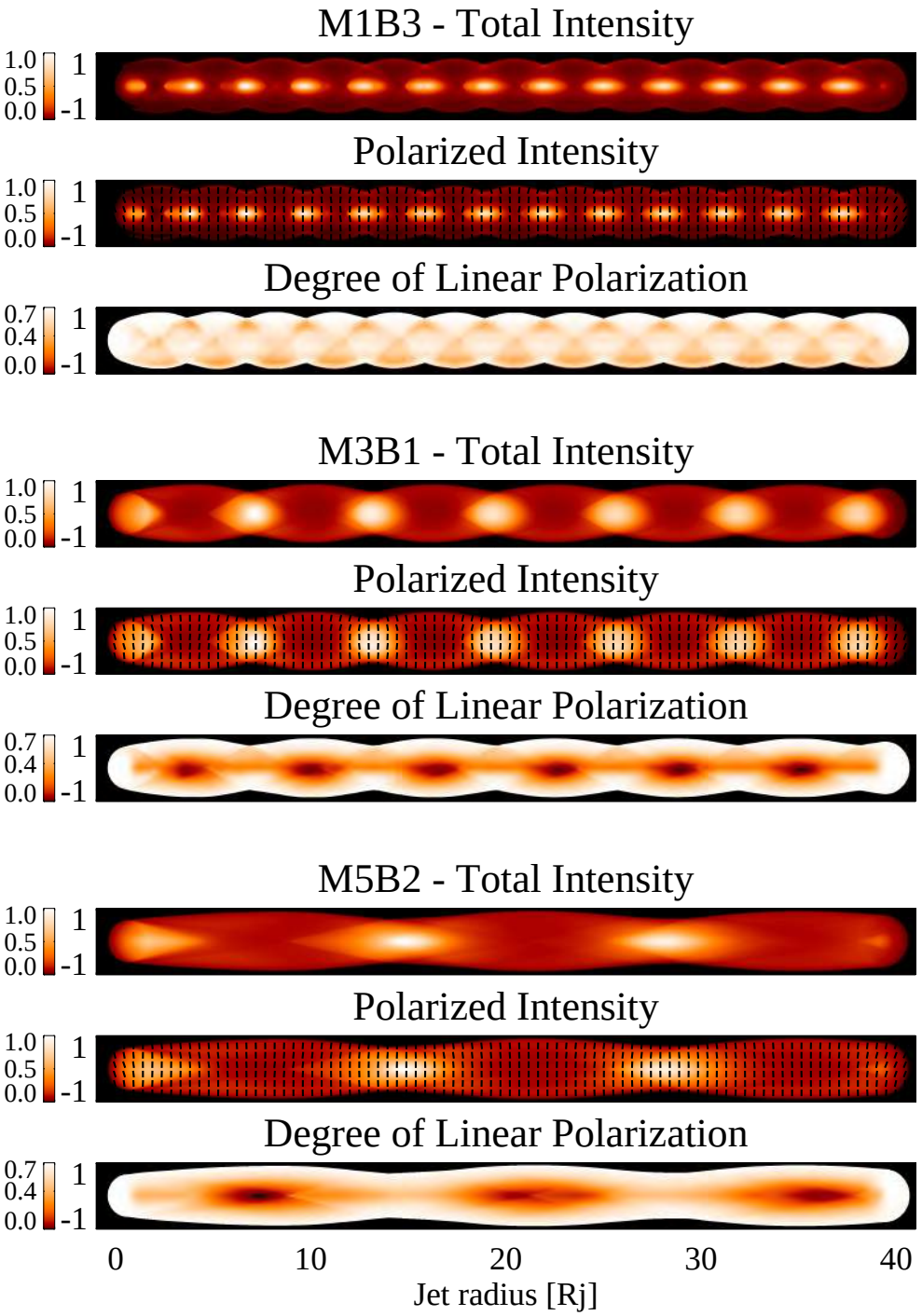

Figure 2.11: Same as Figure 2.8 for a viewing angle of 20°.

$V = 0$. The transfer equations in the observer's frame, characterizing the radiation passing a volume element ds are given by e.g., Pacholczyk, 1970.

$$\begin{aligned}\frac{dI^{(a)}}{ds} =& I^{(a)}\left[-\kappa^{(1)}\sin^4\chi_B - \kappa^{(2)}\cos^4\chi_B - \frac{1}{2}\kappa\sin^2 2\chi_B\right] \\ &+ U\left[\frac{1}{4}(\kappa^{(1)}-\kappa^{(2)})\sin 2\chi_B + \frac{d\chi_F}{ds}\right] \\ &+ \varepsilon^{(1)}\sin^2\chi_B + \varepsilon^{(2)}\cos^2\chi_B, \end{aligned} \tag{2.5}$$

$$\begin{aligned}\frac{dI^{(b)}}{ds} =& I^{(b)}\left[-\kappa^{(1)}\cos^4\chi_B - \kappa^{(2)}\sin^4\chi_B - \frac{1}{2}\kappa\sin^2 2\chi_B\right] \\ &+ U\left[\frac{1}{4}(\kappa^{(1)}-\kappa^{(2)})\sin 2\chi_B - \frac{d\chi_F}{ds}\right] \\ &+ \varepsilon^{(1)}\cos^2\chi_B + \varepsilon^{(2)}\sin^2\chi_B, \end{aligned} \tag{2.6}$$

$$\begin{aligned}\frac{dU}{ds} =& I^{(a)}\left[\frac{1}{2}(\kappa^{(1)}-\kappa^{(2)})\sin 2\chi_B - 2\frac{d\chi_F}{ds}\right] \\ &+ I^{(b)}\left[\frac{1}{2}(\kappa^{(1)}-\kappa^{(2)})\sin 2\chi_B + 2\frac{d\chi_F}{ds}\right] \\ &- \kappa U - (\varepsilon^{(1)}-\varepsilon^{(2)})\sin 2\chi_B, \end{aligned} \tag{2.7}$$

where $\kappa = (\kappa^{(1)} + \kappa^{(2)})/2$ and $\mathrm{d}\chi_F/\mathrm{d}s$ is the polarization plane variation per unit distance due to Faraday rotation. Multi-frequency VLBI images of blazar jets commonly show regions of enhanced Faraday rotation which can be used to determine the line-of-sight component of the magnetic field, as well as probes of the thermal population of electrons in the jet sheaths (e.g., Gómez *et al.,* 2008; 2011; Hovatta *et al.,* 2012; Gabuzda *et al.,* 2015; Gómez *et al.,* 2016; Gabuzda *et al.,* 2017; Lico *et al.,* 2017). We have, however, decided to ignore Faraday rotation effects in our simulations presented here (assuming $\mathrm{d}\chi_F/\mathrm{d}s = 0$) to study the polarization in our models as a function of the dominant type of energy in the jet, disentangled from any possible Faraday rotation effects (which in turn would depend also on the physical parameters chosen for the jet sheath adding extra free parameters in our simulations). Hence our models can also be used as a testbed case for future modeling of Faraday rotation effects in AGN jets.

Figures 2.8 to 2.11 show the total intensity, linearly polarized intensity, and degree of polarization plots at viewing angles $\theta = 2, 5, 10$ and 20° computed for models M1B3, M3B1, and M5B2, chosen as representative for each dominant type of energy in the jet. Note that all the models are computed at a frequency at which the emission is optically thin to discard any opacity effects in our analyses. This is a good approximation for our study of the stationary knots commonly observed at parsec scales in AGN jets (Jorstad *et al.,* 2017), where we expect the emission to be optically thin, but we note that closer to the VLBI core opacity effects are a necessary ingredient to understand the radio emission, specially in polarization (e.g., Gómez *et al.,* 1994a; b; Porth *et al.,* 2011). Emission plots for the whole set of RMHD models considered can be found at Extended Data Figures 2.23 to 2.26. The most salient feature in the emission plots is the presence of knots associated with the recollimation shocks.

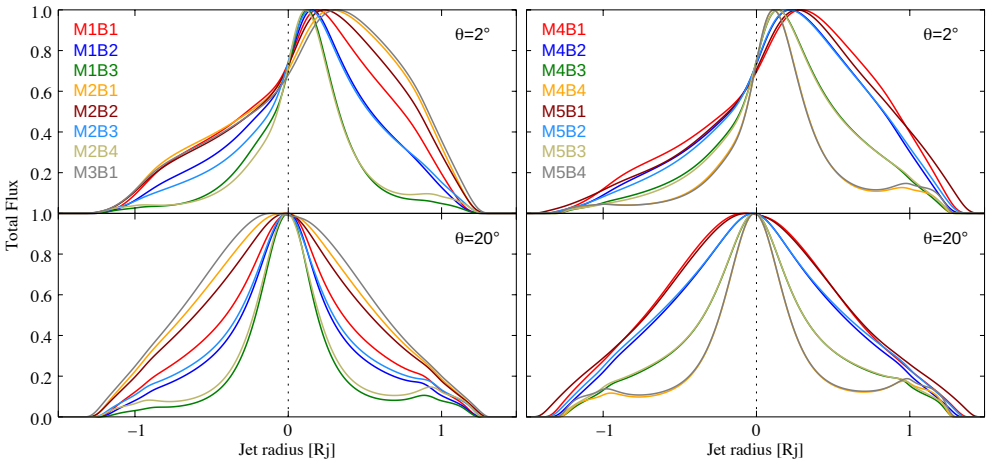

Figure 2.12: Total integrated intensity transverse profiles of the RMHD jet models, computed for the viewing angles $\theta = 2°$ and $20°$. The values of the intensity are normalized to unity. The negative and positive values of the abscissa axis represent the bottom and top halves of the jets expressed in jet radius units, respectively. Due to the large number of models, they appear splitted in two groups (left and right panels).

2.3.2 Top-Down Emission Asymmetry

The threaded helical magnetic field produces a well-known emission asymmetry between the jet top and bottom halves (e.g., Aloy *et al.,* 2000; Lyutikov *et al.,* 2005; Clausen-Brown *et al.,* 2011). This effect is maximized for a magnetic pitch angle of $\phi = 45°$, which is the case we consider in all our models. The enhanced emitting half reverts from top to bottom when the viewing angle in the fluid frame reaches $\theta'_r = 90°$. This can be related to the viewing angle in the observer's frame by using the light aberration equations (e.g., Rybicki & Lightman, 1979):

$$\sin\theta' = \frac{\sin\theta}{\Gamma(1 - v_j\cos\theta)}, \quad \cos\theta' = \frac{\cos\theta - v_j}{(1 - v_j\cos\theta)}, \tag{2.8}$$

from which we obtain that the flip in the dominant section of the jet is obtained when $\cos\theta_r = v_j$. Given that we are considering an axial flow velocity $v_j = 0.95c$ at injection, we expect that the jet cross section asymmetry will reverse at an approximate value of $\theta_r \approx 18°$. For lower values of the viewing angle ($\theta < \theta_r$) the emission in the top half of the jet will dominate over the bottom half. This is clearly visible in the total intensity panels of Figures 2.8 and 2.9 and Extended Data Figures 2.23 and 2.24 where $\theta = 2°$ and $5°$, and to a less extent in Figure 2.10 and Extended Data Figure 2.25 where $\theta = 10°$. When θ approaches θ_r the emission becomes qualitatively axially-symmetric, as can be seen in Figure 2.11 and Extended Data Figure 2.26 where $\theta = 20°$. Although larger viewing angles $\theta > \theta_r$ are not shown, in these cases the bulk of the emission moves progressively to the bottom half of the jet.

The jet cross section asymmetry produced by the helical magnetic field is more clearly seen in Figures 2.12 and 2.13, where transverse profiles of the total and

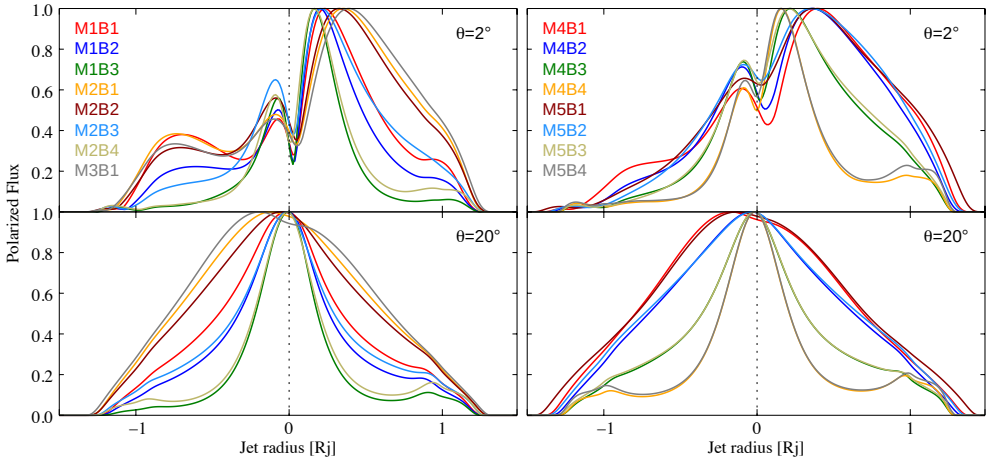

Figure 2.13: Same as Figure 2.12 for polarized integrated intensity.

polarized intensity integrated along the jet are shown for each jet model at viewing angles of $\theta = 2°$ and $20°$. For a viewing angle of $\theta = 2°$ not only the bulk of the jet emission is concentrated on the top half of the jet, but also the peak intensity is displaced from the jet axis. This offset is progressively larger for magnetically dominated, kinetically dominated, and hot jets. At a viewing angle of $\theta = 20°$ the bottom half of the jet starts to dominate the emission, as expected for our choice of jet flow velocity and magnetic field pitch angle.

2.3.3 Spine Brightening

As discussed in Section 2, jet models with large magnetizations concentrate the majority of their internal energy in a hot spine due to the larger magnetic pressure gradient and magnetic tension. As shown in Figures 2.8 to 2.11 and Extended Data Figures 2.23 to 2.26, following our prescription for particle acceleration, in which the internal energy of the non-thermal population is a constant fraction of the thermal one, this translates into a spine brightening in both, total and polarized intensity, which is more clearly seen in the magnetically models M1B3 and M2B4, and in the kinetically dominated models M4B4 and M5B4 (with magnetizations $\beta = 17.5$). For comparison, Figure 2.14 shows the emission plots for the M1B3 model computed considering a non-thermal particle injection based on the magnetic energy density, in which no significant spine brightening is seen. The detection of spine brightening in actual observations of AGN jets can therefore be considered as a good indication for originating in a jet that is magnetically dominated, and in which the internal energy of the non-thermal population of emitting particles is proportional to the internal energy of the thermal gas. Alternatively, spine brightening can also arise through differential Doppler boosting in jets with a significant stratification in velocity across the jet width – a situation that has not been considered in the present simulations.

By looking at the bottom panels of Figures 2.12 and 2.13, with a more symmetric

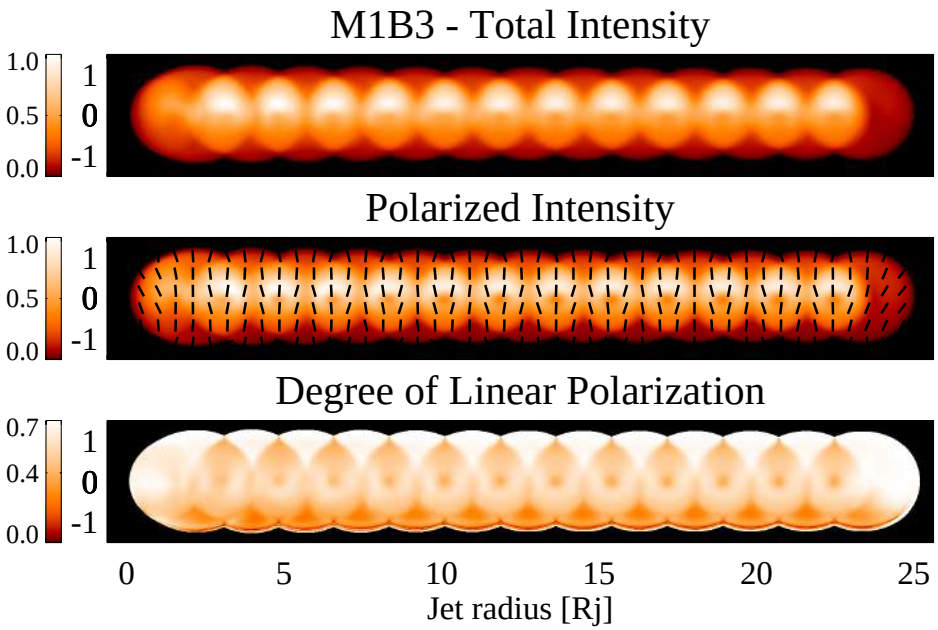

Figure 2.14: Magnetically dominated model M1B3 computed following a power law energy distribution determined by the magnetic energy density, B'^2, instead of the internal energy density, U. Axis and viewing angle as in Figure 2.10.

emission structure across the jet width, we can observe that the models tend to cluster for similar magnetizations, which is the dominant factor determining the spine brightening. Model M1B3, as well as models MxB4, presenting the highest magnetizations have their emission more concentrated around the jet axis; on the other hand, pure hydrodynamic models ($\beta = 0$) present a more evenly distributed emission across the jet width.

To quantify the spine brightening we have computed the distance (in jet radius units) from the axis at which the emission adds to the 50% and 70% of the total jet emission. For this we have selected the models at a viewing angle of 20° (with a more symmetric emission), and considered also the small displacements in the peak emission with respect to the jet axis discussed previously. We also note that for the case of optically thin emission, as considered in these models, the integrated emission along a given integration column is directly proportional to column length; hence for a homogeneous jet model we expect that 50% (70%) of the emission will be concentrated within $0.4R_j$ ($0.59R_j$) from the jet axis. The results are presented in Table 2.4, confirming the higher spine brightening with increasing jet magnetization. We also find that for a given jet magnetization the spine brightening increases with Mach number. Model M1B3 presents the largest spine brightening, reaching 50% (70%) of the integrated emission at $0.16R_j$ ($0.29R_j$) from the peak emission. For the pure hydrodynamic model M5B1 the results agree with the expected values in case there is no significant spine brightening.

Table 2.4: Distance to jet axis

Model	50% I	70% I
M1B1	0.29	0.49
M1B2	0.24	0.44
M1B3	0.16	0.29
M2B1	0.35	0.55
M2B2	0.34	0.54
M2B3	0.26	0.46
M2B4	0.19	0.34
M3B1	0.36	0.56
M4B1	0.38	0.59
M4B2	0.35	0.56
M4B3	0.28	0.49
M4B4	0.20	0.41
M5B1	0.39	0.60
M5B2	0.38	0.59
M5B3	0.29	0.50
M5B4	0.21	0.44

Note. Tabulated data denote jet model and distance from the axis, in R_j, at which the integrated intensity represents the 50% and 70% of the total integrated intensity.

Table 2.5: Knots relative intensity

Model	$\theta = 5^\circ$	$\theta = 10^\circ$	$\theta = 20^\circ$
M1B1	5.7±0.6	52.5±2.2	78.6±5.2
M1B2	···	56.6±1.9	79.2±4.0
M1B3	14.2±2.8	67.5±2.4	80.4±3.0
M2B1	···	67.5±3.5	75.1±7.5
M2B2	···	67.7±3.5	74.7±6.9
M2B3	21.0±2.8	69.9±2.8	74.0±5.3
M2B4	43.6±2.4	74.6±3.1	76.4±3.5
M3B1	15.2±2.2	68.8±3.7	77.8±6.4
M4B1	44.9±1.9	69.8±4.7	78.0±5.7
M4B2	46.8±1.2	68.9±5.0	74.1±6.5
M4B3	52.5±1.9	68.5±6.3	70.8±7.2
M4B4	60.1±3.6	70.8±6.7	67.7±5.9
M5B1	61.9±1.7	75.8±2.3	80.1±0.3
M5B2	59.8±1.2	73.4±2.1	75.5±0.7
M5B3	63.2±1.4	72.2±2.6	71.0±2.3
M5B4	68.1±0.4	72.3±1.0	66.2±1.6

Note. Tabulated data denote jet model and the average relative intensity of the stationary components, in percentage, for viewing angles $\theta = 5^\circ$, 10°, and 20°.

2.3.4 Knots Intensity

One of the main characteristics of the radio emission from the RMHD jet models is the presence of a variable number of bright knots both, in total and polarized emission (see Figures 2.8 to 2.11 and Extended Data Figures 2.23 to 2.26). These are associated with the recollimation shocks, and are a consequence of the increase in density and gas pressure produced by the shocks. These knots can be associated with the stationary features that appear commonly in blazar jets near the VLBI core (e.g., Jorstad *et al.,* 2005; Gómez *et al.,* 2016; Jorstad *et al.,* 2017).

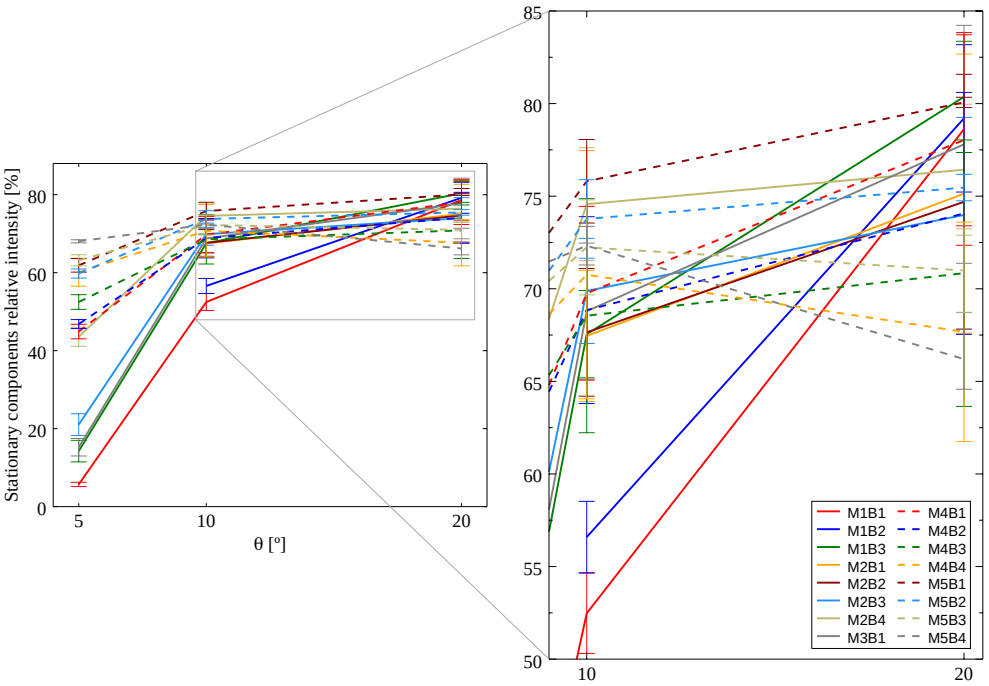

Figure 2.15: Stationary components relative intensity (in percentage) for the viewing angles $\theta = 5^\circ$, 10° and 20°, and a partial zoom-in.

To characterize these stationary knots as a function of the dominant type of energy in the jet we have computed their relative strength, measured as the mean value of the ratio (in percentage) between the peak intensity in the knots and the underlying jet emission once the emission is integrated across the jet width into a one-dimensional profile. The results are tabulated in Table 2.5 and plotted in Figure 2.15. We have not analyzed the models with $\theta = 2^\circ$ since the emission from multiple recollimation shocks is overlapped in the integration column. The same is also true for models M1B2, M2B1, and M2B2 at a viewing angle of $\theta = 5^\circ$. We find an overall trend of increasing relative knots intensity with increasing viewing angle which is due to the variable Doppler factor with viewing angle and to an increase in the ratio between unshocked and shocked cells in the integration column with decreasing viewing angle, as discussed below.

For stationary jet models, as those considered here, the observed emission is enhanced by a factor δ^2, where $\delta = \Gamma^{-1}(1 - \beta\cos\theta)^{-1}$ is the Doppler factor and depends on the flow Lorentz factor Γ and viewing angle θ. These change along the jet as the emitting particles go first through the rarifying, expanding pre-shock state and then through the compressing, recollimating post-shock state forming the recollimation shock structure, leading to a variable δ that will modulate the observed emission. To obtain a better understanding on how the final radiation reaching the observer depends on the jet emissivity and Doppler boosting we have analyzed in more

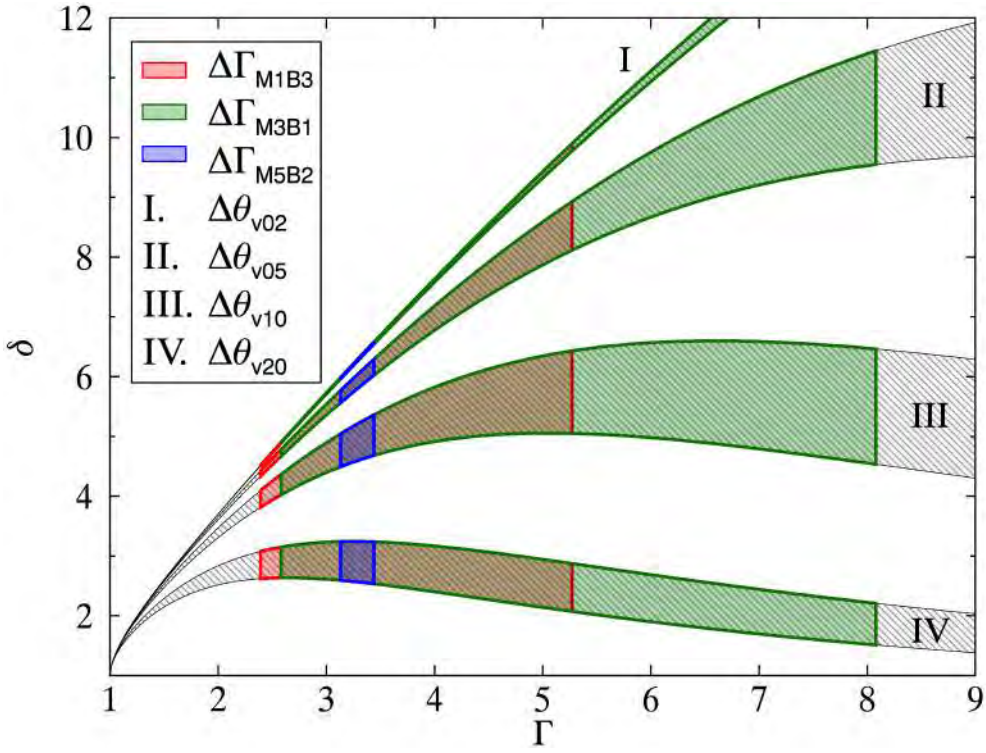

Figure 2.16: Doppler factor (δ) as a function of the Lorentz factor (Γ), for different values of the viewing angle (θ) distributed in four regions: I, II, III and IV. Each region represents the variation of θ around the viewing angle for models v02, v05, v10 and v20, respectively. Overplotted to these regions are, in color red, green, and blue, the values taken by Γ for models M1B3, M3B1, and M5B2, respectively.

detail the variability range of θ and Γ, and their relative contribution to δ along the jet for the representative models M1B3, M3B1, and M5B2. These are analyzed for viewing angles 2, 5, 10 and $20°$ (see also Figures 2.8 to 2.11), hereafter referred to as models v02, v05, v10, and v20, respectively.

The results are presented in Figure 2.16, which shows the change of δ as a function of Γ within the four regions (I-IV) where θ takes values for each viewing angle model vXX. Each color represents also the variability of Γ depending on the model. These values are also detailed in Table 2.6. By looking at Figure 2.16 we observe that Γ is the main parameter contributing to δ when θ oscillates around 2 and $5°$, particularly in the hot jet model M3B1 and the magnetically dominated model M1B3, and to a less extent in the kinetically dominated model M5B2. As θ increases, δ is progressively more influenced by the local variations in θ, more strongly in the case of M5B2 and to a less extent in M1B3.

Therefore, for viewing angles smaller than $10°$ the contribution of the Doppler boosting to the observed emission is larger in the rarefactions (where the flow accelerates and expands) than in the recollimating post-shock states, leading to a reduction

Table 2.6: Variations of θ and Γ along the jet axis

vXX	$\Delta\theta\,[^\circ]$	Model	$\overline{\Gamma}$	$\Delta\Gamma$
v02	$[2.6,\ 2.9]$	M1B3	3.8	$[2.4,\ 5.3]$
v05	$[4.5,\ 5.9]$	M3B1	5.3	$[2.6,\ 8.1]$
v10	$[8.7,\ 11.4]$	M5B2	3.3	$[3.1,\ 3.4]$
v20	$[18.0,\ 22.3]$			

Note. Tabulated data denote the initial viewing angle and its variability range (for all considered models), jet model, and mean Lorentz factor with its variability range.

of the relative intensity of the shocks with respect to the underlying jet emission. The opposite is true for larger viewing angles.

As described in Section 2, kinetically dominated jets have weaker shocks, however Figure 2.15 shows that for small viewing angles ($\theta = 5, 10^\circ$) these models present stronger knots in the emission than hot jets. This is due to the relative number of shocks present in the different models, so that for jet models with a lower Mach number (i.e., larger number of shocks) and small viewing angles we barely observe the underlying jet emission, leading to a larger ratio between the unshocked and shocked cells in the integration columns, and therefore smaller relative intensity in shocks. At larger viewing angles ($\theta = 20^\circ$) magnetically dominated and hot jets present a higher ratio in the Doppler factor between the shocks and rarefactions (~ 1.6 and ~ 1.4, respectively) than for kinetically dominated jets (~ 1.1), causing the observed increase in the relative intensity of the knots at this viewing angle (see Figure 2.15 zoom-in).

Finally we should also note that the knot intensity in our emission simulations will depend on the expected particle acceleration in the shock fronts of the recollimation shocks, which in turn depends on the magnetic field configuration and magnetization, among other parameters (e.g., Sironi *et al.,* 2015). We expect that particle acceleration should have an overall effect of increasing the relative intensity of the knots with respect to that of the underlying jet. Comparison with future simulations including a parametrized description of particle acceleration could serve to obtain a better understanding of shock acceleration and its implication in the radio knots observed in AGN jets.

2.3.5 Emission Polarization

The axial symmetry of our models and the helical magnetic field considered lead to a bimodal distribution of the EVPAs (e.g., Lyutikov *et al.,* 2005), being either perpendicular or parallel to the jet. This is also modulated by the viewing angle, and its Lorentz transformation into the fluid frame, determining what is the dominant

magnetic field component projected onto the plane of the sky. For our chosen magnetic field pitch angle of $\phi = 45°$ (in the lab frame) and jet flow bulk Lorentz factor, the poloidal component of the magnetic field B^z dominates over the toroidal component B^ϕ for viewing angles larger than $5°$, as observed in Figures 2.10 and 2.11 and Extended Data Figures 2.25 and 2.26. At smaller viewing angles these projection effects yield to a bimodal distribution in the EVPAs across the jet width, with a flip in the EVPAs in the bottom half of the jet when the projected toroidal component of the magnetic field dominates (see Figures 2.8 and 2.9 and Extended Data Figures 2.23 and 2.24).

Polarized intensity images in Figures 2.8 to 2.11 and Extended Data Figures 2.23 to 2.26 show small variations in the polarization angle of up to $\sim 26°$ around stationary components regardless of the viewing angle. For this it is necessary to break down the symmetry in our models between the back and front sections of the jet along the integration column to generate some Stokes U.

Figure 2.17 shows, in normalized units, the Stokes U profile along the integration column plotted in red color in the bottom panel, which corresponds to the jet density of the kinetically dominated model M5B2 for a viewing angle of $5°$. The chosen integration column, contained between $31R_j$ and $55R_j$ from the beginning of the jet, maximizes the variation of the polarization angle for this particular model and viewing angle. Note that the column is constrained to a jet width of $[-1, 1]R_j$ (black dashed lines in the bottom panel), i.e. as if the jet was perfectly cylindrical, to assure both parts of the column have the same number of computational cells. Each color of the Stokes U profiles represents a different configuration of the parameters involved in the calculations of Stokes U.

If we consider an idealized jet configuration, with a uniform distribution of non-thermal particles, velocity, and magnetic field, i.e. as if there were no internal structure or recollimation shocks present inside the jet, we would obtain for Stokes U an integrated value of zero, as it is shown in blue color, yielding a polarization angle of $180°$ (or $90°$, depending on the viewing angle and magnetic pitch angle). When the actual RMHD values of the model are considered the jet symmetry is broken, leading to some generation of Stokes U along the integration column (plotted in red) and a final polarization angle of $\chi = 154°$; that is, a variation of $\sim 26°$ with respect to the idealized homogeneous jet model. The underlying process involved in the break of the Stokes U symmetry, and the subsequent change in the polarization angle χ, is the presence of a recollimation shock in the jet that modifies the distribution of the jet flow velocity, magnetic field, and energy density of non-thermal electrons along the integration column, as can be seen in the bottom panel of Figure 2.17.

In an attempt to determine which of the RMHD parameters is more affected by the recollimation shock, and therefore has a larger contribution to the jet asymmetry and generation of Stokes U, we have considered other models setting *ad hoc* values in some of these parameters. We find that for the case of a uniform magnetic field, corresponding to the green profile of Figure 2.17, the variation in the gas pressure leads to some generation of Stokes U, resulting in a final polarization angle of $\sim 160°$. A similar value is obtained when the gas pressure is set to be homogeneous (orange

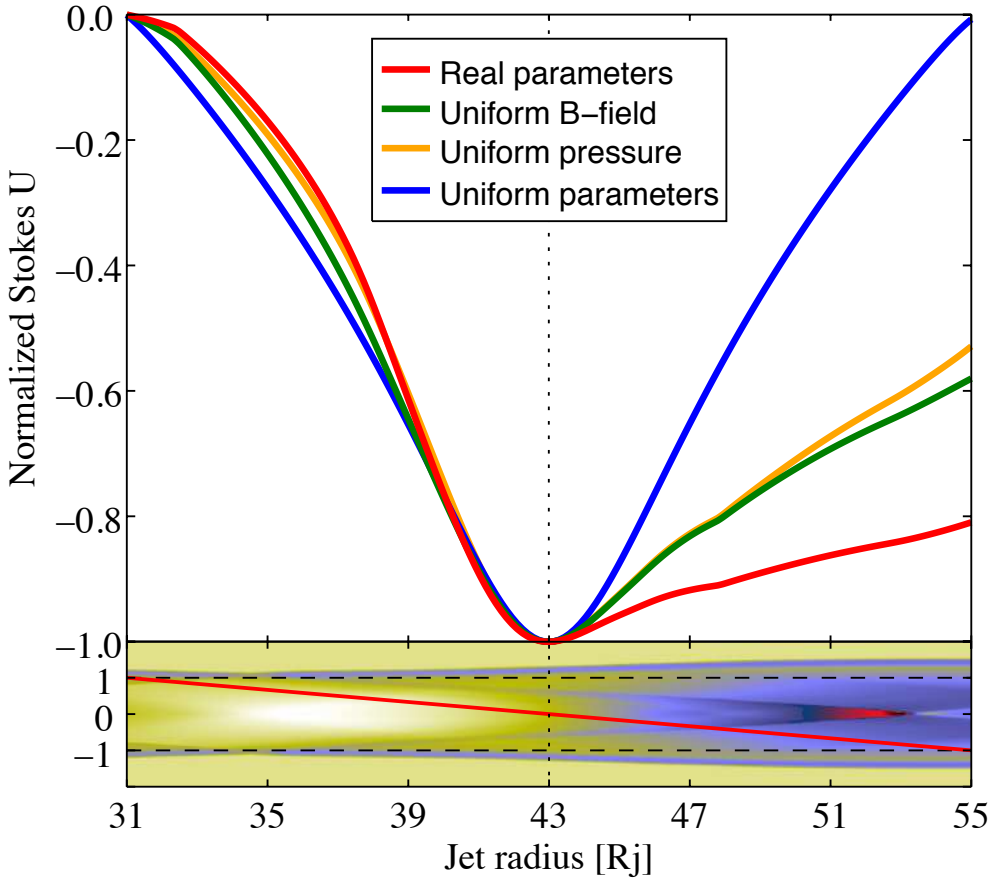

Figure 2.17: Normalized Stokes U profiles (top panel) along the integration column (bottom panel) plotted in color red over the RMHD variable $\log(\rho)$ (jet density), corresponding to the model M5B2 and a viewing angle of $5°$. The bottom panel axes, as well as the abscissa axis of the top panel, represent distance in jet radius units. Each profile of the top panel represents in a different color a particular configuration of parameters. The black dashed lines in the bottom panel indicate the jet width limit used in the calculations. Color palette as in Figure 2.4.

profile), confirming that both, the magnetic field and gas pressure variations in the recollimation shocks contribute similarly to the generation of Stokes U. Finally, we find that the velocity field changes produced by the recollimation shock do not affect significantly the generation of Stokes U.

As discussed previously, *in-situ* particle acceleration in recollimation shocks should increase the relative contribution to the emission of the shocked cells with respect to that of the underlying flow, which in turn may result in larger variations in the polarization angle and degree of polarization in the associated emission knots.

Figures 2.8 to 2.11 and Extended Data Figures 2.23 to 2.26 also show the distribution of the degree of polarization in the jet for the different models analyzed in this work. Given that in our simulations we are considering fully uniform magnetic

fields, the maximum value of the degree of polarization is of the order of 70%, which corresponds to the expected value for optically thin synchrotron emission. We note, however, that polarimetric VLBI observations of AGN jets rarely show linear polarization degrees in excess of few tens of percent (e.g., Jorstad *et al.,* 2005; Hovatta *et al.,* 2012), which suggests the presence of a randomly oriented component of the magnetic field (Burn, 1966; Gómez *et al.,* 1994b; Wardle & Homan, 2003) in turbulent flows (Marscher, 2014). The inclusion of turbulence in RMHD models is, however, particularly difficult, as this requires connecting the scales resolved with the RMHD code with the unresolved turbulent ones by accounting for the kinetic and magnetic energy transfers between them. This connection could be made through the addition of new terms (tensor components) in the dynamical equations whose strength have to be calibrated by direct numerical simulations with varying numerical resolutions (see, e.g., Kessar *et al.,* 2016, on incompressible, non-relativistic, MHD turbulence), or the comparison of direct numerical simulations with PIC simulations. This approach leads to models of turbulence that are dynamically consistent and have a limited number of free parameters but at the cost of a very expensive *a priori* tuning of the transfer terms which is, at present, beyond the current computational capabilities. Turbulence in AGN jets will not only reduce the degree of polarization with respect to that obtained in our simulations, but also produce a more variable polarization throughout the jet.

By looking at the degree of polarization plots we also observe the top-down asymmetry produced by the helical magnetic field (see also Aloy *et al.,* 2000). The recollimation shocks also leave a clear signature in the degree of polarization, presenting variations between the knots and the underlying jet. It is therefore possible to discern whether the stationary jet features present in VLBI images of blazar jets are produced by bends in the jet orientation – through differential Doppler boosting (e.g., Gómez *et al.,* 1993; 1994a; b) – or by recollimation shocks by looking for these distinctive polarization signatures.

The helical structure of the magnetic field produces also a clear stratification in the degree of polarization across the jet width. By looking at Figures 2.10 and 2.11 and Extended Data Figures 2.25 and 2.26 we observe a progressive increase in the degree of polarization with distance from the jet axis (more relevant in the underlying jet emission than in the knots) that is more pronounced as the jet Mach number and viewing angle increase, and magnetization decreases. A similar stratification in degree of polarization across the jet width was observed previously in VLBI images of the radio galaxy 3C 120 (Gómez *et al.,* 2008), which on the light of these simulations may be interpreted as produced by a large scale helical magnetic field field in a jet with relatively low magnetization and high Mach number seen at moderate viewing angles, consistent with previous estimations for this source (e.g., Gómez *et al.,* 2000).

2.4 Summary

The present work represents a first attempt to study the structure of relativistic overpressured superfast-magnetosonic (non force-free) magnetized jets. The injected models are characterized by constant values of the rest-mass density, and axial compo-

nents of the fluid flow velocity and the magnetic field, a toroidal component of the magnetic field with a radial profile, and fixed values of the jet overpressure factor and the ambient pressure. The models are injected in transversal equilibrium. The resulting structure arises from the superposition of the jet's transversal equilibrium, as shaped by the gas pressure gradient, the Lorentz force and the centrifugal force (zero in this case), and the recollimation shocks induced by the total pressure mismatch at the jet/ambient medium interface. The models have been computed numerically following the quasi-one-dimensional approach valid for narrow jets with axial velocities close to the speed of light. The approach allows to study the structure of steady, axisymmetric relativistic (magnetized) flows using one-dimensional time-dependent simulations hence enabling to conduct thorough sweeps of the space of parameters. The selected models are sampled on a magnetosonic (relativistic) Mach number - specific internal energy diagram and set to span a wide region on this diagram covering hot jet models (dominated by their internal energy) as well as kinetically and magnetically dominated jet models.

The equilibrium of the jet against the ambient medium is established by a series of recollimation shocks and gentle expansions and compressions of the jet flow. Superimposed to these periodical structures, as a result of both the magnetic pinch exerted by the toroidal magnetic field and the gradient of the magnetic pressure, models with large magnetizations tend to concentrate most of their internal energy in a thin, hot spine around the axis. For a fixed overpressure factor (as is the case of all the simulations in this work), the properties of the recollimation shocks (i.e., strength, obliquity) and those of the radial oscillations (amplitude, wavelength) in these superfast-magnetosonic jets are governed by the magnetosonic Mach number that controls the angle at which waves penetrate into the jet (Mach angle) whose steepening forms the recollimation shocks, and the specific internal energy that establishes the amount of energy that can be exchanged into kinetic energy at shocks/radial oscillations.

The internal, kinetic and magnetic energies involved in the shocks as well as the shock strength, obliquity and periodicity have been estimated for all the models and their tendencies with the magnetosonic Mach number, the specific internal energy and magnetization analyzed. The same has been done for the cross-sectional averaged jet properties, which suffer periodic variations along the jet axis as a result of the radial expansions and compressions. The internal structure of these jet models is basically determined by the magnetosonic Mach number and so the similarity of models with the same Mach number despite the large variations of internal energy/magnetization. Besides that, the specific internal energy establishes the amount of energy exchangeable into kinetic along the jet and hence controls the strength of the shocks and the variations in the flow Lorentz factor. Finally, the magnetization shapes the jets transversally under the action of the magnetic tension and the magnetic pressure gradient.

The ultimate goal of this work is to connect the properties of the magnetohydrodynamical jets with the structures observed in extragalactic jets at parsec scales. To this aim, we have modelled the optically thin total and linearly polarized synchrotron

emission emanating from our jet simulations assuming that the rest-mass and internal energy densities of the simulated thermal plasma are good tracers of the particle and energy distribution of the non-thermal population responsible of the synchrotron emission. We are neglecting the radiative losses which would change the non-thermal particle distribution along the jet, and any process of particle acceleration at shocks. Only fully uniform magnetic fields are considered in our RMHD formulation for the jet flow, neglecting therefore any turbulence that may be present in actual AGN jets. The presence of a randomly oriented component in the magnetic field would result in a more variable polarization throughout the jet and a net overall decrease in the degree of polarization with respect to those values obtained in our simulations.

The integration of the radiative transfer equations for different viewing angles produce images of jets with a rich transversal structure and knots with a large variety of relative intensities and separations. Our emission simulations exhibit the expected asymmetry across the jet width in the total and polarized intensity for jets threaded by helical magnetic fields, and its dependence with the viewing angle. The selected pitch angle of 45° for all models maximizes the asymmetry in the emission, which is displaced progressively from the top to the bottom of the jets as the viewing angle increases. The helical structure of the magnetic field leads also to a stratification in the degree of polarization across the jet width, more relevant as the jet Mach number and viewing angle increase.

As a consequence of the magnetic pressure gradient and magnetic tension, jet models with large magnetizations concentrate most of their internal energy in a hot spine around the axis. Following our prescription for particle injection, in which the internal energy of the non-thermal population is a constant fraction of the thermal one, this produces also a bright spine present in both total and polarized emission, which in the case of the model M1B3 (with the highest magnetization), concentrates half of its total emission within $[-0.16, 0.16]R_j$ of the jet width. Spine brightening can therefore be used to identify AGN jets that are magnetic dominated, and in which the internal energy of the thermal and non-thermal populations are directly related.

The series of bright knots associated with the recollimation shocks and observed in all of our simulations, present a relative intensity, as compared with the underlying jet emission, modulated by the Doppler boosting ratio between the shocks and the rarefactions. Bearing in mind projection effects due to the variable number of recollimation shocks in the jets, we obtain for small viewing angles less intense knots for hot and magnetically dominated models, and significantly brighter knots for kinetically dominated models. For larger viewing angles hot and magnetically dominated models increase their relative knot intensity as the Doppler boosting in shocks becomes progressively more prominent than in rarefactions. We note that the relative intensity of the knots with respect to that of the underlying flow is probably underestimated in our models, as *in-situ* particle acceleration in the recollimation shocks should increase significantly the energy density of the non-thermal, radiating particles in the knots.

The bimodal distribution of EVPAs expected for axially-symmetric jets with helical magnetic fields is captured in our simulations for small values of the viewing angle. As it increases, the overall trend of the EVPAs is to remain perpendicular to the jet axis,

revealing the dominance of the poloidal component of the magnetic field. However, small variations in the polarization angle of up to $\sim 26^\circ$ appear around stationary components regardless of the viewing angle. Larger rotations in polarization may be expected in case of strong particle acceleration in the recollimation shocks associated with these emission knots. These rotations are produced by a break in the symmetry along the integration column with respect to the jet axis, generating some Stokes U. This asymmetric profile is in turn produced by the presence of recollimation shocks. This characteristic polarization in the stationary emission knots can be used to identify recollimation shocks in VLBI observations of blazar jets.

Despite all the limitations of the magnetohydrodynamical and emission simulations[6], our approach allows for a thorough study of wide regions of the space of parameters defining AGN jets at parsec scales. As a sample, in the present paper we have explored the emission signatures of a set of models spanning ample ranges of magnetosonic Mach number, internal energies and magnetizations. However this study has been restricted to fixed values of other important parameters, such as the flow Lorentz factor and the magnetic pitch angle, and to particular configurations of the magnetic field. Extending our study to different configurations of the magnetic field, jet flow Lorentz factors, and traveling perturbations is required for a more direct comparison with actual VLBI observations of AGN jets, to explore the wealth of different structures and polarizations observed. This is now underway and the results will be published elsewhere.

Acknowledgements
We thank the anonymous referee for helpful comments that have improved our paper. This work has been supported by the Spanish Ministerio de Economía y Competitividad (grants AYA2013-40979-P, AYA2013-48226-C3-2-P, AYA2016-77237-C3-3-P, and AYA2016-80889-P), and the Generalitat Valenciana (grant PROMETEOII/2014/069). JMM wishes to thank Oliver Porth for clarifying the boundary conditions for model A shown in Appendix A.

[6] An additional limitation of our procedure comes from the nature of the numerical approximation used in the computation of the magnetohydrodynamical jet models. Since it is only valid in the relativistic limit, it can not be used to describe jet models with extended (subrelativistic) shear layers and the resulting observational phenomenology associated to them.

2.A Steady relativistic jets as quasi-one-dimensional time-dependent jet models

2.A.1 The approximation

Magnetohydrodynamical models have been computed following the approach developed by Komissarov *et al.* (2015) that allows to study the structure of steady, axisymmetric relativistic (magnetized) flows using one-dimensional time-dependent simulations. The approach is based on the fact that for narrow jets with axial velocities close to the light speed the steady-state equations of relativistic magnetohydrodynamics can be accurately approximated by the one-dimensional time-dependent equations with the axial coordinate acting as the *temporal* coordinate.

The approximation is valid as long as the radial dimension of the flow is much smaller than the axial one, and simple, quasi-one-dimensional flows are considered with the radial and azimuthal components of the flow velocity much smaller than the axial one, which approaches light speed (i.e., $v^r, v^\phi \ll v^z$). Consistency with the one-dimensional version of the divergence free condition forces to consider configurations with very small radial components of the magnetic field ($B^r \ll B^\phi, B^z$). All these constraints can be verified *a posteriori*, once the approximate two-dimensional solution has been obtained.

The more delicate point of the approximation consists in the implementation of the boundary conditions at the jet surface, which in the one-dimensional approximation become a kind of time-dependent boundary conditions. Special actions should be undertaken to mimic the effect of the two-dimensional, steady boundary conditions at the jet surface: i) the jet surface should be tracked along the time, and ii) the ambient gas parameters are reset every computational time step according the prescribed functions of time. Following Komissarov *et al.* (2015) the jet surface is tracked from the injection at the jet base using a passive scalar which is advected with the continuity equation. Secondly, in order to keep the jet surface to behave as a contact, the radial velocity of the ambient gas is reset not to zero but to its value at the last jet cell.

2.A.2 Testing

From a numerical point of view the code used in these simulations is the one-dimensional, radial-cylindrical, time-dependent version of the RMHD code used in Martí (2015a) and Martí *et al.* (2016). It is a second-order conservative, finite-volume code based on high-resolution shock-capturing techniques. An overview of the specific algorithms used in the code and an analysis of its performance can be found in Appendices A and B, respectively of Martí (2015a). Also in that paper this one-dimensional version of the code was used to test the code's ability to keep rotating and non-rotating configurations of axially symmetric relativistic magnetized flows in equilibrium (see their Sect. 5.1).

Figure 2.18 reproduces Figure 6 of Komissarov *et al.* (2015) corresponding to the so-called model A (see their Sect. 4.3). In this test, a moderately magnetized,

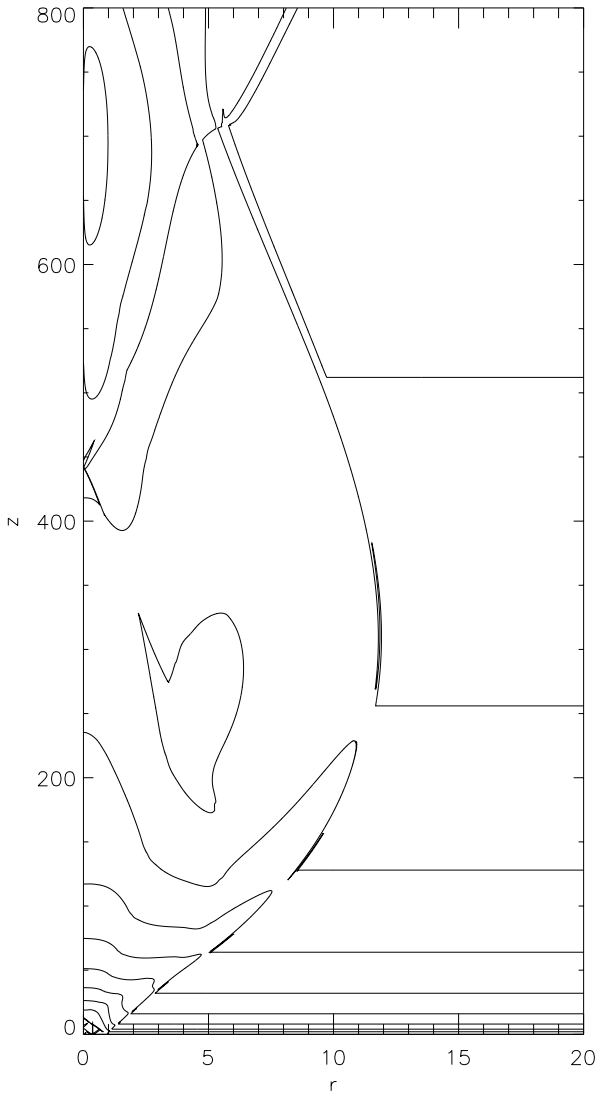

Figure 2.18: Contour plot of the rest-mass density distribution of a stationary magnetized relativistic jet propagating in a pressure decreasing atmosphere corresponding to Model A of Komissarov *et al.* (2015).

relativistic jet with a purely azimuthal magnetic field is injected into an atmosphere with a power law pressure distribution from a nozzle located at some distance of the jet base. As the jet enters the pressure decreasing atmosphere, it expands rapidly and a rarefaction wave propagates towards the axis. Once the jet becomes over-expanded starts to recollimate and a reconfinement shock sets in. The shock reaches the axis at $z \approx 450$, reflects and then returns to the jet boundary at $z \approx 700$, from where the jet re-expands again. Figure 2.18 shows the same rest-mass density contours as in the original Komissarov et al.'s plot. As it can be seen our simulation captures not

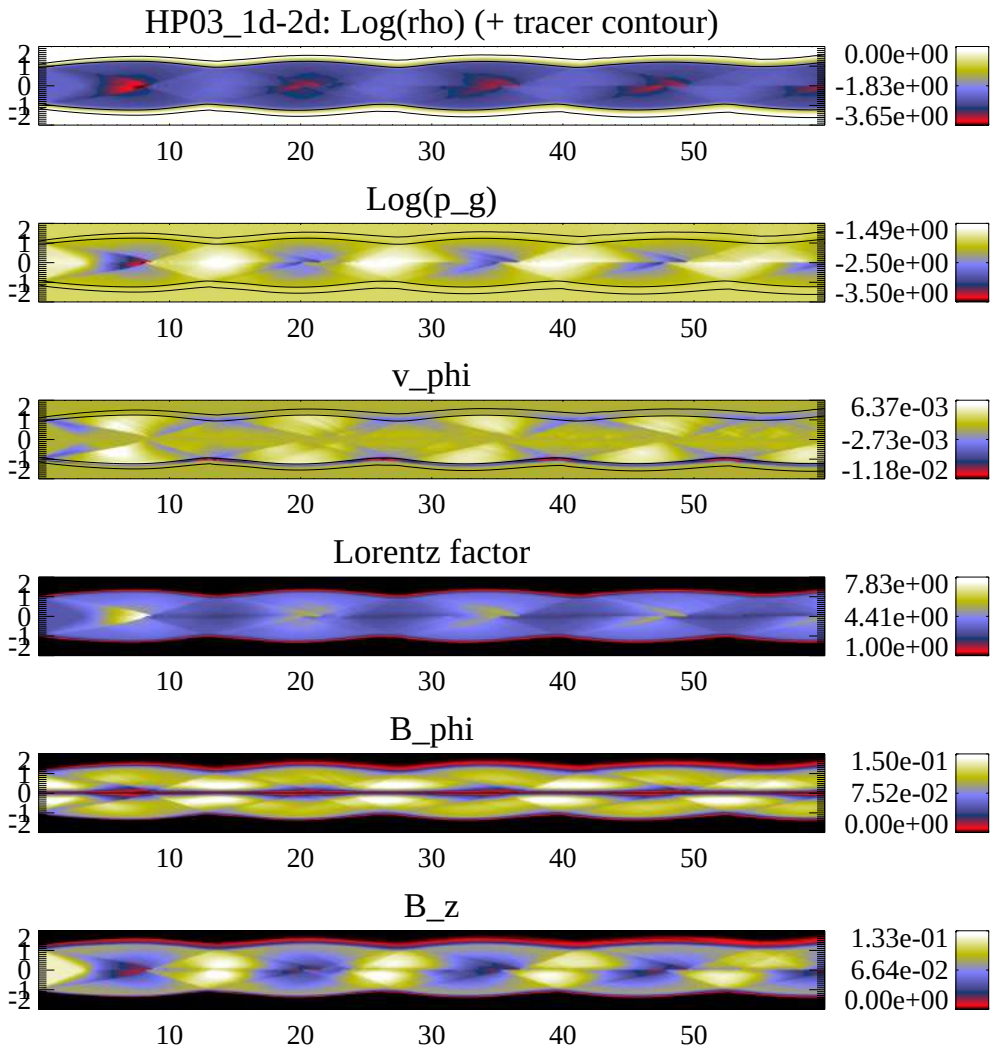

Figure 2.19: Two-dimensional steady-state model HP03 in Martí *et al.* (2016) (top-half panels) versus its quasi-one-dimensional time-dependent counterpart (bottom-half panels). The largest discrepancies between the two approaches are found in the outermost shear layer.

only the essential features of their calculation (the fast expansion of the jet reaching a maximum radius of $r_{\rm max} \approx 12$ at $z \approx 300$, the recollimation shock reaching the axis at $z \approx 450$, and the jet re-expansion beyond $z \approx 700$), but also the tiniest details of the contour lines.

Our simulation was performed with a numerical resolution of 128 cells per initial jet radius (320 cells per initial jet radius in the original simulation of Komissarov and colls.) We used a piecewise-linear reconstruction of the spatial grid with MC limiter, and the HLLC Riemann solver (Mignone & Bodo, 2006). The advance in time was done using the third-order TVD-preserving Runge-Kutta of Shu & Osher (1988, 1989)

with $CFL = 0.3$.

Finally, we can compare the stationary two-dimensional solutions found in Martí *et al.* (2016) with the thinest shear layers (models PH02, HP03) with the corresponding one-dimensional approximations used in the present paper. Figure 2.19 displays this comparison for model HP03 with a shear layer corresponding to $m = 12$. The differences in the extrema of the distributions of the rest mass density, thermal pressure, axial flow velocity and magnetic field components within the jet between the two simulations are small (of a few percent in relative terms). The discrepancies in the shock separation are of the same order ($\approx 3.3\%$). The differences for model PH02 are similar. The rest of simulations of Martí *et al.* (2016), with wider shear layers, do not admit a fair comparison with their corresponding one-dimensional models since the shear layers in these cases can not be treated consistently within the one-dimensional approximation.

2.B Model definition

2.B.1 Functions defining the jet transversal profiles

Axially symmetric, non-rotating, steady jet models are characterized by five functions. Using cylindrical coordinates (referred to an orthonormal cylindrical basis $\{\mathbf{e}_r, \mathbf{e}_\phi, \mathbf{e}_z\}$) in which the jets propagate along the z axis, these functions are the jet density and pressure ($\rho(r)$, $p(r)$, respectively), the jet axial velocity, $v^z(r)$, and the toroidal and axial components of the jet magnetic field ($B^\phi(r)$, $B^z(r)$, respectively), whereas the static unmagnetized ambient medium is characterized by a constant pressure, p_a and a constant density, ρ_a. The equation of transversal equilibrium establishing the radial balance between the total pressure gradient and the magnetic tension, allows to find the equilibrium profile of one of the variables in terms of the others. We shall fix the radial profiles of ρ, v^z, B^ϕ and B^z, and solve for the profile of the gas pressure, p. We use top-hat profiles for ρ, v^z and B^z

$$\rho(r) = \begin{cases} \rho_j, & 0 \leq r \leq R_j \\ \rho_a, & r > R_j, \end{cases} \tag{2.9}$$

$$v^z(r) = \begin{cases} v_j, & 0 \leq r \leq R_j \\ 0, & r > R_j, \end{cases} \tag{2.10}$$

$$B^z(r) = \begin{cases} B^z_j, & 0 \leq r \leq R_j \\ 0, & r > R_j, \end{cases} \tag{2.11}$$

(where ρ_j, v_j and B^z_j are constants) and a particular profile for the toroidal component of the magnetic field

$$B^{\phi}(r) = \begin{cases} \dfrac{2B^{\phi}_{j,\mathrm{m}}(r/R_{B^{\phi},\mathrm{m}})}{1+(r/R_{B^{\phi},\mathrm{m}})^2}, & 0 \le r \le R_j \\ 0, & r > R_j, \end{cases} \tag{2.12}$$

with $R_{B^{\phi},\mathrm{m}}$, the radius at which the toroidal magnetic field reaches its maximum, $B_{j,\mathrm{m}}$, equal to $0.37R_j$ in all the models.

2.B.2 Jet transversal equilibrium

In the general case, the equation of transversal equilibrium establishes the radial balance between the total pressure gradient, the centrifugal force and the magnetic tension,

$$\frac{dp^*}{dr} = \frac{\rho h^* W^2 (v^{\phi})^2 - (b^{\phi})^2}{r}. \tag{2.13}$$

In this equation, p^* and h^* stand for the total pressure and the specific enthalpy including the contribution of the magnetic field

$$p^* = p + \frac{b^2}{2} \tag{2.14}$$

$$h^* = 1 + \varepsilon + p/\rho + b^2/\rho, \tag{2.15}$$

where p is the fluid pressure, ρ its density and ε its specific internal energy. b^{μ} ($\mu = t, r, \phi, z$) are the components of the 4-vector representing the magnetic field in the fluid rest frame and b^2 stands for $b^{\mu}b_{\mu}$, where summation over repeated indices is assumed. v^i ($i = r, \phi, z$) are the components of the fluid 3-velocity in the laboratory frame, which are related to the flow Lorentz factor, W, according to:

$$W = \frac{1}{\sqrt{1 - v^i v_i}}. \tag{2.16}$$

The following relations hold between the components of the magnetic field 4-vector in the comoving frame and the three vector components B^i measured in the laboratory frame:

$$b^0 = W B^i v_i \,, \tag{2.17}$$

$$b^i = \frac{B^i}{W} + b^0 v^i. \tag{2.18}$$

The square of the modulus of the magnetic field, defining the magnetic energy density, can be written as

$$b^2 = \frac{B^2}{W^2} + (B^i v_i)^2 \tag{2.19}$$

with $B^2 = B^i B_i$.

For a non-rotating flow with constant axial velocity v_j and axial magnetic field, the equation of transversal equilibrium can be rewritten

$$\frac{dp}{dr} = -\frac{(B^\phi)^2}{rW_j^2} - \frac{B^\phi}{W_j^2}\frac{dB^\phi}{dr},$$

(where $W_j = (1 - v_j^2)^{-1/2}$) which can be integrated by separation of variables to give

$$p(r) = 2\left(\frac{B^\phi_{j,\mathrm{m}}}{W_j(1 + (r/R_{B^\phi,\mathrm{m}})^2)}\right)^2 + C \quad (0 \le r \le R_j), \tag{2.20}$$

where C is an integration constant set by the boundary condition at R_j.

2.B.3 Parameters defining the jet models

Sections 2.B.1 to 2.B.2 define the jet models for given values of ρ_j, v_j, B^z_j, $B^\phi_{j,m}$ and C. However, some of the parameters of this set are not specially useful (in particular B^z_j, $B^\phi_{j,m}$ and C) and we are going to replace them by some others better suited for our purposes: ϕ_j, the average magnetic pitch angle; β_j, the average jet magnetization; and $\mathcal{M}_{\mathrm{ms},j}$, the average magnetosonic Mach number.

Together with other parameters (significantly the jet overpressure factor, K), the relativistic magnetosonic Mach number

$$\mathcal{M}_{ms} = \frac{W}{W_{ms}}\frac{v}{c_{ms}}, \tag{2.21}$$

governs the properties of internal conical shocks in overpressured magnetized jets in the same way as the Mach number does in purely hydrodynamic, overpressured jets. In the previous expression, W_{ms} is the flow Lorentz factor associated to the magnetosonic speed, c_{ms},

$$c_{ms} = \sqrt{c_A^2 + c_s^2(1 - c_A^2)}. \tag{2.22}$$

which, in turn, is defined in terms of the sound speed, c_s, and the Alfvén speed, c_A,

$$c_A = \sqrt{\frac{b^2}{\rho h + b^2}}. \tag{2.23}$$

Finally, the magnetization, β, is defined as

$$\beta = \frac{b^2}{2p}. \tag{2.24}$$

For fixed values of the jet flow velocity, v_j, and the jet rest-mass density, ρ_j, the averaged values of the magnetosonic Mach number and the magnetization allows one to fix the averaged values of the jet gas pressure, p_j, and the magnetic energy

density, b_j^2. Then, the averaged value of the jet gas pressure determines C, whereas the averaged value of the jet magnetic energy density and the averaged magnetic pitch angle,

$$\phi = \arctan\left(\frac{B^\phi}{B^z}\right), \tag{2.25}$$

allows one to fix the remaining two parameters, B_j^z and $B_{j,m}^\phi$.

The set of parameters is completed with K, the averaged jet overpressure factor, which together with p_j and b_j^2, fixes the ambient pressure p_a.

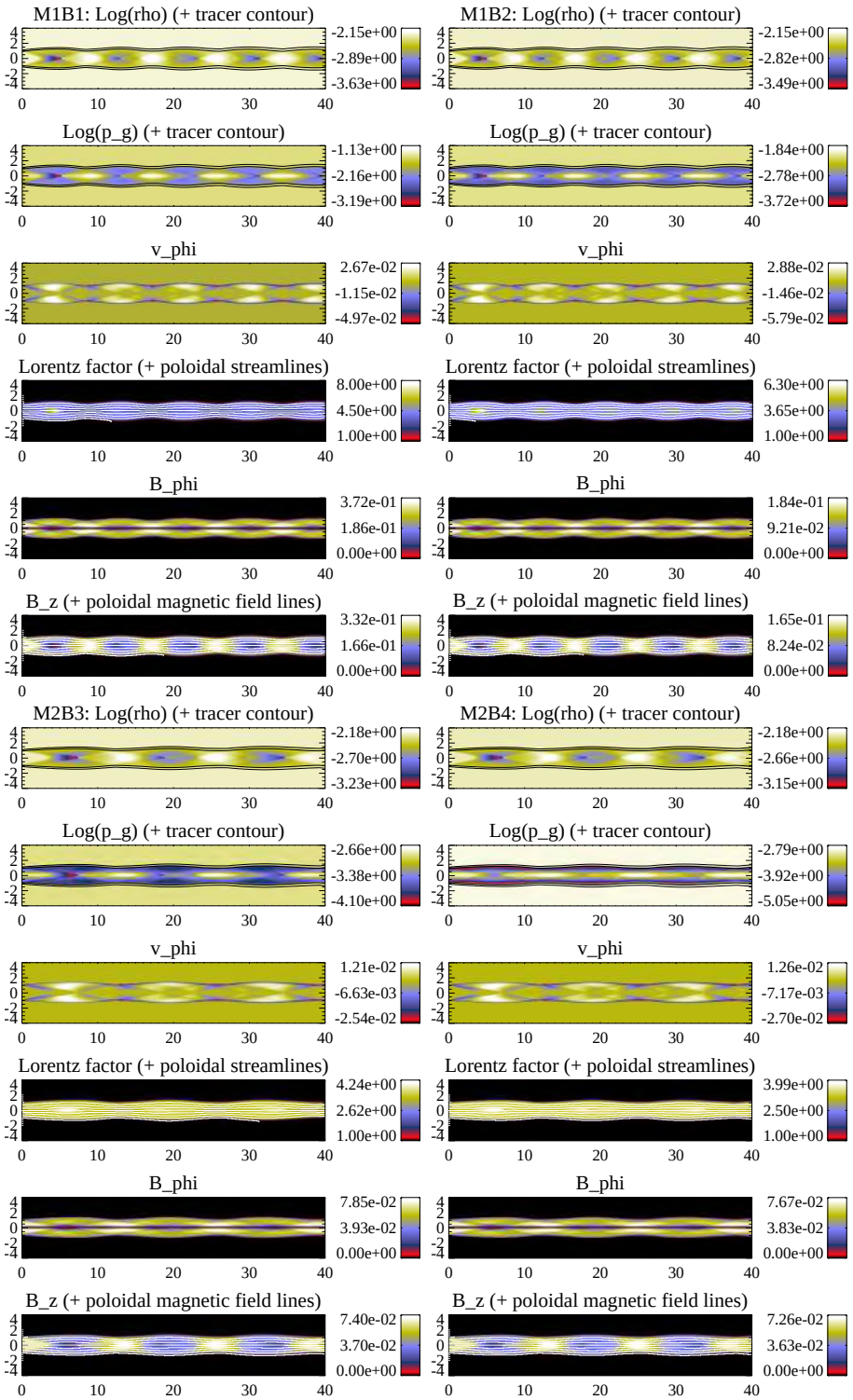

Extended Data Figure 2.20: Steady structure of the magnetically dominated models M1B1 and M1B2, and the magnetically-kinetically dominated models M2B3 and M2B4. Panel distribution as in Figure 2.2.

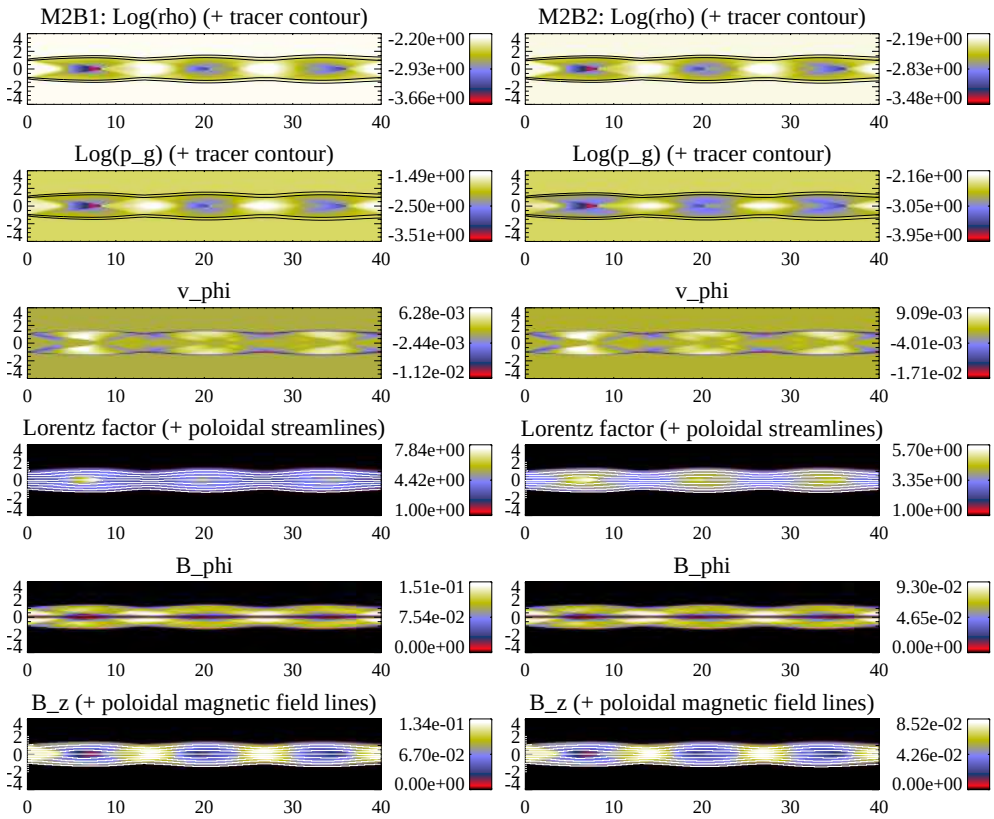

Extended Data Figure 2.21: Steady structure of the hot jet model M2B1 and the hot-magnetically dominated model M2B2. Panel distribution as in Figure 2.2.

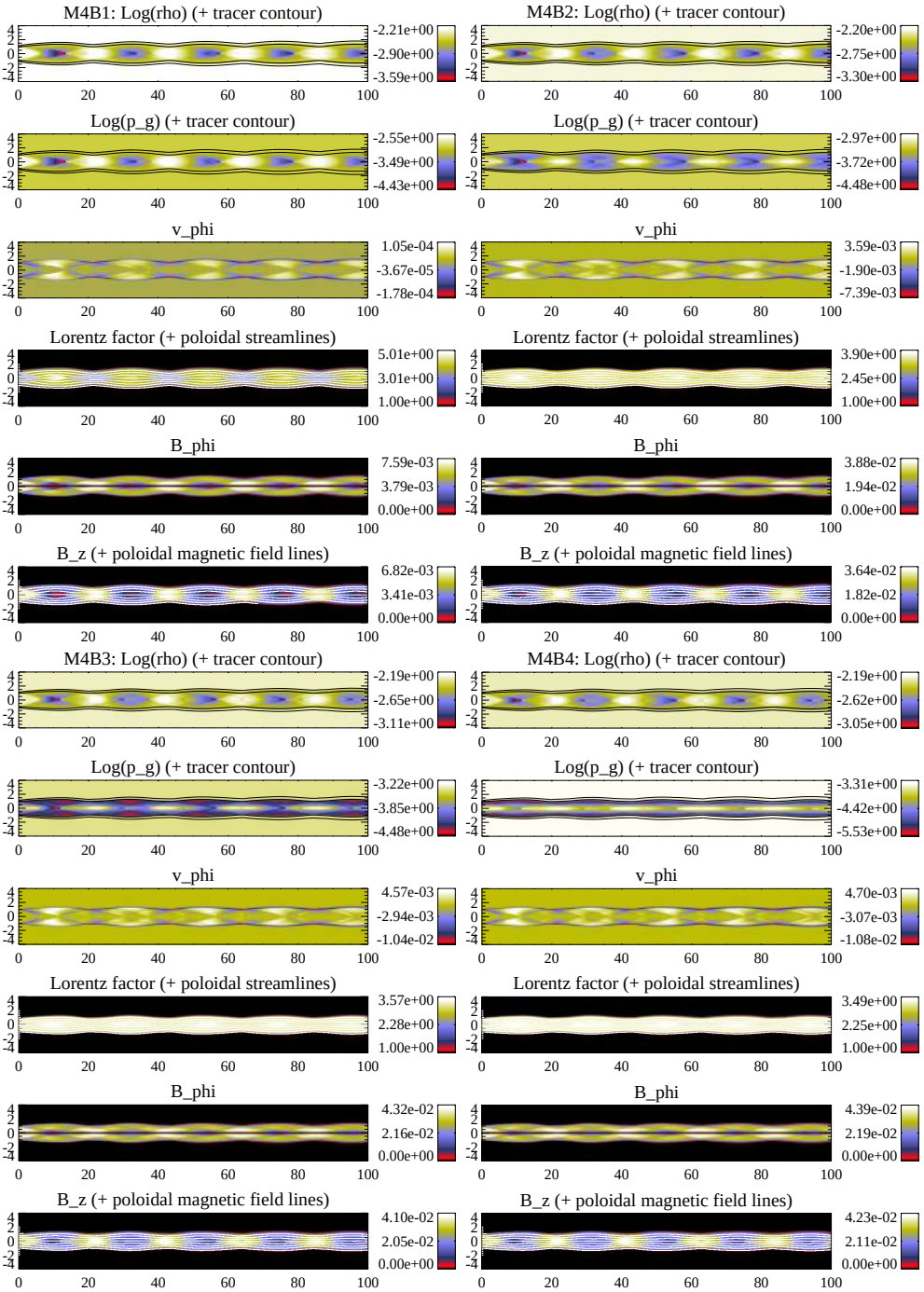

Extended Data Figure 2.22: Steady structure of the hot-kinetically dominated model M4B1 and the kinetically dominated models M4B2, M4B3, M4B4, M5B1, M5B3, M5B4. Panel distribution as in Figure 2.2.

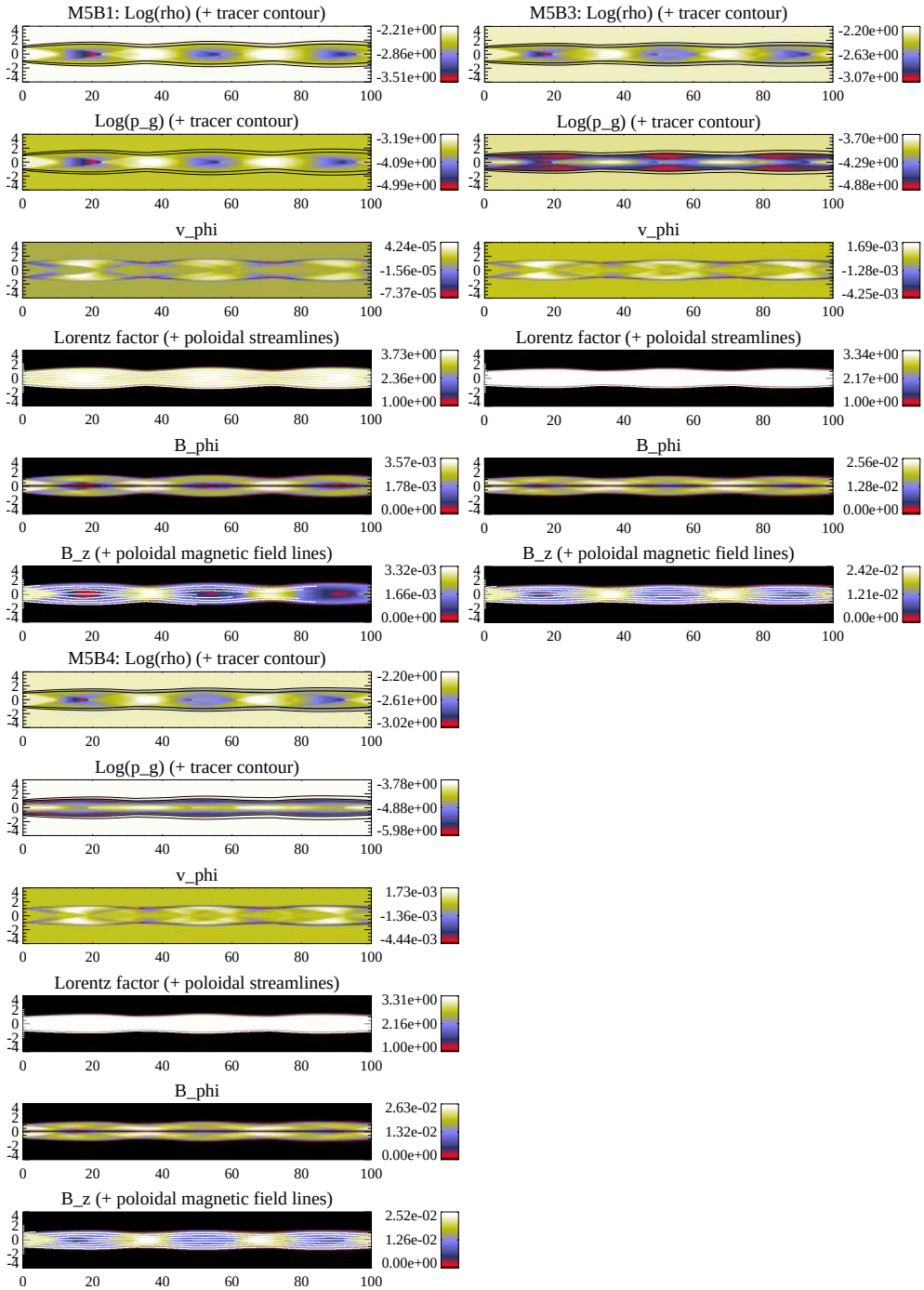

Extended Data Figure 2.22: (continued)

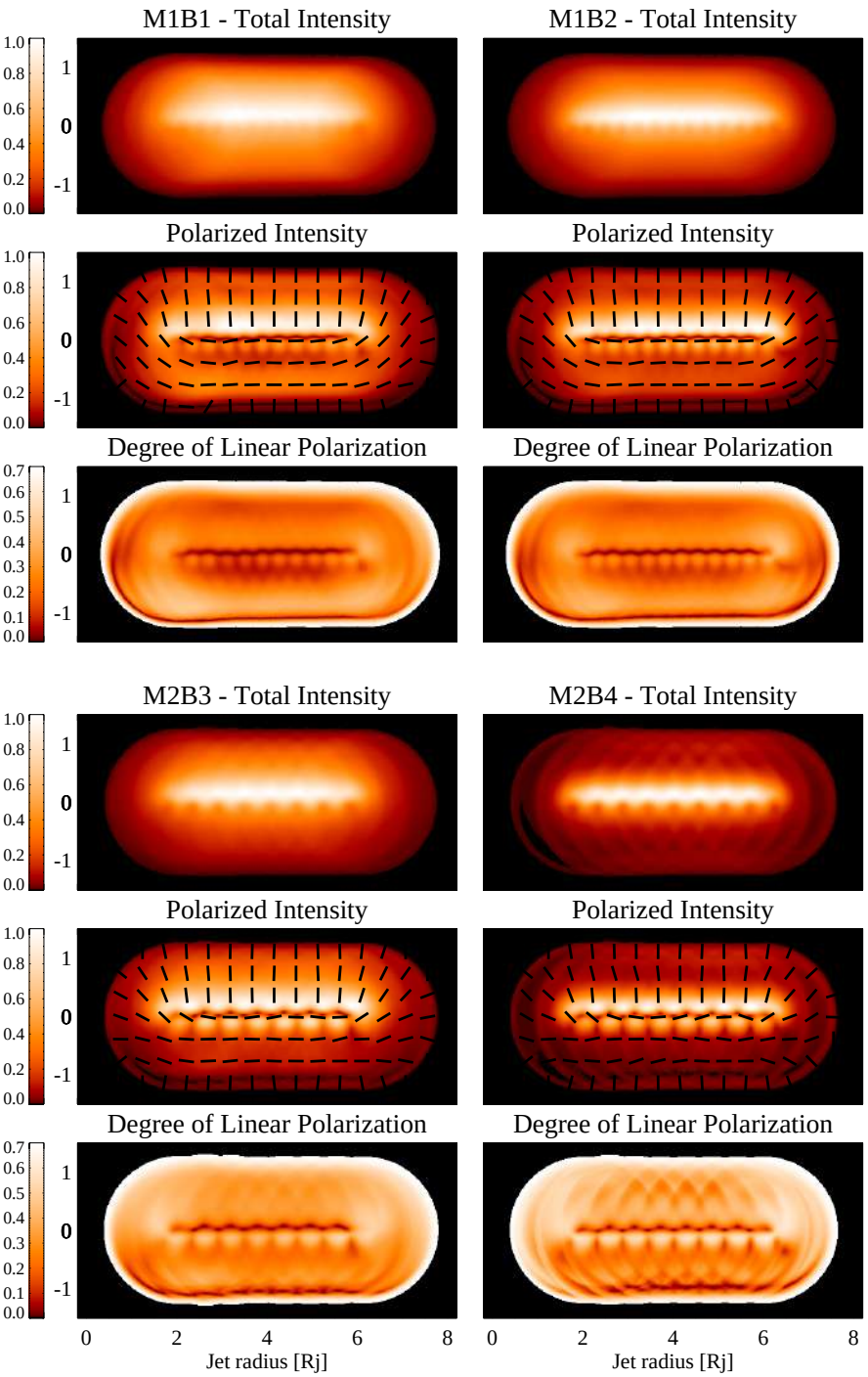

Extended Data Figure 2.23: Same as Figure 2.8, with a viewing angle of 2°, for the magnetically dominated jet models M1B1 and M1B2, the magnetically-kinetically dominated jet models M2B3 and M2B4, the hot jet model M2B1, the hot-magnetically dominated jet model M2B2, the hot-kinetically dominated jet model M4B1, and the kinetically dominated jet models M4B2, M4B3, M4B4, M5B1, M5B3, and M5B4.

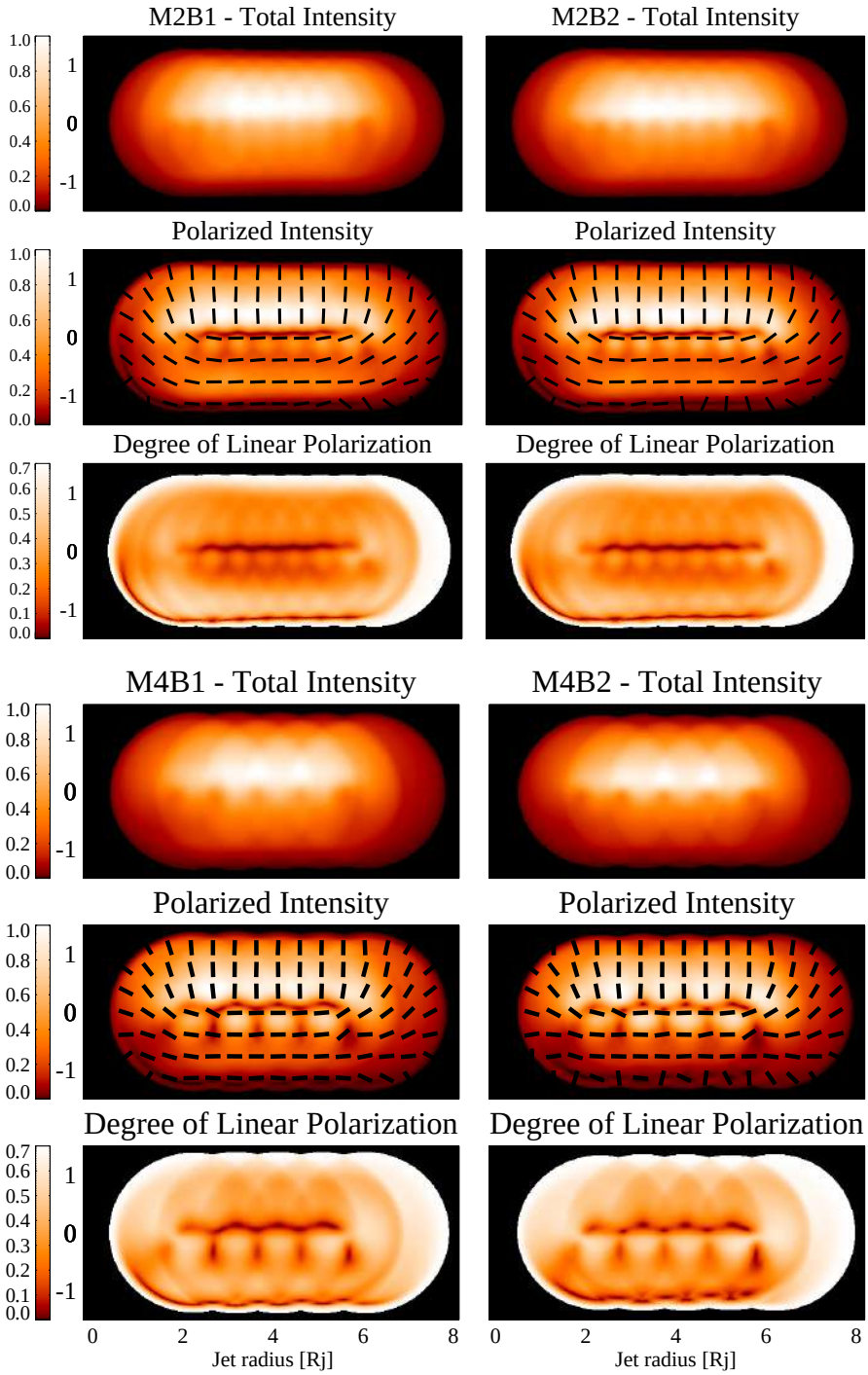

Extended Data Figure 2.23: (continued)

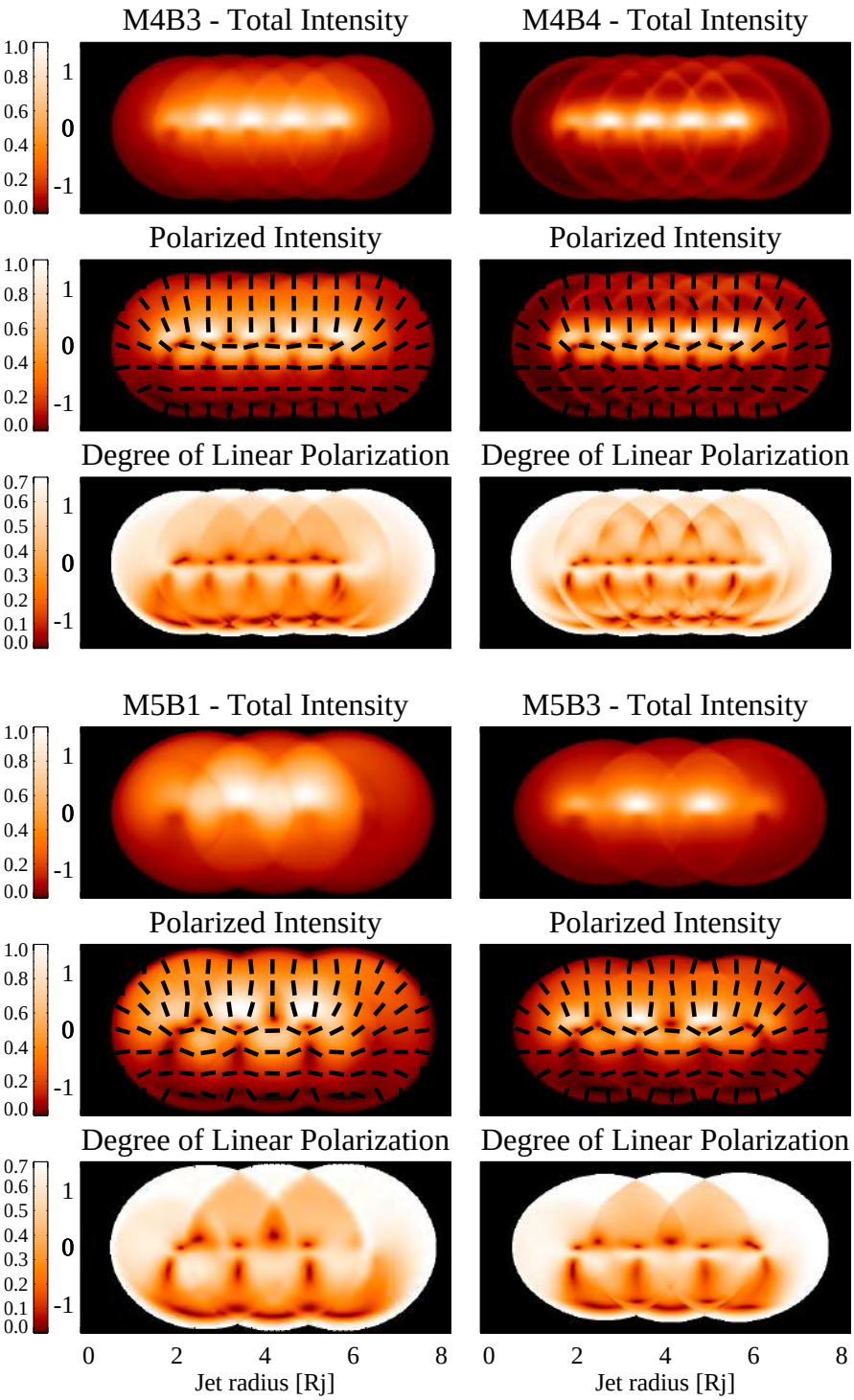

Extended Data Figure 2.23: (continued)

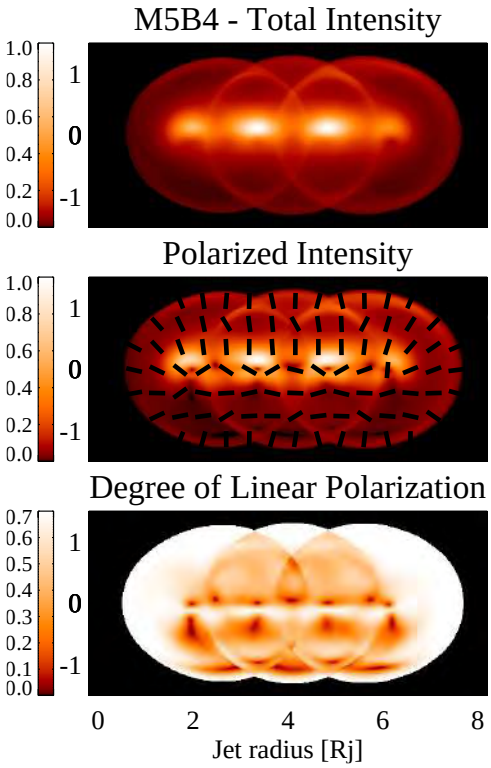

Extended Data Figure 2.23: (continued)

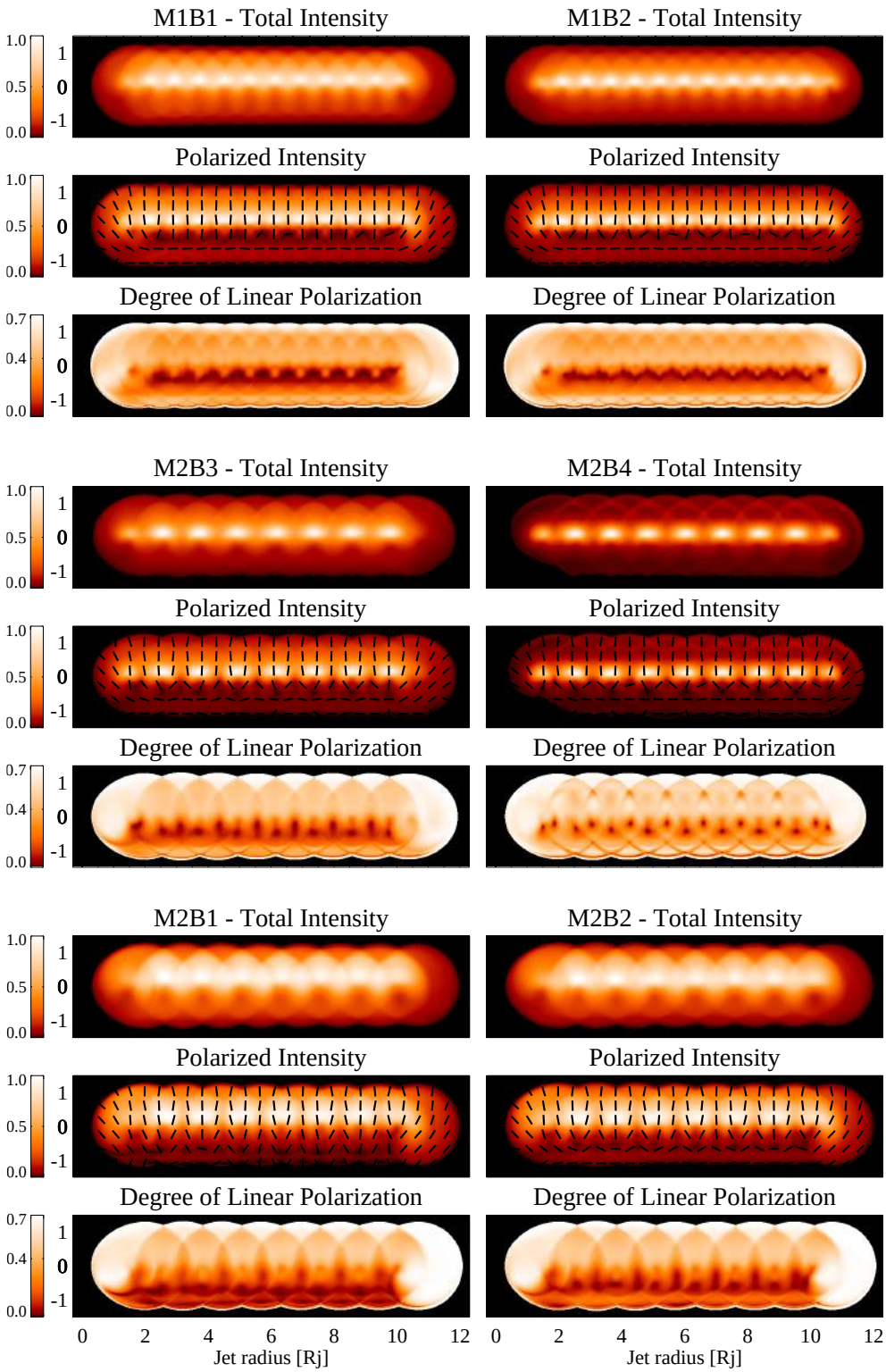

Extended Data Figure 2.24: Same as Extended Data Figure 2.23, with a viewing angle of $5°$.

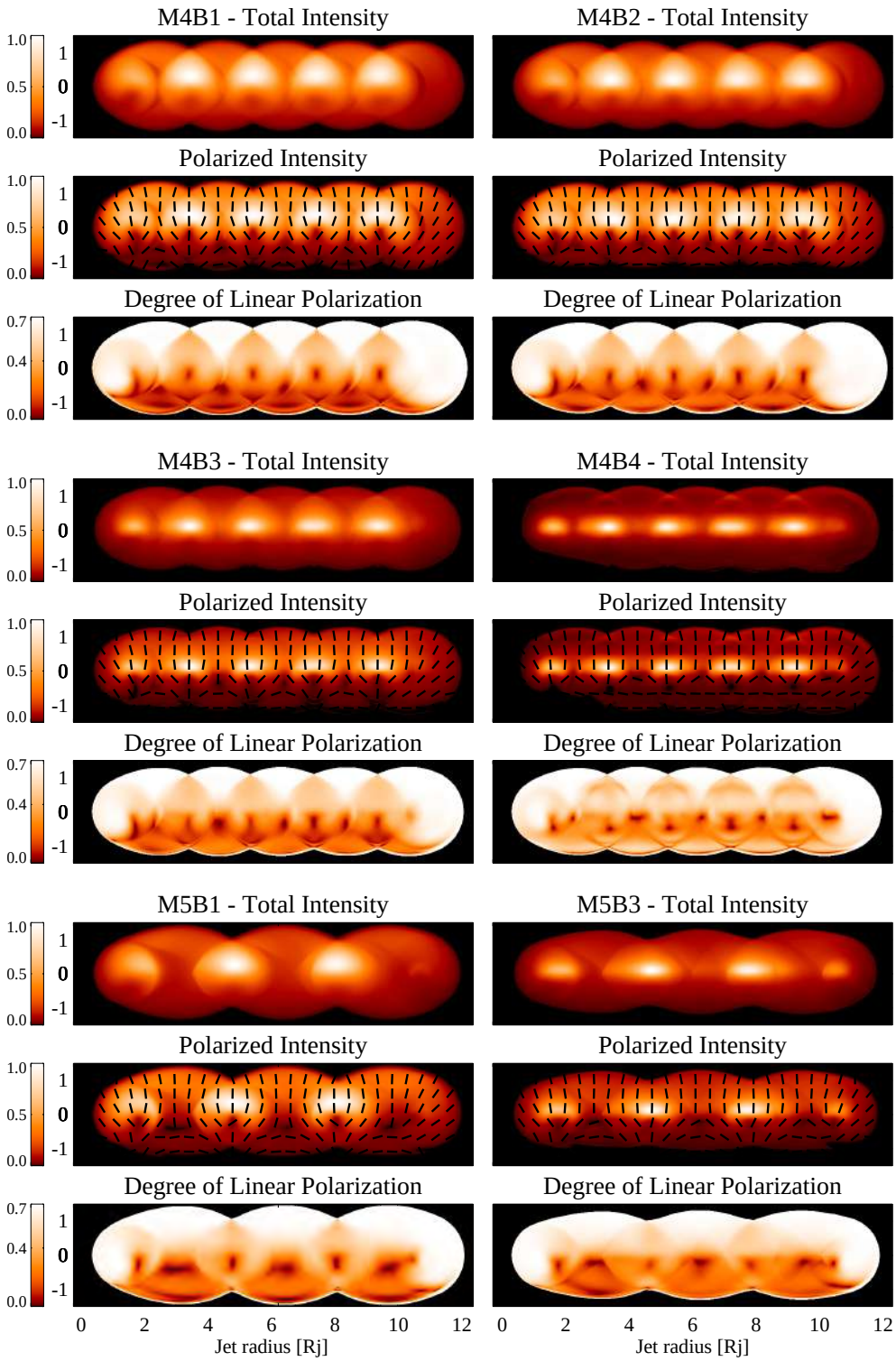

Extended Data Figure 2.24: (continued)

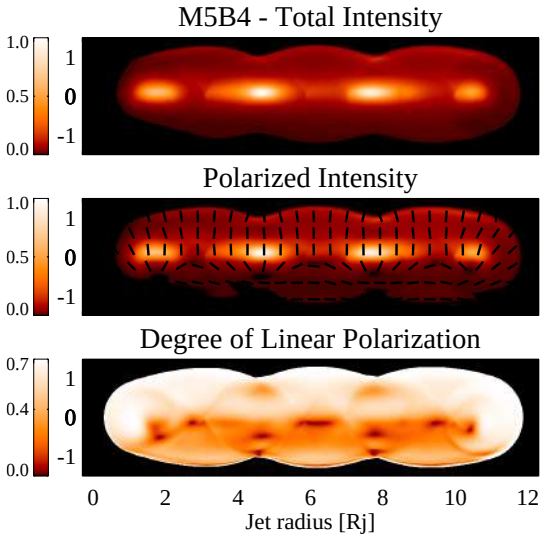

Extended Data Figure 2.24: (continued)

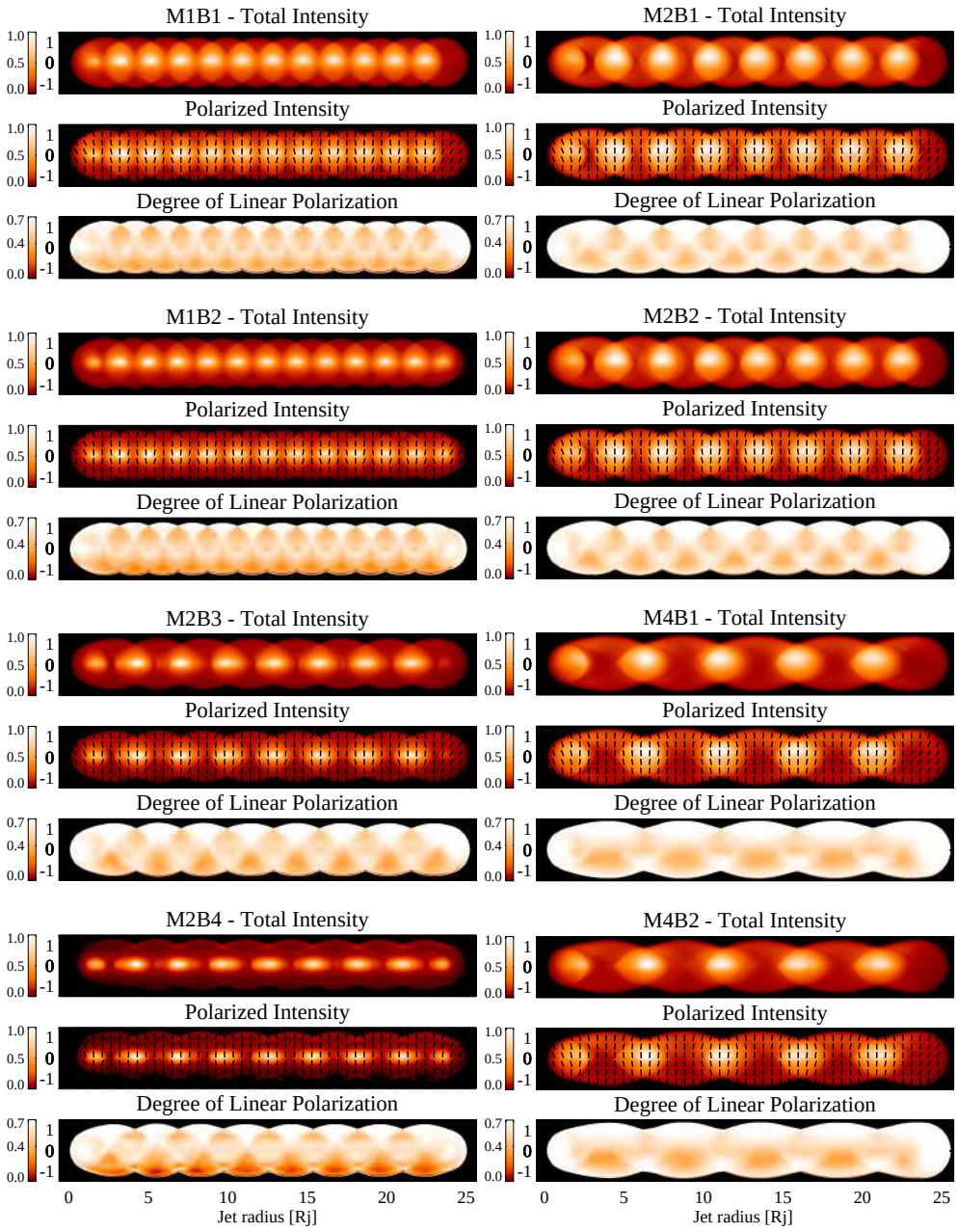

Extended Data Figure 2.25: Same as Extended Data Figure 2.23, with a viewing angle of 10°.

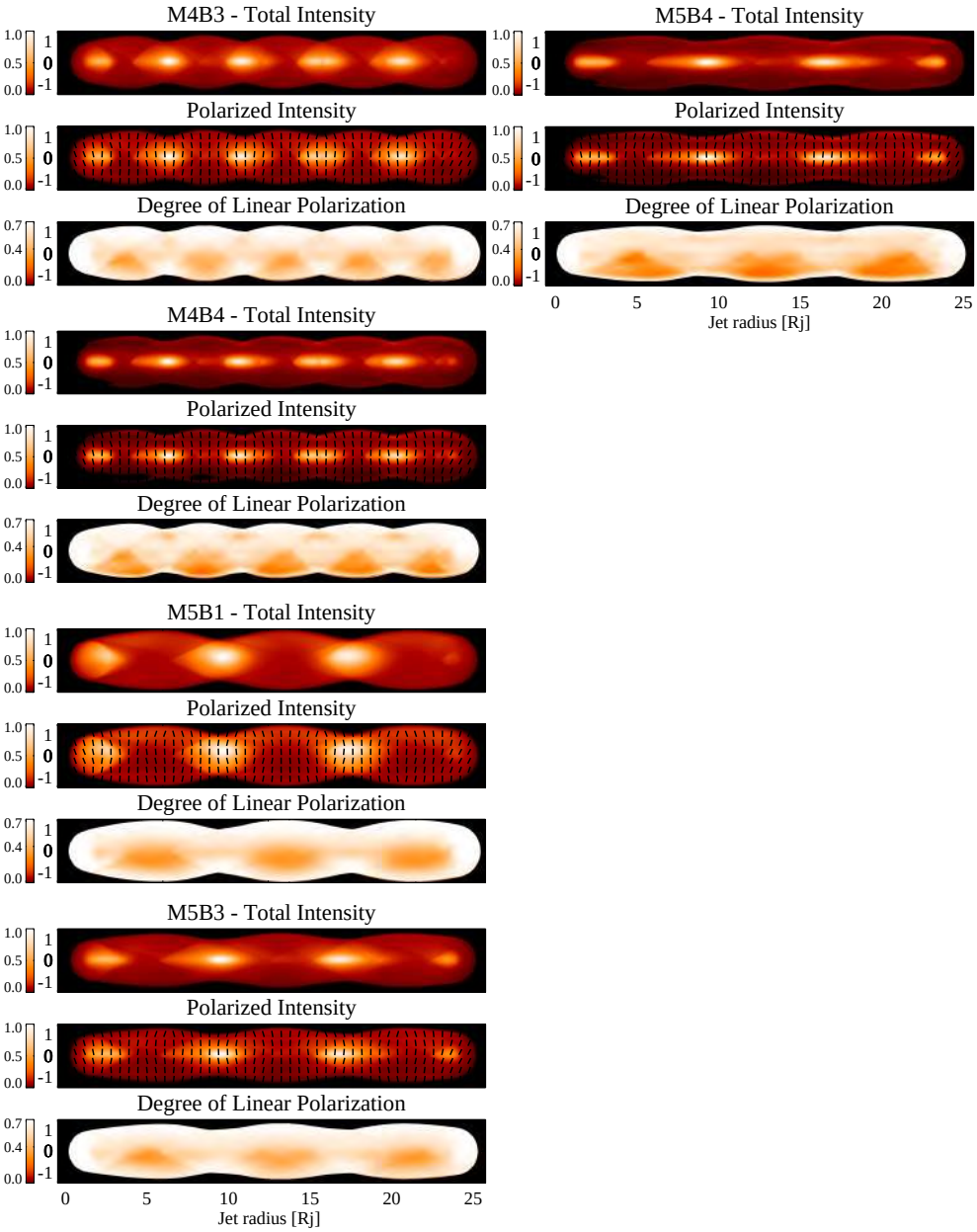

Extended Data Figure 2.25: (continued)

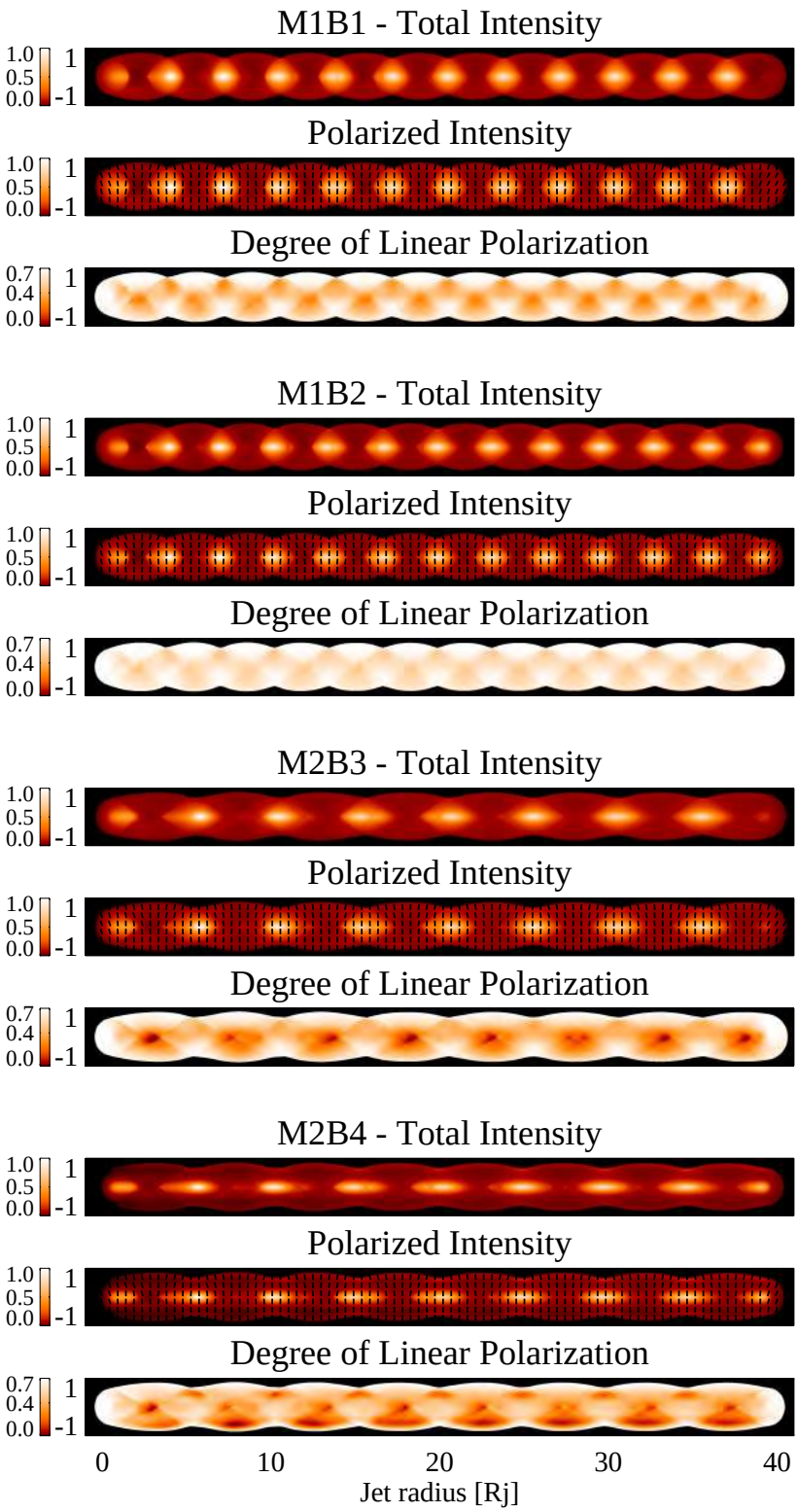

Extended Data Figure 2.26: Same as Extended Data Figure 2.23, with a viewing angle of 20°.

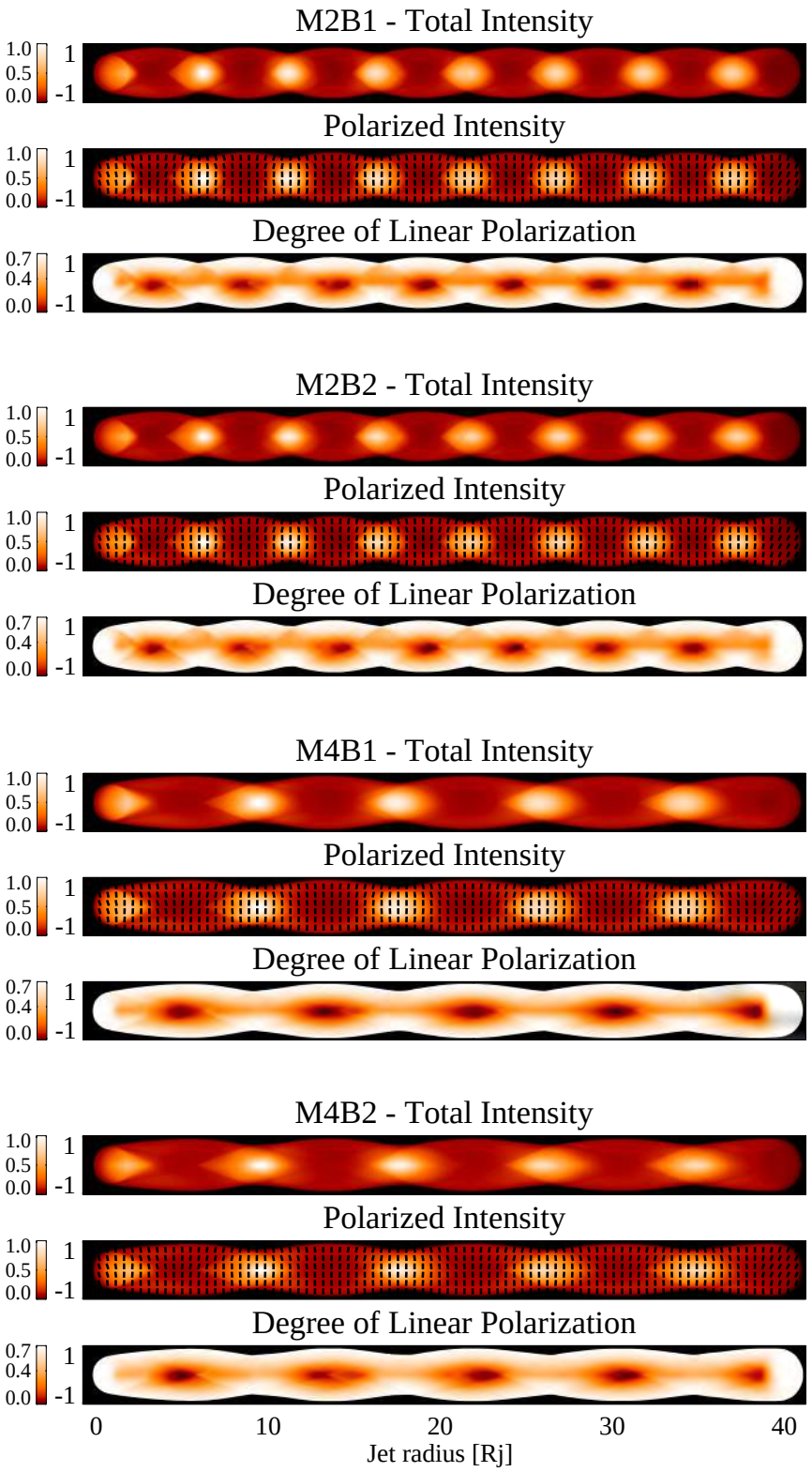

Extended Data Figure 2.26: (continued)

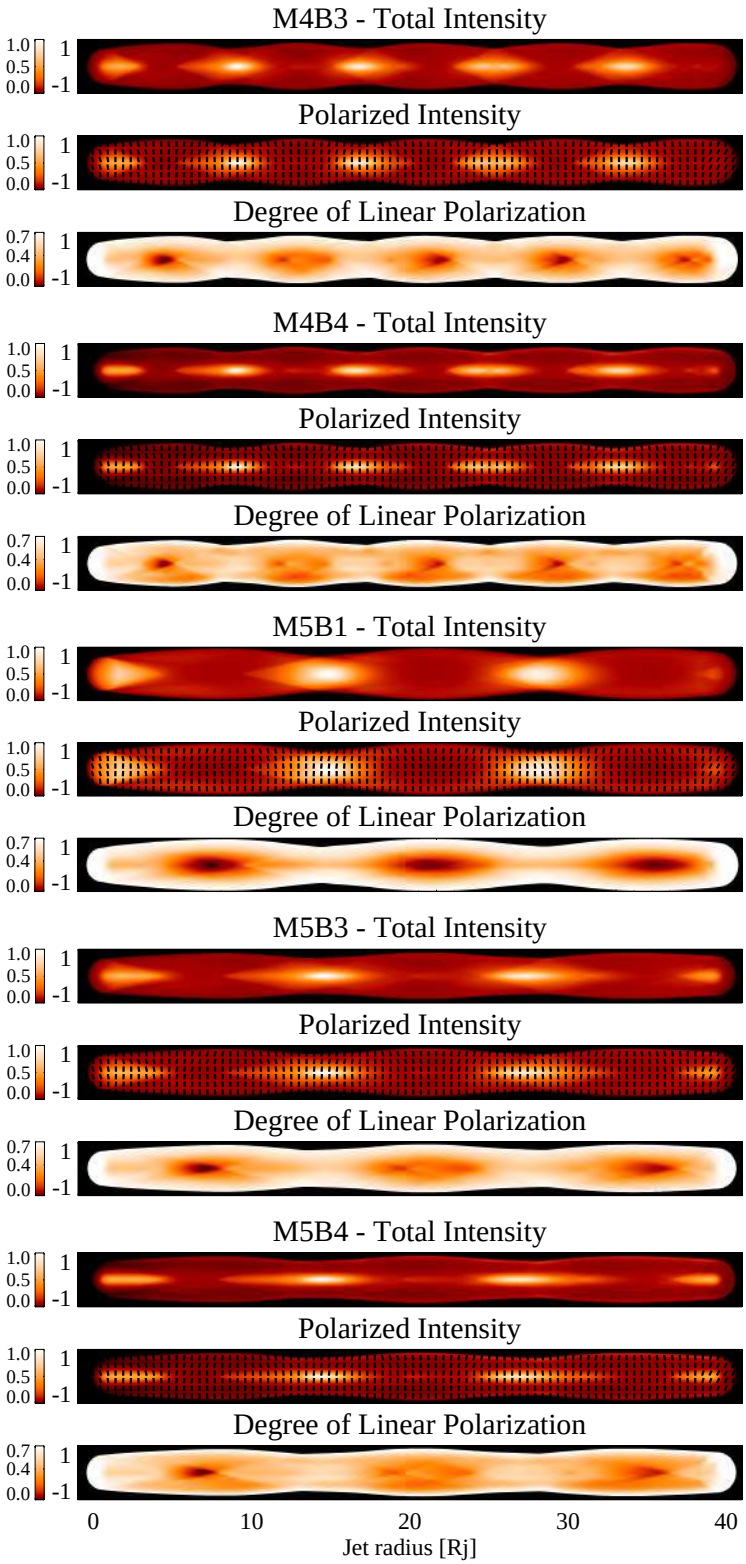

Extended Data Figure 2.26: (continued)

Chapter 3 | Polarimetric Emission from RMHD Jets. II.

A. Fuentes, I. Moya-Torregrosa, J. M. Martí, J. L. Gómez, and M. Perucho
Magnetized relativistic jets and helical magnetic fields. II. Radiation
Astronomy & Astrophysics, **650**, A61 (2021)

Abstract

This is the second of a series of two papers that deepen our understanding of the transversal structure and the properties of recollimation shocks of axisymmetric, relativistic, superfast magnetosonic, overpressured jets. They extend previous work that characterized these properties in connection with the dominant type of energy (internal, kinetic, or magnetic) in the jet to models with helical magnetic fields with larger magnetic pitch angles and force-free magnetic fields. In the first paper of this series, the magnetohydrodynamical models were computed following an approach that allows studying the structure of steady, axisymmetric, relativistic (magnetized) flows using one-dimensional time-dependent simulations. In this paper, synthetic radio images of the magnetohydrodynamical models are produced based on two different models to connect the thermal particle population, modeled by the hydrodynamical code, and the nonthermal particle population (added in post-processing) that causes the synchrotron radiation. The role of the magnetic tension and the Lorentz force in modeling the observational appearance of jets, namely the cross-section emission asymmetries, spine brightening, relative intensity of the knots, and polarized emission is analyzed. A cross-section emission asymmetry caused by a differential change in the angle between the helical magnetic field and the line of sight across the jet width is observed in all models and for both synchrotron emission approximations, as expected from a purely geometrical origin, for viewing angles $< 10^{\circ}$. Models with the highest magnetizations and/or magnetic pitch angles lead to an uneven distribution of the internal energy as a consequence of the larger relative magnetic tension and radial Lorentz force, which translates into a spine brightening in the total and linearly polarized intensity maps. Force-free models display a distinct spine brightening that originates in the radial gradient of the axial magnetic field. Highly magnetized jets with large toroidal fields tend to have weaker shocks and correspondingly weaker radio knots. Signatures of this toroidal field can be found in the linearly polarized synchrotron emission for jets with large enough magnetic pitch angles and large enough viewing angles.

3.1 Introduction

The dynamics of relativistic jets have been studied through numerical simulations for more than twenty years now with great success (e.g., Martí, 2019, and references therein). However, the importance of relativistic and projection effects dominating the emission (e.g., Gómez *et al.,* 1993; 1994a; b), makes computing the radiative output a necessary step for a comparison with very long baseline interferometric (VLBI) observations of active galactic nuclei (AGN) jets. This paper studies the nonthermal radio emission that is expected based on the magnetohydrodynamic jet models that we presented in the accompanying paper in this series (Moya-Torregrosa *et al.,* 2021, Paper I here after), and analyzes the most salient features with a clear focus on the interpretation of VLBI observations of AGN jets.

Paper I focused on understanding the transversal structure and the properties of recollimation shocks of axisymmetric, relativistic, superfast magnetosonic, overpressured jets. These relativistic magnetohydrodynamical (RMHD) jet models were computed following the approach developed by Komissarov *et al.* (2015). In this work, the emphasis is on the signature of these structural ingredients in synthetic synchrotron maps mimicking radio observations of AGN jets at parsec scales. The radiative simulations are performed using the same code as in Fuentes *et al.* (2018), which are thoroughly described in Gómez *et al.* (1993, 1994a,b, 1995, 1997). The code connects the thermal particle population (modeled by the RMHD code) and the nonthermal particle population to obtain synthetic radio maps for the total and polarized synchrotron emission. These works extend the previous work by Fuentes *et al.* (2018) to models with helical magnetic fields with larger magnetic pitch angles and force-free configurations.

Establishing a relation between the thermal and nonthermal populations requires a detailed prescription for the particle acceleration processes that connect both populations, presumably taking place in strong shocks or in magnetic reconnection events (see, e.g., Sironi *et al.,* 2015). A proper treatment of particle acceleration or injection in shocks (e.g., Kirk *et al.,* 2000) or magnetic reconnection (e.g., Lyubarsky, 2005) requires a microscopic description of the fluid that is not implemented in our RMHD approach. Nevertheless, as a first-order approximation, two approaches connecting the thermal and nonthermal particle populations in a post-processing phase were considered. In the first approach (following Gómez *et al.* (1995, 1997), Komissarov & Falle (1997), Broderick & McKinney (2010), and Porth *et al.* (2011)), the particle acceleration takes place at shocks, and the internal energy of the nonthermal population is a constant fraction of the thermal electron energy density considered in the RMHD simulations. In the second approach, which mimicks the transfer of energy at magnetic reconnection sites, the nonthermal population energy density is taken as proportional to the magnetic energy density (Porth *et al.,* 2011). In the case of force-free models, only the emission of the strongly magnetically dominated cases under the second particle acceleration approach was computed.

The paper is organized as follows. Section 3.2 summarizes the properties of the magnetohydrodynamic models that constitute the basis of the emission study undertaken in this work. Section 3.3 describes the numerical code connecting the thermal particle population (modeled by the RMHD code) and the nonthermal particles population that causes the synchrotron radiation. In Sections 3.4 to 3.6, we focus our analysis on the total intensity features (in particular, cross-section emission asymmetries, spine brightening, and the relative intensity of the knots) as a function of the magnetic field geometry and internal jet structure. In Section 3.7 we discuss the polarization properties from our numerical models and their relevance for the interpretation of actual observations of AGN jets. A summary of the paper along with the most relevant conclusions is given in Section 3.8.

3.2 Summary of magnetohydrodynamical models

In Paper I we presented a series of numerical models of steady, axisymmetric, relativistic, nonrotating jets with helical magnetic fields. These models are characterized by five functions, namely the density and the pressure, $\rho_j(r)$ and $p_j(r)$, respectively, the axial component of the velocity, $v_j^z(r)$, and the azimuthal and axial components of the magnetic field, $B_j^\phi(r)$ and $B_j^z(r)$. Top-hat functions with fixed values for the jet density and the axial flow speed (Lorentz factor, 3.20) were chosen. Jets were injected into a homogeneous nonmagnetized ambient medium at rest with an overpressure factor, $K = 2$. Finally, two different magnetic field configurations, force-free and non-force-free, were considered. The averaged helical magnetic pitch angle in the force-free models, $\mathcal{F}\phi_{77.5}$, is $77.5°$. Non-force-free models were constructed with two different averaged magnetic pitch angles, $45°$ ($\mathcal{N}\phi_{45}$) and $77.5°$ ($\mathcal{N}\phi_{77.5}$). The parameters defining the models appear in Table 1 of Paper I. Figure 2 of that paper displays the models in the (fast-magnetosonic) relativistic Mach number-specific internal energy plane.

When the remaining parameters are the same, increasing the magnetic pitch angle from $45°$ to $77.5°$ leads to an increase in the magnetic tension. In non-force-free models, an increase in the magnetic pitch angle like this leads to an increase in the radial Lorentz force as well. In force-free models, the radial Lorentz force is zero by construction.

Our results showed that the internal structure of overpressured, superfast magnetosonic jets results from the superposition of (i) the internal transversal equilibrium of the jet (governed by the Lorentz force), and (ii) recollimation shocks and sideways expansions and compressions of the jet flow (whose amplitudes depend on the magnetic tension and the internal energy content). In Figure 3.1 we reproduce the content of Figures 3, 5, 7, and 9 of Paper I, which present the steady internal structure of the jet models considered for the emission computations in this Chapter.

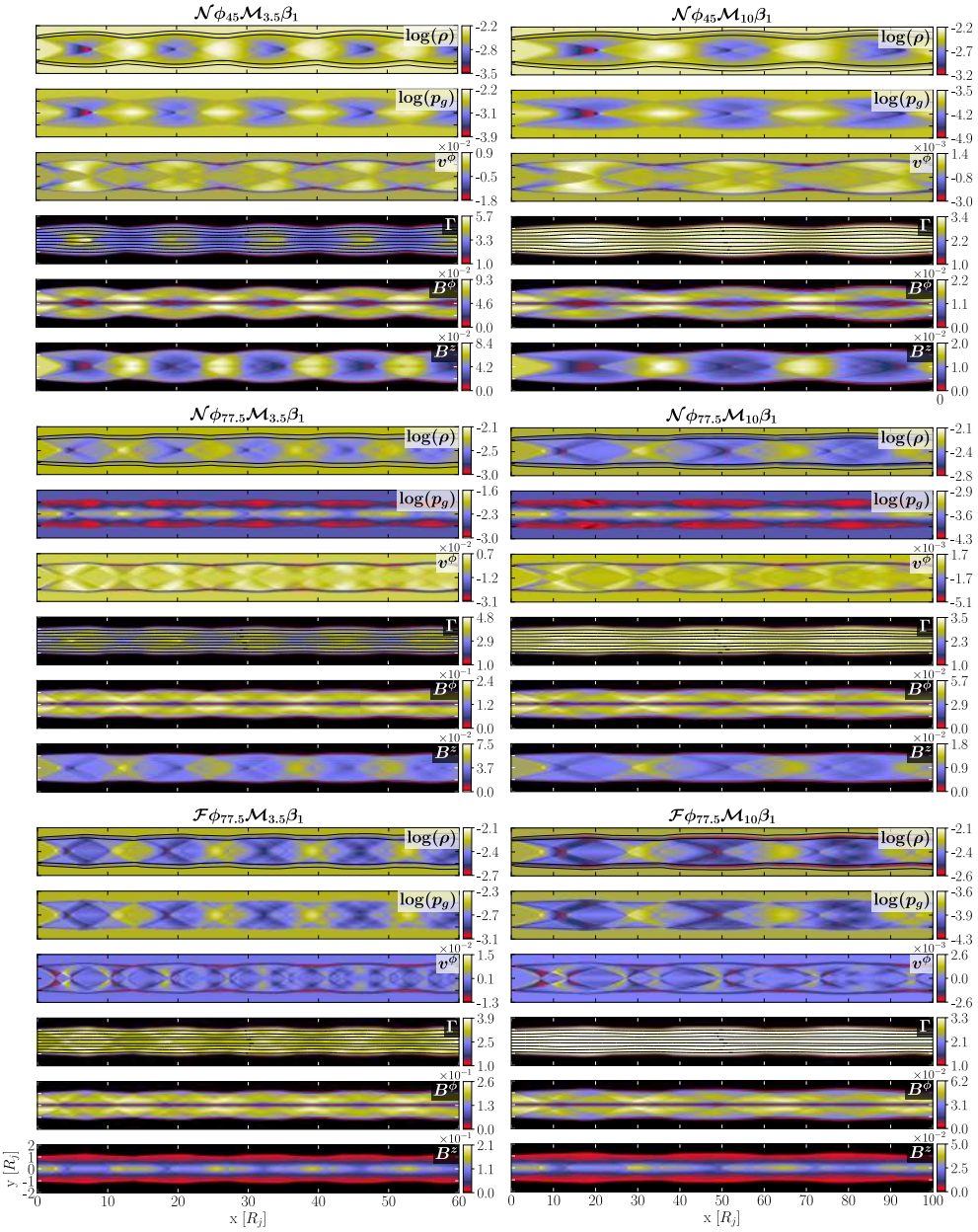

Figure 3.1: Steady structure of the relatively hot models in equipartition $\mathcal{N}\phi_{45}\mathcal{M}_{3.5}\beta_1$, $\mathcal{N}\phi_{77.5}\mathcal{M}_{3.5}\beta_1$, and $\mathcal{F}\phi_{77.5}\mathcal{M}_{3.5}\beta_1$; cold models in equipartition $\mathcal{N}\phi_{45}\mathcal{M}_{10}\beta_1$, $\mathcal{N}\phi_{77.5}\mathcal{M}_{10}\beta_1$, and $\mathcal{F}\phi_{77.5}\mathcal{M}_{10}\beta_1$; magnetically dominated models $\mathcal{N}\phi_{45}\mathcal{M}_{3.5}\beta_{17.5}$, $\mathcal{N}\phi_{77.5}\mathcal{M}_{3.5}\beta_{2.34}$, and $\mathcal{F}\phi_{77.5}\mathcal{M}_{3.5}\beta_{100}$; and kinetically dominated models $\mathcal{N}\phi_{45}\mathcal{M}_{10}\beta_{17.5}$, $\mathcal{N}\phi_{77.5}\mathcal{M}_{10}\beta_{2.34}$, and $\mathcal{F}\phi_{10}\mathcal{M}_{3.5}\beta_{100}$. From top to bottom: distributions of rest-mass density, gas pressure, toroidal flow velocity, flow Lorentz factor, and toroidal and axial magnetic field components. The poloidal flow and magnetic field lines are superposed onto the Lorentz factor and axial magnetic field panels, respectively. Two contour lines for the jet mass fraction values 0.05 and 0.95 are overplotted on the rest-mass density panel.

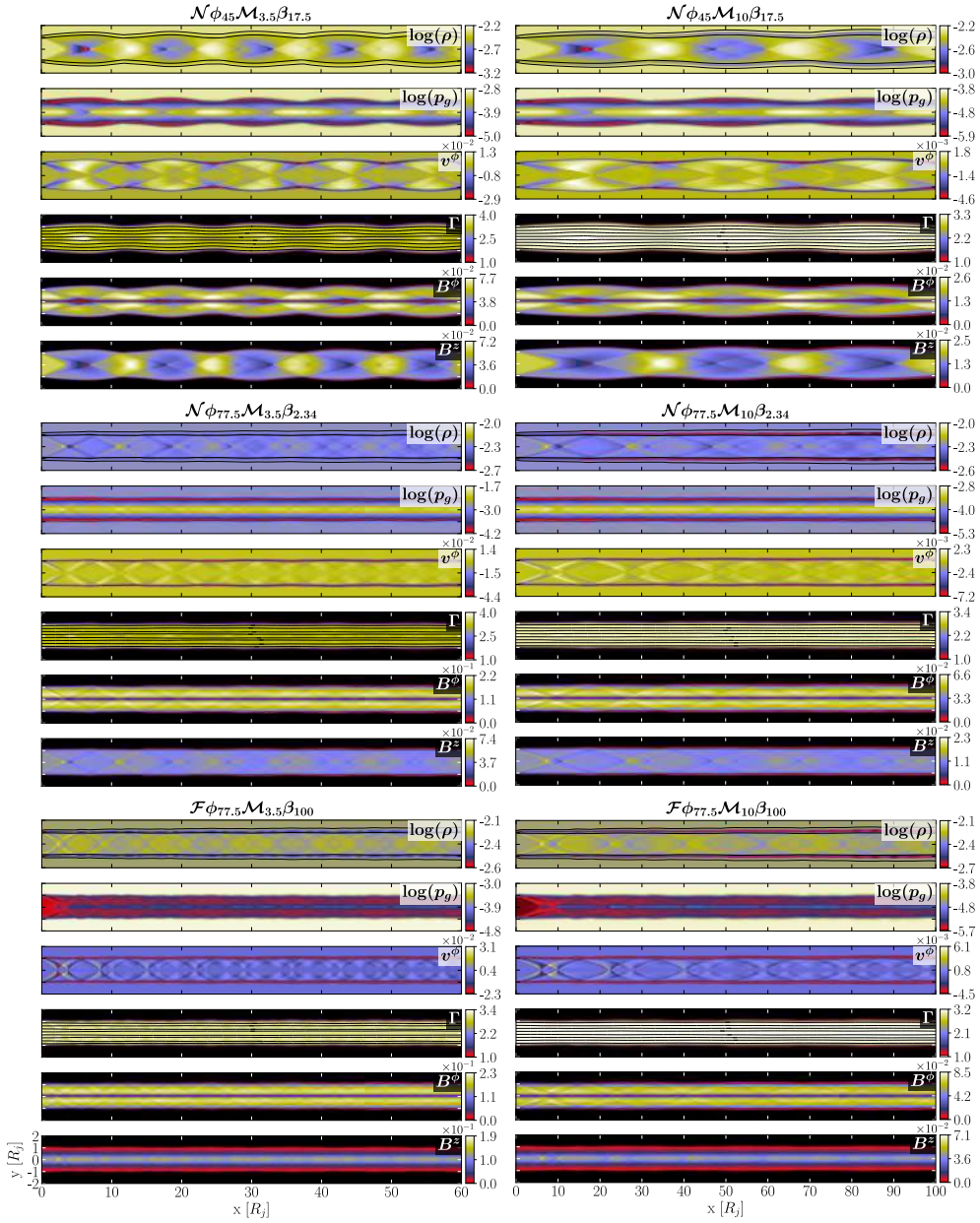

Figure 3.1: (continued)

3.3 Emission code and nonthermal particle injection model

The numerical code used to compute the synchrotron emission radiated by the jet models described in the previous sections is thoroughly discussed in Gómez *et al.* (1993, 1994a,b, 1995, 1997), Fuentes *et al.* (2018), and references therein. We note that one of the key aspects when computing the radio continuum emission from RMHD jets is to establish a connection between the thermal particle population, which is modeled by the RMHD code, and the nonthermal particle population, which is responsible for the synchrotron radiation. As was discussed in Fuentes *et al.* (2018), a complete description of particle acceleration mechanisms connecting both populations within the jet, either through magnetic reconnection (Lyubarsky, 2005) or acceleration at shock fronts (Kirk *et al.,* 2000), would invoke vastly different scales and hence a computational cost that is not affordable for global RMHD jet simulations. It is therefore usually assumed that the internal energy of the nonthermal particle population is either proportional to that of the thermal population, that is, to the simulated gas pressure (Zakamska *et al.,* 2008; Porth *et al.,* 2011), or to the magnetic energy density (Broderick & McKinney, 2010; Porth *et al.,* 2011). This last approach is of special interest because of the extensive analysis of the magnetic field configuration that is carried out in this work. We call these two emission approximations hereinafter model–p (M_p) and model–B (M_B), respectively.

When we assume a typical power-law function $N(E)dE = N_0 E^{-\gamma} dE$, where $E_{\rm min} \leq E \leq E_{\rm max}$, the distribution of the nonthermal particles energy is then determined by the expressions (e.g., Gómez *et al.,* 1995)

$$N_0 = \left[\frac{\Lambda(\gamma-2)}{1-C_E^{2-\gamma}}\right]^{\gamma-1} \left[\frac{1-C_E^{1-\gamma}}{\rho(\gamma-1)}\right]^{\gamma-2}, \tag{3.1}$$

$$E_{\rm min} = \frac{\Lambda}{\rho}\frac{\gamma-2}{\gamma-1}\frac{1-C_E^{1-\gamma}}{1-C_E^{2-\gamma}}. \tag{3.2}$$

In the previous expressions, Λ is a constant fraction of the internal energy density of the thermal particles or of the magnetic energy density ($B'^2/8\pi$, where B' is the magnetic field computed in the fluid frame), depending on the desired particle acceleration model (M_p or M_B, respectively). ρ is a constant fraction of the rest-mass density computed by the RMHD code in the fluid frame, and the ratio $C_E = E_{\rm max}/E_{\rm min}$ is kept constant throughout the jet because radiative losses are marginal. In our models we neglect any Faraday rotation effects on the plane of polarization to better isolate the polarization properties of our models as a function of the internal jet structure and magnetic field configuration. Similarly, we neglect any opacity effects by setting the model parameters so that the jets are optically thin. Total and linearly polarized intensity values are given in arbitrary units.

The analysis of the observational imprints associated with the magnetic field configuration is based on a selection of the models considered in the previous sections:

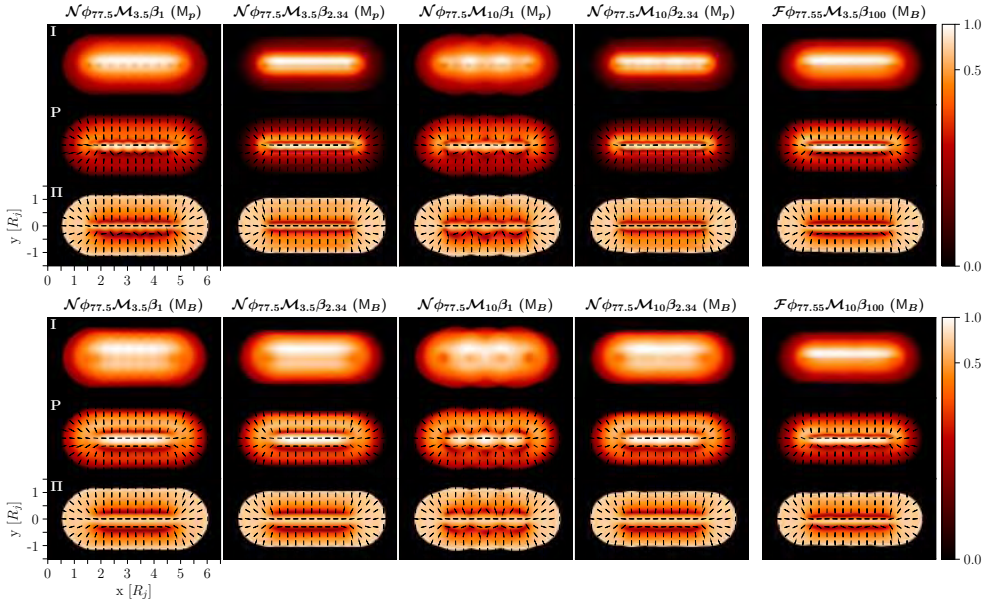

Figure 3.2: Total intensity (I), linearly polarized intensity (P), with EVPAs overplotted as black bars, and degree of linear polarization (Π) of the $\mathcal{N}\phi_{77.5}$ and $\mathcal{F}\phi_{77.5}$ jet models, computed for the two particle injection approximations (M$_p$ and M$_B$) and a viewing angle of 2°. Total and polarized intensity values are normalized to unity. Axis units represent the distance in jet radius units.

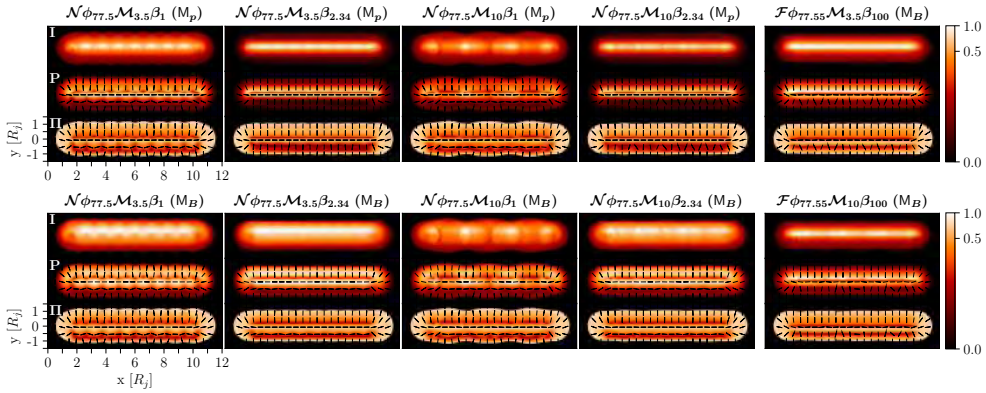

Figure 3.3: Same as Figure 3.2, but for a viewing angle of 5°.

i) $\mathcal{N}\phi_{45}$ models: $\mathcal{M}_{3.5}\beta_1$, $\mathcal{M}_{3.5}\beta_{17.5}$, $\mathcal{M}_{10}\beta_1$, and $\mathcal{M}_{10}\beta_{17.5}$, corresponding to models M2B2, M2B4, M5B2, and M5B4, respectively, of Fuentes *et al.* (2018), are taken as reference; ii) $\mathcal{N}\phi_{77.5}$ models: $\mathcal{M}_{3.5}\beta_1$, $\mathcal{M}_{3.5}\beta_{2.34}$, $\mathcal{M}_{10}\beta_1$, and $\mathcal{M}_{10}\beta_{2.34}$; iii) $\mathcal{F}\phi_{77.5}$ models: $\mathcal{M}_{3.5}\beta_{100}$ and $\mathcal{M}_{10}\beta_{100}$. Non-force-free models are considered under both M$_p$ and M$_B$ particle injection approaches. Consistently with their force-free character, only the strongly magnetically dominated $\mathcal{F}\phi_{77.5}$ models $\mathcal{M}_{3.5}\beta_{100}$ and $\mathcal{M}_{10}\beta_{100}$ were

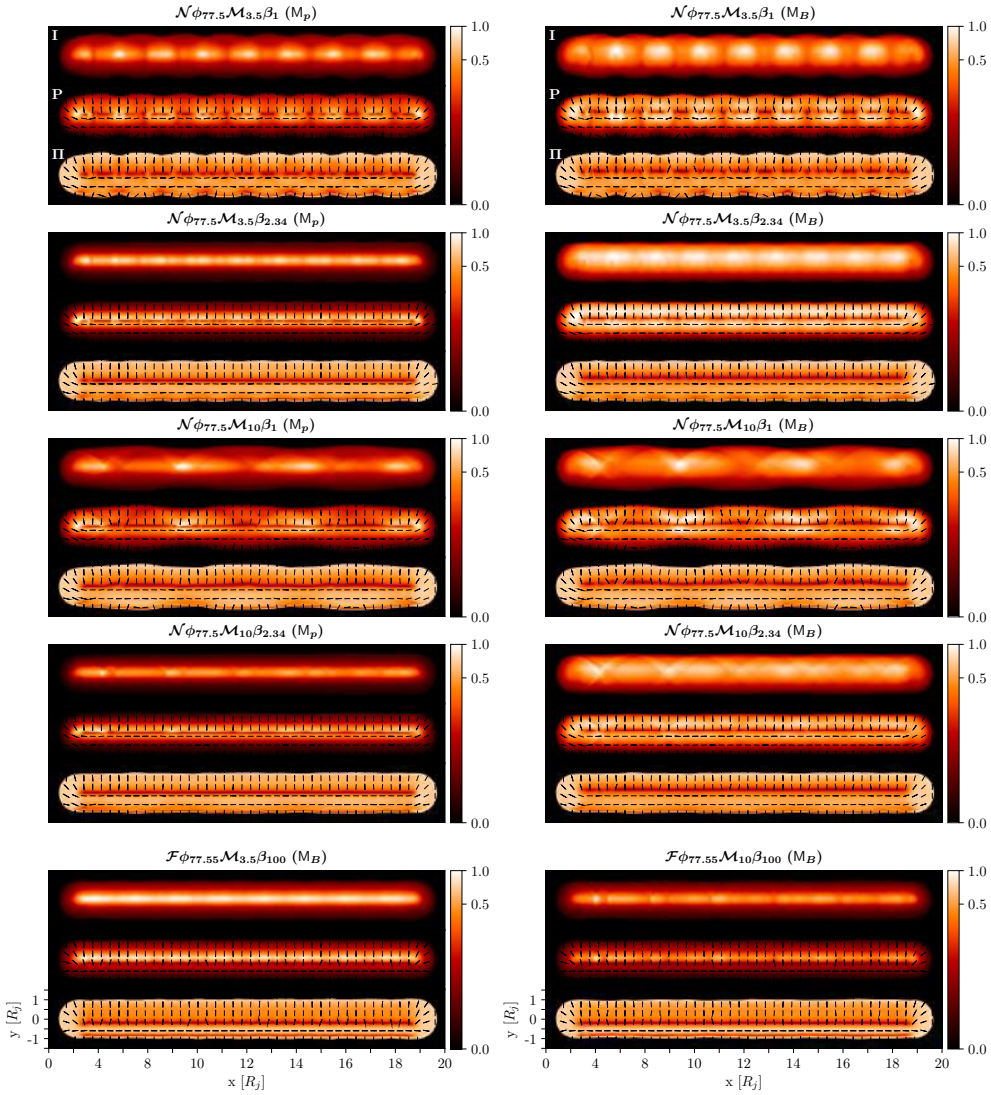

Figure 3.4: Same as Figure 3.2, but for a viewing angle of 10°.

considered, and only under the M_B particle acceleration model.

The radio-continuum total and linearly polarized flux density images for models $\mathcal{N}\phi_{45}$ are shown in Figures 11–18 of Fuentes *et al.* (2018). We note that only the M_p particle acceleration model was used for the emission computation of these models because the M_p and M_B models yield very similar results, with the exception of a much brighter central spine in the highly magnetized models $\mathcal{N}\phi_{45}\mathcal{M}_{3.5}\beta_{17.5}$ and $\mathcal{N}\phi_{45}\mathcal{M}_{10}\beta_{17.5}$ under the M_B particle acceleration model (see Sect. 3.3 of Fuentes *et al.,* 2018). In Figures 3.2 to 3.5 we show the total intensity, linearly polarized intensity, and degree of linear polarization of the $\mathcal{N}\phi_{77.5}$ and $\mathcal{F}\phi_{77.5}$ jet models for viewing angles $\theta = 2^\circ$, 5°, 10°, and 20°.

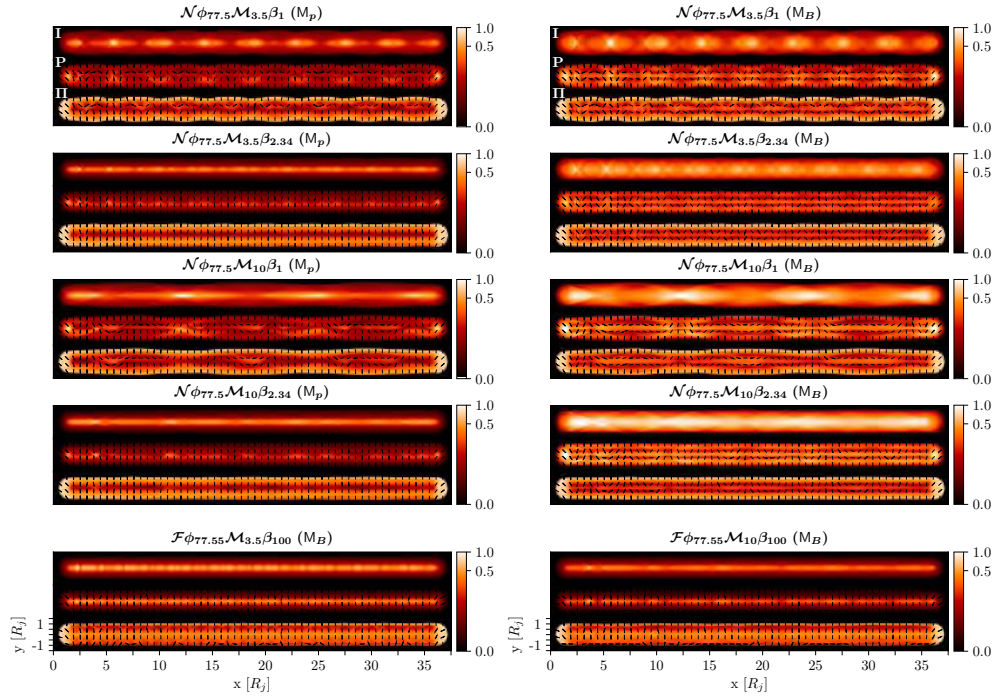

Figure 3.5: Same as Figure 3.2, but for a viewing angle of 20°.

3.4 Cross-section emission asymmetry

The helical geometry of the magnetic field leaves a clear imprint on the emission models. Following the discussion in Sect. 3.2 of Fuentes *et al.* (2018), the angle between the magnetic field and the line of sight in the fluid frame ϑ' introduces an asymmetry in the emission via the $\sin\vartheta'$ term in the emission coefficients (Aloy *et al.*, 2000; Lyutikov *et al.*, 2005; Clausen-Brown *et al.*, 2011). This is clearly visible across the jet when the viewing angle in the fluid frame deviates from 90°, which corresponds to $\approx 18°$ in the observer's frame for a flow velocity of $v_j \sim 0.95c$. This asymmetry is clearly visible in Figures 3.2 to 3.4, showing a brighter emission in the top halves of the jets, whereas the asymmetry is not present in Figure 3.5, as expected for a viewing angle close to 18°.

Figure 3.6 shows for the M_p (Figure 3.6a) and M_B (Figure 3.6b) injection models the transverse profiles of the total and polarized intensity and the degree of polarization integrated along the jet for each jet model at viewing angles of 2° and 20°, which maximizes and minimizes the cross-section asymmetry, respectively. The emission asymmetry discussed and analyzed in Fuentes *et al.* (2018) for $\mathcal{N}\phi_{45}$ jet models under M_p is now also seen in models $\mathcal{N}\phi_{77.5}$ and $\mathcal{F}\phi_{77.5}$ for the injection approximations M_p and M_B (see also Figure 3.2), as expected from the purely geometrical origin of the effect. For a viewing angle of 2° , the bulk of the jet emission is concentrated in the top half of the jet, and the peak intensity is displaced from the jet axis. In addition, the

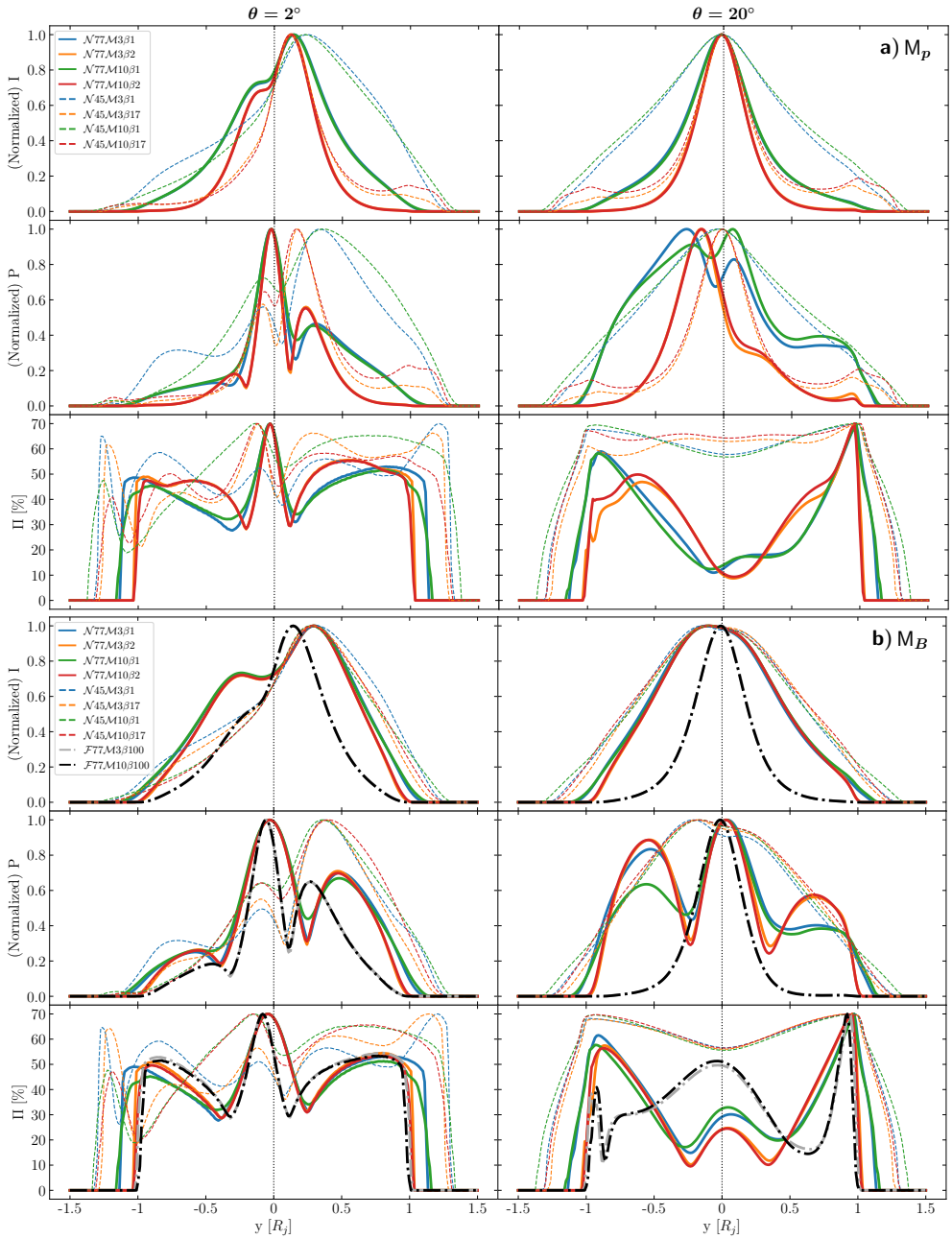

Figure 3.6: a) Total intensity (I), linearly polarized intensity (P), and degree of linear polarization (II) integrated transverse profiles of the $\mathcal{N}\phi_{45}$ and $\mathcal{N}\phi_{77.5}$ jet models, computed for viewing angles $\theta = 2°$ (left) and $20°$ (right), and for the particle injection model M_p. Models with equal color but different line style differ only in the magnetic pitch angle value. Total and linearly polarized intensity values are normalized to unity. The negative and positive values of the abscissa axes represent the bottom and top halves of the jets (assuming they propagate horizontally from left to right), expressed in jet radius units, respectively. **b)** Same panel distribution as above, but computed following the particle injection model M_B, which includes the $\mathcal{F}\phi_{77.5}$ jet models.

transversal emission profiles of models $\mathcal{N}\phi_{77.5}$ display a striking bump in the bottom half of the jet for M_p, which turns into a plateau for M_B. At 20° , the asymmetry in the total intensity profiles has almost disappeared (see Figure 3.5). The $\mathcal{F}\phi_{77.5}$ models under consideration display the most symmetric emission (M_B) at any viewing angle.

We now focus on the profiles of the polarized intensity. The most remarkable feature is that they are much more complex than those of the total intensity, displaying multiple (two or three) peaks, bumps, and plateaus in most cases. At 2°, the largest peak in $\mathcal{N}\phi_{45}$ models is in the top half of the jet, whereas the smallest peak is in the bottom half. The situation is reversed for the $\mathcal{N}\phi_{77.5}$ and $\mathcal{F}\phi_{77.5}$ models (although the top half of the jet dominates the bulk of the polarized emission). At 20°, the polarized emission of models $\mathcal{N}\phi_{45}$ is almost symmetric, whereas the emission of $\mathcal{N}\phi_{77.5}$ models show asymmetric peaks (as in the case of models $\mathcal{N}\phi_{77.5}\mathcal{M}_{3.5}\beta_1$ and $\mathcal{N}\phi_{77.5}\mathcal{M}_{10}\beta_1$ for the M_p and M_B injection models; or models $\mathcal{N}\phi_{77.5}\mathcal{M}_{3.5}\beta_{2.34}$ and $\mathcal{N}\phi_{77.5}\mathcal{M}_{10}\beta_{2.34}$ for M_B) or asymmetric bumps ($\mathcal{N}\phi_{77.5}\mathcal{M}_{3.5}\beta_{2.34}$ and $\mathcal{N}\phi_{77.5}\mathcal{M}_{10}\beta_{2.34}$ for M_p). In Section 3.7 we discuss the physical origin of these features.

3.5 Spine brightening

As discussed previously, magnetic tension and the radial component of the Lorentz force are the key parameters governing the transversal structure of jets. The magnetic tension (together with the overpressure factor) controls the sideways expansion of the jet models and hence the amplitude of their radial oscillations. The radial component of the Lorentz force regulates the gas pressure profile across the jet and hence the distribution of internal energy. Finally, magnetic tension and the radial Lorentz force shape the distribution of magnetic energy density across the jet. It can therefore be predicted that these two quantities, magnetic tension and Lorentz force, leave their imprints on the synchrotron emission maps obtained with the M_p and M_B particle injection models.

The distribution of the synchrotron emission across the jet for models $\mathcal{N}\phi_{45}$ was analyzed in Fuentes *et al.* (2018) for M_p. Jets with high magnetizations are narrower and concentrate a larger part of their internal energy in a central spine than their counterparts with the same magnetosonic Mach number and lower magnetizations. This is due to their higher relative magnetic tension and radial Lorentz force. The uneven distribution of the internal energy in the models with the highest magnetizations translates into a spine brightening in the total and polarized intensity (M_p), which is clearly seen in the bottom panels of Figs. 19 and 20 of Fuentes *et al.* (2018), and also in Figure 3.6a (models $\mathcal{N}\phi_{45}\mathcal{M}_{3.5}\beta_{17.5}$ and $\mathcal{N}\phi_{45}\mathcal{M}_{10}\beta_{17.5}$ versus $\mathcal{N}\phi_{45}\mathcal{M}_{3.5}\beta_1$ and $\mathcal{N}\phi_{45}\mathcal{M}_{10}\beta_1$). The spine brightening in total emission under the M_p approach for models $\mathcal{N}\phi_{45}\mathcal{M}_{3.5}\beta_{17.5}$ and $\mathcal{N}\phi_{45}\mathcal{M}_{10}\beta_{17.5}$ is also seen in Table 3.1. This table displays the distance in jet radius units from the relative total intensity peak of each model (at a viewing angle of 20°) at which the accumulated emission reaches 50% and 70% of the total emission with the M_p and M_B models. The enhancement of the total emission close to the jet axis under the M_p approach for models $\mathcal{N}\phi_{77.5}\mathcal{M}_{3.5}\beta_{2.34}$ and $\mathcal{N}\phi_{77.5}\mathcal{M}_{10}\beta_{2.34}$ with respect to their less magnetized counterparts ($\mathcal{N}\phi_{77.5}\mathcal{M}_{3.5}\beta_1$

Table 3.1: Emission confinement around the jet axis.

Model	50% I		70% I	
	M_p	M_B	M_p	M_B
$\mathcal{N}\phi_{45}\mathcal{M}_{3.5}\beta_1$	0.35	0.35	0.54	0.54
$\mathcal{N}\phi_{45}\mathcal{M}_{3.5}\beta_{17.5}$	0.17	0.35	0.31	0.53
$\mathcal{N}\phi_{45}\mathcal{M}_{10}\beta_1$	0.38	0.36	0.57	0.56
$\mathcal{N}\phi_{45}\mathcal{M}_{10}\beta_{17.5}$	0.21	0.36	0.40	0.55
$\mathcal{N}\phi_{77.5}\mathcal{M}_{3.5}\beta_1$	0.20	0.29	0.34	0.44
$\mathcal{N}\phi_{77.5}\mathcal{M}_{3.5}\beta_{2.34}$	0.12	0.28	0.20	0.42
$\mathcal{N}\phi_{77.5}\mathcal{M}_{10}\beta_1$	0.20	0.29	0.34	0.45
$\mathcal{N}\phi_{77.5}\mathcal{M}_{10}\beta_{2.34}$	0.12	0.28	0.20	0.42
$\mathcal{F}\phi_{77.5}\mathcal{M}_{3.5}\beta_{100}$	$\cdots$	0.14	$\cdots$	0.23
$\mathcal{F}\phi_{77.5}\mathcal{M}_{10}\beta_{100}$	$\cdots$	0.14	$\cdots$	0.23

Note. The tabulated data denote the jet model and the distance from the axis in jet radius units R_j at which the integrated intensity represents the 50% and 70% of the jet total integrated intensity for the viewing angle $\theta = 20^\circ$ and the two particle injection models (M_p and M_B). In a homogeneous jet model, 50% (70%) of the integrated emission is concentrated within $0.40\,R_j$ ($0.59\,R_j$) from the jet axis.

and $\mathcal{N}\phi_{77.5}\mathcal{M}_{10}\beta_1$, respectively) is also seen in Table 3.1 (and Figures 3.2 to 3.5 and Figure 3.6a).

The same result is obtained when comparing $\mathcal{N}\phi_{45}$ and $\mathcal{N}\phi_{77.5}$ models at the same point of the diagram of the magnetosonic Mach number and internal energy. Again, the higher magnetic tension and radial Lorentz force of $\mathcal{N}\phi_{77.5}$ models with respect to the their $\mathcal{N}\phi_{45}$ counterparts produce narrower jets and spine brightening under M_p (see Figures 3.2 to 3.5, and compare models $\mathcal{N}\phi_{77.5}\mathcal{M}_{3.5}\beta_1$ and $\mathcal{N}\phi_{77.5}\mathcal{M}_{10}\beta_1$ with their counterparts, models $\mathcal{N}\phi_{45}\mathcal{M}_{3.5}\beta_1$ and $\mathcal{N}\phi_{45}\mathcal{M}_{10}\beta_1$ in Figure 3.6a and Table 3.1).

For the M_B particle injection model (Figures 3.2 to 3.5 and Figure 3.6b, and Table 3.1), the homogeneous distribution of the axial magnetic field component in the $\mathcal{N}\phi_{45}$ and $\mathcal{N}\phi_{77.5}$ models contributes to smooth out the spine brightening (especially in $\mathcal{N}\phi_{45}$ models, where the axial magnetic field is relatively more important). Conversely, force-free models display a distinct spine brightening that originates from the radial

Table 3.2: Relative intensity of the stationary components.

Model	$\theta = 5°$		$\theta = 10°$		$\theta = 20°$	
	M_p	M_B	M_p	M_B	M_p	M_B
$\mathcal{N}\phi_{45}\mathcal{M}_{3.5}\beta_1$	2.8 ± 3.0	7.8 ± 3.6	68.4 ± 3.6	66.9 ± 5.7	75.7 ± 6.0	74.4 ± 8.2
$\mathcal{N}\phi_{45}\mathcal{M}_{3.5}\beta_{17.5}$	43.9 ± 3.6	9.7 ± 4.2	75.1 ± 2.7	64.4 ± 5.7	76.3 ± 3.6	69.6 ± 8.0
$\mathcal{N}\phi_{45}\mathcal{M}_{10}\beta_1$	61.5 ± 1.9	68.9 ± 2.0	73.4 ± 1.2	79.4 ± 1.9	75.3 ± 0.6	82.5 ± 1.0
$\mathcal{N}\phi_{45}\mathcal{M}_{10}\beta_{17.5}$	71.7 ± 5.1	61.6 ± 3.5	75.4 ± 4.4	74.2 ± 2.9	69.7 ± 6.0	75.9 ± 1.7
$\mathcal{N}\phi_{77.5}\mathcal{M}_{3.5}\beta_1$	17.2 ± 1.8	3.4 ± 3.8	51.0 ± 4.6	45.9 ± 4.4	53.7 ± 9.4	47.4 ± 9.2
$\mathcal{N}\phi_{77.5}\mathcal{M}_{3.5}\beta_{2.34}$	11.2 ± 1.3	1.8 ± 3.4	26.4 ± 4.4	17.7 ± 4.0	33.1 ± 7.3	23.6 ± 5.4
$\mathcal{N}\phi_{77.5}\mathcal{M}_{10}\beta_1$	47.7 ± 5.7	43.1 ± 5.7	52.7 ± 5.1	43.1 ± 3.4	53.0 ± 4.7	44.1 ± 4.1
$\mathcal{N}\phi_{77.5}\mathcal{M}_{10}\beta_{2.34}$	14.9 ± 6.3	13.3 ± 5.1	18.0 ± 7.1	14.3 ± 2.2	21.5 ± 7.6	18.1 ± 3.9
$\mathcal{F}\phi_{77.5}\mathcal{M}_{3.5}\beta_{100}$	$\cdots$	5.1 ± 2.6	$\cdots$	14.8 ± 2.8	$\cdots$	24.2 ± 4.0
$\mathcal{F}\phi_{77.5}\mathcal{M}_{10}\beta_{100}$	$\cdots$	21.1 ± 2.9	$\cdots$	22.3 ± 4.7	$\cdots$	21.6 ± 4.6

Note. The tabulated data denote the jet model and the average relative intensity, in percentage, of the stationary components with respect to the underlying jet emission for the viewing angles $\theta = 5°$, $10°$, and $20°$ and the two particle injection models (M_p and M_B).

gradient of the axial magnetic field.

3.6 Knot intensity

Associated with recollimation shocks within the jets, a series of bright stationary knots arises over the base emission of the models. These knots may correspond to the stationary components seen in actual VLBI observations of AGN jets, as reported in several works (e.g., Jorstad *et al.,* 2017) and were analyzed in Fuentes *et al.* (2018) by attending to the dominant type of energy in the jet models. As concluded in that paper for models $\mathcal{N}\phi_{45}$, at large viewing angles, hot jets present stronger emission knots than colder jets (consistent with the higher relative intensity of recollimation shocks and wider radial oscillations in the hot models), while at smaller viewing angles, a differential Doppler factor in the pre- and post-shock zones inverts the trend. In this work we analyze the strength of stationary knots in terms of the magnetic field configuration.

Table 3.2 and Figure 3.7 show the averaged knot intensity for each model and under both particle acceleration approximations, computed as the total intensity percentage of consecutive peaks above the underlying emission of the jet and at viewing angles $\theta = 5°$, $10°$, and $20°$. The viewing angle $\theta = 2°$ was excluded from the analysis because the emitting structures within the jets overlapped too strongly to distinguish

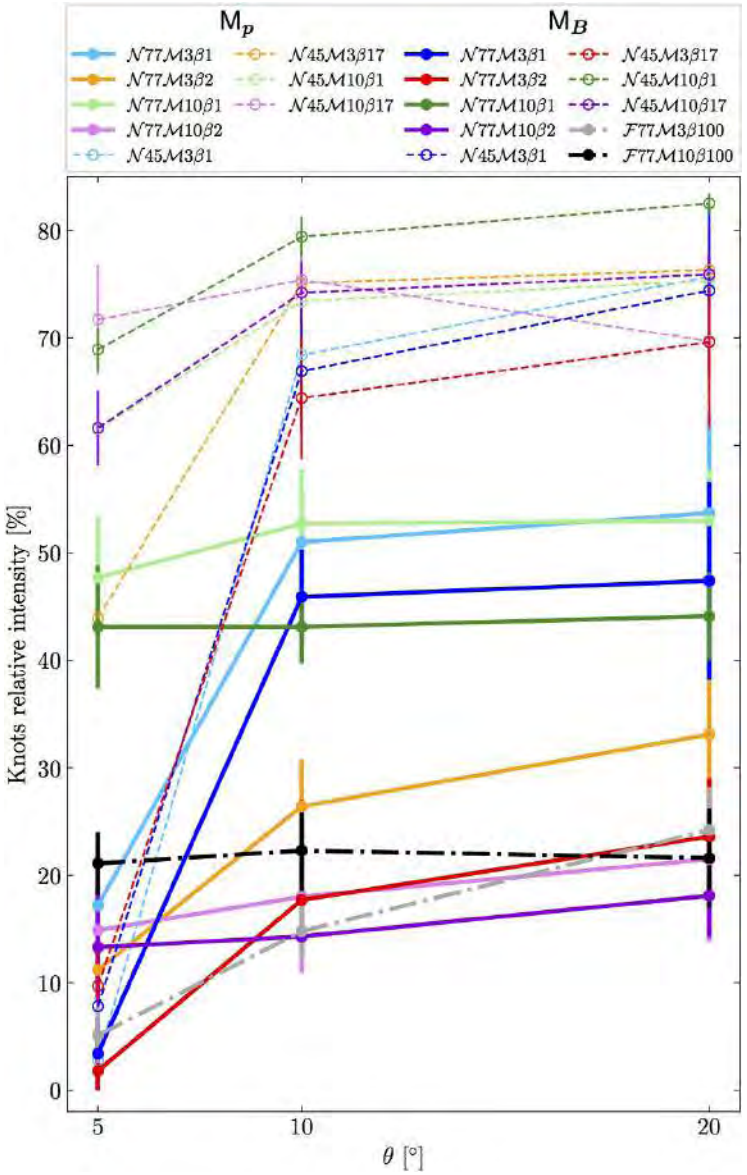

Figure 3.7: Knots relative intensity, measured as the integrated total intensity percentage corresponding to knots when the underlying jet emission is removed. Calculations are made for viewing angles $\theta = 5°$, $10°$, and $20°$ and the two particle injection methods, M_p and M_B, shown as solid and dashed lines, respectively. $\mathcal{F}\phi_{77.5}$ models are drawn as dot-dashed lines.

them correctly.

We focus on the results at $\theta = 20°$ and refer to Fuentes *et al.* (2018) for a deeper analysis on the dependence of the knot intensity on the viewing angle. One of the main trends observed is the large difference in intensity between $\mathcal{N}\phi_{45}$ models, which ranges from 70% to 83% of the total emission, and the rest, whose knot intensity peaks

at 54% for $\mathcal{N}\phi_{77.5}$ models and at 24% for $\mathcal{F}\phi_{77.5}$ models. The explanation of the drop in the relative intensity of stationary knots from $\phi_B = 45°$ to $\phi_B = 77.5°$ models is again the difference in the relative intensity of recollimation shocks and the amplitude of radial oscillations, which is much smaller in the latter (see Tables 4 and 5 of Paper I). According to the discussion in Sect. 5 of Paper I, it follows from Eq. 20 that the smaller magnetic pitch angle ϕ_B, and hence magnetic tension τ_m, of the $\mathcal{N}\phi_{45}$ models implies greater radial oscillations, which in turn increase the strength of recollimation shocks and ultimately that of stationary emission knots.

Among the models with $\phi_B = 77.5°$, with a relative knot intensity (44%-54%) intermediate between the $\mathcal{N}\phi_{45}$ (70%-83%) and the rest ($< 34\%$), we find the $\mathcal{N}\phi_{77.5}\mathcal{M}_{3.5}\beta_1$ and $\mathcal{N}\phi_{77.5}\mathcal{M}_{10}\beta_1$ models under both M_p and M_B particle injection approaches. These jets have the same magnetic pitch angle as those with lower relative knot intensities, but differ in their lower magnetization ($\beta = 1$), which implies a higher relative intensity of recollimation shocks and a wider amplitude of the radial oscillations (see again Tables 4 and 5 and the discussion related to Eq. 20 in Sect. 5 of Paper I).

Regarding the particle injection approximation, emitting models computed following M_p usually have more intense knots than their M_B counterparts, except for models $\mathcal{N}\phi_{45}\mathcal{M}_{10}\beta_{17.5}$ and $\mathcal{N}\phi_{45}\mathcal{M}_{10}\beta_1$, especially the last one, which systematically presents about 7% more intense knots at all viewing angles than its M_p counterpart. Again, the differences between the two emission approaches are related to the relative strength of the jumps at shocks and the variations at radial oscillations, specifically, those of the gas pressure in the M_p approach and those of the magnetic energy (magnetic pressure) in the M_B approach. Models $\mathcal{N}\phi_{45}\mathcal{M}_{10}\beta_{17.5}$ and $\mathcal{N}\phi_{45}\mathcal{M}_{10}\beta_1$ have the largest difference between changes in the thermal and magnetic pressures along the jet (see Tables 4 and 5 in Paper I).

3.7 Polarized emission

As discussed in Sections 2 and 3 of Paper I, the jet models computed in this work preserve the axial symmetry and helical geometry of the magnetic field of those computed in Fuentes *et al.* (2018). We therefore obtained the characteristic bimodal configuration of the polarization angle throughout the jets, whether perpendicular to or aligned with the jet propagation direction (Lyutikov *et al.*, 2005). We recall that this distribution indicates which component of the magnetic field, projected over the plane of the sky, dominates the other. We find the electric vector position angles (EVPAs) perpendicular ($\sim 0°$) or parallel ($\sim 90°$) to the jet axis if the projected poloidal or toroidal component dominates, respectively. The new magnetic field configurations explored in this work reveal a remarkable difference in the polarized emission of jets with different magnetic pitch angles. This is particularly clear in Figure 3.8, which shows the median polarization angle (and its variability) across the $\mathcal{N}\phi_{45}$, $\mathcal{N}\phi_{77.5}$, and $\mathcal{F}\phi_{77.5}$ jet models for different viewing angles and the two particle injection approaches. Median polarization angles for model M_p are only shown for $\theta = 20°$ because there are no qualitative differences with model M_B for lower values of the

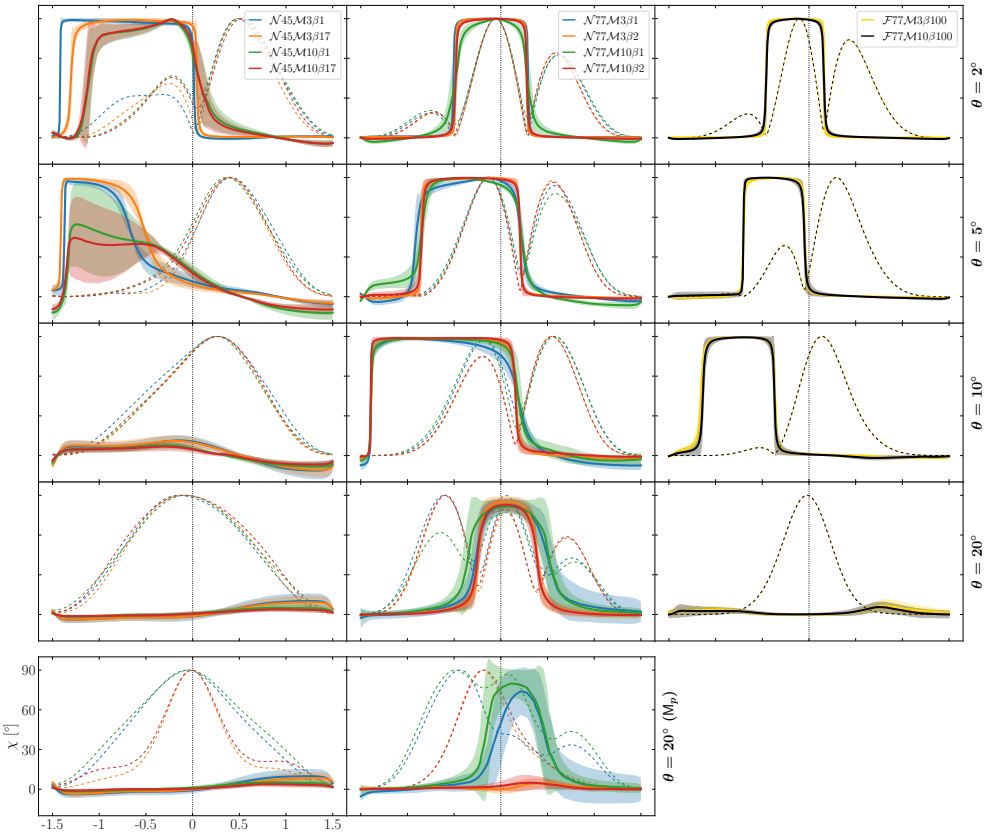

Figure 3.8: Median polarization angle across all jet models and viewing angles $\theta = 2°, 5°, 10°$, and $20°$, for the particle injection model M_B (median polarization angles for model M_p are only shown for $\theta = 20°$ because there are no qualitative differences with model M_B for lower values of the viewing angle; see the linearly polarized intensity maps in Figures 3.2 to 3.4). Shaded regions represent the median absolute deviation of each model. Thin dashed lines represent the integrated polarized intensity (normalized). Models were smoothed for the computations through a convolution with a beam of size 0.5 R_j FWHM. Abscissa axis units as in Figure 3.6.

viewing angle (see the linearly polarized intensity maps in Figures 3.2 to 3.4).

The magnetic pitch angle ϕ_B, the viewing angle θ, and their transformations from the fluid into the observer frame through the Lorentz factor Γ are the main drivers determining the imprints of the polarized emission that is radiated by the jet models. The following results therefore apply for an average Lorentz factor of 3.2 (value at injection). Fuentes *et al.* (2018) showed that for viewing angles up to $\theta = 5°$, the $\mathcal{N}\phi_{45}$ models ($\phi_B = 45°$) still display some signatures of the toroidal magnetic field component. This result is seen in the plots of the polarization angle for $\mathcal{N}\phi_{45}$ models at $\theta = 2°, 5°$ displayed in Figure 3.8, together with an increasing variability of the EVPAs with θ (especially in models $\mathcal{M}_{10}\beta_1$ and $\mathcal{M}_{10}\beta_{17.5}$). For larger viewing angles, the projected poloidal component of the magnetic field dominates and the EVPA profiles remain perpendicular to the jet axis. On the other hand, with a magnetic pitch angle of

$\phi_B = 77.5°$ and hence a larger contribution of the toroidal magnetic field component, the $\mathcal{N}\phi_{77.5}$ and $\mathcal{F}\phi_{77.5}$ jet models exhibit a persistent EVPA bimodal structure not only for the viewing angle $\theta = 2°$, but also for $\theta = 5°$ and $10°$ (some of them even at $20°$). At small viewing angles, a central region of EVPAs aligned with the jet propagation direction defines a bright spine of polarized emission, which is progressively widened and displaced to the bottom of the jets as θ increases, especially for $\mathcal{N}\phi_{77.5}$, and to a lower extent, for $\mathcal{F}\phi_{77.5}$ models. This toroidal spine is recovered and centered around the jet axis again at $\theta = 20°$ (with large variabilities in the polarization angles) for all $\mathcal{N}\phi_{77.5}$ models under the M_B approximation, and for $\mathcal{M}_{3.5}\beta_1$ and $\mathcal{M}_{10}\beta_1$ models alone (jet models in equipartition) under the M_p approximation. However, despite the median polarization angle results, a closer look at the maps in Figure 3.5 for these models and viewing angle reveals an irregular toroidal spine that is mainly defined between stationary knots. At the location of the stationary components, the EVPAs turn perpendicular, thus describing a rotation along the jet axis. This is more evident as the number of stationary knots decreases and therefore, model $\mathcal{N}\phi_{77.5}\mathcal{M}_{10}\beta_1$ under both injection approximations is the best example of this longitudinal polarization angle rotation (see Figure 3.5). In contrast to their non-force-free counterparts, $\mathcal{F}\phi_{77.5}$ models show no trace of the projected toroidal component at this viewing angle.

Regarding the degree of linear polarization, Π, the differences between $\mathcal{N}\phi_{45}$, $\mathcal{N}\phi_{77.5}$, and $\mathcal{F}\phi_{77.5}$ models are also significant, especially for a viewing angle of $\theta = 20°$. The bottom panels of Figure 3.6a,b show that the distribution of Π across the jet for a viewing angle of 2° is similar for the three families of models. It is more chaotic in the $\mathcal{N}\phi_{45}$ case and is qualitatively axisymmetric in the $\mathcal{N}\phi_{77.5}$ and $\mathcal{F}\phi_{77.5}$ cases. Nonetheless, at a viewing angle of 20°, these three sets of models differ considerably from each other. The $\mathcal{N}\phi_{45}$ models present an overall large degree of linear polarization and a flat profile with a mild depression around the jet axis for the two particle acceleration approximations. In contrast, the degree of linear polarization in the $\mathcal{N}\phi_{77.5}$ models experiences a large drop toward the center for the M_p and M_B approximations, plus a moderate bump at the axis in the last case. The degree of linear polarization of the $\mathcal{F}\phi_{77.5}$ models displays a similar drop to that of the $\mathcal{N}\phi_{77.5}$ models, but a larger bump. In addition, all models regardless of the magnetic pitch angle and particle injection approximation coincide in their higher values of Π at the jet edges, as expected for jets threaded by a helical magnetic field and reported by Gómez *et al.* (2008) for the jet of the radio galaxy 3C 120.

In order to compare these polarization signatures with actual VLBI observations, we convolved our models with two different beams, one with a size of half the jet models radius, which can resolve the jets transversally and simulates high angular resolution observations, and another with the size of the jet diameter, which cannot resolve the fine structure of the models and is typical of centimeter–wavelength observations. The jet length was restricted to that where integration columns of the emission code are complete, that is, where they pass through the entire jet width, to avoid incomplete emitting regions at the jet ends, which can induce interpretation errors. Figure 3.9 shows the linearly polarized intensity (P) and degree of polarization (Π) of the jet models $\mathcal{N}\phi_{45}\mathcal{M}_{10}\beta_1$ and $\mathcal{N}\phi_{77.5}\mathcal{M}_{10}\beta_1$ convolved with the two beams described above

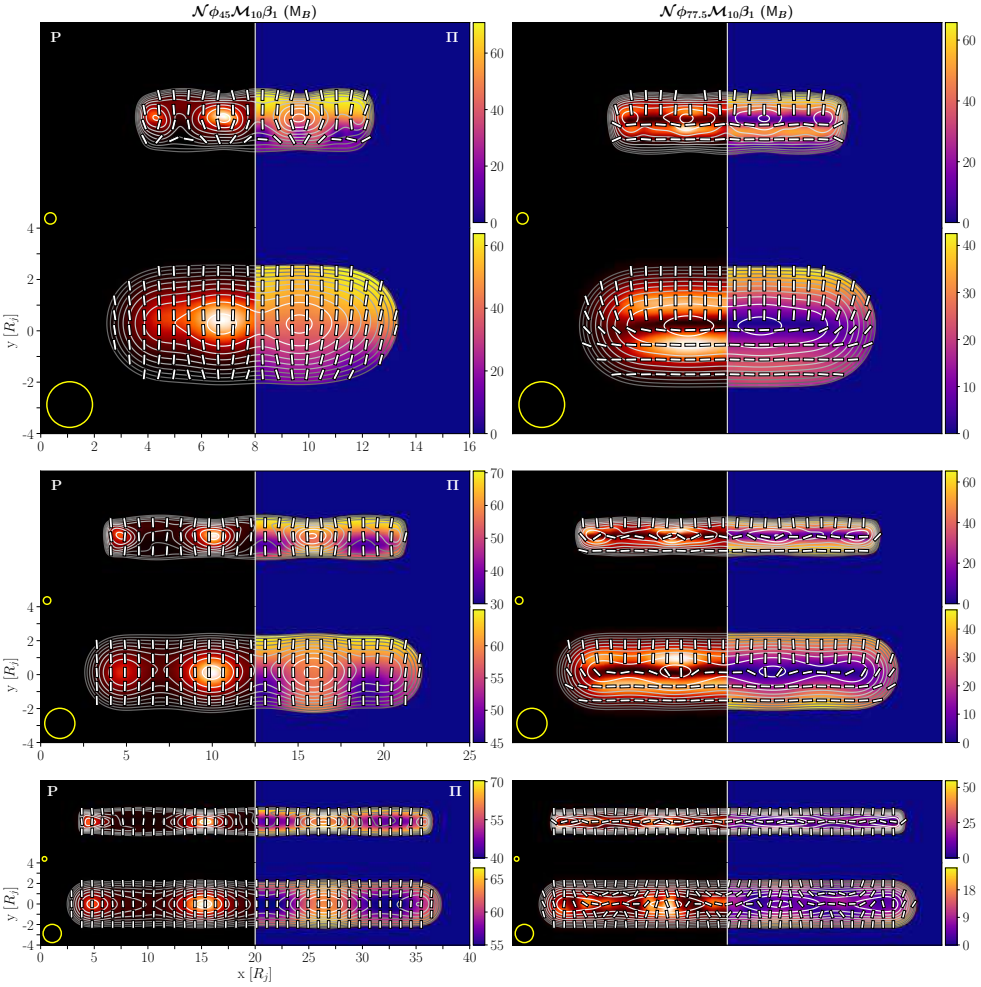

Figure 3.9: Linearly polarized intensity and degree of linear polarization (left and right halves of each panel, respectively) of the jet models $\mathcal{N}\phi_{45}\mathcal{M}_{10}\beta_1$ and $\mathcal{N}\phi_{77.5}\mathcal{M}_{10}\beta_1$, convolved with two different beams for viewing angles of 5° (top), 10° (middle), and 20° (bottom) and computed following the particle injection model M_B. The linear polarization intensity is plotted in normalized units and follows a linear color scale. Color bars at the right of each panel show the scale for the degree of linear polarization at the corresponding panel. The total intensity is superimposed as contours from 5×0.5% to 90% of the total intensity peak, following the sequence $c_n = (3/2) \times c_{n-1}$. The beam sizes (lower left corner of each panel) are $\sim 0.5\ R_j$ and $2\ R_j$ FWHM. EVPAs are displayed as white bars.

(0.5 R_j and 2 R_j FWHM) and for the viewing angles $\theta = 5^\circ$, 10°, and 20°. The panels are split into two halves, displaying P and Π on the left and right sides, respectively, because the models are qualitatively symmetric with respect to the dividing white line. These two models were selected for the figure because their lower number of stationary knots and more extended emission (M_B approximation) allowed us to better

distinguish the effects of the convolution, although all models were convolved for the study.

For both beam sizes, the $\mathcal{N}\phi_{45}$ model essentially retains its polarization angle distribution throughout the jet because it is constantly perpendicular to the axis, with the exception of $\theta = 5°$, for which the large beam removes some traces of EVPA rotation at the bottom part of the jet, which is still resolved by the high angular resolution beam. These results apply for all $\mathcal{N}\phi_{45}$ models. The $\mathcal{N}\phi_{77.5}$ model, in contrast, features a rich structure for all viewing angles. At $\theta = 5°$ and 10°, the transition zone between regions with EVPAs perpendicular to and aligned with the jet propagation direction, where the linearly polarized intensity drops, is enhanced by the convolution, mainly in the unresolved case, forming two bright polarized limbs of orthogonal polarization angles. This structure is persistent regardless of the beam size in the non-force-free models, while the high magnetic tension of the force-free models and the emission asymmetry still present at these values of θ confines their polarized emission above the jet axis, which causes the bottom part of these jets, in which the projected toroidal component dominates, to radiate with low intensity (see $\mathcal{F}\phi_{77.5}$ models in Figure 3.8). VLBI observations of blazar jets performed either at centimeter- or millimeter-wavelengths, which usually span viewing angles up to 10°, should feature this bimodal EVPA structure if the jets magnetic pitch angle is about 77.5° and the dynamic range is large enough ($\sim$ 1:100). For a viewing angle of 20°, the transverse bimodality of the polarization angle is lost because in this case, it is amplified by the convolution the longitudinal polarization angle rotation, as we mentioned before, with EVPAs perpendicular to the jet axis over stationary knots and parallel between them. This change in the EVPA is the consequence of the strengthening of the poloidal component of the magnetic field when the (highly oblique) shocks associated with the knots are crossed, as can be seen in the panel of the axial magnetic field of model $\mathcal{N}\phi_{77.5}\mathcal{M}_{10}\beta_1$ in Fig. 6 and in the drop of the averaged magnetic pitch angle for the same model in Fig. 7 of Paper I. We note that in contrast to our result, Beuchert *et al.* (2018) reported parallel EVPAs at an alleged recollimation shock at 3 mas from the core of the radio galaxy 3C 111. However, as remarked by the authors, the aligned EVPAs at the recollimation shock in the case of 3C 111 could likely be the result of the interaction with a traveling shock, which may enhance the toroidal field component.

3.8 Summary and conclusions

Synthetic polarized synchrotron emission maps were obtained from the magneto-hydrodynamical simulations based on two models connecting the thermal particles population, modeled by the hydrodynamical code, and the nonthermal particle population, which is responsible for the synchrotron radiation (see Section 3.3). Our results can be of interest in the interpretation of the VLBI observations of blazar jets. We list the results below.

i) The helical geometry of the magnetic field leaves a clear imprint on the emission

models, which manifests itself in an asymmetry in the emission across the jet for small enough viewing angles. This cross-section emission asymmetry, caused by the change of the angle between the helical magnetic field and the line of sight across the jet (Aloy *et al.,* 2000; Lyutikov *et al.,* 2005; Clausen-Brown *et al.,* 2011; Fuentes *et al.,* 2018), is confirmed in all the models discussed in this paper and for both particle injection approximations, as expected from the purely geometrical origin of the effect, for viewing angles $< 10°$. The emission asymmetry manifests itself in total and linearly polarized synchrotron intensities, although the transversal profiles for the polarized emission are much more complex.

ii) As concluded in Paper I, magnetic tension and the radial component of the Lorentz force are the key parameters governing the transversal structure of jets. It is then expected that these two quantities leave their imprints on the synchrotron emission maps obtained with the two particle injection models. Because of their higher relative magnetic tension and radial Lorentz force, in the models with the largest magnetizations and/or magnetic pitch angles, the uneven distribution of internal energy translates into a spine brightening in total and polarized intensities. Force-free models display a distinct spine brightening that originates from the radial gradient of the axial magnetic field.

iii) If the radio knots often observed in these jets are associated with recollimation shocks in the underlying flow, jets with strong radio knots must correspond to hot jets with low magnetization (at about or below equipartition). This conclusion, which was already established in Martí *et al.* (2016) and Fuentes *et al.* (2018), is now corroborated for a wider sample of models with different magnetic pitch angles and helical magnetic fields corresponding to force-free and non-force-free configurations. The strength of the shocks in these sources tends to decrease with decreasing internal energy and increasing magnetization in the small and large magnetic pitch angle jets and force-free and non-force-free jets. In addition to this and as a new result, jets with prominent radio knots must have a moderately small magnetic pitch angle because the magnetic tension tends to damp the strength of recollimation shocks.

iv) The jet models computed in this work preserve the axial symmetry and helical geometry of the magnetic field. We therefore obtain the characteristic bimodal configuration of the polarization angle throughout the jets, whether perpendicular to or aligned with the jet propagation direction (Lyutikov *et al.,* 2005). Blazar jets with large magnetic pitch angles should feature two bright limbs of linearly polarized emission with orthogonal EVPAs between them, tracing the poloidal and toroidal components of the magnetic field, regardless of the angular resolution achieved in the observations. Jets observed with large viewing angles could display EVPA rotation along the propagation direction if the jet is in equipartition and the polarized emission is not strongly confined around the jet axis. Conversely, if the magnetic pitch angle is about 45°, only jets with viewing

angles up to $\sim 2^{\circ}$ will present some clear signatures of a toroidal magnetic field component. Beyond this value, EVPAs will remain perpendicular to the jet axis, with the exception of some variations at recollimation shocks.

v) Jets with moderately open viewing angles will present a higher degree of linearly polarized emission values at the edges. As the magnetic pitch angle increases, the drop in the polarization degree toward the jet axis will also increase, featuring a bump of variable intensity depending on the connection of thermal and nonthermal particle populations.

Our conclusions are limited by the imposed axisymmetry and stationarity of the magnetohydrodynamical models, the simplicity of the flat-topped axial velocity profile, and the absence of rotation, among other important simplifications, as the nature of the numerical approach used to compute the magnetohydrodynamical models, which is only valid in the relativistic limit and is not suitable for describing jet models with extended (subrelativistic) shear layers and the resulting observational phenomenology associated with them. However, despite all the limitations of the dynamical and emission simulations, our approach allows for a thorough study of wide regions of the parameter space defining AGN jets at parsec scales, aiming to understand the origin of their observational phenomenology. Following the line of thought started in Fuentes *et al.* (2018), in this paper we extended the original study to wide ranges of magnetosonic Mach number, internal energies, and magnetizations to models with larger magnetic pitch angles and force-free magnetic field configurations.

Acknowledgements
AF and JLG acknowledge financial support from the Spanish Ministerio de Economía y Competitividad (grants AYA2016-80889-P, PID2019-108995GB-C21), the Consejería de Economía, Conocimiento, Empresas y Universidad of the Junta de Andalucía (grant P18-FR-1769), the Consejo Superior de Investigaciones Científicas (grant 2019AEP112), and the State Agency for Research of the Spanish MCIU through the Center of Excellence Severo Ochoa award for the Instituto de Astrofísica de Andalucía (SEV-2017-0709). JMM and MP acknowledge financial support from the Spanish Ministerio de Economía y Competitividad (grant AYA2016-77237-C3-3-P), the Spanish Ministerio de Ciencia (PID2019-107427GB-C33), and from the local Autonomous Government (Generalitat Valenciana, grant PROMETEO/2019/071). JMM acknowledges further financial support from the Spanish Ministerio de Economía y Competitividad (grant PGC2018-095984-B-I00). MP acknowledges further financial support from the Spanish Ministerio de Ciencia through grant PID2019-105510GB-C31. This research made use of Python (`http://www.python.org`), Numpy (van der Walt *et al.,* 2011), Pandas (McKinney, 2010), and Matplotlib (Hunter, 2007). We also made use of Astropy (`http://www.astropy.org`), a community-developed core Python package for Astronomy (Astropy Collaboration *et al.,* 2013; 2018).

Chapter 4 Filamentary Structures as the Origin of Blazar Jet Variability

A. Fuentes, J. L. Gómez, J. M. Martí, M. Perucho, G. -Y. Zhao, R. Lico, A. P. Lobanov, G. Bruni, Y. Y. Kovalev, A. Chael, K. Akiyama, K. L. Bouman, H. Sun, I. Cho, E. Traianou, T. Toscano, R. Dahale, M. Foschi, L. I. Gurvits, S. Jorstad, J. -Y. Kim, A. P. Marscher, Y. Mizuno, E. Ros, and T. Savolainen

Filamentary structures as the origin of blazar jet variability
Submitted to Nature Astronomy (2022)

Abstract

Supermassive black holes at the centre of active galactic nuclei power some of the most luminous objects in the Universe (Zensus, 1997). Typically, very long baseline interferometric (VLBI) observations of blazars have revealed only funnel-like morphologies with little information of the ejected plasma internal structure (Jorstad *et al.,* 2005; Lister *et al.,* 2009), or lacked the sufficient dynamic range to reconstruct the extended jet emission (Kim *et al.,* 2020). Here we show microarcsecond-scale angular resolution images of the blazar 3C 279 obtained at 22 GHz with the space VLBI mission *RadioAstron* (Kardashev *et al.,* 2013), which allowed us to resolve the jet transversely and reveal several filaments produced by plasma instabilities in a kinetically dominated flow. Our high angular resolution and dynamic range image allow us to challenge the standard shock-in-jet model (Marscher & Gear, 1985) invoked to explain blazar jet variability. Instead, we propose that emission features traveling down the jet may manifest as a result of differential Doppler-boosting within the filaments. Moreover, we can infer that the filaments in 3C 279 are threaded by a helical magnetic field rotating clockwise, as seen in the direction of the flow motion, with an intrinsic helix pitch angle of $\sim 45^\circ$ in a jet with a Lorentz factor of $\sim$13 at the time of observation.

4.1 Main

We observed 3C 279 on 10 March 2014 at 22 GHz (1.3 cm) with the space very long baseline interferometry (VLBI) mission *RadioAstron* (Kardashev *et al.,* 2013), a 10-m space radio telescope (SRT) onboard of the *Spektr-R* satellite, and an array of 23 ground-based radio telescopes spanning baseline distances from hundreds of kilometers to the Earth diameter (see Methods for a description of the array). The highly eccentric orbit of the SRT, with an apogee of $\sim 350\,000$ km, provided us with ground-space fringe detections of the source up to a projected baseline distance of 8 Earth diameters, probing a wide range of spatial frequencies perpendicular to the jet propagation direction (see Extended Data Figure 4.3). At the longest projected baselines to *RadioAstron*, we achieved a resolving power of 27 microarcseconds (μas), similar to that obtained by the Event Horizon Telescope (EHT) at 1.3 mm (~ 20 μas) (Kim *et al.,* 2020). The large number of detections reported within the *RadioAstron* active galactic nuclei (AGN) survey program (Kovalev *et al.,* 2020) made 3C 279 an ideal target for detailed imaging. Figure 4.1 presents our *RadioAstron* space VLBI polarimetric image of the blazar 3C 279. A representative image reconstruction obtained using novel regularized maximum likelihood methods (Chael *et al.,* 2016; 2018) is shown along with the closest in time 7 mm VLBA-BU-BLAZAR program image obtained on 25 February 2014, and the 1.3 mm EHT image obtained in April 2017. We show a field of view of around 1×1 milliarcseconds (mas) with an image total flux density of 27.16 Jy, and note that all extended emission outside this region is resolved out by *RadioAstron*. The robustness of our image is demonstrated in Extended Data Figure 4.4, where we show how it fits the data used for both total intensity and linearly polarized image reconstruction. We acknowledge, however, that VLBI imaging is an ill-posed problem, and any image reconstruction that fits the data is not unique (e.g., see the comprehensive image analysis carried out in Event Horizon Telescope Collaboration *et al.,* 2019d). The image in Figure 4.1 is complemented by the 48 images presented in Extended Data Figure 4.5 (see Methods).

In contrast to the contemporaneous 7 mm and classical centimetre-wave VLBI jet images (Lister *et al.,* 2009), where the observed synchrotron emission seems to be contained in a funnel with a uniform cross section, we show in great detail the internal structure of a blazar jet and find strong evidence of the filamentary nature of the emitting regions within it. We identify the jet core as the upstream bright component, and the so-called 'core region' encompasses the inner ~ 200 μas, roughly the extent of the features probed at 1.3 mm. The base is slightly elongated and tilted in the southeast-northwest direction, as reported in Kim *et al.* (2020). However, contrary to the EHT sparse sampling of the Fourier plane (Event Horizon Telescope Collaboration *et al.,* 2019b; Kim *et al.,* 2020), the ground array supporting our space-VLBI observations provided a significantly larger filling fraction, which enabled us to reconstruct images with a dynamic range that is two orders of magnitude larger. Thus, while we can recover up to three different filaments emanating perpendicularly from the jet base, the EHT could only recover one and is "blind" to the extended, filamentary structure, primarily due to the lack of short baselines. If aligned with respect to the brightness

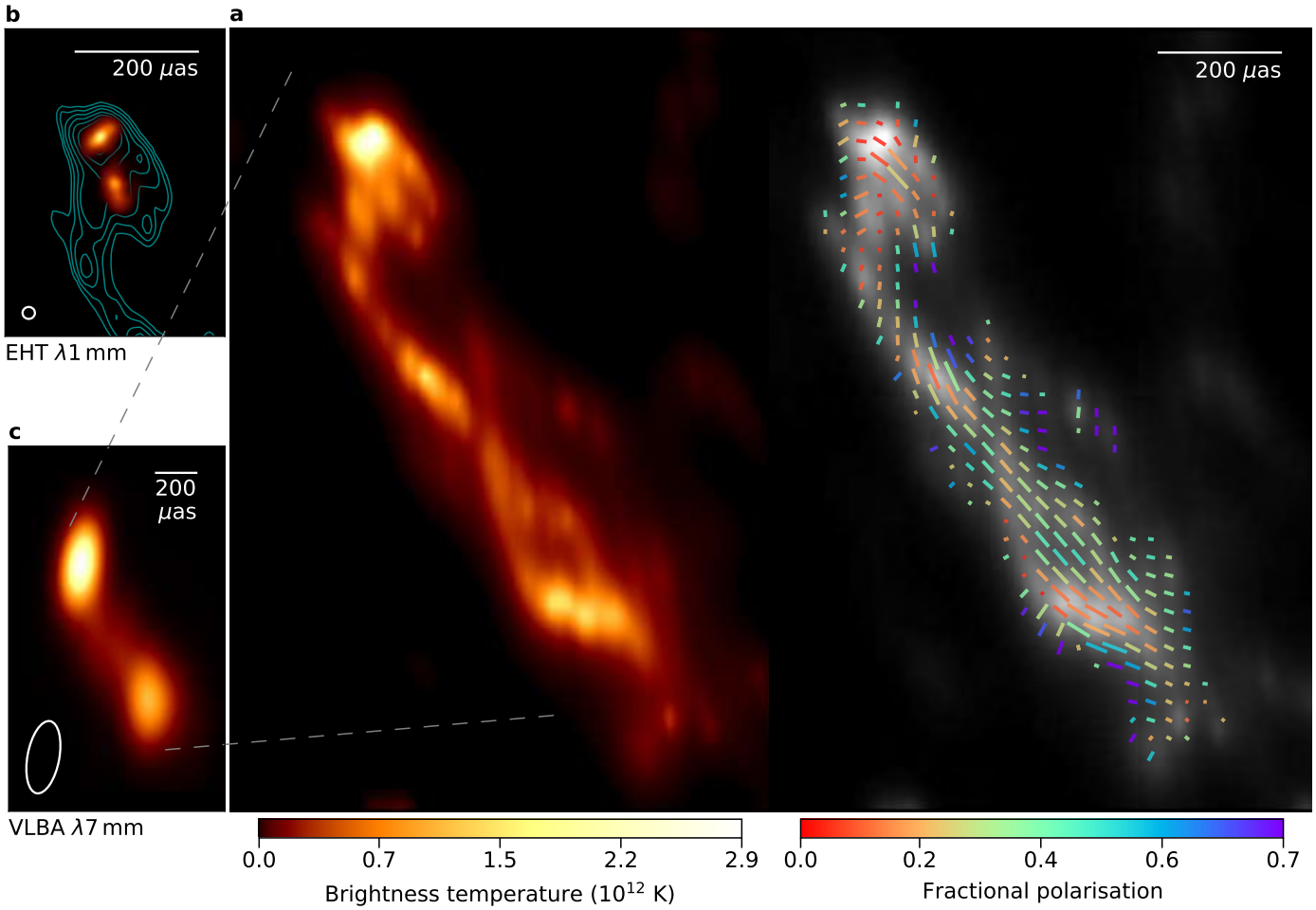
b
200 μas
EHT λ1 mm
a
200 μas
c
200
μas
VLBA λ7 mm
0.0
0.7
1.5
2.2
2.9
Brightness temperature (10^12 K)
0.0
0.2
0.4
0.6
0.7
Fractional polarisation

Figure 4.1: The filamentary structure of the jet in 3C 279 revealed by *RadioAstron*. **a**, Total intensity (left) and linearly polarized (right) *RadioAstron* image at 1.3 cm obtained on 10 March 2014. While both left and right images in **a** show brightness temperature in colour scale, the image on the right shows as well the recovered electric vector position angle overplotted as ticks. Their length and colour are proportional to the level of linearly polarized intensity and fractional polarization, respectively. **b**, The 1:1 scale 1.3 mm EHT image obtained in April 2017. Contours correspond to our *RadioAstron* image, which are shown to compare the different scales probed. These start at 90% of the peak brightness and decrease by successive factors of 3/2 until they reach 5%. Both images were aligned with respect to the pixel with maximum brightness. **c**, The 7 mm VLBA-BU-BLAZAR program image obtained on 25 February 2014. White ellipses at the bottom-left corner of **b** and **c** indicate the 20×20 μas and 150×360 μas convolving beams, respectively. Bottom colour bars refer only to information displayed on **a**.

peak, both images match remarkably well, and the jet feature observed at 1.3 mm is coincident in position and extension with our central filament, ignoring the small ($\lesssim 35$ μas) core shift between the two frequencies (Pushkarev *et al.,* 2012). Within our uncertainty, we do not measure a significant change in the core position angle with respect to the EHT image, taken three years later. The single-epoch results presented here do not allow us to discern whether this elongated structure corresponds to the accretion disk or to another extended jet component. Nonetheless, based on the small viewing angle inferred ($\theta \sim 1.9°$; Jorstad *et al.,* 2017) and the multi-epoch kinematic analysis of the model-fitted jet components, Kim *et al.* (2020) raised the possibility for this structure to correspond to a highly bent part of the inner jet.

Moving beyond the core region, we show in the top panel of Figure 4.2 the de-projected and on-sky coordinates of the two main (hereinafter g and b), and possibly third (r), filaments obtained from the fitting of three Gaussian curves to transverse cuts to the main jet axis (see Methods). Further downstream, filament is continuously recovered and contains most of the eastern extended structure flux density. Initially propagating in the southern direction, it displays a sharp bend of $\sim 45°$ to the west, close to the core region boundary. Although not continuously, we are also able to reconstruct filament beyond the inner 200 μas in what seems to be a helical-like morphology. These two filaments converge at ~ 500 μas down the jet, where filament crosses over . Further downstream, they bend and converge again at ~ 950 μas, where the brightness of the weaker filament is largely enhanced as it bends, dominating now the reconstructed emission in the southernmost jet region. Some diffuse emission is also systematically recovered parallel to filament after the first crossing, which might indicate the presence of a third filament ().

As detailed in the Methods section, there is a physically consistent domain in the space of parameters (Γ, $a_{\rm j}/a_{\rm ex}$), with Γ within the previously determined range of jet flow Lorentz factor for c ($\Gamma \in [10, 40]$; Bloom *et al.,* 2013), which allows us to interpret the observed approximate spatial periodicity, $\lambda_{\rm m}$, as the wavelength of the elliptical surface mode of a kinetically dominated, cold jet. More intriguing is the fact that the filaments associated with the elliptical mode are brighter in particular locations separated by half a wavelength (~ 400 μas for filament , ~ 850 μas for filament), just

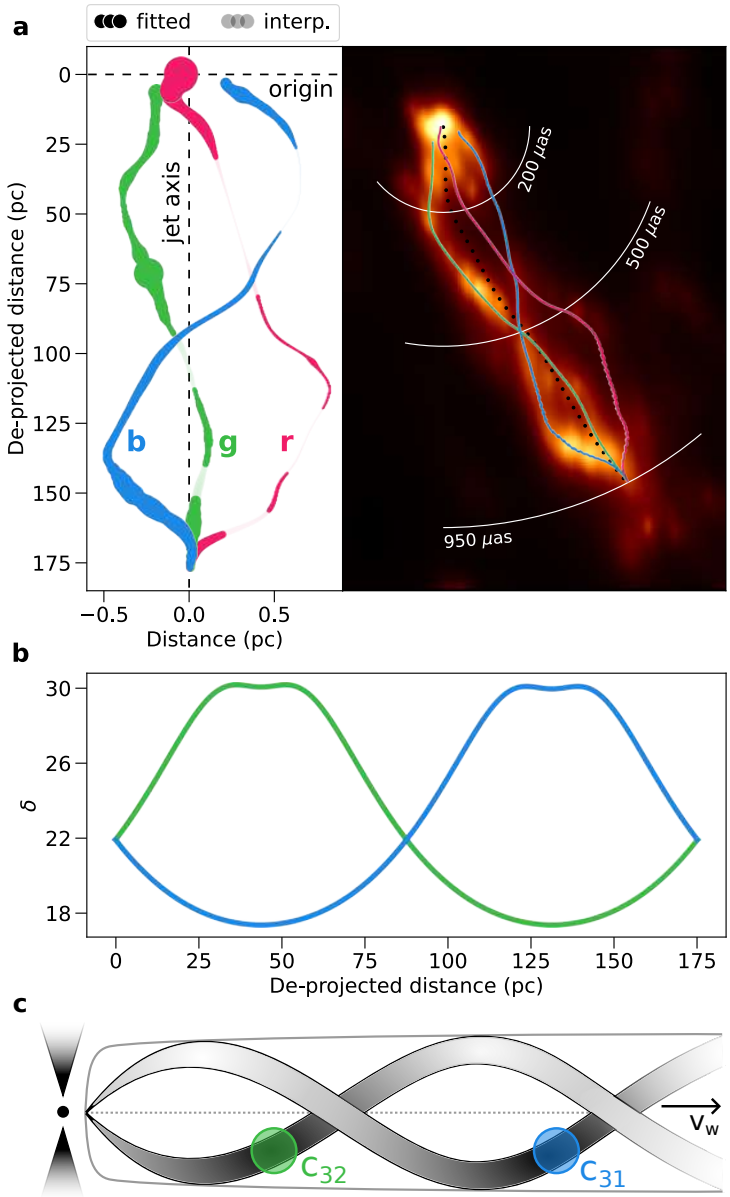

Figure 4.2: Analysis of the recovered filamentary structure. **a**, Left: de-projected filament coordinates fitted using three Gaussian curves (see Methods). Dimmer points indicate regions where the coordinates have been interpolated. Marker size scales with the flux density. Note the scales in the x- and y-axis are different. Right: position of the fitted filaments on top of the reconstructed image. The black, dotted curve denotes the main jet axis. **b**, Doppler factor computed for a plasma propagating along a double thread, as expected for elliptical modes, with $\Gamma = 13$ and $\theta = 1.9^{\circ}$. **c**, Schematic figure of the proposed model for blazar jet variability. The developing of plasma instabilities within the jet flow lead to filamentary structures with heterogeneous emissivity. Local changes in the plasma properties, which evolve and travel down the jet with the wave velocity, can explain these commonly observed moving components as a result of differential Doppler boosting. Darker colours mean brighter observed emission.

before the crossings of the filaments. The properties of the flow (e.g., pressure, density, flow velocity) are modified locally by the elliptical wave, the magnitude of the changes depending on position and time as modulated by the wave phase. Such small changes in the properties of the flow could explain the differences in brightness between regions inside the jet and, in particular, along the filaments. Here, the perturbation in the three-velocity vector and the subsequent changes in the local Doppler boosting play a major role. The middle panel of Figure 4.2 shows how the Doppler factor, δ, evolves along two threads originated by an elliptical mode in a plasma characterized by $\Gamma = 13$ and $\theta = 1.9°$. With a ratio $\delta_{\rm max}/\delta_{\rm min} \simeq 1.7$, the brightness of certain regions can increase by a factor of ~ 5, in agreement with the brightness excess observed at ~ 400 μas in filament , and at ~ 850 μas in filament . This enhanced emission would then be the result of the Doppler boosted emission along the line of sight. This interpretation is supported by the fact that both enhanced emission regions are found at approximately the same phase of the corresponding helical filament, with the local flow velocity pointing along the same direction (the line of sight).

Continuing with this interpretation, it is important to note that the enhanced emission regions will not be steady but will propagate downstream at a (pattern) speed equal to the wave's phase velocity. The fact that these brighter regions in filaments and match with the jet features observed at 7 mm (components C32 and C31 in Jorstad *et al.,* 2017, respectively) leads to the appealing possibility that these features correspond to the propagation of an elliptical perturbation mode and not to the propagation of a shock as proposed by the standard shock-in-jet model (Marscher & Gear, 1985). In particular, the estimated apparent speed of $\sim 7.23\,c$ (component C31, Jorstad *et al.,* 2017), corresponding to a propagation speed of $\sim 0.996\,c$ ($\Gamma \simeq 11$) and close to the lower limit of the c jet Lorentz factor estimates, supports this possibility as these waves propagate downstream along the jet with velocities smaller than or equal to that of the jet bulk flow (see Hardee, 2000; Vega-Garcıa *et al.,* 2019 and Methods). We illustrate our proposed model for the jet variability in c in the schematic figure shown in the bottom panel of Figure 4.2. Likewise, filamentary structures triggered by plasma instabilities can potentially explain the variability observed in other blazar sources and, in some cases, they could coexist with components originating from shock waves. An important implication of our study is that the main emission occurs in thin filaments that cover only a fraction of the jet cross-section. The time-scale of variability of such features can therefore be much less than the light-travel time across the entire jet width, a fact that can help to explain extremely rapid variability (Hayashida *et al.,* 2015).

The analysis of the linearly polarized emission captured by *RadioAstron* and the supporting ground array reveals clear signatures of a toroidal magnetic field threaded to the relativistic jet. The source is mildly polarized, with an integrated degree of linear polarization of ∼10%. The electric vector position angle indicates a magnetic field predominantly perpendicular to the flow propagation direction, that is, consistent with a helical magnetic field dominated by its toroidal component. Relativistic magneto-hydrodynamic simulations of jets at parsec scales have shown that, in the presence of a helical magnetic field, the observed synchrotron emission is unevenly distributed

across the jet width (Aloy *et al.,* 2000; Fuentes *et al.,* 2018; 2021; Moya-Torregrosa *et al.,* 2021). Based on the strong asymmetry in the reconstructed emission between the eastern and western sides of the jet axis, and following the analysis described in the Methods section, we can infer a jet bulk flow Lorentz factor of $\Gamma \simeq 13$, which is in excellent agreement with the estimates provided by analyzing the kinematics of the parsec-scale jet. Moreover, this allow us to further infer a helical magnetic field, with an intrinsic pitch angle of $\sim 45°$, rotating clockwise as seen in the direction of flow motion.

The findings presented in this paper, supported as well by previous VSOP (e.g., Lobanov & Zensus, 2001) and *RadioAstron* (e.g., Bruni *et al.,* 2021; Gómez *et al.,* 2022) space VLBI observations, strongly suggest that blazar jets have a complex and rich internal structure beyond the funnel-like morphologies reported by ground-based VLBI studies at lower angular resolutions. Future space VLBI missions and enhanced millimetre-wave global arrays, enabling high dynamic range observations capable to spatially resolving the jet width, should prove decisive in determining the true nature of jets powered by supermassive black holes.

4.2 Methods

4.2.1 Observations

Observations of c (1253−055) were conducted at 22.2 GHz (1.3 cm) on 2014 March 10-11, spanning a total of 11:44 h from 14:15 to 01:59 UT. During the observing session, *RadioAstron* recorded evenly spaced (every 80−90 min) blocks of data of 30 min and one final block of ∼2 h, corresponding to its orbit perigee. This allowed the spacecraft to cool down its high-gain antenna drive in between observing segments. Together with *RadioAstron*, a ground array of 23 antennas observed the target, namely ATCA (AT), Ceduna (CD), Hobart (HO), Korean VLBI Network (KVN) antennas Tanman (KT), Ulsan (KU), and Yonsei (KY), Mopra (MP), Parkes (PA), Sheshan (SH), Badary (BD), Urumqi (UR), Hartebeesthoek (HH), Kalyazin (KL), Metsähovi (MH), Noto (NT), Torun (TR), Medicina (MC), Onsala (ON), Yebes (YS), Jodrell Bank (JB), Effelsberg (EF), Svetloe (SV), and Zelenchukskaya (ZC).

Left and right circularly polarized signals (LCP and RCP, respectively) were recorded simultaneously at each station, with a total bandwith of 32 MHz per polarization. Collected data were then processed at the Max-Planck-Institut für Radiostronomie using the upgraded version of the DiFX correlator (Bruni *et al.,* 2016). Fringes between *RadioAstron* and ground stations were searched using the largest dishes, separately for each scan. This provides a first-order clock correction, to be later refined with baseline stacking in `AIPS` (Greisen, 1990). When no signal was found, we adopted a best-guess clock value extrapolated from scans giving fringes, with the aim of performing a further global fringe search at a later stage with `AIPS`.

4.2.2 Data reduction

For the initial data reduction, we made use of `ParselTongue` (Kettenis *et al.,* 2006), a Python interface for `AIPS`. At a first stage, we performed an *a priori* calibration of the correlated visibility amplitudes using the system temperatures and gain curves registered at each station. Some of the antennas participating in the observations failed to deliver system temperature information, which we compensated by using nominal values modulated by the antenna's elevation at each scan. Since we chose the average system temperature as the station's default value, visibility amplitudes were not properly scaled. We overcame this issue by determining, every two minutes, the gain corrections needed for each IF and polarization from a preliminary image where only closure-quantities (closure phases and log-closure amplitudes) were involved, using the software library `SMILI` (Akiyama *et al.,* 2017a; b). Then, we applied to each antenna the mean gain value obtained, allowing for further residual corrections during the final imaging and self-calibration. The image total flux density was fixed to that measured by the intra-KVN baselines (27.65 Jy), whose *a priori* calibration was excellent (Cho *et al.,* 2017). Finally, we corrected the phase rotation introduced by the receiving systems as the source's parallactic angle changes.

We then solved for residual single- and multi-band delays, phases, and phase rates by incrementally fringe-fitting the data. In the first iteration we excluded *RadioAstron* and performed a global fringe search on the ground array with a solution interval of 60 s, using MP and EF as reference antennas for the first and second part of the experiment, respectively. Once fully calibrated, the ground array was coherently combined (trough baseline stacking) to increase the signal-to-noise ratio of possible fringe detections to *RadioAstron*. To account for the acceleration of the spacecraft near its perigee and the low sensitivity of the longest projected baseline lengths to it, we adopted different solution intervals (from 10 s to 240 s) and data total bandwidth (by combining IFs). With a signal-to-noise ratio cutoff of 5, reliable ground-space fringes were detected up to $\sim$8 Earth's diameters, corresponding to the first observing block of *RadioAstron* (around 14 UT), achieving a maximum angular resolution of 27 μas in the transverse direction to the jet axis. Lastly, we solved for the antennas' bandpass, the delay difference between polarizations using the task RLDLY, and exported the frequency averaged data along each IF. The fringe-fitted visibility coverage in the Fourier plane is shown in Extended Data Figure 4.3.

4.2.3 Imaging

Imaging of the data was carried out using novel regularized maximum likelihood (RML) methods (Narayan & Nityananda, 1986), implemented in the `eht-imaging` software library (Chael *et al.,* 2016; 2018). While the CLEAN algorithm (Högbom, 1974) has been widely used in the past for VLBI image reconstruction, novel RML methods are not extensively used, especially at centimetre wavelengths and space VLBI experiments. Generally speaking, RML methods try to solve for the image I that

minimizes the objective function:

$$J(I) = \sum_{\text{data terms}} \alpha_D \chi^2_D(I, V) - \sum_{\text{reg. terms}} \beta_R S_R(I), \tag{4.1}$$

where α and β are hyperparameters that weight the contribution of the image fitting to the data χ^2, and the image-domain regularization S, to the minimization of the previous equation. Contrary to traditional CLEAN, full closure data products (closure phases and log closure amplitudes) can be employed during image reconstruction in addition to complex visibilities, further constraining the proposed image. Given the large number of telescopes participating in the experiment, closure quantities have proven quite useful since atmospheric phase corruption and gain uncertainties are mitigated. Multiple regularization over the proposed image can be imposed too, like smoothness between adjacent pixels or similarity to a prior image.

Prior to imaging, we first performed an initial phase-only self-calibration to a point source model with a solution interval of 5 s and coherently averaged the data in 120 s intervals, using the `DIFMAP` package (Shepherd, 1997). We compared these results with those obtained with the `AIPS` task CALIB, for which a signal-to-noise ratio cutoff of 5 was set, to ensure no artificial signal was introduced in the data. In the following paragraphs we describe the imaging procedure.

As a first a step, we flagged all baselines to *RadioAstron* and imaged the data collected only by ground radio telescopes. The pre-processed data noise budget is inflated by a small amount (1.5 %), to account for non-closing errors, and the image is initialized with an elliptical Gaussian, oriented in roughly the same angle as the 7 mm image and enclosed in a 1.5×1.5 mas field of view gridded by 200×200 pixels. As mentioned above, because of the poor *a priori* amplitude calibration due to missing antennas' system temperature, we opted for a first round of imaging where only closure quantities (closure phases and log closure amplitudes) were used to constrain the image likelihood. This likelihood takes the form of the mean squared standardized residual (similar to a reduced χ^2) as defined in Event Horizon Telescope Collaboration *et al.* (2019d). Each imaging iteration takes as initial guess the image reconstructed in the previous step blurred to the ground array nominal resolution, i.e., 223 μas, which prevents the algorithm of being caught in local minima during optimization of Equation 4.1. We then self-calibrate the data to the closure-only image obtained and incorporate full complex visibilities to the imaging process, which is finalized by repeating the imaging and self-calibration cycle two more times. In addition to the data products mentioned, we impose several regularizations to the proposed images. These include maximum entropy (mem), which favors similarity to a prior image; total variation (tv) and total squared variation (tv2), which favor smoothness between adjacent pixels; ℓ_1-norm, which favors sparsity in the image; and total flux regularization, which encourages a certain total flux density in the image. Finally, we restore all baselines to *RadioAstron* and repeat this procedure, substituting the Gaussian initialization with the blurred, ground-only image previously reconstructed and using the full array nominal resolution (27 μas) between imaging iterations to blur intermediate reconstructions.

Contrary to full Bayesian methods, RML techniques do not estimate the posterior distribution of the underlying image, but instead compute the maximum a posteriori solution, i.e., the single image that best minimizes Equation 4.1. The hyperparameters chosen will necessarily have an impact on the reconstructed image features, thus we conducted a scripted parameter survey to ensure the robustness of the subtle structures seen in Figure 4.1 and to impartially determine which parameters perform better on the image reconstruction. From the many images obtained, we show in Extended Data Figure 4.5 the complete collection of images which could potentially describe the observed source structure. These fit the data equally well and preserve the total flux measured by the KVN to a certain level. The regularizers and hyperparameters used to obtain these images are listed on each panel of Extended Data Figure 4.5. Apart from these, we gave the same weight to complex visibilities and closure quantities data terms.

4.2.4 Polarimetric imaging

The polarization results presented in Figure 4.1 were obtained using the `eht-imaging` library as well. A more complete description of the method can be found in Chael *et al.* (2016) and Event Horizon Telescope Collaboration *et al.* (2021a), here we briefly outline the procedure followed. For polarimetric imaging, `eht-imaging` minimizes again Equation 4.1, substituting complex visibilities and closure quantities data terms with polarimetric visibilities $\mathcal{P} = \tilde{\mathcal{Q}} + i\tilde{\mathcal{U}}$ and the visibility domain polarimetric ratio $\breve{m} = \mathcal{P}/\tilde{\mathcal{I}}$. Note that total intensity and linearly polarized intensity images are reconstructed independently. Image regularization includes now total variation which, as for total intensity imaging, encourages smoothness between adjacent pixels; and the Holdaway-Wardle regularizer (Holdaway & Wardle, 1990), which prefers pixels with polarization fraction values below the theoretical maximum of 0.75 for optically thin synchrotron emission. The pipeline then alternates between minimizing the polarimetric objective function and solving for the complex instrumental polarization, the so-called D-terms. The instrumental polarization calibration is performed by maximizing the consistency between the self-calibrated data and sampled data from corrupted image reconstructions. After D-terms solutions are found for each antenna, the reconstructed polarimetric image is blurred, as was done for Stokes $\mathcal{I}$ imaging, and the imaging-calibration cycle is repeated until convergence of the solutions. Apart from instrumental polarization, VLBI polarimetric analyses rely on the calibration of the absolute polarization angle. To account for this, we compared our polarization results with the closest in time 7 mm results. The recovered polarization angle patterns match remarkably well when our image is convolved with the 7 mm beam. Ignoring Faraday rotation of the polarization angle between the two frequencies, based on the small rotation measure values reported in Hovatta *et al.* (2012) and Park *et al.* (2018), we estimate an overall median difference of $\sim 8°$, that we applied to the results presented in Figure 4.1.

4.2.5 Filament fitting

The relative right ascension and declination coordinates of the filaments were obtained from the fitting of three Gaussian curves to transverse profiles of the brightness distribution. We first computed the main jet axis, commonly referred to as ridge line, from a convolved version of the reconstructed image. Using a sufficiently large Gaussian kernel, we blurred our image until the emission blends into a unique stream and the filaments are no longer distinguishable, similarly to the 7 mm VLBA-BU-BLAZAR image. We then project this image into polar coordinates, centred at the jet origin, and slice it horizontally, storing the position of the flux density peak for each cut. These positions are then transformed back to Cartesian coordinates, obtaining thus the main jet axis. To each pair of consecutive points conforming the axis, we compute the local perpendicular line and retrieve the flux density of the pixels contained in the cut. With this procedure, we assemble a set of transverse brightness profiles to which we fit the sum of three Gaussian curves using the python package `lmfit` (Newville *et al.,* 2021). The number of Gaussian components used is motivated by the number of filaments observed emanating from the core region, although we note that two Gaussian components are enough to fit the two main threads. Finally we select the coordinates as the position of the peak(s) found in the curve best fitting each cut. In Figure 4.2, coordinates are de-projected assuming a source redshift $z = 0.536$ (Marziani *et al.,* 1996), a viewing angle $\theta = 1.9°$ (Jorstad *et al.,* 2017), and a cosmology $H_0 = 67.7\,\mathrm{km\,s^{-1}\,Mpc^{-1}}$, $\Omega_m = 0.307$, and $\Omega_\Lambda = 0.693$ (Planck Collaboration *et al.,* 2016).

4.2.6 Instability analysis

Based on the aforementioned Gaussian fitting to the observed filaments, we estimate an approximate spatial periodicity λ_m of 950 μas (projected on the plane of the sky) or 175 pc (de-projected), which corresponds to $\sim 2.3 \times 10^6$ gravitational radii assuming a black hole mass of $M_\mathrm{BH} \simeq 8 \times 10^8\,M_\odot$ (Nilsson *et al.,* 2009). The possibility for these filaments to reflect a fundamental periodicity of the black hole or inner accretion disk directly associated with their rotation should be dismissed, as it would imply propagation speeds along the filaments larger than the speed of light by orders of magnitude. At the same time, explaining such a fundamental periodicity in terms of precession of a jet nozzle, caused by the Lense-Thirring effect (Bardeen & Petterson, 1975) or a supermassive black hole binary system, invoked to explain a sharp bend in the nuclear region, have been recently discarded (Kim *et al.,* 2020). On the other hand, anchoring the filaments to the outer accretion disk to allow for a subluminal propagation of the helical pattern would imply a exceedingly large (Keplerian) disk radius, that is, larger than ~ 1 light-year, about two orders of magnitude larger than the expected disk sizes (Morgan *et al.,* 2010).

According to Kim *et al.* (2020), the jet no longer accelerates beyond ∼100 μas from the core, suggesting a kinetically dominated flow in which the observed filaments show a magnetic field structure dominated by the toroidal component. Taking this into account, we conclude that these bright filaments reveal compressed regions

with enhanced gas and magnetic pressure – favouring an increased synchrotron emissivity and ordering of the magnetic field. Thus, these might be associated with the triggering and development of flow instabilities. Current-driven kink or Kelvin-Helmholtz (KH) instabilities are the most plausible mechanisms capable of developing such helical structures (Mizuno *et al.,* 2012; Perucho *et al.,* 2012; Vega-Garcıa *et al.,* 2019). Rayleigh-Taylor (RT) instabilities have also been discussed in the context of jet expansion and recollimation, as a possible trigger of small-scale distortions of the jet surface and turbulent mixing (see Perucho, 2019 for a review). However, RT instabilities would not produce filaments as the ones we observe, so we neglect this option. Current-driven instabilities dominate in Poynting-flux regimes with strong helical magnetic fields, that is, in the jet's acceleration and collimation region. On the contrary, KH instabilities have the largest growth in kinetically dominated flows, thus favored in our case. The extension of the filaments greatly exceeds the jet radius, which is expected for KH surface modes. While two filaments could be generated by an elliptical mode, the possible third filament observed might indicate the presence of an additional helical mode interfering with the elliptical.

Assuming the jet is kinetically dominated and cold, as expected for powerful jets already expanded and accelerated, the fastest growing frequency of a mode is given by $\omega^*_{nm} R/a_{\rm ex} = (n + 2m + 1/2)\pi/2$ (Hardee, 1987; 2000), where R is the radius, $a_{\rm ex}$ the sound speed of the ambient medium, and n and m the type of mode ($n = 1, 2$ for helical and elliptical modes, respectively; and $m = 0$ for a surface mode). Taking $\omega \leq 2\pi c/\lambda_{\rm m}$, we find $a_{\rm ex} \approx 10^{-2} c$ for both the helical and elliptical modes. At this maximum growth frequency, and for a highly supersonic jet (i.e., with jet Mach number $M_{\rm j} \gg 1$), the wavelength of the mode and wave velocity are given, respectively, by

$$\lambda^*_{\rm m} \approx \frac{4}{n + 1/2} M_{\rm ex} \frac{\Gamma}{a_{\rm j}/a_{\rm ex} + \Gamma} R \quad \text{and} \tag{4.2}$$

$$v^*_{\rm w} \approx \frac{\Gamma}{a_{\rm j}/a_{\rm ex} + \Gamma} u, \tag{4.3}$$

where u is the jet flow velocity (which approximates the light speed c given the large Lorentz factors inferred), Γ is the jet flow Lorentz factor, $M_{\rm ex}$ is the Mach number of the jet with respect to the ambient sound speed ($M_{\rm ex} = u/a_{\rm ex} \approx c/a_{\rm ex} \approx 100$), and a_j is the sound speed of the jet flow.

In our interpretation, described in the main body of the paper, the wave velocity $v^*_{\rm w}$ coincides with the (pattern) speed of the jet feature observed at 7 mm (component C31 in Jorstad *et al.,* 2017), very close to c, leading to the condition (see Equation 4.3) $a_{\rm j}/a_{\rm ex} \ll \Gamma$ or, equivalently, $M_{\rm j} \gg M_{\rm ex}/\Gamma$. With $M_{\rm ex} \approx 100$ and $\Gamma \in [10, 40]$, the last condition implies $M_{\rm j} \gg 1$, hence validating our assumption of a kinetically dominated flow at the observed scales.

4.2.7 Jet properties derived from the reconstructed polarimetric emission

The synchrotron radiation coefficients are a function of the angle between the magnetic field and the line of sight in the fluid frame. Thus, for a fixed viewing angle and jet

flow velocity, the bulk of the emission will be located on either side of the main jet axis depending on the magnetic field helical pitch angle. This asymmetry is maximized when the helical magnetic field pitch angle (in the fluid frame) ϕ' equals to $45°$ (Aloy *et al.,* 2000). Given the strong asymmetry in the reconstructed emission between the eastern and western sides of the jet axis, we can assume that the viewing angle in the fluid's frame approximates ϕ', that is $\theta' \simeq \phi'$. Hence, given the estimated viewing angle in the observer's frame ($\theta \sim 1.9°$) (Jorstad *et al.,* 2017) and the light aberration transformations (Rybicki & Lightman, 1979)

$$\sin\theta' = \frac{\sin\theta}{\Gamma(1-\beta\cos\theta)}, \quad \cos\theta' = \frac{\cos\theta-\beta}{1-\beta\cos\theta}, \tag{4.4}$$

where $\beta = \sqrt{1-1/\Gamma^2}$, we can infer a jet bulk flow Lorentz factor of $\Gamma \simeq 13$, which is in excellent agreement with the estimates provided by analyzing the kinematics of the parsec-scale jet (Jorstad *et al.,* 2017), and satisfies the upper limit previously established by our KH instability analysis. Moreover, this allows us to estimate the viewing angle θ_r at which the emission asymmetry will reverse from one side to the other as $\cos\theta_r = (1-1/\Gamma^2)^{1/2}$ (Aloy *et al.,* 2000), which results in $\theta_r \simeq 4.4°$ for $\Gamma = 13$. Since $\theta < \theta_r$ and the bulk of the reconstructed emission is located to the east of the jet axis, we infer a helical magnetic field rotating clockwise as seen in the direction of flow motion. The Lorentz-transformation of the magnetic field from the fluid's to the observer's frame boosts the toroidal component by Γ (Lyutikov *et al.,* 2005), and therefore the helix pitch angle transforms as $\tan\phi = \Gamma\tan\phi'$. This makes $\phi \simeq 86°$ in the observer frame, which is in agreement with the predominantly toroidal magnetic field observed.

Code availability

The software packages used to calibrate, image, and analyze the data are available at the following sites: `AIPS`, `ParselTongue`, `DIFMAP`, `SMILI`, `eht-imaging`, and `lmfit`.

Acknowledgements
We thank L. Hermosa for useful comments on the manuscript. The work at the IAA-CSIC is supported in part by the Spanish Ministerio de Economía y Competitividad (grants AYA2016-80889-P, PID2019-108995GB-C21), the Consejería de Economía, Conocimiento, Empresas y Universidad of the Junta de Andalucía (grant P18-FR-1769), the Consejo Superior de Investigaciones Científicas (grant 2019AEP112), and the State Agency for Research of the Spanish MCIU through the "Center of Excellence Severo Ochoa" award to the Instituto de Astrofísica de Andalucía (SEV-2017-0709). JMM and MP acknowledge support from the Spanish *Ministerio de Ciencia* through grant PID2019-107427GB-C33, and from the *Generalitat Valenciana* through grant PROMETEU/2019/071. JMM acknowledges additional support from the Spanish *Ministerio de Economía y Competitividad* through grant PGC2018-095984-B-l00. MP acknowledges additional support from the Spanish *Ministerio de Ciencia* through grant PID2019-105510GB-C31. MP acknowledges Manuel Perucho-Franco, his father, for standing up as an example through his whole life. YYK was supported by the Russian Science Foundation grant 21-12-00241. AC is supported by Hubble Fellowship grant HST-HF2-51431.001-A awarded by the Space Telescope Science Institute, which is operated by the Association of Universities for Research in Astronomy, Inc., for NASA, under contract NAS5-26555. TS was supported by the Academy of Finland projects 274477, 284495, 312496, and 315721. The *RadioAstron* project is led by the Astro Space Center of the Lebedev Physical Institute of the Russian Academy of Sciences and the Lavochkin Scientific and Production Association under a contract with the Russian Federal Space Agency, in collaboration with partner organizations in Russia and other countries. The European VLBI Network is a joint facility of independent European, African, Asian, and North American radio astronomy institutes. Scientific results from data presented in this publication are derived from the EVN project code GA030D. This research is partly based on observations with the 100 m telescope of the MPIfR at Effelsberg. This publication makes use of data obtained at Metsähovi Radio Observatory, operated by Aalto University in Finland. Our special thanks to the people supporting the observations at the telescopes during the data collection. This research is based on observations correlated at the Bonn Correlator, jointly operated by the Max-Planck-Institut für Radioastronomie, and the Federal Agency for Cartography and Geodesy. This study makes use of 43 GHz VLBA data from the VLBA-BU Blazar Monitoring Program (VLBA-BU-BLAZAR; http://www.bu.edu/blazars/BEAM-ME.html), funded by NASA through the Fermi Guest Investigator grant 80NSSC20K1567.

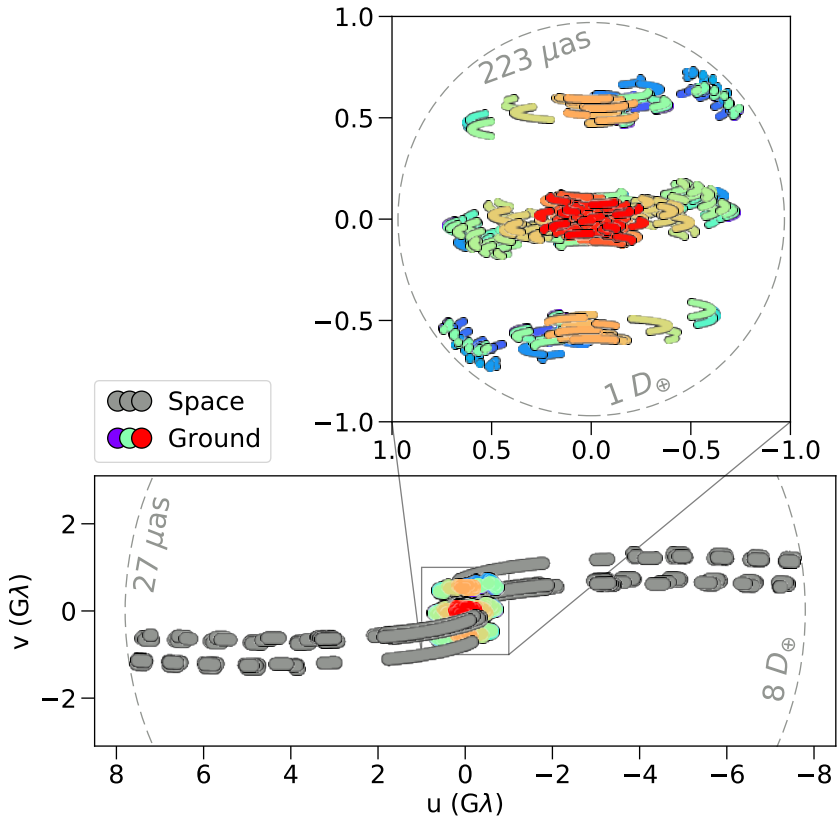

Extended Data Figure 4.3: Baseline coverage for our RadioAstron observations of c in March 2014. Rainbow-coloured and grey points indicate individual ground-ground baselines and space-ground baselines, respectively. Dashed circles indicate the baseline length in Earth's diameter units ($D_\oplus$) and the corresponding angular resolution.

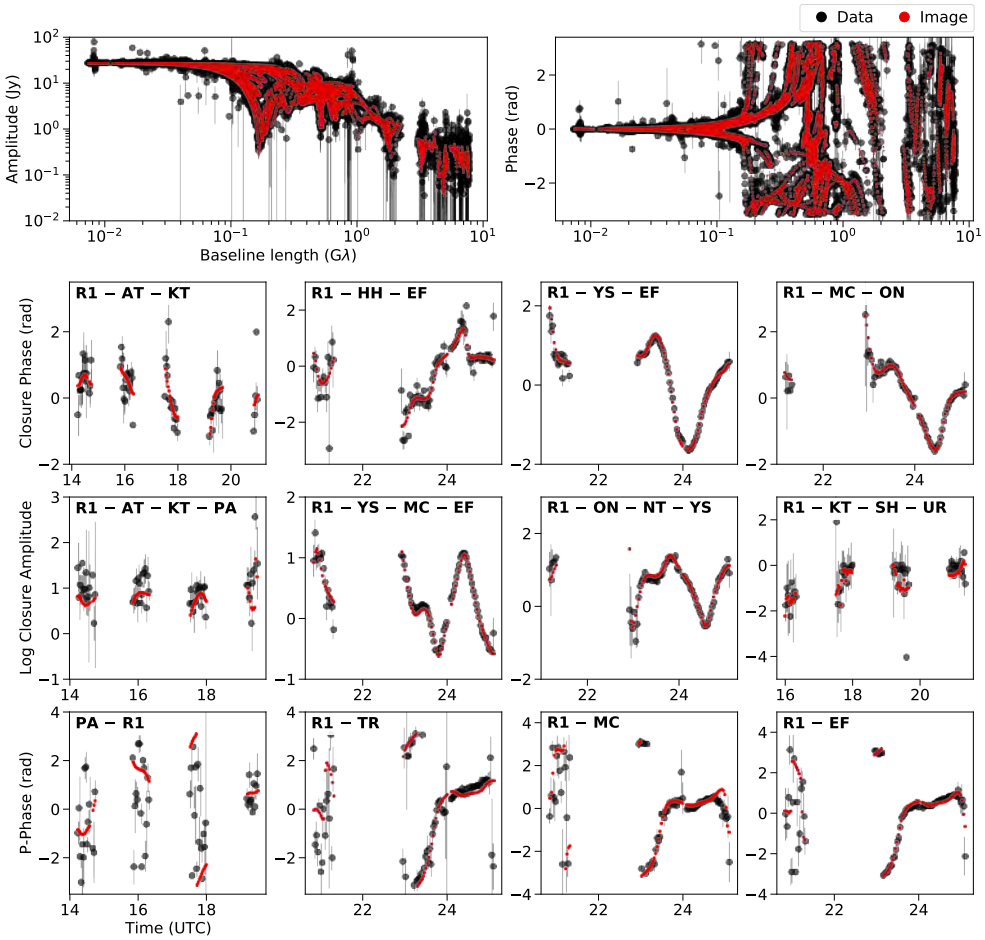

Extended Data Figure 4.4: Fitting of the polarimetric RadioAstron image to a selection of data products. Data (black points) and image model (red points) self-calibrated visibility amplitudes and phases, closure phases, log closure amplitudes, and polarimetric visibility phases as a function of time. All these examples include *RadioAstron* measurements.

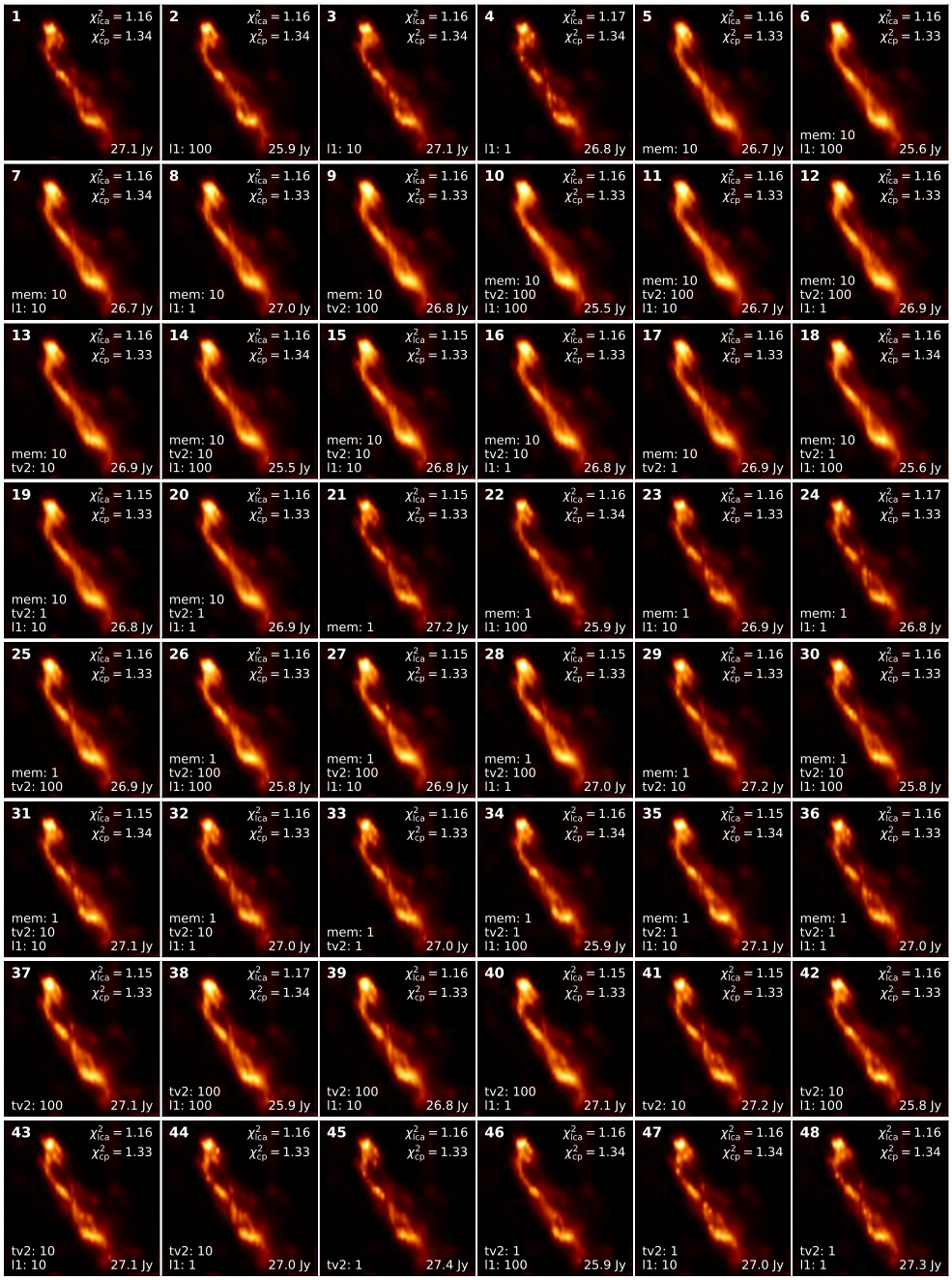

Extended Data Figure 4.5: Top 48 image reconstructions from the parameter survey conducted. Each image includes the closure phase (cp) and log closure amplitude (lca) reduced χ^2, the image regularizers used and their weight, and the total flux reconstructed. The image presented in Figure 4.1 corresponds to #21, which has the overall minimum reduced χ^2.

Chapter 5 Dynamic Imaging of Sagittarius A*, the SMBH at the Galactic Center

‘

Partially reproduced from

The Event Horizon Telescope Collaboration *et al.*
First Sagittarius A* Event Horizon Telescope Results. III.
Imaging of the Galactic Center Supermassive Black Hole
The Astrophysical Journal Letters, **930**, L14 (2022)

Abstract

The content of this Chapter corresponds to Section 9 and Appendix J of Event Horizon Telescope Collaboration *et al.* (2022c). Here we present the first event-horizon-scale dynamic reconstructions of the compact structure surrounding Sagittarius A* (Sgr A*), obtained with the Event Horizon Telescope in 2017 April at a wavelength of 1.3 mm. We have both explored dynamic imaging and snapshot geometric modeling of Sgr A* during a selected time window with the best (u, v)-coverage. Imaging has been conducted trough surveys over a range of assumptions using the `StarWarps` algorithm. For modeling, we fit several types of simple geometric models to the data using the `DPI` and `Comrade` software packages. Different prescriptions have been used to account for scattering effects by the interstellar medium toward the Galactic center, while no mitigation of the rapid intraday variability that characterizes Sgr A* has been carried out whatsoever. Leveraging the persistent ring-morphology obtained trough classical “static" imaging and the preferred ring geometry inferred from full-track geometric modeling, we impose strong prior assumptions that Sgr A*'s underlying structure is ring-like, and explore the dependence of the results on these and other assumptions. While current EHT measurements of Sgr A* show interesting dynamics, the EHT's 2017 coverage does not allow us to conclusively determine the evolution of the gas surrounding Sgr A*. This analysis, however, shows promising potential to actually recover the dynamics of Sgr A* in future EHT observations with improved coverage.

5.1 Introduction

The dynamical timescale at the location of the innermost stable circular orbit for Sagittarius A* (Sgr A*), $t_{\rm g} = 12\pi\sqrt{6}GM/c^3$ for zero spin, is approximately 30 min and can be smaller by a factor of ~ 10 if the black hole is spinning rapidly. Variability at these timescales across the electromagnetic spectrum, including at 230 GHz, is one of Sgr A*'s salient features – see Wielgus *et al.* (2022) and references therein. As discussed in Section 3.2 of Event Horizon Telescope Collaboration *et al.* (2022c) and Event Horizon Telescope Collaboration *et al.* (2022b), a few EHT closure phase triangles show measurable variability across the 2017 observing campaign that can be attributed to intrinsic source variability. In this section, we explore the level and characteristics of structural changes in the Sgr A* image that are consistent with the observed variability.

Recovering time-resolved structures on these short timescales is especially challenging due to the sparse snapshot (u, v)-coverage for the EHT array. Indeed, without additional constraints, any observed change in the visibility domain can be interpreted as caused either by intrinsic variability or simply by the rotation of the baselines with the Earth and their probing of different spatial structures – though fitting fast fluctuations in the visibilities with static emission requires larger fields-of-view. This is especially true for baselines that probe regions of the (u, v)-space in which the visibility amplitudes show deep minima (or nulls), across which the complex visibilities change by order unity over infinitesimal changes in baseline length.

In attempts to describe the EHT observations with a static image, we assign any observed variation to spatial structures and mitigate potential effects of variability by inflating the error budget. In this section, we instead attempt to fit the time-evolving data directly to produce spatially- and temporally-resolved images of Sgr A* on minute timescales. Our analysis of dynamic properties presuppose that the 230 GHz emission from Sgr A* is compact (see Section 2.3 of Event Horizon Telescope Collaboration *et al.*, 2022c) and ring-like such that the short-timescale variability we see can be attributed to changes in the image with time. We combine two independent analysis methods – dynamic imaging with temporal regularization between frames and snapshot geometric modeling – to identify trends in the spatial evolution of Sgr A*.

Our analysis shows that significant uncertainty exists in any attempt to characterize the spatially-resolved dynamics of Sgr A* using EHT 2017 data. We expect that future observations with an expanded EHT array will yield significantly improved time- and spatially-resolved movies of Sgr A*.

5.2 Selecting an Observation Window

The rotation of the Earth causes the EHT's snapshot (u, v)-coverage to change over time. Static imaging and modeling approaches assume the source is unchanging in time, which allows these approaches to combine data from a full night of observations. However, recovery of short-timescale evolution requires that we only consider coverage

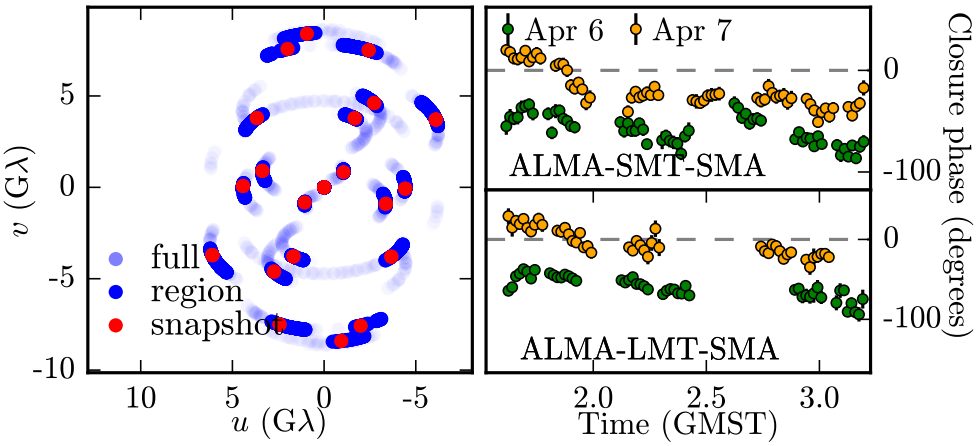

Figure 5.1: (Left) (u, v)-coverage for the selected time window for dynamic imaging and modeling. The light blue points show the coverage of the full night of observation, while the dark blue points and the red points represent the coverage for the selected dynamic imaging region and a single 60s snapshot from that region, respectively. (Right) Closure phases for Sgr A* (green and yellow) on two representative triangles during the selected time region.

synthesized on the variability timescale. This “snapshot" coverage is extremely sparse and introduces artifacts into image reconstructions. To minimize these artifacts, we constructed and evaluated metrics to assess the performance of the snapshot coverage and identify the most promising time windows for dynamic analysis. These metrics rely purely on the (u, v)-coverage rather than the properties of the underlying Sgr A* visibilities. The construction and validation of a suite of these metrics are reviewed in Farah *et al.* (2022).

We consider metrics that assess several attributes of the (u, v)-coverage, including the largest gap in coverage (Wielgus *et al.* 2020), the fraction of the (u, v) plane covered (Palumbo *et al.* 2019), and the geometric properties of the coverage (Farah *et al.* 2022). We summarize the application of these metrics to the 2017 April 7 EHT Sgr A* data set in Section 5.A. These three metrics identify a period from approximately 1.5-3.2 GMST on April 6 and 7 that maximally mitigates the EHT’s snapshot coverage limitations. During this time window, all sites participate in observing Sgr A* except PV, though there is a notable dropout of the LMT between approximately 2.4-2.9 GMST on both days. All dynamic analyses discussed in the remainder of this Chapter are performed *only in this selected time window*.

Figure 5.1 shows the (u, v)-coverage for April 7 during the roughly 100 min observation window selected for dynamic analysis, along with the coverage for a single 60 second “snapshot" integration. Closure phases from two informative triangles are overlaid for April 6 and 7 during this time window. These closure phases show distinct evolution in the resolved structure of Sgr A* during the same 100 min window on April 6 and 7.

5.3 Dynamic Imaging and Modeling Methods

To analyze Sgr A*'s spatially-resolved dynamics during the 100 min selected region of time on April 6 and 7, we use two methods: dynamic imaging and snapshot geometric modeling (also simply referred to as dynamic modeling). Both methods fit EHT 2017 data on 60 s snapshot integrations within the selected observation window but make different prior assumptions about the structure of the source in space and time. Note that unlike in static imaging, we do not flux normalize the data before dynamic analysis. Because the (u, v)-coverage is sparse even in the best available time window, both methods need to make strong prior assumptions about the spatial and/or temporal structure of the source to constrain the fits to the data. Note that when performing dynamic imaging/modeling fits we *do not* include a variability noise budget as is done in static imaging (Section 3.2.2 in Event Horizon Telescope Collaboration *et al.,* 2022c).

5.3.1 Dynamic Imaging

Dynamic imaging methods reconstruct a time-evolving image that best fits the observed evolution of Sgr A*. Our dynamic imaging approach is based on `StarWarps` (Bouman *et al.,* 2018), which enforces continuity across an image and in time by means of spatial and temporal regularization (Section 1.3.3.3). Temporal regularization is set by a parameter β_Q^{-1} which corresponds to the allowed variance between pixels in snapshots that are typically 60 s apart[1]; smaller values of β_Q^{-1} correspond to stronger continuity in time. Spatial regularization is imposed by a multivariate Gaussian prior on snapshots with a mean μ and covariance Λ that encourages spatial smoothness (see Equation 1.59 and Bouman *et al.* 2018). We examine the sensitivity of time-variable image features (e.g., position angle) to different settings in the `StarWarps` imaging algorithm by running surveys over different values of the spatial regularization covariance Λ and data weights of the visibility amplitude and log closure amplitude; we typically keep β_Q^{-1} and the mean image μ fixed and examine the sensitivity of our results to these parameters separately across different surveys. Unless specified otherwise, in this paper we set β_Q^{-1} to 5×10^{-6} (Jy/pixel)^2 and the prior mean μ and initialization image to an image of a uniform ring blurred by a 25 μas beam. These surveys result in distributions of the image features at each snapshot in time. For each of the measurements obtained from 54 parameter combinations, we draw 100 random samples from a normal distribution characterized by the image feature measurement and its associated error. These survey results are *not* posterior probability distributions, but they do provide a sense of the robustness of the sensitivity movie reconstructions to changes in the algorithm parameters.

[1] Frames are sometimes separated by more than 60 s due to the interval between scans.

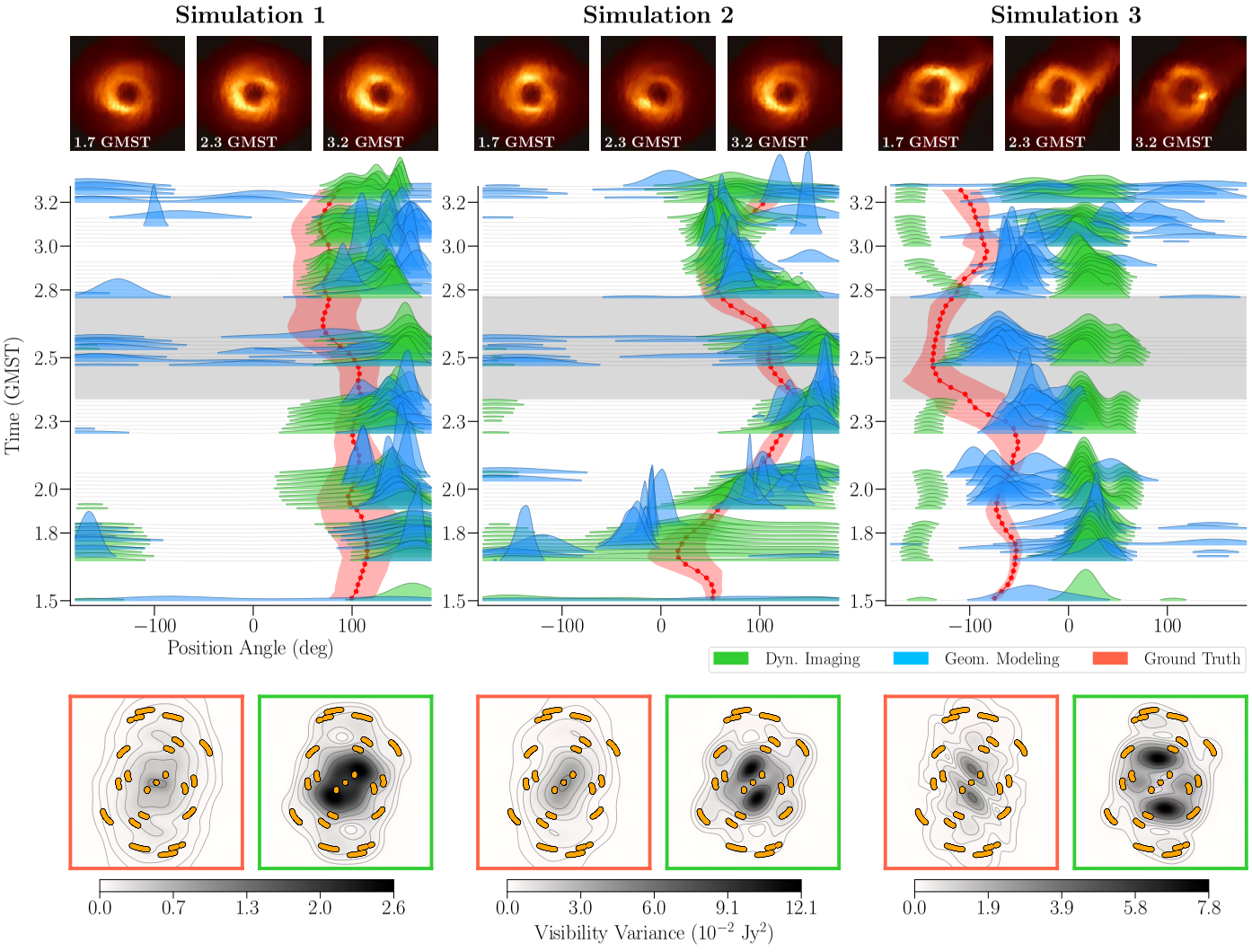
Simulation 1
Simulation 2
Simulation 3
1.7 GMST
2.3 GMST
3.2 GMST
Time (GMST)
Position Angle (deg)
Dyn. Imaging
Geom. Modeling
Ground Truth
Visibility Variance (10^{-2} Jy^2)

Figure 5.2: Position angle (PA) recovered from synthetic data from three different GRMHD simulations on April 7 EHT coverage during the dynamic analysis window using both `StarWarps` dynamic imaging and `DPI` snapshot geometric modeling techniques. (Top row) Ground truth GRMHD movie snapshots (including interstellar scattering) from each of the three simulations at 1.7, 2.3, and 3.2 GMST. (Middle row) Plots of PA vs time for the reconstructions compared with the simulation ground truth (in red). The shaded red region indicates the circular standard deviation of the ground truth PA computed using `REx` (refer to Section 8 of Event Horizon Telescope Collaboration *et al.,* 2022c and Chael, 2019). Modeling histograms (blue) correspond to actual marginal posterior distributions, whereas for `StarWarps` imaging the histograms represent the distribution of PAs and their associated uncertainties for a collection of movies reconstructed under different parameter settings. The gray band at roughly 2.6 GMST indicates the time period where the LMT dropped out of the observation. (Bottom row) Visibility variance in the (u, v) plane over the selected time window for the ground truth simulation movies (left, red) and the reconstruction (right, green). In Simulations 1 & 2, both dynamic imaging and snapshot geometric modeling methods are often able to correctly identify the PA of evolving GRMHD movies during this time window, but they show significant offsets from the correct PA in Simulation 3. From left to right, the maximum variance of the ground-truth (reconstructed) movie is 0.85 (2.62), 4.45 (12.07), and 3.94 (7.79) $\times 10^{-2}$ Jy^2. Contours start at 90% of the peak variance and decrease by successive factors of 2 until they reach 0.7%.

5.3.2 Geometric modeling

In our geometric modeling approach, a simple geometric model is fit to each 60 s snapshot *independently*, with no enforced correlations in time.[2] We consider several different m-ring models (Johnson *et al.,* 2020), described by infinitesimally thin rings with azimuthal brightness variations decomposed into Fourier modes, which are subsequently blurred with a circular Gaussian kernel. The complexity of an m-ring model depends on the maximum number of Fourier modes, m, that are added (e.g. $m = 1$ corresponds to a simple crescent). To model a central floor we include a Gaussian that is located at the center of the ring; the size and brightness of the Gaussian are additional model parameters.

For each m-ring model considered, we produce a multi-dimensional posterior using two modeling approaches. First, we consider a variational inference based approach, `DPI`, that fits to the log closure amplitudes and closure phases (Sun & Bouman, 2021; Sun *et al.,* 2022). Second, we consider a sampling based method, `Comrade` (Tiede, 2022)[3], which fits to visibility amplitudes and closure phases. `Comrade` uses the nested sampling package `dynesty` (Speagle, 2020) and the probabilistic programming language `Soss` (Scherrer & T. Zhao, 2020). The different data products used by `DPI` and `Comrade` imply different assumptions made about the telescope amplitude gains – they are unconstrained in `DPI`, while in `Comrade` the gain amplitudes are more constrained and are included as model parameters during fitting (see Event Horizon Telescope Collaboration *et al.,* 2022d). As a result of these different data products, `DPI`

[2] In the language of the temporal regularization parameter defined above, for geometric modeling $\beta_Q^{-1} \to \infty$.

[3] https://github.com/ptiede/Comrade.jl

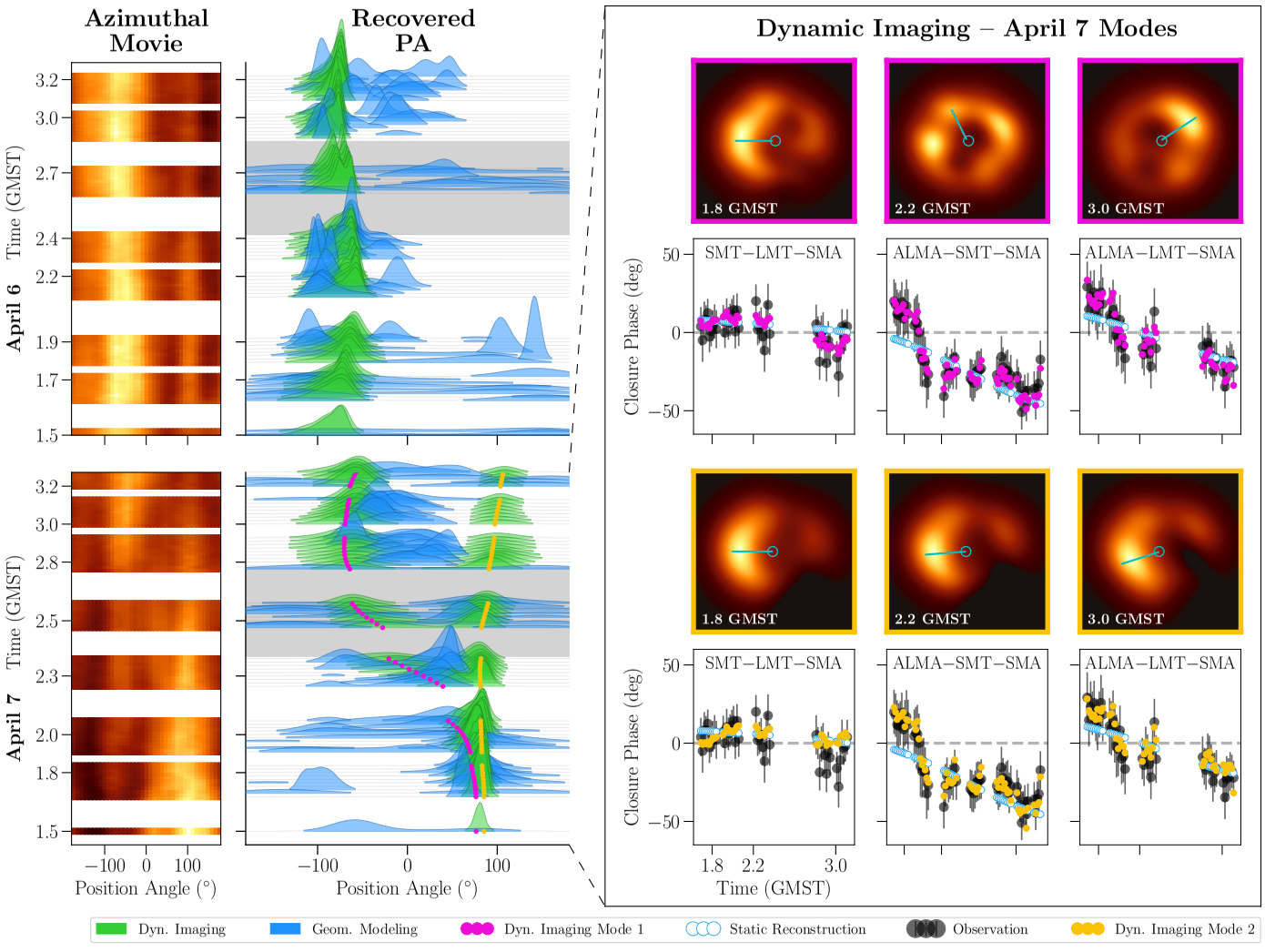
Azimuthal Movie
Recovered PA
April 6
April 7
Time (GMST)
Position Angle (°)
Dynamic Imaging – April 7 Modes
1.8 GMST
2.2 GMST
3.0 GMST
SMT−LMT−SMA
ALMA−SMT−SMA
ALMA−LMT−SMA
Closure Phase (deg)
Time (GMST)
Dyn. Imaging
Geom. Modeling
Dyn. Imaging Mode 1
Static Reconstruction
Observation
Dyn. Imaging Mode 2

Figure 5.3: (Left) Mean azimuthal brightness profiles from the `StarWarps` movie reconstructions, unwrapped around the ring as a function of time, and PA distributions obtained from dynamic imaging and snapshot geometric modeling reconstructions of EHT Sgr A* data on April 6 (top) and 7 (bottom) in the selected time window. Geometric modeling distributions are marginal PA posteriors from `DPI`. Imaging histograms represent the distribution of PAs and their associated uncertainties from a collection of `StarWarps` movies reconstructed under different parameter settings with the spatial prior mean μ and temporal regularization β_Q^{-1} held fixed (refer to Equation 1.59). Blank spaces indicate time regions without any data. The gray band at roughly 2.6 GMST indicates the region where the LMT dropped out and data coverage is poor. Both dynamic imaging and modeling appear to identify a nearly constant PA on April 6 but a variable PA over the same time window on April 7. In the reconstructions in this figure, both dynamic imaging and modeling make a prior assumption that the source morphology is ring-like; `StarWarps` imaging uses a prior/initialization image of a uniform ring, while geometric modeling uses a second order m-ring ($m = 2$) model. Both dynamic imaging and modeling recover "descattered" movies using the `J18model1` refractive noise model. (Right) Focus on the two modes reconstructed by `StarWarps` on April 7. For each mode, the top panels show three reconstructed snapshots at different times, and bottom panels compare the fitting of the corresponding reconstructed movie (magenta or yellow) and a representative static reconstruction from the `eht-imaging` static imaging pipeline (white) to the closure phase data measured by three key triangles. The dynamic reconstruction on the top (magenta) shows an evolving PA shift over the observation window. In contrast, the reconstruction on the bottom has a nearly constant PA of $\sim 100^\circ$ (yellow). In the selected closure phase plots (bottom rows), the measured data is averaged in 60 s snapshots and the error bars do not include a variability noise model. The static image visibilities (white) capture the general trend of the data, but they do not well fit variability in the closure phases. In contrast, both selected `StarWarps` dynamic reconstructions better fit the data on minute timescales. We find that the fit's behavior on the SMT-LMT-SMA triangle has a large influence on the resulting PA of the movie on April 7. A positive SMT-LMT-SMA closure value tends to result in a southeast PA ($\sim 100^\circ$) whereas a negative value results in a more northwest PA ($\sim -80^\circ$).

and `Comrade` produce slightly different posteriors. Details of the geometric modeling approaches are further explained in Event Horizon Telescope Collaboration *et al.* (2022d)[4].

5.3.3 Comparing dynamic imaging & modeling

Both dynamic imaging and modeling share a common goal of extracting time- and spatially-resolved structure in Sgr A* but there are key differences between the methods in how prior assumptions about the spatial and temporal variability are incorporated. `StarWarps` imaging allows for more freedom in the recovered spatial structure but assumes strong temporal regularization between frames. In contrast, snapshot geometric modeling is restricted to a parameterized set of spatial structures, but makes no assumptions on image correlations in time. Although snapshot geometric modeling

[4]Note that model fits in Event Horizon Telescope Collaboration *et al.* (2022d) use 120 s snapshots, while in this Chapter, we use 60 s snapshots.

cannot recover spatial structures outside of the m-ring model specifications, it allows for quantifying the uncertainty in m-ring model features (and their temporal variability) as it estimates full posterior distributions for the particular geometric model used.

5.3.4 Diagnostics

To characterize our dynamic reconstructions, we mostly investigate trends of the brightness position angle (PA; see Eq. 21 in Event Horizon Telescope Collaboration *et al.,* 2019d) with time. The PA is a simple and easily characterizable feature of the brightness distribution around an asymmetric ring. For `Starwarps` reconstructed movies, we extract the ring PA on the different snapshots using `REx`; in $m-$ring model fitting results, the PA is obtained directly from the fitted model as the argument of the first azimuthal Fourier mode.

5.3.5 Ring assumption

Many of the results in this section apply strong prior assumptions that Sgr A*'s underlying structure is ring-like, motivated by the ring morphology recovered in static image reconstructions using the full (u, v)-coverage (Section 7 in Event Horizon Telescope Collaboration *et al.,* 2022c). `StarWarps` reconstructions enforce a ring constraint by setting the mean prior image μ to a ring with $\approx 50\,\mu$as diameter and a width set by a circular Gaussian blurring kernel. In geometric modeling, the ring assumption is intrinsically imposed by the structure of the m-ring model. In Section 5.5.1 and in Section 5.A we explore the sensitivity of our results to the choice of mean image μ in `StarWarps`.

5.4 Synthetic Data Tests

Sparse snapshot (u, v)-coverage can lead to artifacts in both imaging and geometric modeling results. These artifacts appear in static imaging, but are further amplified in dynamic imaging due to the far-sparser coverage (Farah *et al.,* 2022). Thus, it is important to assess how the sparse (u, v)-coverage during the selected time window may affect the recovered results and whether it may introduce biases in recovered image features, particularly the position angle of ring-like images.

5.4.1 Static Crescents

In Section 5.A.3 we present synthetic data tests conducted to characterize the effect of the sparse snapshot EHT2017 (u, v)-coverage on PA recovery from static crescent images. These tests show that there are significant biases in the recovered PA from 60s snapshots when the brightness asymmetry of the ground truth ring image is low. When there is a strong asymmetry in the brightness distribution around the ring, however, the PA is accurately recovered even with 60 s snapshot (u, v)-coverage.

5.4.2 GRMHD Simulations

We explored how our methods perform in recovering time-varying position angles from three selected GRMHD simulation movies. We used three representative GRMHD movies from the GRMHD library presented in Event Horizon Telescope Collaboration *et al.* (2022e) [5] (see Section 5.2 in Event Horizon Telescope Collaboration *et al.,* 2022c). We generated visibility data from the three movies over the 100 min dynamic analysis window on April 7 using the same procedure described in Section 5 of Event Horizon Telescope Collaboration *et al.* (2022c), including atmospheric noise, telescope gain errors, and polarimetric leakage.

Figure 5.2 presents results obtained from both dynamic imaging and modeling reconstructions of these three synthetic data sets. The ground truth simulation PA evolution is recovered (with $\sim$30°) for the first two models (Simulation 1 & 2). However, there are several localized deviations in the recovered PA distributions from the ground truth in these models, especially when the the instantaneous (u, v)-coverage worsens (e.g. during the LMT dropout time region). For the third model (Simulation 3) both the dynamic imaging and modeling methods recover significant offset from the true PA. One potential cause of this offset is the prominent extended jet structure to the northwest of the ring in the SANE simulation. This extended structure cannot be captured in either the dynamic imaging or modeling methods due to their strong prior assumptions of a ring-like morphology.

In the bottom row of Figure 5.2, we investigate the complex variance of the Fourier transform of the reconstructed images across the selected time window for both the ground truth (scattered) movies and the reconstructions. We find that in all three cases the reconstructions tend to introduce more variability than is present in the ground truth. In Simulation 1 and 2 this excess variability does not prevent the reconstructions from qualitatively recovering the correct PA trend, but the PA results are not correctly recovered in Simulation 3.

These results indicate that although we often recover the PA accurately from some realistic synthetic GRMHD data sets, we should remain cautious when interpreting Sgr A* dynamic results. Our methods sometimes incorrectly recover the PA, especially if extended structure is present that is not captured by the prior assumptions on the source structure made by the dynamic imaging and modeling methods. In addition to effects from extended structure, there may be additional uncharacterized systematic uncertainty from prior assumptions in the reconstructions in these results derived from extremely sparse snapshot Sgr A* coverage.

[5] Simulation 1 & 2 is using a MAD GRMHD model with parameters $a_* = 0$, $i = 10$, $R_{\rm high} = 10$. Simulation 3 is using a SANE GRMHD model with $a_* = -0.94$, $i = 50$, $R_{\rm high} = 160$.

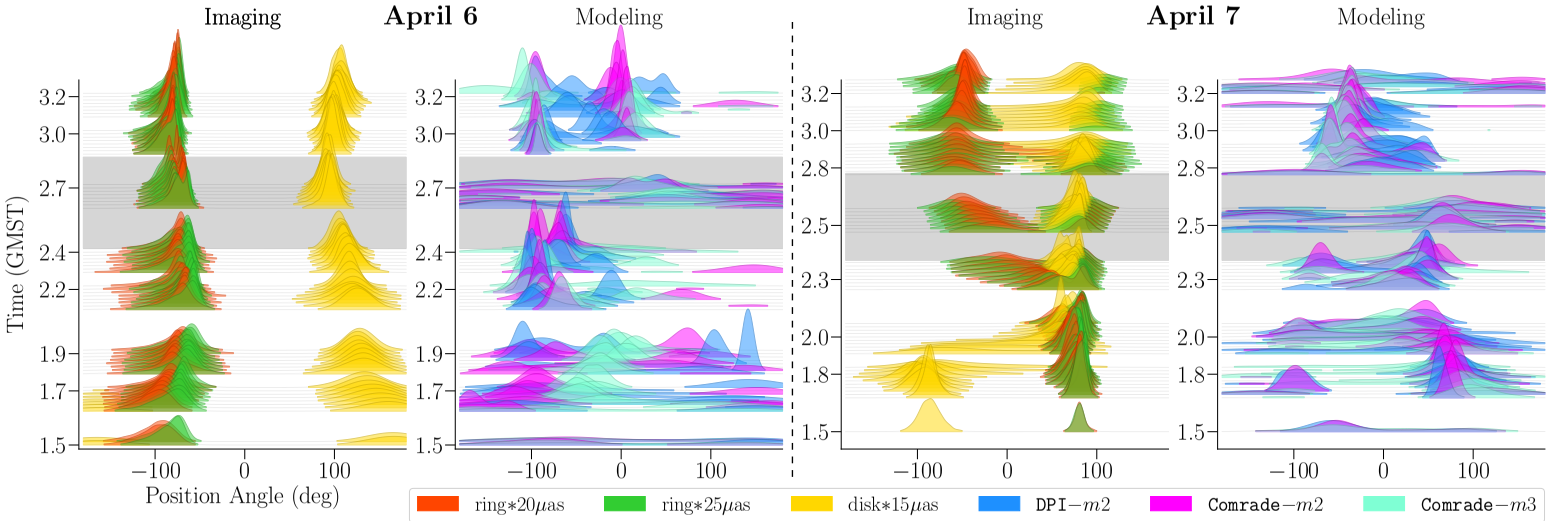

Figure 5.4: The PA for the 2017 Sgr A* data recovered using dynamic imaging and geometric modeling techniques under different assumptions. `StarWarps` imaging results were obtained using a spatial prior image set to either a uniform ring convolved with a circular Gaussian kernel with FWHM of 20 or 25 μas (see Figure 7 of Event Horizon Telescope Collaboration *et al.*, 2022c), or a uniform disk blurred with a kernel with FWHM of 15 μas. Descattered modeling results were obtained from geometric models with increasing complexity (m-ring 2 vs m-ring 3) and different fitting software packages (`DPI` vs `Comrade`). All results were obtained from low-band data on April 6 and 7 that has been descattered with a `J18model1` refractive noise floor. The gray band at roughly 2.6 GMST indicates the region where the LMT has dropped out and data coverage is poor.

5.5 Sgr A* Spatiotemporal Characterization and Uncertainty

Here we present results of our analysis on Sgr A*'s spatially resolved temporal variability on minute timescales on April 6 and 7, using both dynamic imaging and snapshot geometric modeling methods. In Figure 5.3, we show detailed results for the Sgr A* PA evolution and data fits reconstructed using a restricted range of dynamic imaging and modeling parameters. In Figure 5.4 we show PA results obtained under a broader range of parameter settings.

In general, we find that snapshot geometric modeling results performed under different m-ring orders, scattering mitigation strategies, and modeling codes produce fairly consistent results. The modeling results show broad posteriors of PA at each 60 s snapshot but still indicate significant differences between April 6 and 7 and between the first and second halves of the 100 min window on April 7. In rough terms, the PA on April 6 is centered around $\sim -50°$, with some scatter around this value over the time window. In contrast, on April 7 the modeling results show PA posteriors that are initially centered around $\sim 90°$ and then shift to values centered around $\sim -50°$ in the second half of the time window.

Compared to snapshot geometric modeling, dynamic imaging allows for more freedom in spatial and temporal regularization, and as a result is more sensitive to parameter choices. Dynamic imaging results can produce movies that reproduce the PA trends on April 6 and 7 recovered by snapshot modeling. These PA trends – a stable PA on April 6 and a shifting PA on April 7 – are predominantly seen in dynamic imaging reconstructions with low temporal regularization and ring-like spatial priors. Geometric modeling makes similar assumptions, imposing no temporal regularization and enforcing ring structure in the form of the model. In Figure 5.3, we directly compare dynamic modeling and imaging results under these strong assumptions.

Even in the limited space of dynamic imaging reconstructions conducted with weak temporal regularization and ring-like mean prior images, the imaging results are sensitive to other hyperparameters. In particular Figure 5.3 indicates that we recover two modes of position angle evolution on April 7 even with the mean prior image and temporal regularization level fixed. We present representative snapshots and fit to the closure phase data from these two modes in the right panels of Figure 5.3.

When the ring-like mean image prior is changed or the weak temporal regularization is increased in `StarWarps` dynamic imaging, significantly different PA variations can be recovered from the same data. In Figure 5.4, we show that when the ring assumption is relaxed and a disk prior is used in reconstruction, `StarWarps` results show drastically different PA trend over time. In particular, in reconstructions initialized with a disk prior, the PA curves on April 6 and 7 appear to be flipped by $180°$ (i.e., on April 7 the PA transitions from $\sim 90°$ to $\sim -50°$). We further show in Figure 5.5 that when using stronger temporal regularization in the `StarWarps` dynamic imaging, the PA stays constant, eliminating the shift from positive to negative PA trend on April 7. We discuss these tests further in the Section 5.5.1 and Section 5.A.5.

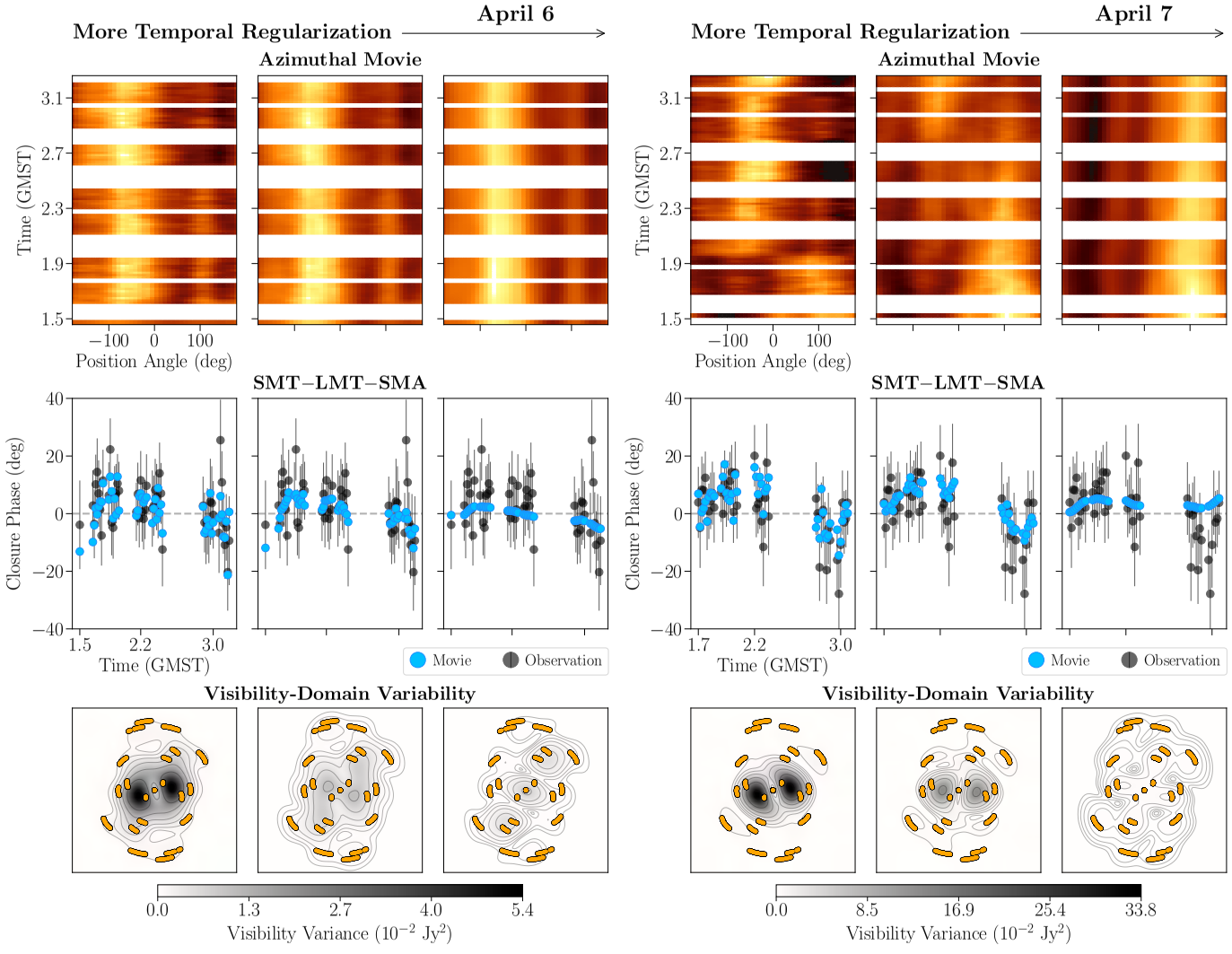
April 6
More Temporal Regularization
Azimuthal Movie
Time (GMST)
Position Angle (deg)
SMT−LMT−SMA
Closure Phase (deg)
Time (GMST)
Movie
Observation
Visibility-Domain Variability
Visibility Variance (10^{-2} Jy^2)
April 7
More Temporal Regularization
Azimuthal Movie
Time (GMST)
Position Angle (deg)
SMT−LMT−SMA
Closure Phase (deg)
Time (GMST)
Movie
Observation
Visibility-Domain Variability
Visibility Variance (10^{-2} Jy^2)

Figure 5.5: Comparing the effect of temporal regularization on the reconstructed `StarWarps` movies for April 6 and 7. The temporal regularization strength is increased from left to right ($\beta_Q^{-1} = 5 \times 10^{-4}$, 5×10^{-6}, and 5×10^{-8} (Jy/pixel)^2). For each value of β_Q^{-1}, we show the mean unwrapped movie around the ring (top), the mean closure phase values on the triangle SMT-LMT-SMA (middle), and the variance of the complex visibilities across the (u, v) plane (bottom). As temporal regularization is increased the recovered movies become more static, and the degree of (u, v) plane variability decreases. From weak to strong regularization, the maximum variance of the reconstructed movie is 5.37, 1.11, and 0.73 $\times 10^{-2}$ Jy^2 on April 6, and 33.81, 13.24, and 0.50 $\times 10^{-2}$ Jy^2 on April 7. Contours start at 90% of the peak variance and decrease by successive factors of 2 until they reach 0.7%. For comparison, the variance in the light curve over this interval is $\sim 0.5 \times 10^{-2}$Jy^2. Thus, the leftmost reconstruction with the weakest temporal regularization produces a movie with visibility variance substantially exceeding the light curve variance due to overfitting to the thermal noise.

Note that April 6 and 7 have nearly identical (u, v)-coverage during the selected 100 min region of time. We can thus compare the results obtained over these two days to help disentangle effects of (u, v)-coverage from any effects due to intrinsic evolution. If the PA trends that we recover are due primarily to biases from the (u, v)-coverage, we would expect to recover the same PA trends on both days. However, we consistently see different PA trends with time using the same parameter settings in both dynamic imaging and modeling methods. This implies that differences in the visibilities, not the (u, v)-coverage, drive differences in the PA evolution we see on the two nights in some reconstructions, but it does not help select among any of the different reconstruction modes on either day.

5.5.1 Effect of Model and Imaging Choices

The PA evolution recovered with dynamic imaging and modeling methods is sensitive to choices made in the imaging and modeling procedures that enforce constraints on the spatial and temporal structure of the reconstructions. Enforcing strong spatial or temporal priors will suppress any structural variability while adding too much flexibility in a model with sparse data constraints will lead to overfitting or uninformative posteriors. In Section 5.A.5 we present in detail several tests of these choices for both imaging and modeling methods; here, we highlight the most important results.

5.5.1.1 Spatial Priors

Constraints on the spatial structure are enforced via the m-ring order in geometric model fitting and via the choice of mean image prior in dynamic imaging. To test the effects of different mean prior images in `StarWarps`, we produced reconstructions using uniform ring priors with increasing widths (from convolution of the ring described in Section 5 of Event Horizon Telescope Collaboration *et al.,* 2022c with circular beams of 11, 15, 20, and 25 μas FWHM). We also used a tapered disk with diameter $\sim$ 74 μas (see Figure 7 of Event Horizon Telescope Collaboration *et al.,* 2022c) as a prior that does not feature any central dip. We discuss the details of these prior choices

in Section 5.A.5.1. For geometric modeling, we tested ring-like models of increasing complexity in their azimuthal brightness distribution, from crescent models ($m = 1$) to higher order m-rings. When fitting m-rings to Sgr A* snapshot data, we explored m from 1 to 4 and selected the order to use based on the Bayesian evidence across all data sets – settling on $m = 2$ (see Section 5.A.5.2).

Figure 5.4 shows histograms of the dynamic imaging PA results made using different mean prior images and PA posterior distributions from geometric modeling results from different $m-$ring orders. We also compare modeling results from two different modeling codes in Figure 5.4. The reconstructed PA trends are fairly consistent on both days among the different m-ring orders in geometric model fitting. In `StarWarps` imaging, reconstructions using ring-like mean prior images of several different thicknesses produce similar trends, with a stable PA on April 6 and a PA transition from positive to negative values on April 7. However, when a disk prior is used in `StarWarps` the PA trends of both April 6 and 7 change drastically and appear to be flipped by $180°$. Figure 5.12 in Section 5.A shows image snapshots and data fits for `StarWarps` reconstructions with both disk and ring mean prior images. Note that although the position angle evolution is different than the movie reconstructed using a ring prior, the movie reconstructed with a disk prior still results in a ring-like structure, though with a less prominent central brightness depression.

5.5.1.2 Temporal Regularization

Geometric modeling enforces no correlations in between temporal snapshots, while dynamic imaging can enforce correlations via temporal regularization. Figure 5.5 shows that when using stronger temporal regularization in `StarWarps` (lower values of β_Q^{-1}) the PA becomes constant in time on both April 6 and 7 – a result of the method enforcing strong continuity between frames. Note that in the case of high temporal regularization, the SMT-LMT-SMA closure triangle fits in the second half of the time window on April 7 appear offset with respect to the data, although still within two standard deviations of most data points.

We also show that reconstructions with low levels of temporal regularization produce prominent variance in the model visibilities plane at (u, v) points that are not sampled by our coverage during this time window[6]. In contrast, reconstructions with more temporal regularization lower the overall variance of model visibilities everywhere in the Fourier plane and place the peaks in the variance maps at (u, v) points sampled by the EHT. We discuss the interpretation of the different temporal regularization values β_Q^{-1} used here in Section 5.A.2 and further tests of the `StarWarps` temporal regularization further in Section 5.A.5.1.

5.5.1.3 Scattering

Another choice made in both dynamic imaging and modeling procedures common to both static and dynamic reconstruction methods is the strategy for mitigating the

[6] As shown in the GRMHD synthetic data tests, it is not necessary that the peaks in the (u, v)-plane variability map align with measured data points to correctly identify PA evolution.

effects of interstellar scattering in Sgr A* data. We investigate the effects of the same five prescriptions for scattering mitigation we use in static imaging on the dynamic reconstructions in Section 5.A.4. In general, we find that choices made in the scattering mitigation procedure contribute less to our overall uncertainty than choices related to the spatial prior or temporal regularization.

5.6 Sgr A* Dynamic Property Conclusions

Our aim in this chapter has been to use the 2017 EHT data to explore the spatially-resolved dynamics of Sgr A* on minute timescales. First, we identified the time windows with the best (u, v)-coverage during the observation run – a roughly 100 min window on April 6 and 7. We identify a significant difference between the closure phases on April 6 and 7, signifying that the underlying structure is different on the two days. We reconstruct movies from this small slice of the EHT data using dynamic imaging and geometric snapshot modeling methods. We track the average position angle (PA) in our dynamic imaging and modeling results as a way of following a specific, dynamic, and measurable aspect of the source over time. We find that we are able to recover the PA in synthetic EHT data from some GRMHD simulation movies; however, there are prominent cases when this is not the case and both geometric modeling and dynamic imaging methods recover biased results.

On April 6, most dynamic imaging and modeling results show a stable PA in the Sgr A* images over the selected window. In contrast, the recovered PA evolution on April 7 is more dependent on prior assumptions on the spatial structure and temporal regularization. On April 7, when using a ring image as a spatial prior and weak temporal regularization, dynamic imaging results largely align with geometric modeling results and show an evolution in the PA of $\sim 140^\circ$ over the ~ 100 min window. However, we also see several other PA trends in the dynamic imaging results, including a PA evolution in the opposite direction and modes where the PA is static on both days.

These results, along with our synthetic data tests, show that while the 230 GHz image of Sgr A* may exhibit interesting and measurable dynamics, our current methods cannot conclusively determine the PA evolution of Sgr A*. Dynamic reconstructions of Sgr A* with the 2017 EHT's coverage should thus be interpreted with caution. This analysis provides a promising starting point for further studies of the evolution seen in Sgr A* with future EHT observations with denser (u, v)-coverage.

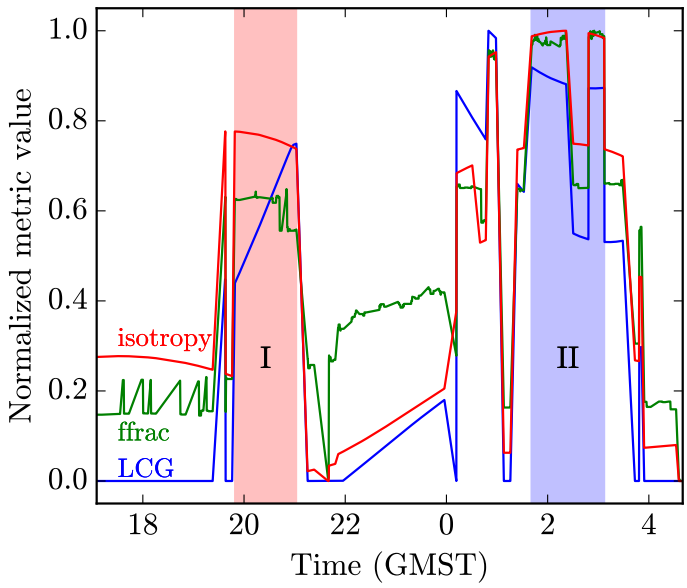

Figure 5.6: Normalized metric computations for every scan of the April 7, 2017 EHT coverage of Sgr A*. 0:00 GMST marks the day change from April 7 to April 8. Though the metrics have different considerations, all highlight the region (labelled "II") from ∼1:30 GMST to ∼3:10 GMST as a candidate region for dynamic imaging.

5.A Dynamic Imaging and Snapshot Model Fitting tests

5.A.1 Selection of Time Windows with the Best (u, v)-coverage

Farah *et al.* (2022) demonstrates that the changing (u, v)-coverage created by the Earth's rotation during the aperture synthesis process leads to regions of time that produce dynamic reconstructions of varying quality. The quality of a short-timescale reconstruction is partially determined by the snapshot (u, v)-coverage geometry, which introduces certain artifacts during the imaging process.

The scale and severity of these artifacts can be predicted by quantitatively scoring the (u, v)-coverage as a function of time, which can be done in a number of ways. Some metrics examine how much of the Fourier plane is covered by an interferometer (e.g., Palumbo *et al.,* 2019), while others look at gaps created by the sparse coverage (e.g., Wielgus *et al.,* 2020). In addition to these metrics, Farah *et al.* (2022) derives a novel metric that probes both the anisotropy and radial homogeneity of the coverage.

By applying these metrics to the April 6 and 7 EHT (u, v)-coverage on Sgr A*, we can assess the scan-by-scan performance and identify regions of time which are likely to produce the best reconstructions, independent of the underlying source structure. The result of such an analysis for April 7 is shown in Figure 5.6, and two candidate regions are highlighted. The metrics predict dynamic imaging reconstructions will have the highest quality in the region from 1.5-3.2 GMST (Region II); the reconstructions will produce substantially worse results in the region from 19.4-21 GMST (Region I). We validate this prediction by testing on high *S/N* data in Farah *et al.* (2022) and show that Region II indeed allows for significantly better recovery of the source

variability than Region I. Therefore, based only on the EHT's (u, v)-coverage, we focus on dynamic imaging/modeling Region II throughout this Chapter.

5.A.2 Starwarps Temporal Regularizer Normalization

Temporal regularization in `StarWarps` is controlled by a parameter β_Q^{-1}. This parameter corresponds to the variance of the conditional distribution of pixel intensities for a given snapshot holding the previous snapshot fixed: $p(I_k|I_{k-1}) = \mathcal{N}(I_{k-1}, \beta_Q^{-1}\mathbb{1})$. The units of β_Q^{-1} are $(\text{Jy/pixel})^2$. In the main text, we consider values $\beta_Q^{-1} \in \{5 \times 10^{-4}, 5 \times 10^{-6}, 5 \times 10^{-8}\}$. Larger values of β_Q^{-1} correspond to less temporal regularization, as the conditional distribution $p(I_k|I_{k-1})$ becomes wider.

We can also interpret the values β_Q^{-1} in visibility space. The Fourier transform of the image I_k is given by a $N_{\text{pix}} \times N_{\text{pix}}$ matrix $\mathbf{F}$:

$$V_k = \mathbf{F} I_k. \tag{5.1}$$

In our convention, the pixel values in I_k have units Jy/pixel, so the entries of $\mathbf{F}$ are pure phase terms without a $1/\sqrt{N}$ normalization (so that, for instance, the zero-baseline visibility in Jy is just the sum of the pixel intensities). As a result $\mathbf{F}\mathbf{F}^\dagger = N_{\text{pix}}\mathbb{1}$. Because Equation 5.1 is a linear transformation, $p(V_k|I_{k-1})$ is also a normal distribution, with a mean V_{k-1} and a covariance:

$$\mathbf{\Sigma} = \mathbf{F}\left[\beta_Q^{-1}\mathbb{1}\right]\mathbf{F}^\dagger = \beta_Q^{-1} N_{\text{pix}}\mathbb{1}. \tag{5.2}$$

Thus, $\sigma_{\text{vis}} \equiv \sqrt{\beta_Q^{-1} N_{\text{pix}}}$ is the standard deviation of a snapshot visibility measurement in `StarWarps`, holding the previous frame fixed.

In Figure 5.7, we compare this quantity to the measured EHT visibility amplitudes in the selected dynamic imaging window on April 11. The `StarWarps` movie reconstructions in the main text have $N_{\text{pix}} = 40 \times 40 = 1600$. GRMHD simulations (see Event Horizon Telescope Collaboration *et al.,* 2022d and Georgiev *et al.,* 2022) and the light curve of Sgr A* (see Wielgus *et al.,* 2022) suggest that the variations on minute timescales should have a zero-baseline standard deviation of $\sigma_{\text{vis}} \sim 10\,\text{mJy}$. Thus, reconstructions with $\beta_Q^{-1} \sim 10^{-7}(\text{Jy/pixel})^2$ are expected to give variability that is consistent with what is measured in Sgr A*.

Larger values of β_Q^{-1} correspond to lower temporal regularization and allow for larger variations in the visibility amplitudes. For instance, the reconstructions presented in this Chapter with $\beta_Q^{-1} = 5 \times 10^{-6}$ permit somewhat more variability than is seen in simulations and observations of Sgr A*. Nevertheless, we have also found that allowing excess variability helps to trace evolution in tests on synthetic data from GRMHD simulations.

5.A.3 Testing (u, v)-coverage Effects

As discussed in Section 5.3, the geometry of the (u, v)-coverage can have an effect on the recovered image structure, especially in cases where the coverage is extremely

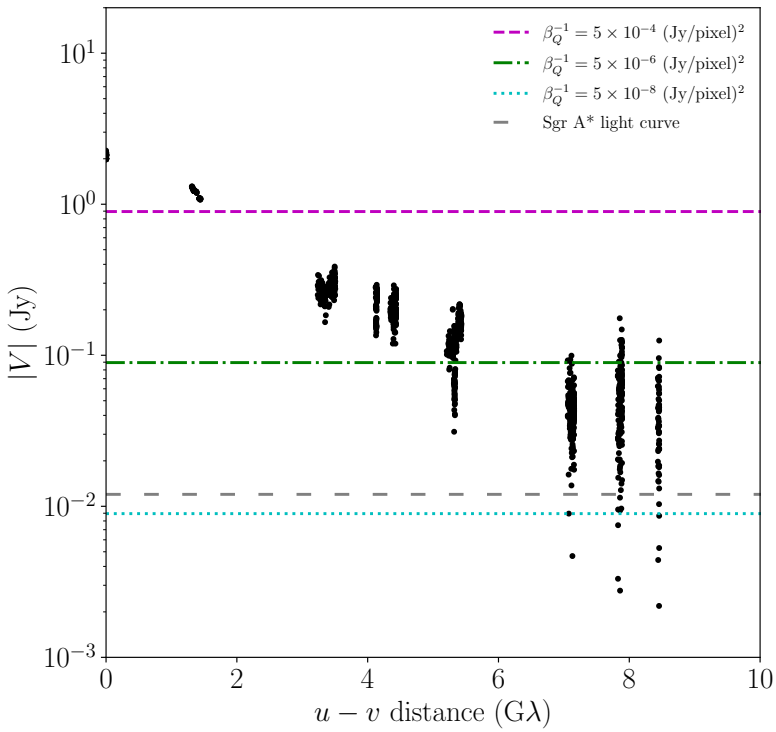

Figure 5.7: April 7 EHT visibility amplitudes over the selected window for dynamic imaging and modeling (black points). The horizontal lines show the expected standard deviation of the visibility amplitudes in `StarWarps` reconstructions for different values of β_Q^{-1} in units of (Jy/pixel)^2: 5×10^{-4} (magenta), 5×10^{-6} (green), and 5×10^{-8} (cyan). The gray dashed line shows the estimated variability level from the structure function of the ALMA light curve on 60 s time scales (Wielgus *et al.,* 2022).

sparse. To study the effects of (u, v)-coverage on dynamic fits to Sgr A* data, we perform a number of tests on synthetic data sets and study the effect of different (u, v) baselines on fits to the real data.

5.A.3.1 Recovering the Position Angle of a Static Crescent

As most of our analysis of the dynamic structure of Sgr A* revolves around tracking the position angle (PA) of brightness around the ring, it is important to assess our ability to recover the PA accurately in realistic synthetic data. To that end, we constructed synthetic EHT data sets from 4 static crescent models with peak brightness points rotated at 60° increments around the ring. The brightness ratio of each crescent model was chosen to roughly match the 1.5:1 ratio recovered from geometric model fitting to Sgr A* data. Figure 5.8 shows the imaging and geometric modeling results obtained by fitting to these synthetic data sets in the selected 1.7 h region. Note that, for both approaches, the true PA is recovered as the primary mode for most of the crescents. The imaging methods contain temporal regularization, which likely makes it easier to

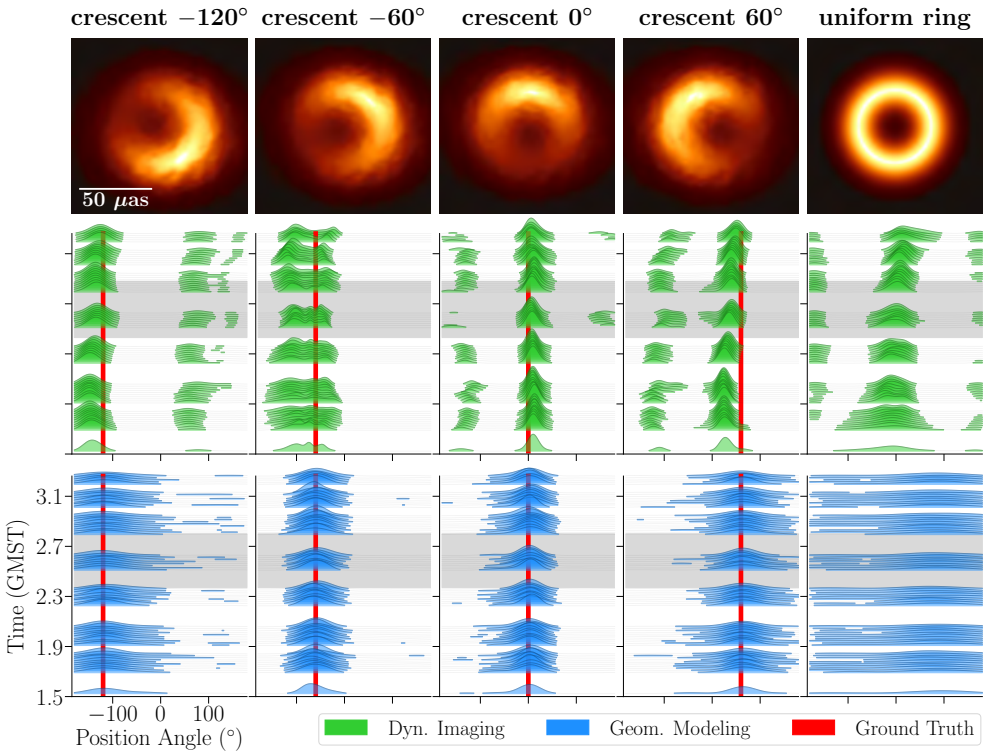

Figure 5.8: Position angle (PA) recovered from differently oriented static crescents synthetic data sets and a uniform ring synthetic data set, using both dynamic imaging (green) and geometric modeling (blue) techniques. The crescents' ground truth PA is shown as a vertical red line. Imaging uses a prior image μ of a uniform ring convolved with a 25 μas beam.

recover a static underlying structure; however, the geometric modeling results do not assume any temporal regularization.

5.A.3.2 Uniform Ring Synthetic Data

The interplay between the source size and sidelobes in the dirty beam pattern from sparse coverage can cause imaging artifacts that appear in the form of bright "knots" around ring sources. Computing the dirty image of an underlying uniform ring source reveals the location of these knots when using calibrated visibilities. To assess the impact of these knot artifacts on our analysis we performed imaging and geometric model fitting on data generated from a uniform ring (with no brightness changes in azimuth) with diameter of 49 μas (refer to the uniform ring in Figure 7 of Event Horizon Telescope Collaboration *et al.,* 2022c). As can be seen in Figure 5.8, both the imaging and modeling results result in an image structure with a preferred PA – $\sim 0°$ or $\sim 90°$ for imaging and $\sim 100°$ for modeling. However, the associated asymmetry of the recovered uniform ring is very low, a brightness ratio of less than 1.1:1 compared to 1.5:1 for Sgr A*. Thus, in combination with the results of Section 5.A.3.1, we

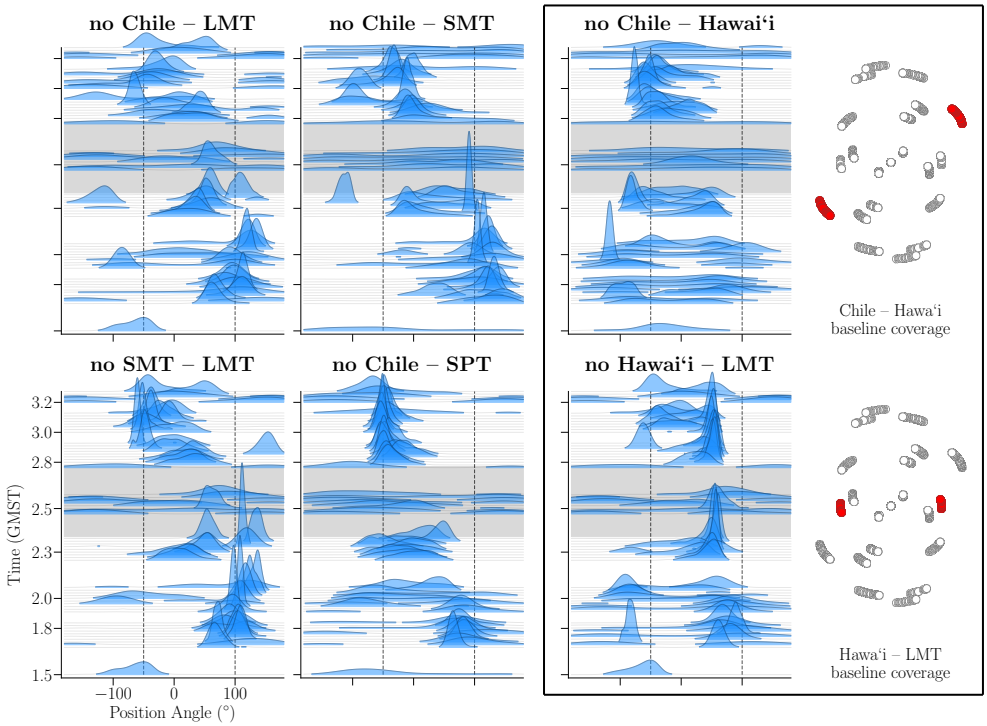

Figure 5.9: Position angle (PA) recovered using `DPI` geometric modeling after removal of a particular baseline from Sgr A* data on April 7. The flagged baseline appears in the title of each panel. The Chile-Hawai'i and Hawai'i-LMT baselines are highlighted and their location in the (u, v) plane is shown. These two baselines probe the east–west and southeast–northwest orientations.

conclude that although the (u, v)-coverage will bias the PA in the limit of low image asymmetry, for the level of image asymmetry recovered in Sgr A* this bias should have a small effect.

5.A.3.3 Baseline Test

In order to evaluate the contribution of each baseline to the recovered evolution in Sgr A*, we compared results obtained on data sets modified to remove a particular baseline. In particular, we compared the PA posteriors obtained using geometric modeling on 11 different data sets – 10 data set each with a single baselines removed and one complete data set. As can be seen in Figure 5.9, we find that most baselines do not heavily affect the trends we see on April 7. However, there are two baselines that appear to have a significant effect on the results: Chile–Hawai'i and LMT–Hawai'i. Without the Chile–Hawai'i baseline we are not able to discriminate between the northwest and southeast PA; without the LMT–Hawai'i baseline we do not recover as significant of a PA shift. Upon inspecting the (u, v)-coverage of these baselines it becomes apparent that these two baselines probe the northwest to southeast

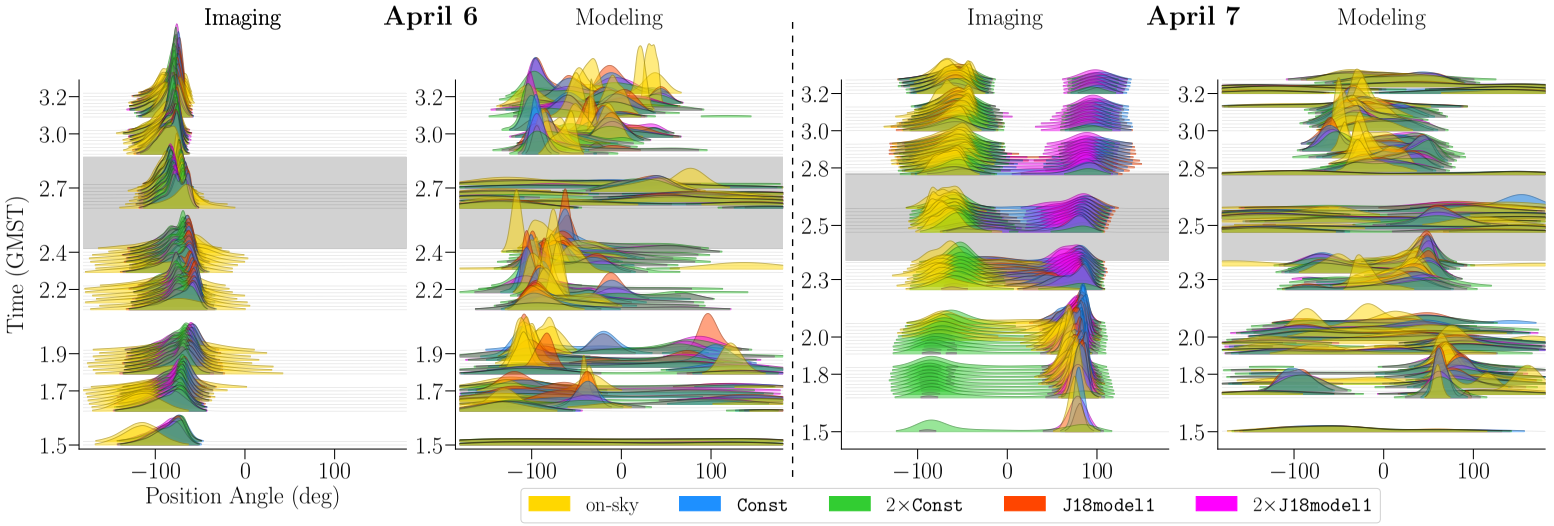

Figure 5.10: The position angle (PA) recovered using dynamic imaging and geometric modeling techniques under different scattering mitigation assumptions. These range from no scattering mitigation whatsoever (yellow), to different amounts of refractive noise added to the deblurred data: a constant noise floor (blue), the refractive noise model `J18model1` (red), and these two scaled by a factor of two (green and magenta, respectively). Imaging results were obtained using an initialization/prior image of a uniform ring blurred with a Gaussian kernel with FWHM of 25 μas. Modeling results were obtained from the `DPI` pipeline using the m-ring 2 geometric model. The gray band at roughly 2.6 GMST indicates the region where the LMT has dropped out and data coverage is poorer.

orientations that we are interested in, and thus without them we are unable to properly discriminate between these two PA orientations. It is also worth noting that removal of the Chile-SPT baseline appears to “clean up" the modeling results, suggesting that small-scale features probed by this baseline may not be properly captured in our geometric model fits.

5.A.4 Testing Scattering Mitigation Strategies

In producing dynamic reconstructions and model fits of the Sgr A* data, the choice of scattering mitigation strategy is a potential source of uncertainty. We have explored the sensitivity of our dynamic imaging and snapshot model fitting results to the same five scattering mitigation strategies we consider in the static image surveys in Section 6 and Section 7.5.2. of Event Horizon Telescope Collaboration *et al.* (2022c). Namely, we produce reconstructions and model fits to the unmodified data (i.e., on-sky with no descattering), as well as with visibilities deblurred by the Sgr A* diffractive scattering kernel and with the thermal noise error bars inflated by four models of the refractive noise: the `Const` model, the `J18model1` model, and then double the additional error tolerance from each of these models (2×`Const`, 2×`J18model1`). Based on the analysis done in Section 3.1 of Event Horizon Telescope Collaboration *et al.* (2022c), this selection is conservative and spans our uncertainty in Sgr A*'s refractive noise.

Figure 5.10 presents comparisons of the `StarWarps` reconstructions and snapshot model fitting results on the April 6 and 7 Sgr A* data with all five scattering mitigation strategies. We find that the general trends in the ring position angle we discuss in Section 5.5 are not significantly changed by any of the five scattering mitigation strategies we explore for geometric modeling, although the position angle posteriors are significantly broader (sometimes spanning a full 360°) when using the larger refractive noise budgets of 2×`Const` and 2×`J18model1`. In contrast, for imaging, on April 7, we observe a transition from positive to negative PA to be the most commonly recovered trend with all of the on-sky, `Const` and `J18model1` scattering mitigation strategies when using a ring prior. However, when we add a very large amount of refractive noise tolerance to the error bars in the 2×`Const` and 2×`J18model1` models, the PA becomes more stable over the observation window. This is due to the interplay of temporal regularization with an increased flexibility in fitting the data with a static model due to the expanded noise budget. In this figure, imaging with `StarWarps` makes use of the ring⋆25μas ring prior/initialization and modeling with `DPI` uses a second order m-ring ($m = 2$) model with a parameterized central Gaussian floor.

5.A.5 Testing the Effects of Different Imaging Priors and Model Specifications

As overviewed in Section 5.5.1, the recovered PA of the azimuthal brightness distribution in the ring-like morphology of Sgr A* is sensitive to the modeling choices made in both imaging and geometric modeling. In this section we go into further detail on some of the effects seen.

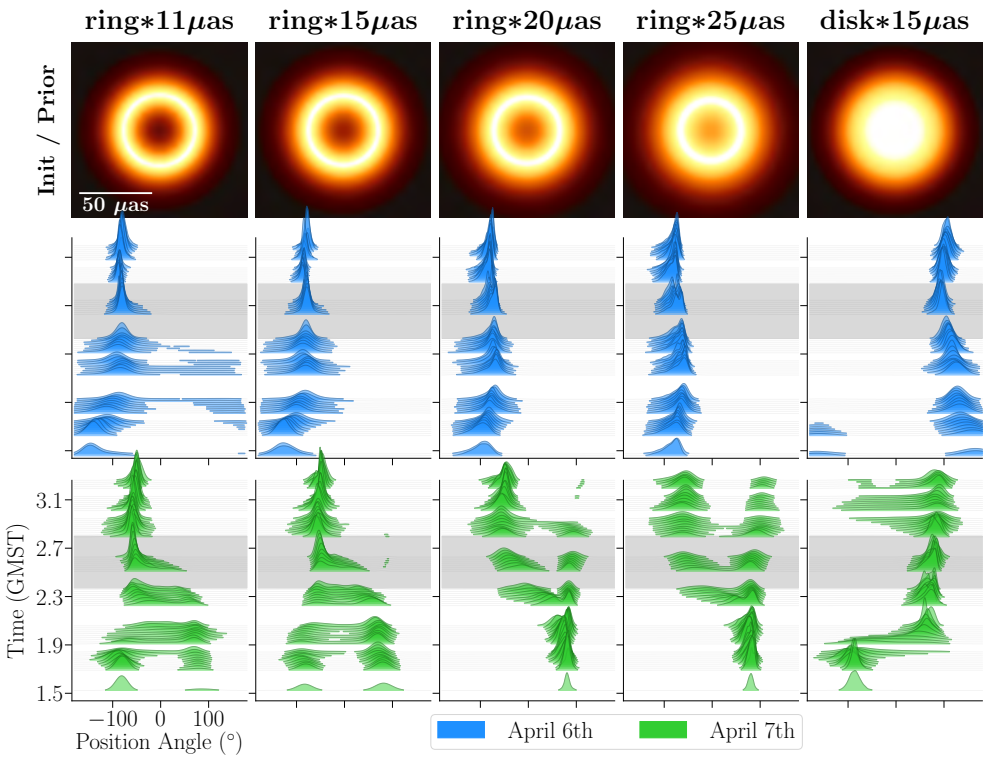

Figure 5.11: Position angle (PA) reconstructed using `StarWarps` under different init/prior assumptions for both April 6 (blue) and 7 (green). These include uniform rings with increasing Gaussian blurring and a uniform disk with no central brightness depression.

5.A.5.1 Imaging

Temporal regularization The level of continuity enforced between recovered frames is controlled by temporal regularization. In particular, `StarWarps` encourages frames to be similar by probabilistically modeling each frame I_k as being a sample from a normal distribution with mean I_{k-1} and covariance $\beta_Q^{-1}\mathbb{1}$ (see Equation 1.59). Thus, decreasing the multiplier β_Q^{-1} will increase recovered continuity between frames. This is seen, as expected, in the recovered movies of Sgr A* visualized in Figure 5.5; recovered movies with low temporal regularization experience fast and drastic variability on large scale features, while movies with high temporal regularization experience slow yet steady variability on large-scale features and absorb the remaining variability in the data with small scale fluctuations. Due to the extreme sparsity of data on each snapshot, although these movies contain significantly different levels of recovered variability, they all fit the data in terms of χ^2 fairly well. The only substantial difference between data fits can be seen when inspecting the SMT-LMT-Hawai'i closure triangle. It is worth noting that the positive to negative flip on the April 7's closure triangle is not reproduced by the recovered video with high temporal regularization. Nonetheless, since all movies still match all remaining baselines indistinguishably well it is difficult

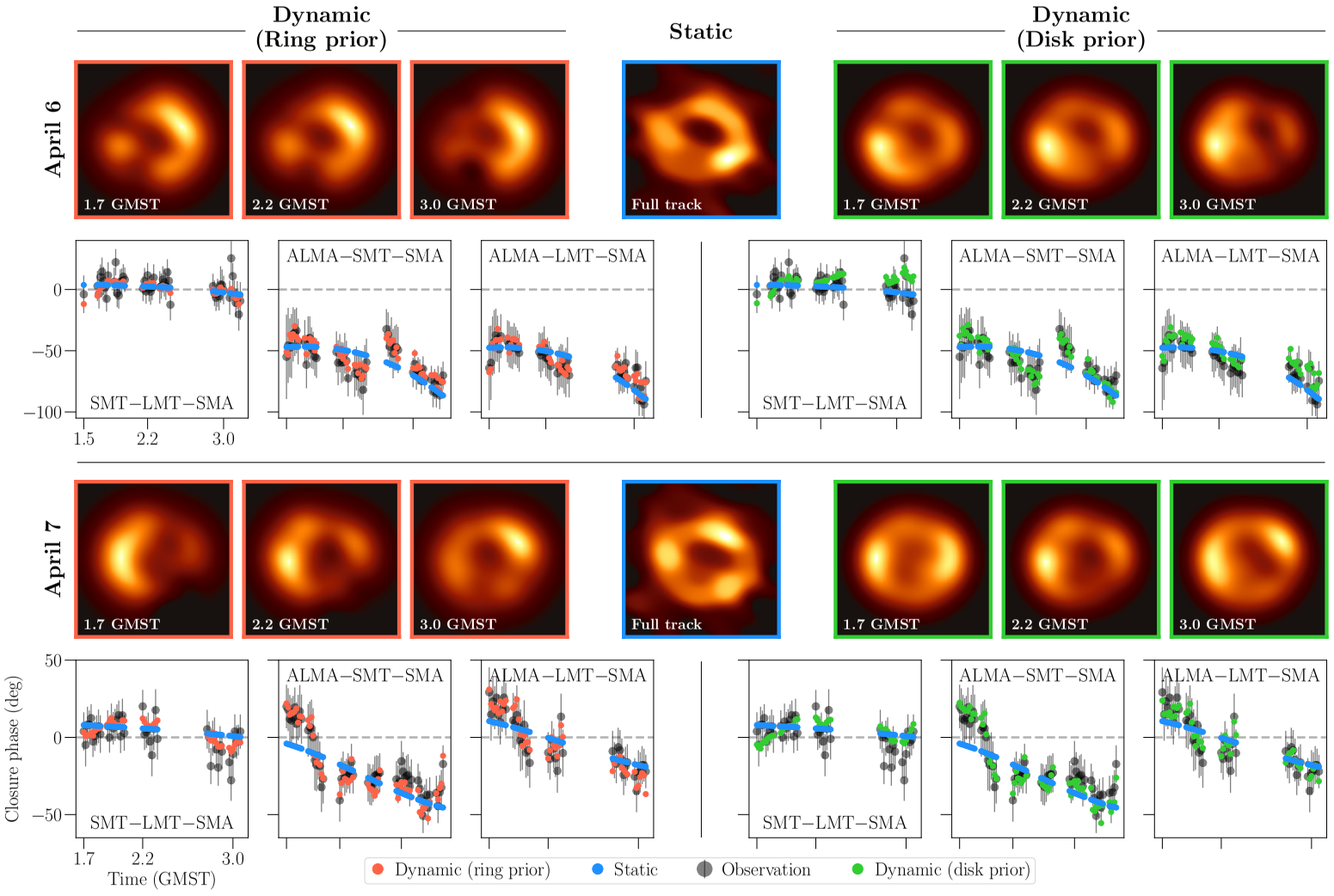
Dynamic (Ring prior)
Static
Dynamic (Disk prior)
April 6
April 7
1.7 GMST
2.2 GMST
3.0 GMST
Full track
ALMA−SMT−SMA
ALMA−LMT−SMA
SMT−LMT−SMA
Closure phase (deg)
Time (GMST)
Dynamic (ring prior)
Static
Observation
Dynamic (disk prior)

Figure 5.12: Comparing data fit of descattered dynamic imaging versus static imaging on April 7. A representative descattered image from the `eht-imaging` static imaging pipeline is shown. In the selected closure plots below the measured data (60 s averaging without a variability noise budget) is shown overlaid with the corresponding closure phases.

to form any solid conclusions on the type of variability in Sgr A* based on this one closure triangle.

StarWarps spatial prior images To explore the sensitivity of results to the ring features encouraged during imaging, we introduce 5 different images used as both the initialization and mean prior image μ in `StarWarps`. Figure 5.11 shows the mean prior images explored for imaging the original data and deblurred data. Note that recovered flux is constrained to evolve within the regions that have flux in the prior image, therefore the puffier rings and the tapered disk with more extended flux are less constraining during imaging. As expected, movies recovered with the less constraining puffier prior images result in recovered movies with a less clear underlying ring structures. Nonetheless, in all these cases (with a ring init/prior), the same general trend in PA is recovered in one of the modes, even when the central indent is very weak. When a disk prior is used with no central indent whatsoever the same PA trend is not recovered; instead, the PA trend appears to be reversed in sign (as discussed in Figure 5.4). Figure 5.12 shows more detailed comparisons of `StarWarps` movies reconstructed with ring and disk mean prior images on April 6 and 7, including data fits to representative closure phases.

5.A.5.2 Geometric Modeling

For snapshot geometric modeling, we have two competing effects. One is that we require a geometric model that can adequately explain the on-sky image. However, given the sparseness of the (u, v)-coverage for each snapshot, the risk of over-fitting the data is considerable and potentially leads to artificially un-informative posteriors. However, under-fitting the data can lead to large biases in the recovered parameters, and artificially narrow posteriors. To find the preferred model we use relative measures. That is, we don't compare the absolute fit quality using a metric like the χ^2 statistic, but rather how well a model does compared to the others considered. For this purpose we use the Bayesian evidence (also referred to as evidence),

$$Z(\text{data}|M) = \int \mathcal{L}(\text{data}|\theta, M)p(\theta|M)\text{d}\theta. \tag{5.3}$$

The evidence measures the marginal probability of the data, after averaging over all possible parameter values of the model. The preferred model is then the one that maximizes the evidence of the model. For snapshot modeling we select the preferred model by computing the log-evidence in each snapshot, and then sum the log-evidence across all snapshots. Note, that we are only able to estimate the evidence for the

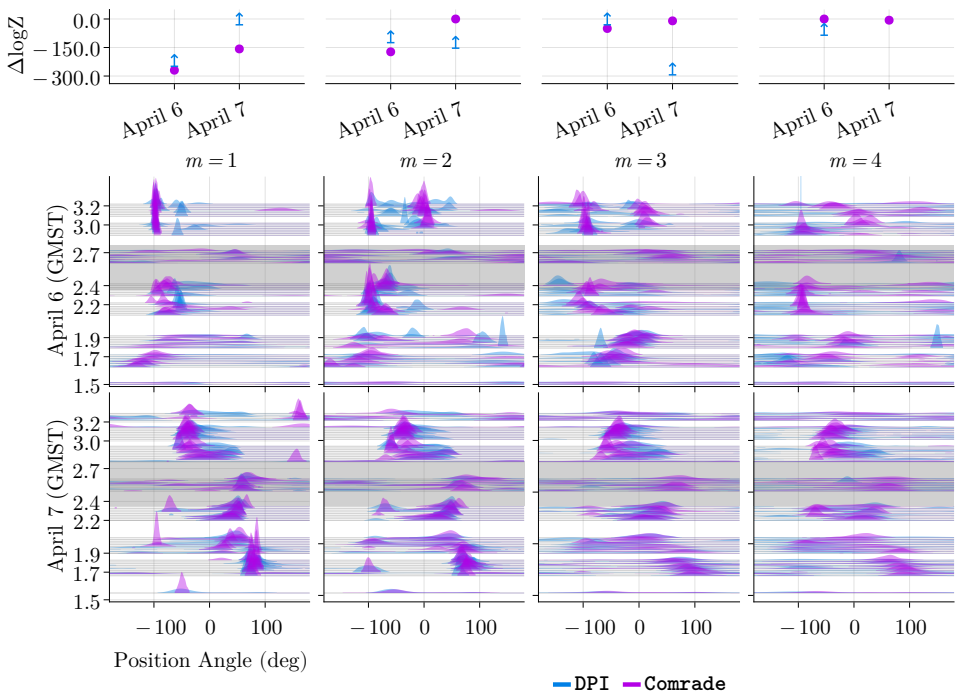

Figure 5.13: Comparing the m-ring results across orders 1, 2, 3, and 4 in both `Comrade` (magenta) and `DPI` (blue). The impact of the different m-ring orders on the position angle evolution for April 6 and 7 are shown in the middle and bottom rows. The top row is the change in the log-evidence across m-ring orders and days. The evidence lower bound produced by `DPI` is shown as a blue upwards arrow.

`Comrade` pipeline. `DPI`/Variational inference cannot estimate the evidence, but instead can compute an effective lower bound to use as a proxy.

M-ring Order To assess the impact of different model choices on the posterior samples, we considered an m-ring model with 1–4 modes. The results for the m-ring model from the `Comrade` pipeline are shown in Figure 5.13. We find that the trend for the dipole moment phase is consistent across model specifications, albeit the posteriors become more uncertain for the higher-order m-ring models. The recovered total evidence for each model is shown in Figure 5.13. For April 6 $m = 4$ is the preferred model with a log-evidence of 1499. On April 7, the $m = 2$ m-ring is preferred with a log-evidence of 1667. On both days the overall trend of the position angle maintains stable for $m = 1, 2, 3$, but the distributions become noticeably wider.

For the `DPI` pipeline we find similar PA trends for April 6 and 7. Using the evidence-lower-bound (ELBO) that is calculated as part of variational methods, $m = 3$ being preferred on April 6 and $m = 1$ on April 7. Furthermore, on April 7 the PA posterior for $m = 3, 4$ is very broad, becoming essentially unconstrained.

Comparing the `DPI` results to `Comrade` we find that $m = 1$ is preferred on April 7

and $m = 3$ on April 6 according to the evidence lower bound. `DPI` fits closure products which are equivalent to placing uniform priors on gains, meaning that the data is less constraining. Therefore, it is not surprising that `DPI` prefers simpler models compared to `Comrade`. To select a fiducial model across days and bands we considered both the evidence, the relative impact on the posterior, and impact on each pipeline. For these reasons we take $m = 2$ for `DPI` and $m = 2$ and sometimes $m = 3$ for `Comrade`. The $m = 2$ model is preferred for `Comrade` on April 7 and the $m = 2$ distribution for `DPI` is similar but broader than the $m = 1$.

Conclusions

In this thesis we studied and characterized the polarimetric properties and internal structure of blazar jets and the dynamics of the compact structure that surrounds the supermassive black holes that power them. To that aim, we followed two approaches. First, we analyzed the synchrotron emission produced by several types of relativistic magnetohydrodynamic jet models at the parsec scale (Fuentes *et al.,* 2018; 2021). Secondly, we exploited the data collected from space and millimeter VLBI observations of the archetypal blazar 3C 279 (Fuentes *et al.,* submitted 2022) and Sagittarius A*, the SMBH at the center of the Milky Way (Event Horizon Telescope Collaboration *et al.,* 2022c). In the following paragraphs we summarize the main conclusions obtained from the results presented in the previous chapters.

Polarimetric emission from RMHD jets. I In this chapter we present a first attempt to study the structure of a suite of relativistic overpressured magnetized jets characterized by their dominant type of energy, namely internal (hot jet models), kinetic, and magnetic. The models are defined by constant values of the rest-mass density and axial components of the fluid flow velocity and the magnetic field, a toroidal component of the magnetic field with a radial profile, and fixed values of the jet overpressure factor and the ambient pressure. The pressure mismatch between the jet and ambient medium induces a series of recollimation shocks and gentle expansions and compressions of the jet flow, whose properties (i.e., strength, obliquity, amplitude, wavelength) are mainly governed by the magnetosonic Mach number and the specific internal energy. The transversal profile of the jet models is determined by the magnetic tension and the magnetic pressure gradient, that is, the jet magnetization.

To connect the properties of the RMHD jet models with the structures observed in extragalactic jets at parsec scales, we have computed the expected synchrotron emission radiated by our jet simulations. The integration of the radiative transfer equations for different viewing angles produced images of jets with a rich transversal structure and bright knots with a large variety of relative intensities and separations. The intensity of these components is modulated by the Doppler boosting ratio between the shocks and the rarefactions, and strongly depends on the viewing angle. As expected for jets threaded by a helical magnetic field, these images feature an asymmetry across the jet width in both total and polarized intensity, a stratified degree of polarization which increases towards the jet edges, and a bimodal distribution of the polarization angle (mainly for small viewing angles). As the viewing angle increases, the polariza-

tion angle becomes perpendicular to the jet propagation direction, highlighting the dominance of the poloidal component of the magnetic field. Nonetheless, moderate variations can be found around the bright knots which originate at recollimation shocks. Therefore, these polarized signatures can be used to identify recollimation shocks in VLBI observations of blazar jets.

Polarimetric emission from RMHD jets. II Here we extend the work done in the previous chapter and present the synchrotron emission obtained from a new suite of relativistic magnetohydrodynamical jet models which explore different magnetic field configurations (force-free and non-force-free) and magnetic pitch angles (45° and 77.5°). The emission calculations are now based on two different models connecting the thermal and non-thermal particles population, that is, we either assume that the internal energy of the non-thermal population is proportional to that of the thermal population or to the magnetic energy density.

Because of its purely geometrical origin, we recover again the cross-section emission asymmetry induced by the helical magnetic field in both total and polarized intensity, for all jet and particle injection models and viewing angles $< 10°$. Force-free models display a distinct spine brightening that originates from the radial gradient of the axial magnetic field. As found in the previous chapter, the radio knots associated with recollimation shocks are particularly strong in the case of jet models dominated by the internal energy. In addition, we predict that extragalactic jets with prominent knots, or stationary components, must have a moderately small magnetic pitch angle, as magnetic tension tends to damp the strength of recollimation shocks.

The jet models computed in this work preserve the axial symmetry and helical geometry of the magnetic field. We therefore obtain the characteristic bimodal configuration of the polarization angle throughout the jets. Blazar jets with large magnetic pitch angles should feature two bright limbs of linearly polarized emission with orthogonal polarization angles between them, regardless of the angular resolution achieved in the observations. Jets observed with large viewing angles could display EVPA rotation along the propagation direction if the jet is in equipartition and the polarized emission is not strongly confined around the jet axis. Conversely, if the magnetic pitch angle is about 45°, only jets with viewing angles up to $\sim 2°$ will present some clear signatures of a toroidal magnetic field component. Beyond this value, the polarization angle will remain perpendicular to the jet axis, with the exception of some variations at recollimation shocks.

Filamentary structures as the origin of blazar jet variability In this chapter, we leave behind jet simulations and move to VLBI observations at centimeter wavelengths. Specifically, we present microarcsecond-scale angular resolution images of the blazar 3C 279 obtained at 22 GHz (or 1.3 cm) with the space VLBI mission *RadioAstron*. Together with 23 ground-based radio telescopes, *RadioAstron*, a 10-m space radio telescope onboard of the *Spektr-R* satellite, forms a space-ground interferometer with full polarimetric capabilities. With clear fringe detections of the source up to a projected baseline distance of 8 Earth diameters, the highly eccentric orbit of the

spacecraft allowed us to resolve the jet transversely and reveal several filamentary structures forming a helical pattern.

The estimated spatial periodicity of the filaments, as well as previously published results on the source, allow us to discard several possible origins for the structures observed. Thus, the most plausible mechanisms capable of developing such helical structures are plasma instabilities. In particular, since the jet is no longer accelerating at the scales probed by our image, we argue in favor of Kelvin-Helmholtz instabilities triggered in a kinetically dominated flow. Based on the numerical simulations presented in the previous chapters and the reconstructed cross-section asymmetry and polarization angle distribution, we can infer a jet bulk flow Lorentz factor of ~ 13 at the time of observation, in excellent agreement with the estimates provided by analyzing the kinematics of the parsec-scale jet. Moreover, this further allow us to infer a helical magnetic field with an intrinsic pitch angle of $\sim 45^{\circ}$ rotating clockwise as seen in the direction of flow motion.

Another remarkable feature observed in our image is the presence of brighter regions within the filaments, separated by half a wavelength. This enhanced emission can be explained in terms of differential Doppler boosting along the filaments, and therefore we can expect that these regions will propagate downstream the jet with a pattern speed equal to the wave phase velocity. Taking into account the jet properties derived above and previous works on the kinematics of moving components in 3C 279, we propose a novel model in which the jet variability in c, and possibly in other blazar sources, results from the propagation of plasma instabilities, as opposed to the standard shock-in-jet model usually invoked (Marscher & Gear, 1985).

Dynamic imaging of Sagittarius A*, the SMBH at the Galactic Center Our aim in this chapter has been to use the 2017 EHT data to explore the spatially-resolved dynamics of Sgr A* on minute timescales. First, we identified the time windows with the best (u, v)-coverage during the observation run – a roughly 100 min window on April 6 and 7. We identify a significant difference between the closure phases on April 6 and 7, signifying that the underlying structure is different on the two days. We reconstruct movies from this small slice of the EHT data using dynamic imaging and geometric snapshot modeling methods. We track the average position angle (PA) in our dynamic imaging and modeling results as a way of following a specific, dynamic, and measurable aspect of the source over time. We find that we are able to recover the PA in synthetic EHT data from some GRMHD simulation movies; however, there are prominent cases when this is not the case and both geometric modeling and dynamic imaging methods recover biased results.

On April 6, most dynamic imaging and modeling results show a stable PA in the Sgr A* images over the selected window. In contrast, the recovered PA evolution on April 7 is more dependent on prior assumptions on the spatial structure and temporal regularization. On April 7, when using a ring image as a spatial prior and weak temporal regularization, dynamic imaging results largely align with geometric modeling results and show an evolution in the PA of $\sim 140^{\circ}$ over the ~ 100 min window. However, we also see several other PA trends in the dynamic imaging results,

including a PA evolution in the opposite direction and modes where the PA is static on both days.

These results, along with our synthetic data tests, show that while the 230 GHz image of Sgr A* may exhibit interesting and measurable dynamics, our current methods cannot conclusively determine the PA evolution of Sgr A*. Dynamic reconstructions of Sgr A* with the 2017 EHT's coverage should thus be interpreted with caution. This analysis provides a promising starting point for further studies of the evolution seen in Sgr A* with future EHT observations with denser (u, v)-coverage.

Conclusiones

En esta tesis hemos estudiado y caracterizado las propiedades polarimétricas y la estructura interna de jets en blázares, y la dinámica del plasma que rodea a los agujeros negros supermasivos que los generan. Para ello, hemos utlizado dos enfoques. En primer lugar, analizamos la emisión sincrotrón producida por varios tipos de simulaciones magnetohidrodinámicas de jets relativistas a escalas del pársec (Fuentes *et al.,* 2018; 2021). En segundo lugar, explotamos los datos obtenidos en observaciones con interferometría de muy larga línea de base espacial y milimétrica del blazar 3C 279 (Fuentes *et al.,* submitted 2022) y de Sagitario A*, el SMBH en el centro de la Vía Láctea (Event Horizon Telescope Collaboration *et al.,* 2022c). En los siguientes párrafos resumimos las principales conclusiones obtenidas a partir de los resultados presentados en los capítulos anteriores.

Emisión polarimétrica de jets RMHD. I En este capítulo presentamos un primer intento de estudiar la estructura de un conjunto de jets magnetizados, relativistas y sobrepresionados caracterizados por el tipo de energía dominante, a saber, interna, cinética y magnética. Los modelos están definidos por valores constantes de la densidad de masa en reposo y de las componentes axiales de la velocidad de flujo del fluido y del campo magnético, una componente toroidal del campo magnético con un perfil radial y valores fijos del factor de sobrepresión del jet y de la presión externa. El desequilibrio de presión entre el jet y el medio externo induce una serie de choques de recolimación, expansiones y compresiones suaves del flujo del jet, cuyas propiedades (fuerza, oblicuidad, amplitud, longitud de onda) se rigen principalmente por el número de Mach magnetosónico y la energía interna específica. El perfil transversal de los jets está determinado por la tensión magnética y el gradiente de presión magnética, es decir, por la magnetización del jet.

Para conectar las propiedades de los jets RMHD con las estructuras observadas en jets extragalácticos a escalas del pársec, calculamos la emisión sincrotrón radiada por nuestras simulaciones. Al integrar las ecuaciones de transferencia radiativa para diferentes ángulos de visión, obtenemos imágenes de jets con una rica estructura transversal y *componentes* brillantes con una gran variedad de intensidades y separaciones relativas. La intensidad de estas componentes está modulada por la relación de reforzamiento Doppler entre los choques y las rarefacciones, y depende fuertemente del ángulo de visión. Como es de esperar en el caso de jets confinados por un campo magnético helicoidal, estas imágenes presentan una asimetría transversal tanto en

intensidad total como en polarizada, un grado de polarización estratificado que aumenta hacia los bordes del jet, y una distribución bimodal del ángulo de polarización (principalmente para ángulos de visión pequeños). A medida que aumenta el ángulo de visión, el ángulo de polarización se vuelve perpendicular a la dirección de propagación del jet, lo que pone de manifiesto el predominio de la componente poloidal del campo magnético. No obstante, se pueden encontrar variaciones moderadas alrededor de las componentes brillantes que se originan en los choques de recolimación. Por lo tanto, estas trazas polarizadas pueden utilizarse para identificar choques de recolimación en observaciones VLBI de jets en blázares.

Emisión polarimétrica de jets RMHD. II En este capítulo ampliamos el trabajo realizado en el capítulo anterior y presentamos la emisión sincrotrón obtenida a partir de un nuevo conjunto de simulaciones magnetohidrodinámicas de jets relativistas que exploran diferentes configuraciones del campo magnético (*force-free* y *non-force-free*) y ángulo *pitch* (45° y 77.5°). Los cálculos de emisión se basan ahora en dos modelos distintos que conectan la población de partículas térmicas y no térmicas, es decir, suponemos que la energía interna de la población no térmica es proporcional a la de la población térmica o a la densidad de energía magnética.

Debido a su origen puramente geométrico e inducida por el campo magnético helicoidal, recuperamos de nuevo la asimetría transversal tanto en intensidad total como polarizada, para todos los jets, modelos de inyección de partículas y ángulos de visión $< 10°$. Los modelos *force-free* muestran un claro aumento del brillo en el eje que se origina por el gradiente radial del campo magnético axial. Tal y como se concluyó en el capítulo anterior, las componentes estacionarias asociadas a los choques de recolimación son particularmente fuertes en el caso de jets dominados por la energía interna. Además, los jets extragalácticos con componentes prominentes deben tener un ángulo *pitch* magnético moderadamente pequeño, ya que la tensión magnética tiende a amortiguar la fuerza de los choques de recolimación.

Los modelos de jets calculados en este trabajo conservan la simetría axial y la geometría helicoidal del campo magnético. Por lo tanto, obtenemos la característica configuración bimodal del ángulo de polarización en todos los modelos. Los jets en blázares con un ángulo *pitch* magnético lo suficientemente grande deberían presentar dos "carriles" brillantes de emisión linealmente polarizada con ángulos de polarización ortogonales entre si, independientemente de la resolución angular alcanzada en las observaciones. Los jets observados con ángulos de visión lo suficientemente grandes podrían mostrar una rotación de los EVPA a lo largo de la dirección de propagación si el jet está en equipartición y la emisión polarizada no está fuertemente confinada alrededor del eje del jet. Por el contrario, si el ángulo *pitch* magnético es aproximadamente 45°, sólo los jets con ángulos de visión de hasta $\sim 2°$ presentarán trazas claras de la componente toroidal del campo magnético. Más allá de este valor, el ángulo de polarización permanecerá perpendicular al eje del jet, con la excepción de algunas variaciones en los choques de recolimación.

Filamentos internos como origen de la variabilidad de jets en blázares En este capítulo dejamos atrás las simulaciones de jets y pasamos a las observaciones VLBI en longitudes de onda centimétricas. En concreto, presentamos imágenes del blazar 3C 279 con una resolución angular de microsegundos de arco obtenidas a 22 GHz (o 1.3 cm) con la misión espacial para VLBI *RadioAstron*. Junto con 23 radiotelescopios terrestres, *RadioAstron*, un radiotelescopio espacial de 10 m a bordo del satélite *Spektr-R*, forma un interferómetro espacio-tierra con plenas capacidades polarimétricas. Con claras detecciones de franjas de interferencia de la fuente hasta una distancia (en proyección) de 8 diámetros terrestres, la gran excentricidad de la orbita de *RadioAstron* nos ha permitido resolver el jet transversalmente y revelar varios filamentos internos que forman un patrón helicoidal.

La periodicidad espacial estimada de los filamentos, así como resultados publicados anteriormente sobre esta fuente, nos permiten descartar varios posibles orígenes para las estructuras observadas. Así, los mecanismos más plausibles capaces de generar dichas estructuras helicoidales son inestabilidades en el plasma. En particular, dado que el jet ha dejado de acelerarse a las escalas que muestra nuestra imagen, argumentamos en favor de inestabilidades Kelvin-Helmholtz desencadenadas en un flujo dominado por la energía cinética. Basándonos en las simulaciones numéricas presentadas en los capítulos anteriore, en la asimetría transversal reconstruida y en la distribución del ángulo de polarización, podemos inferir un factor de Lorentz del flujo de ~ 13 en el momento de observación, en excelente acuerdo con las estimaciones proporcionadas por el análisis de la cinemática del jet a escalas del pársec. Además, esto nos permite inferir un campo magnético helicoidal con un ángulo *pitch* intrínseco de $\sim 45^\circ$ que gira en el sentido de las agujas del reloj, visto en la dirección de movimiento del flujo.

Otra característica interesante observada en nuestras imágenes es la presencia de regiones más brillantes dentro de los filamentos, separadas por media longitud de onda. Este aumento de la emisión puede explicarse en términos de un reforzamiento Doppler diferencial a lo largo de los filamentos, y por tanto podemos esperar que estas regiones se propaguen por el jet con una velocidad igual a la velocidad de fase de la onda. Teniendo en cuenta las propiedades del jet derivadas anteriormente y trabajos previos sobre la cinemática de los componentes móviles en 3C 279, proponemos un nuevo modelo en el que la variabilidad del jet en c, y posiblemente en otros blázares, resulta de la propagación de inestabilidades del plasma, en contraposición al modelo estándar de choques en jets que se suele invocar (Marscher & Gear, 1985).

Imágenes dinámicas de Sagitario A*, el SMBH del centro galáctico Nuestro objetivo en este capítulo ha sido utilizar los datos del EHT obtenidos en 2017 para explorar la dinámica espacialmente resuelta de Sgr A* en escalas de tiempo muy reducidas. En primer lugar, identificamos las ventanas temporales con el mejor cubrimiento (u, v) durante el período de observación - una ventana de aproximadamente 100 min el 6 y 7 de abril. Identificamos una diferencia significativa entre las clausuras de fase de los días 6 y 7 de abril, lo que significa que la estructura subyacente es diferente en los dos días. Con esto, hemos reconstruidos películas a partir de dicha porción de los datos del EHT utilizando métodos de imagen dinámica y modelado geométrico

instantáneo. Para cuantificar un aspecto específico, dinámico y medible de la fuente a lo largo del tiempo, empleamos el ángulo de posición medio (PA) en nuestras imágenes dinámicas y modelado. Encontramos que somos capaces de recuperar el PA real para algunas simulaciones de SMBHs; sin embargo, hay casos en los que no es así y tanto el modelado geométrico como los métodos de imagen dinámica recuperan resultados sesgados.

El 6 de abril, la mayoría de los resultados de imagen dinámica y modelado muestran un PA estable en las imágenes de Sgr A* a lo largo de la ventana seleccionada. Por el contrario, la evolución del PA reconstruido el 7 de abril depende más de las suposiciones previas sobre la estructura espacial y la regularización temporal. El 7 de abril, cuando utilizamos una imagen de un anillo como información previa sobre la estructura subyacente y una regularización temporal débil, los resultados de imagen dinámica se alinean en gran medida con los resultados del modelado geométrico y muestran una evolución del PA de $\sim 140^\circ$ a lo largo de la ventana de ~ 100 min. Sin embargo, también observamos otras tendencias del PA en los resultados de imagene dinámica, incluyendo una evolución del PA en la dirección opuesta y "modos" en los que el PA permanece estático en ambos días.

Junto con los tests con datos sintéticos llevados a cabo, estos resultados muestran que, aunque la imagen a 230 GHz de Sgr A* pueda mostrar una dinámica interesante y medible, nuestros métodos actuales no pueden determinar de forma concluyente la evolución del PA de Sgr A*. Por tanto, las reconstrucciones dinámicas de Sgr A* con el cubrimiento (u, v) del EHT en 2017 deben interpretarse con precaución. Este análisis proporciona un punto de partida prometedor para futuros estudios sobre la evolución temporal de Sgr A* en observaciones del EHT con un cubrimiento (u, v) más denso.

Bibliography

Abbott, B. P. *et al.* GWTC-1: A Gravitational-Wave Transient Catalog of Compact Binary Mergers Observed by LIGO and Virgo during the First and Second Observing Runs. *Phys. Rev. X* **9,** 031040 (2019).

Agudo, I. *et al.* Jet Stability and the Generation of Superluminal and Stationary Components. *Astrophys. J. Lett.* **549,** L183–L186 (2001).

Akiyama, K. *et al.* Imaging the Schwarzschild-radius-scale Structure of M87 with the Event Horizon Telescope Using Sparse Modeling. *Astrophys. J.* **838,** 1 (2017).

Akiyama, K. *et al.* Superresolution Full-polarimetric Imaging for Radio Interferometry with Sparse Modeling. *Astron. J.* **153,** 159 (2017).

Aloy, M. A. *et al.* Radio Emission from Three-dimensional Relativistic Hydrodynamic Jets: Observational Evidence of Jet Stratification. *Astrophys. J. Lett.* **528,** L85–L88 (2000).

Aloy, M. A. *et al.* Three-dimensional Simulations of Relativistic Precessing Jets Probing the Structure of Superluminal Sources. *Astrophys. J. Lett.* **585,** L109–L112 (2003).

Antonucci, R. Unified models for active galactic nuclei and quasars. *Ann. Rev. Astron. Astrophys.* **31,** 473–521 (1993).

Arras, P. *et al.* Variable structures in M87* from space, time and frequency resolved interferometry. *Nature Astron.* **6,** 259–269 (2022).

Astropy Collaboration *et al.* Astropy: A community Python package for astronomy. *Astron. & Astrophys.* **558,** A33 (2013).

Astropy Collaboration *et al.* The Astropy Project: Building an Open-science Project and Status of the v2.0 Core Package. *Astron. J.* **156,** 123 (2018).

Baade, W. & Minkowski, R. Identification of the Radio Sources in Cassiopeia, Cygnus A, and Puppis A. *Astrophys. J.* **119,** 206 (1954).

Baczko, A.-K. *et al.* A highly magnetized twin-jet base pinpoints a supermassive black hole. *Astron. & Astrophys.* **593,** A47 (2016).

Baloković, M. *et al.* Multiwavelength Study of Quiescent States of Mrk 421 with Unprecedented Hard X-Ray Coverage Provided by NuSTAR in 2013. *Astrophys. J.* **819,** 156 (2016).

Bardeen, J. M. & Petterson, J. A. The Lense-Thirring Effect and Accretion Disks around Kerr Black Holes. *Astrophys. J. Lett.* **195,** L65–L67 (1975).

Beuchert, T. *et al.* VLBA polarimetric monitoring of 3C 111. *Astron. & Astrophys.* **610,** A32 (2018).

Biretta, J. A. *et al.* The Radio to X-ray Spectrum of the M87 Jet and Nucleus. *Astron. J.* **101,** 1632 (1991).

Blackburn, L. *et al.* EHT-HOPS Pipeline for Millimeter VLBI Data Reduction. *Astrophys. J.* **882,** 23 (2019).

Blandford, R. D. & Königl, A. Relativistic jets as compact radio sources. *Astrophys. J.* **232,** 34–48 (1979).

Blandford, R. D. & Payne, D. G. Hydromagnetic flows from accretion disks and the production of radio jets. *Mon. Not. R. Astron. Soc.* **199,** 883–903 (1982).

Blandford, R. D. & Znajek, R. L. Electromagnetic extraction of energy from Kerr black holes. *Mon. Not. R. Astron. Soc.* **179,** 433–456 (1977).

Blandford, R. D. *et al.* Relativistic Jets from Active Galactic Nuclei. *Ann. Rev. Astron. Astrophys.* **57,** 467–509 (2019).

Bloom, S. D. *et al.* The Accelerating Jet of 3C 279. *Astron. J.* **145,** 12 (2013).

Bondi, H. On spherically symmetrical accretion. *Mon. Not. R. Astron. Soc.* **112,** 195 (1952).

Bouman, K. L. Extreme imaging via physical model inversion: Seeing around corners and imaging black holes. PhD thesis (Massachusetts Institute of Technology, 2017).

Bouman, K. L. *et al.* Reconstructing Video of Time-Varying Sources From Radio Interferometric Measurements. *IEEE Trans. Comput. Imag.* **4,** 512–527 (2018).

Broderick, A. E. & McKinney, J. C. Parsec-scale Faraday Rotation Measures from General Relativistic Magnetohydrodynamic Simulations of Active Galactic Nucleus Jets. *Astrophys. J.* **725,** 750–773 (2010).

Broderick, A. E. *et al.* Hybrid Very Long Baseline Interferometry Imaging and Modeling with THEMIS. *Astrophys. J.* **898,** 9 (2020).

Bruni, G. *et al.* RadioAstron reveals a spine-sheath jet structure in 3C 273. *Astron. & Astrophys.* **654,** A27 (2021).

Bruni, G. *et al.* The RadioAstron Dedicated DiFX Distribution. *Galaxies* **4,** 1–4 (2016).

Burn, B. J. On the depolarization of discrete radio sources by Faraday dispersion. *Mon. Not. R. Astron. Soc.* **133,** 67 (1966).

Casadio, C. Multi-wavelength polarimetric studies of relativistic jets in active galactic nuclei. PhD thesis (Instituto de Astrofísica de Andalucía, 2016).

Chael, A. A. *et al.* High-resolution Linear Polarimetric Imaging for the Event Horizon Telescope. *Astrophys. J.* **829,** 11 (2016).

Chael, A. A. *et al.* Interferometric Imaging Directly with Closure Phases and Closure Amplitudes. *Astrophys. J.* **857,** 23 (2018).

Chael, A. A. Simulating and imaging supermassive black hole accretion flows. PhD thesis (Harvard University, Massachusetts, 2019).

Chandrasekhar, S. The Maximum Mass of Ideal White Dwarfs. *Astrophys. J.* **74,** 81 (1931).

Cheung, C. C. *et al.* Superluminal Radio Features in the M87 Jet and the Site of Flaring TeV Gamma-Ray Emission. *Astrophys. J. Lett.* **663,** L65–L68 (2007).

Cho, I. *et al.* A comparative study of amplitude calibrations for the East Asia VLBI Network: A priori and template spectrum methods. *Publ. Astron. Soc. Japan* **69,** 87 (2017).

Clausen-Brown, E. *et al.* Signatures of large-scale magnetic fields in active galactic nuclei jets: transverse asymmetries. *Mon. Not. R. Astron. Soc.* **415,** 2081–2092 (2011).

Cohen, M. H. *et al.* The Small-Scale Structure of Radio Galaxies and Quasi-Stellar Sources at 3.8 Centimeters. *Astrophys. J.* **170,** 207–217 (1971).

Curtis, H. D. Descriptions of 762 Nebulae and Clusters Photographed with the Crossley Reflector. *Publ. Lick Obs.* **13,** 9–42 (1918).

Duncan, G. C. & Hughes, P. A. Simulations of relativistic extragalactic jets. *Astrophys. J. Lett.* **436,** L119–122 (1994).

Einstein, A. Die Grundlage der allgemeinen Relativitätstheorie. *Ann. Phys. (Leipzig)* **354,** 769–822 (1916).

Event Horizon Telescope Collaboration *et al.* First M87 Event Horizon Telescope Results. I. The Shadow of the Supermassive Black Hole. *Astrophys. J. Lett.* **875,** L1 (2019).

Event Horizon Telescope Collaboration *et al.* First M87 Event Horizon Telescope Results. II. Array and Instrumentation. *Astrophys. J. Lett.* **875,** L2 (2019).

Event Horizon Telescope Collaboration *et al.* First M87 Event Horizon Telescope Results. III. Data Processing and Calibration. *Astrophys. J. Lett.* **875,** L3 (2019).

Event Horizon Telescope Collaboration *et al.* First M87 Event Horizon Telescope Results. IV. Imaging the Central Supermassive Black Hole. *Astrophys. J. Lett.* **875,** L4 (2019).

Event Horizon Telescope Collaboration *et al.* First M87 Event Horizon Telescope Results. V. Physical Origin of the Asymmetric Ring. *Astrophys. J. Lett.* **875,** L5 (2019).

Event Horizon Telescope Collaboration *et al.* First M87 Event Horizon Telescope Results. VI. The Shadow and Mass of the Central Black Hole. *Astrophys. J. Lett.* **875,** L6 (2019).

Event Horizon Telescope Collaboration *et al.* First M87 Event Horizon Telescope Results. VII. Polarization of the Ring. *Astrophys. J. Lett.* **910,** L12 (2021).

Event Horizon Telescope Collaboration *et al.* First M87 Event Horizon Telescope Results. VIII. Magnetic Field Structure near The Event Horizon. *Astrophys. J. Lett.* **910,** L13 (2021).

Event Horizon Telescope Collaboration *et al.* First Sagittarius A* Event Horizon Telescope Results. I. The Shadow of the Supermassive Black Hole in the Center of the Milky Way. *Astrophys. J. Lett.* **930,** L12 (2022).

Event Horizon Telescope Collaboration *et al.* First Sagittarius A* Event Horizon Telescope Results. II. EHT and Multiwavelength Observations, Data Processing, and Calibration. *Astrophys. J. Lett.* **930,** L13 (2022).

Event Horizon Telescope Collaboration *et al.* First Sagittarius A* Event Horizon Telescope Results. III. Imaging of the Galactic Center Supermassive Black Hole. *Astrophys. J. Lett.* **930,** L14 (2022).

Event Horizon Telescope Collaboration *et al.* First Sagittarius A* Event Horizon Telescope Results. IV. Variability, Morphology, and Black Hole Mass. *Astrophys. J. Lett.* **930,** L15 (2022).

Event Horizon Telescope Collaboration *et al.* First Sagittarius A* Event Horizon Telescope Results. V. Testing Astrophysical Models of the Galactic Center Black Hole. *Astrophys. J. Lett.* **930,** L16 (2022).

Event Horizon Telescope Collaboration *et al.* First Sagittarius A* Event Horizon Telescope Results. VI. Testing the Black Hole Metric. *Astrophys. J. Lett.* **930,** L17 (2022).

Falcke, H. *et al.* Viewing the Shadow of the Black Hole at the Galactic Center. *Astrophys. J. Lett.* **528,** L13–L16 (2000).

Fanaroff, B. L. & Riley, J. M. The morphology of extragalactic radio sources of high and low luminosity. *Mon. Not. R. Astron. Soc.* **167,** 31P–36P (1974).

Farah, J. *et al.* Selective Dynamical Imaging of Interferometric Data. *Astrophys. J. Lett.* **930,** L18 (2022).

Finkelstein, D. Past-Future Asymmetry of the Gravitational Field of a Point Particle. *Phys. Rev.* **110,** 965–967 (1958).

Fossati, G. *et al.* A unifying view of the spectral energy distributions of blazars. *Mon. Not. R. Astron. Soc.* **299,** 433–448 (1998).

Fromm, C. M. *et al.* Spectral evolution of flaring blazars from numerical simulations. *Astron. & Astrophys.* **588,** A101 (2016).

Fromm, C. M. *et al.* Jet-torus connection in radio galaxies. Relativistic hydrodynamics and synthetic emission. *Astron. & Astrophys.* **609,** A80 (2018).

Fuentes, A. *et al.* Total and Linearly Polarized Synchrotron Emission from Overpressured Magnetized Relativistic Jets. *Astrophys. J.* **860,** 121 (2018).

Fuentes, A. *et al.* Magnetized relativistic jets and helical magnetic fields. II. Radiation. *Astron. & Astrophys.* **650,** A61 (2021).

Fuentes, A. *et al.* Filamentary structures as the origin of blazar jet variability (submitted 2022).

Gabuzda, D. C. *et al.* Transverse Faraday-rotation gradients across the jets of 15 active galactic nuclei. *Mon. Not. R. Astron. Soc.* **450,** 2441–2450 (2015).

Gabuzda, D. C. *et al.* Parsec scale Faraday-rotation structure across the jets of nine active galactic nuclei. *Mon. Not. R. Astron. Soc.* **472,** 1792–1801 (2017).

Georgiev, B. *et al.* A Universal Power-law Prescription for Variability from Synthetic Images of Black Hole Accretion Flows. *Astrophys. J. Lett.* **930,** L20 (2022).

Ghisellini, G. *et al.* Relativistic Bulk Motion in Active Galactic Nuclei. *Astrophys. J.* **407,** 65 (1993).

Ghisellini, G. *et al.* A theoretical unifying scheme for gamma-ray bright blazars. *Mon. Not. R. Astron. Soc.* **301,** 451–468 (1998).

Ghisellini, G. Radiative Processes in High Energy Astrophysics (2013).

Giovannini, G. *et al.* A wide and collimated radio jet in 3C84 on the scale of a few hundred gravitational radii. *Nature Astron.* **2,** 472–477 (2018).

Gómez, J. L. *et al.* Synchrotron Emission from Bent Shocked Relativistic Jets - Part One - Bent Relativistic Jets. *Astron. & Astrophys.* **274,** 55 (1993).

Gómez, J. L. *et al.* Synchrotron emission from bent shocked relativistic jets. 2: Shock waves in helical jets. *Astron. & Astrophys.* **284,** 51–64 (1994).

Gómez, J. L. *et al.* Synchrotron emission from bent shocked relativistic jets. 3: Aberration of light and time delay effects. *Astron. & Astrophys.* **292,** 33–44 (1994).

Gómez, J. L. *et al.* Parsec-Scale Synchrotron Emission from Hydrodynamic Relativistic Jets in Active Galactic Nuclei. *Astrophys. J. Lett.* **449,** L19 (1995).

Gómez, J. L. *et al.* Hydrodynamical Models of Superluminal Sources. *Astrophys. J. Lett.* **482,** L33–L36 (1997).

Gómez, J. L. *et al.* Flashing Superluminal Components in the Jet of the Radio Galaxy 3C120. *Science* **289,** 2317–2320 (2000).

Gómez, J. L. *et al.* Faraday Rotation and Polarization Gradients in the Jet of 3C 120: Interaction with the External Medium and a Helical Magnetic Field? *Astrophys. J. Lett.* **681,** L69 (2008).

Gómez, J. L. *et al.* On the Source of Faraday Rotation in the Jet of the Radio Galaxy 3C 120. *Astrophys. J.* **733,** 11 (2011).

Gómez, J. L. *et al.* Probing the Innermost Regions of AGN Jets and Their Magnetic Fields with RadioAstron. I. Imaging BL Lacertae at 21 Microarcsecond Resolution. *Astrophys. J.* **817,** 96 (2016).

Gómez, J. L. *et al.* Probing the Innermost Regions of AGN Jets and Their Magnetic Fields with RadioAstron. V. Space and Ground Millimeter-VLBI Imaging of OJ 287. *Astrophys. J.* **924,** 122 (2022).

Greisen, E. W. The Astronomical Image Processing System. in *Acquisition, Processing and Archiving of Astronomical Images* (1990), 125–142.

Greisen, E. W. AIPS, the VLA, and the VLBA. in *Inf. Handling Astron.* (ed Heck, A.) **285** (2003), 109.

Hardee, P. E. Spatial Stability of Jets: The Nonaxisymmetric Fundamental and Reflection Modes. *Astrophys. J.* **313,** 607 (1987).

Hardee, P. E. On Three-dimensional Structures in Relativistic Hydrodynamic Jets. *Astrophys. J.* **533,** 176–193 (2000).

Hardee, P. E. *et al.* GRMHD/RMHD simulations & stability of magnetized spine-sheath relativistic jets. *Astrophys. Space Sci.* **311,** 281–286 (2007).

Hargrave, P. J. & Ryle, M. Observations of Cygnus A with the 5-km radio telescope. *Mon. Not. R. Astron. Soc.* **166,** 305–327 (1974).

Hayashida, M. *et al.* Rapid Variability of Blazar 3C 279 during Flaring States in 2013-2014 with Joint Fermi-LAT, NuSTAR, Swift, and Ground-Based Multi-wavelength Observations. *Astrophys. J.* **807,** 79 (2015).

Hazard, C. *et al.* Investigation of the Radio Source 3C 273 By The Method of Lunar Occultations. *Nature* **197,** 1037–1039 (1963).

Högbom, J. A. Aperture Synthesis with a Non-Regular Distribution of Interferometer Baselines. *Astron. & Astrophys. Suppl. Ser.* **15,** 417–426 (1974).

Holdaway, M. A. & Wardle, J. F. C. Maximum entropy imaging of polarization in very long baseline interferometry. in *Dig. Image Synth. Inv. Opt.* (eds Gmitro, A. F. *et al.*) **1351** (1990), 714–724.

Hovatta, T. *et al.* MOJAVE: Monitoring of Jets in Active Galactic Nuclei with VLBA Experiments. VIII. Faraday Rotation in Parsec-scale AGN Jets. *Astron. J.* **144,** 105 (2012).

Huarte-Espinosa, M. *et al.* Interaction of Fanaroff-Riley class II radio jets with a randomly magnetized intracluster medium. *Mon. Not. R. Astron. Soc.* **418,** 1621–1639 (2011).

Hughes, P. A. Beams and Jets in Astrophysics (1991).

Hunter, J. D. Matplotlib: A 2D Graphics Environment. *Comp. Sci. Eng.* **9,** 90–95 (2007).

Issaoun, S. Lifting the Veil on Black Holes: Approaching the Event Horizon with High-resolution Imaging. PhD thesis (Radboud Universiteit Nijmegen, 2021).

Jansky, K. G. Radio Waves from Outside the Solar System. *Nature* **132,** 66 (1933).

Janssen, M. *et al.* Event Horizon Telescope observations of the jet launching and collimation in Centaurus A. *Nature Astron.* **5,** 1017–1028 (2021).

Jennison, R. C. & Das Gupta, M. K. Fine Structure of the Extra-terrestrial Radio Source Cygnus I. *Nature* **172,** 996–997 (1953).

Johnson, M. D. *et al.* Universal interferometric signatures of a black hole's photon ring. *Science Adv.* **6,** eaaz1310 (2020).

Johnson, M. D. *et al.* Dynamical Imaging with Interferometry. *Astrophys. J.* **850,** 172 (2017).

Jorstad, S. G. *et al.* Polarimetric Observations of 15 Active Galactic Nuclei at High Frequencies: Jet Kinematics from Bimonthly Monitoring with the Very Long Baseline Array. *Astron. J.* **130,** 1418–1465 (2005).

Jorstad, S. G. *et al.* Kinematics of Parsec-scale Jets of Gamma-Ray Blazars at 43 GHz within the VLBA-BU-BLAZAR Program. *Astrophys. J.* **846,** 98 (2017).

Kardashev, N. S. *et al.* "RadioAstron"-A telescope with a size of 300 000 km: Main parameters and first observational results. *Astron. Rep.* **57,** 153–194 (2013).

Kellermann, K. I. The road to quasars. in *Extragalactic Jets from Every Angle* (eds Massaro, F. *et al.*) **313** (2015), 190–195.

Kerr, R. P. Gravitational Field of a Spinning Mass as an Example of Algebraically Special Metrics. *Phys. Rev. Lett.* **11,** 237–238 (1963).

Kessar, M. *et al.* The effect of subgrid-scale models on grid-scale/subgrid-scale energy transfers in large-eddy simulation of incompressible magnetohydrodynamic turbulence. *Phys. Plasmas* **23,** 102305 (2016).

Kettenis, M. *et al.* ParselTongue: AIPS Talking Python. in *Astron. Data Analysis Software Syst. XV* (eds Gabriel, C. *et al.*) **351** (2006), 497–500.

Kim, J.-Y. *et al.* The limb-brightened jet of M87 down to the 7 Schwarzschild radii scale. *Astron. & Astrophys.* **616,** A188 (2018).

Kim, J.-Y. High spatial resolution millimeter VLBI Studies of the nearby radio galaxies M 87 and 3C 84. PhD thesis (Max-Planck-Institut für Radioastronomie, 2018).

Kim, J.-Y. *et al.* Event Horizon Telescope imaging of the archetypal blazar 3C 279 at an extreme 20 microarcsecond resolution. *Astron. & Astrophys.* **640,** A69 (2020).

King, A. Black Holes, Galaxy Formation, and the M_{BH}-σ Relation. *Astrophys. J. Lett.* **596,** L27–L29 (2003).

King, A. & Pounds, K. Powerful Outflows and Feedback from Active Galactic Nuclei. *Ann. Rev. Astron. Astrophys.* **53,** 115–154 (2015).

Kirk, J. G. *et al.* Particle Acceleration at Ultrarelativistic Shocks: An Eigenfunction Method. *Astrophys. J.* **542,** 235–242 (2000).

Koide, S. A Two-dimensional Simulation of a Relativistic Jet Bent by an Oblique Magnetic Field. *Astrophys. J.* **478,** 66–69 (1997).

Koide, S. *et al.* A Two-dimensional Simulation of Relativistic Magnetized Jet. *Astrophys. J. Lett.* **463,** L71 (1996).

Komissarov, S. S. & Falle, S. A. E. G. Simulations of Superluminal Radio Sources. *Mon. Not. R. Astron. Soc.* **288,** 833–848 (1997).

Komissarov, S. S. & Falle, S. A. E. G. The large-scale structure of FR-II radio sources. *Mon. Not. R. Astron. Soc.* **297,** 1087–1108 (1998).

Komissarov, S. S. *et al.* Magnetic acceleration of relativistic active galactic nucleus jets. *Mon. Not. R. Astron. Soc.* **380,** 51–70 (2007).

Komissarov, S. S. *et al.* Stationary relativistic jets. *Comp. Astrophys. Cosmo.* **2,** 9 (2015).

Kormendy, J. & Ho, L. C. Coevolution (Or Not) of Supermassive Black Holes and Host Galaxies. *Ann. Rev. Astron. Astrophys.* **51,** 511–653 (2013).

Kormendy, J. & Richstone, D. Inward Bound—The Search For Supermassive Black Holes In Galactic Nuclei. *Ann. Rev. Astron. Astrophys.* **33,** 581 (1995).

Kovalev, Y. Y. *et al.* Detection statistics of the RadioAstron AGN survey. *Adv. Space Res.* **65.** High-resolution space-borne radio Astron., 705–711 (2020).

Kraft, R. P. *et al.* Chandra Observations of the X-Ray Jet in Centaurus A. *Astrophys. J.* **569,** 54–71 (2002).

Laing, R. A. *et al.* Multifrequency VLA observations of the FR I radio galaxy 3C 31: morphology, spectrum and magnetic field. *Mon. Not. R. Astron. Soc.* **386,** 657–672 (2008).

Laing, R. A. & Bridle, A. H. Relativistic models and the jet velocity field in the radio galaxy 3C 31. *Mon. Not. R. Astron. Soc.* **336,** 328–352 (2002).

Lico, R. *et al.* Interpreting the time variable RM observed in the core region of the TeV blazar Mrk 421. *Mon. Not. R. Astron. Soc.* **469,** 1612–1616 (2017).

Lister, M. L. *et al.* MOJAVE: Monitoring of Jets in Active Galactic Nuclei with VLBA Experiments. V. Multi-Epoch VLBA Images. *Astron. J.* **137,** 3718–3729 (2009).

Lister, M. L. *et al.* MOJAVE. XV. VLBA 15 GHz Total Intensity and Polarization Maps of 437 Parsec-scale AGN Jets from 1996 to 2017. *Astrophys. J. Suppl.* **234,** 12 (2018).

Lister, M. L. *et al.* MOJAVE: XIII. Parsec-scale AGN Jet Kinematics Analysis Based on 19 years of VLBA Observations at 15 GHz. *Astron. J.* **152,** 12 (2016).

Lobanov, A. P. & Zensus, J. A. A Cosmic Double Helix in the Archetypical Quasar 3C273. *Science* **294,** 128–131 (2001).

Luminet, J.-P. Image of a spherical black hole with thin accretion disk. *Astron. & Astrophys.* **75,** 228–235 (1979).

Lynden-Bell, D. Galactic Nuclei as Collapsed Old Quasars. *Nature* **223,** 690–694 (1969).

Lyubarsky, Y. E. On the relativistic magnetic reconnection. *Mon. Not. R. Astron. Soc.* **358,** 113–119 (2005).

Lyubarsky, Y. E. Asymptotic Structure of Poynting-Dominated Jets. *Astrophys. J.* **698,** 1570–1589 (2009).

Lyutikov, M. *et al.* Polarization and structure of relativistic parsec-scale AGN jets. *Mon. Not. R. Astron. Soc.* **360,** 869–891 (2005).

Marscher, A. P. Turbulent, Extreme Multi-zone Model for Simulating Flux and Polarization Variability in Blazars. *Astrophys. J.* **780,** 87 (2014).

Marscher, A. P. & Gear, W. K. Models for high-frequency radio outbursts in extragalactic sources, with application to the early 1983 millimeter-to-infrared flare of 3C 273. *Astrophys. J.* **298,** 114–127 (1985).

Marscher, A. P. *et al.* Multi-Waveband Emission Maps of Blazars. *J. Astrophys. Astron.* **32,** 233–237 (2011).

Martí, J. M. On the correction of conserved variables for numerical RMHD with staggered constrained transport. *Comp. Phys. Comm.* **191,** 100–105 (2015).

Martí, J. M. The structure of steady, relativistic, magnetized jets with rotation. *Mon. Not. R. Astron. Soc.* **452,** 3106–3123 (2015).

Martí, J. M. *et al.* Hydrodynamical simulations of relativistic jets. *Astron. & Astrophys.* **281,** L9–L12 (1994).

Martí, J. M. *et al.* Morphology and Dynamics of Highly Supersonic Relativistic Jets. *Astrophys. J. Lett.* **448,** L105 (1995).

Martí, J. M. *et al.* Morphology and Dynamics of Relativistic Jets. *Astrophys. J.* **479,** 151–163 (1997).

Martí, J. M. *et al.* The Internal Structure of overpressured, Magnetized, Relativistic Jets. *Astrophys. J.* **831,** 163 (2016).

Martí, J. M. Numerical Simulations of Jets from Active Galactic Nuclei. *Galaxies* **7,** 24 (2019).

Marziani, P. *et al.* Comparative Analysis of the High- and Low-Ionization Lines in the Broad-Line Region of Active Galactic Nuclei. *Astrophys. J. Suppl.* **104,** 37–70 (1996).

McKinney, J. C. General relativistic magnetohydrodynamic simulations of the jet formation and large-scale propagation from black hole accretion systems. *Mon. Not. R. Astron. Soc.* **368,** 1561–1582 (2006).

McKinney, J. C. & Blandford, R. D. Stability of relativistic jets from rotating, accreting black holes via fully three-dimensional magnetohydrodynamic simulations. *Mon. Not. R. Astron. Soc.* **394,** L126–L130 (2009).

McKinney, W. Data Structures for Statistical Computing in Python. in *Proc. 9th Python Sci. Conf.* (eds van der Walt, S. & Millman, J.) (2010), 56–61.

McMullin, J. P. *et al.* CASA Architecture and Applications. in *Astron. Data Analysis Software Syst. XVI* (eds Shaw, R. A. *et al.*) **376** (2007), 127.

Mignone, A. & Bodo, G. An HLLC Riemann solver for relativistic flows - II. Magnetohydrodynamics. *Mon. Not. R. Astron. Soc.* **368,** 1040–1054 (2006).

Mimica, P. *et al.* Spectral Evolution of Superluminal Components in Parsec-Scale Jets. *Astrophys. J.* **696,** 1142–1163 (2009).

Mioduszewski, A. J. *et al.* Simulated VLBI Images from Relativistic Hydrodynamic Jet Models. *Astrophys. J.* **476,** 649–665 (1997).

Mizuno, Y. *et al.* RAISHIN: A High-Resolution Three-Dimensional General Relativistic Magnetohydrodynamics Code. *ArXiv* (2006).

Mizuno, Y. *et al.* Three-dimensional Relativistic Magnetohydrodynamic Simulations of Current-driven Instability with a Sub-Alfvénic Jet: Temporal Properties. *Astrophys. J.* **734,** 19 (2011).

Mizuno, Y. *et al.* Three-dimensional Relativistic Magnetohydrodynamic Simulations of Current-driven Instability. III. Rotating Relativistic Jets. *Astrophys. J.* **757,** 16 (2012).

Morgan, C. W. *et al.* The Quasar Accretion Disk Size-Black Hole Mass Relation. *Astrophys. J.* **712,** 1129–1136 (2010).

Mościbrodzka, M. *et al.* General relativistic magnetohydrodynamical simulations of the jet in M 87. *Astron. & Astrophys.* **586,** A38 (2016).

Moya-Torregrosa, I. *et al.* Magnetized relativistic jets and helical magnetic fields. I. Dynamics. *Astron. & Astrophys.* **650,** A60 (2021).

Napier, P. J. *et al.* The Very Long Baseline Array. *IEEE Proc.* **82,** 658–672 (1994).

Narayan, R. & Nityananda, R. Maximum entropy image restoration in astronomy. *Ann. Rev. Astron. Astrophys.* **24,** 127–170 (1986).

Netzer, H. Revisiting the Unified Model of Active Galactic Nuclei. *Ann. Rev. Astron. Astrophys.* **53,** 365–408 (2015).

Newman, E. T. *et al.* Metric of a Rotating, Charged Mass. *J. Math. Phys.* **6,** 918–919 (1965).

Newville, M. *et al.* lmfit/lmfit-py: 1.0.3. Version 1.0.3. 2021.

Nilsson, K. *et al.* The host galaxy of 3C 279. *Astron. & Astrophys.* **505,** 601–604 (2009).

Nishikawa, K.-I. *et al.* Three-Dimensional Magnetohydrodynamic Simulations of Relativistic Jets Injected along a Magnetic Field. *Astrophys. J. Lett.* **483,** L45–L48 (1997).

Nishikawa, K.-I. *et al.* Three-dimensional Magnetohydrodynamic Simulations of Relativistic Jets Injected into an Oblique Magnetic Field. *Astrophys. J.* **498,** 166–169 (1998).

Nishikawa, K.-I. *et al.* Evolution of Global Relativistic Jets: Collimations and Expansion with kKHI and the Weibel Instability. *Astrophys. J.* **820,** 94 (2016).

Oppenheimer, J. R. & Volkoff, G. M. On Massive Neutron Cores. *Phys. Rev.* **55,** 374–381 (1939).

Pacholczyk, A. G. Radio astrophysics. Nonthermal processes in galactic and extragalactic sources (1970).

Padovani, P. *et al.* Active galactic nuclei: what's in a name? *Astron. Astrophys. Rev.* **25,** 2 (2017).

Palumbo, D. C. M. *et al.* Metrics and Motivations for Earth-Space VLBI: Time-resolving Sgr A* with the Event Horizon Telescope. *Astrophys. J.* **881,** 62 (2019).

Park, J. *et al.* Revealing the Nature of Blazar Radio Cores through Multifrequency Polarization Observations with the Korean VLBI Network. *Astrophys. J.* **860,** 112 (2018).

Pasetto, A. *et al.* Broadband radio spectro-polarimetric observations of high-Faraday-rotation-measure AGN. *Astron. & Astrophys.* **613,** A74 (2018).

Pasetto, A. *et al.* Reading M87's DNA: A Double Helix Revealing a Large-scale Helical Magnetic Field. *Astrophys. J. Lett.* **923,** L5 (2021).

Perley, R. A. *et al.* The jet and filaments in Cygnus A. *Astrophys. J. Lett.* **285,** L35–L38 (1984).

Perucho, M. *et al.* Anatomy of Helical Extragalactic Jets: The Case of S5 0836+710. *Astrophys. J.* **749,** 55 (2012).

Perucho, M. Dissipative Processes and Their Role in the Evolution of Radio Galaxies. *Galaxies* **7,** 70 (2019).

Planck Collaboration *et al.* Planck 2015 results. XIII. Cosmological parameters. *Astron. & Astrophys.* **594,** A13 (2016).

Porth, O. Three-dimensional structure of relativistic jet formation. *Mon. Not. R. Astron. Soc.* **429,** 2482–2492 (2013).

Porth, O. *et al.* Synchrotron Radiation of Self-collimating Relativistic Magnetohydrodynamic Jets. *Astrophys. J.* **737,** 42 (2011).

Pushkarev, A. B. *et al.* MOJAVE: Monitoring of Jets in Active galactic nuclei with VLBA Experiments. IX. Nuclear opacity. *Astron. & Astrophys.* **545,** A113 (2012).

Reber, G. Notes: Cosmic Static. *Astrophys. J.* **91,** 621–624 (1940).

Rees, M. J. Black Hole Models for Active Galactic Nuclei. *Ann. Rev. Astron. Astrophys.* **22,** 471–506 (1984).

Remillard, R. A. & McClintock, J. E. X-Ray Properties of Black-Hole Binaries. *Ann. Rev. Astron. Astrophys.* **44,** 49–92 (2006).

Rybicki, G. B. & Lightman, A. P. Radiative processes in astrophysics (1979).

Ryle, M. The New Cambridge Radio Telescope. *Nature* **194,** 517–518 (1962).

Ryle, M. *et al.* High-Resolution Observations of the Radio Sources in Cygnus and Cassiopeia. *Nature* **205,** 1259–1262 (1965).

Ryle, M. The 5-km Radio Telescope at Cambridge. *Nature* **239,** 435–438 (1972).

Ryle, M. & Hewish, A. The synthesis of large radio telescopes. *Mon. Not. R. Astron. Soc.* **120,** 220 (1960).

Ryle, M. & Vonberg, D. D. Solar Radiation on 175 Mc./s. *Nature* **158,** 339–340 (1946).

Salpeter, E. E. Accretion of Interstellar Matter by Massive Objects. *Astrophys. J.* **140,** 796–800 (1964).

Scherrer, C. & Zhao, T. Soss: Declarative Probabilistic Programming via Runtime Code Generation. 2020.

Schmidt, M. 3C 273 : A Star-Like Object with Large Red-Shift. *Nature* **197,** 1040 (1963).

Schwab, F. R. & Cotton, W. D. Global fringe search techniques for VLBI. *Astron. J.* **88,** 688–694 (1983).

Schwarzschild, K. On the Gravitational Field of a Mass Point According to Einstein's Theory. *Abh. Konigl. Preuss. Akad. Wiss.* **1916,** 189–196 (1916).

Seyfert, C. K. Nuclear Emission in Spiral Nebulae. *Astrophys. J.* **97,** 28 (1943).

Shepherd, M. C. Difmap: an Interactive Program for Synthesis Imaging. in *Astron. Data Analysis Software Syst. VI* (eds Hunt, G. & Payne, H.) **125** (1997), 77–84.

Shu, C.-W. & Osher, S. Efficient Implementation of Essentially Non-oscillatory Shock-Capturing Schemes. *J. Comp. Phys.* **77,** 439–471 (1988).

Shu, C.-W. & Osher, S. Efficient Implementation of Essentially Non-oscillatory Shock-Capturing Schemes, II. *J. Comp. Phys.* **83,** 32–78 (1989).

Sironi, L. *et al.* Relativistic jets shine through shocks or magnetic reconnection? *Mon. Not. R. Astron. Soc.* **450,** 183–191 (2015).

Speagle, J. S. DYNESTY: a dynamic nested sampling package for estimating Bayesian posteriors and evidences. *Mon. Not. R. Astron. Soc.* **493,** 3132–3158 (2020).

Stokes, G. G. On the Composition and Resolution of Streams of Polarized Light from different Sources. *Trans. Cambridge Philos. Soc.* **9,** 399 (1851).

Sun, H. *et al.* α-deep Probabilistic Inference (α-DPI): Efficient Uncertainty Quantification from Exoplanet Astrometry to Black Hole Feature Extraction. *Astrophys. J.* **932,** 99 (2022).

Sun, H. & Bouman, K. L. Deep Probabilistic Imaging: Uncertainty Quantification and Multi-modal Solution Characterization for Computational Imaging. *Proc. AAAI Con. AI* **35,** 2628–2637 (2021).

Tchekhovskoy, A. *et al.* Efficient generation of jets from magnetically arrested accretion on a rapidly spinning black hole. *Mon. Not. R. Astron. Soc.* **418,** L79–L83 (2011).

Thompson, A. R. *et al.* The Very Large Array. *Astrophys. J. Suppl.* **44,** 151–167 (1980).

Thompson, A. R. *et al.* Interferometry and Synthesis in Radio Astronomy, 3rd Edition (2017).

Tiede, P. Comrade: Composable Modeling of Radio Emission. *J. Open Sour. Software* **7,** 4457 (2022).

Tolman, R. C. Static Solutions of Einstein's Field Equations for Spheres of Fluid. *Phys. Rev.* **55,** 364–373 (1939).

Ulrich, M.-H. *et al.* Variability of Active Galactic Nuclei. *Ann. Rev. Astron. Astrophys.* **35,** 445–502 (1997).

Urry, C. M. & Padovani, P. Unified Schemes for Radio-Loud Active Galactic Nuclei. *Publ. Astron. Soc. Pac.* **107,** 803 (1995).

van Cittert, P. H. Die Wahrscheinliche Schwingungsverteilung in Einer von Einer Lichtquelle Direkt Oder Mittels Einer Linse Beleuchteten Ebene. *Physica* **1,** 201–210 (1934).

van der Walt, S. *et al.* The NumPy Array: A Structure for Efficient Numerical Computation. *Comp. Sci. Eng.* **13,** 22–30 (2011).

Vega Garcıa, L. Space VLBI studies of internal structure and physical processes in extragalactic relativistic jets. PhD thesis (Max-Planck-Institut für Radioastronomie, 2018).

Vega-Garcıa, L. *et al.* Derivation of the physical parameters of the jet in S5 0836+710 from stability analysis. *Astron. & Astrophys.* **627,** A79 (2019).

Vlahakis, N. & Königl, A. Magnetic Driving of Relativistic Outflows in Active Galactic Nuclei. I. Interpretation of Parsec-Scale Accelerations. *Astrophys. J.* **605,** 656–661 (2004).

Walker, R. C. *et al.* The Structure and Dynamics of the Subparsec Jet in M87 Based on 50 VLBA Observations over 17 Years at 43 GHz. *Astrophys. J.* **855,** 128 (2018).

Wardle, J. F. C. & Homan, D. C. Theoretical Models for Producing Circularly Polarized Radiation in Extragalactic Radio Sources. *Astrophys. Space Sci.* **288,** 143–153 (2003).

Webster, B. L. & Murdin, P. Cygnus X-1-a Spectroscopic Binary with a Heavy Companion? *Nature* **235,** 37–38 (1972).

Weiß, A. *et al.* LABOCA observations of nearby, active galaxies. *Astron. & Astrophys.* **490,** 77–86 (2008).

Whitney, A. R. *et al.* Quasars Revisited: Rapid Time Variations Observed Via Very-Long-Baseline Interferometry. *Science* **173,** 225–230 (1971).

Wielgus, M. *et al.* LCG metric. `https://github.com/wielgusm/mwtools/blob/master/LCG_metric.py`. 2020.

Wielgus, M. *et al.* Millimeter Light Curves of Sagittarius A* Observed during the 2017 Event Horizon Telescope Campaign. *Astrophys. J. Lett.* **930,** L19 (2022).

Wilkinson, P. N. Very-Long-Baseline Radio Interferometry Surveys of the Compact Structure in Active Galactic Nuclei. *Proc. Nat. Acad. Sci.* **92,** 11342–11347 (1995).

Zakamska, N. L. *et al.* Hot Self-Similar Relativistic Magnetohydrodynamic Flows. *Astrophys. J.* **679,** 990–999 (2008).

Zamaninasab, M. *et al.* Dynamically important magnetic fields near accreting supermassive black holes. *Nature* **510,** 126–128 (2014).

Zensus, J. A. Parsec-Scale Jets in Extragalactic Radio Sources. *Ann. Rev. Astron. Astrophys.* **35,** 607–636 (1997).

Zernike, F. The concept of degree of coherence and its application to optical problems. *Physica* **5,** 785–795 (1938).

Zhao, G.-Y. *et al.* Unraveling the Innermost Jet Structure of OJ 287 with the First GMVA + ALMA Observations. *Astrophys. J.* **932,** 72 (2022).

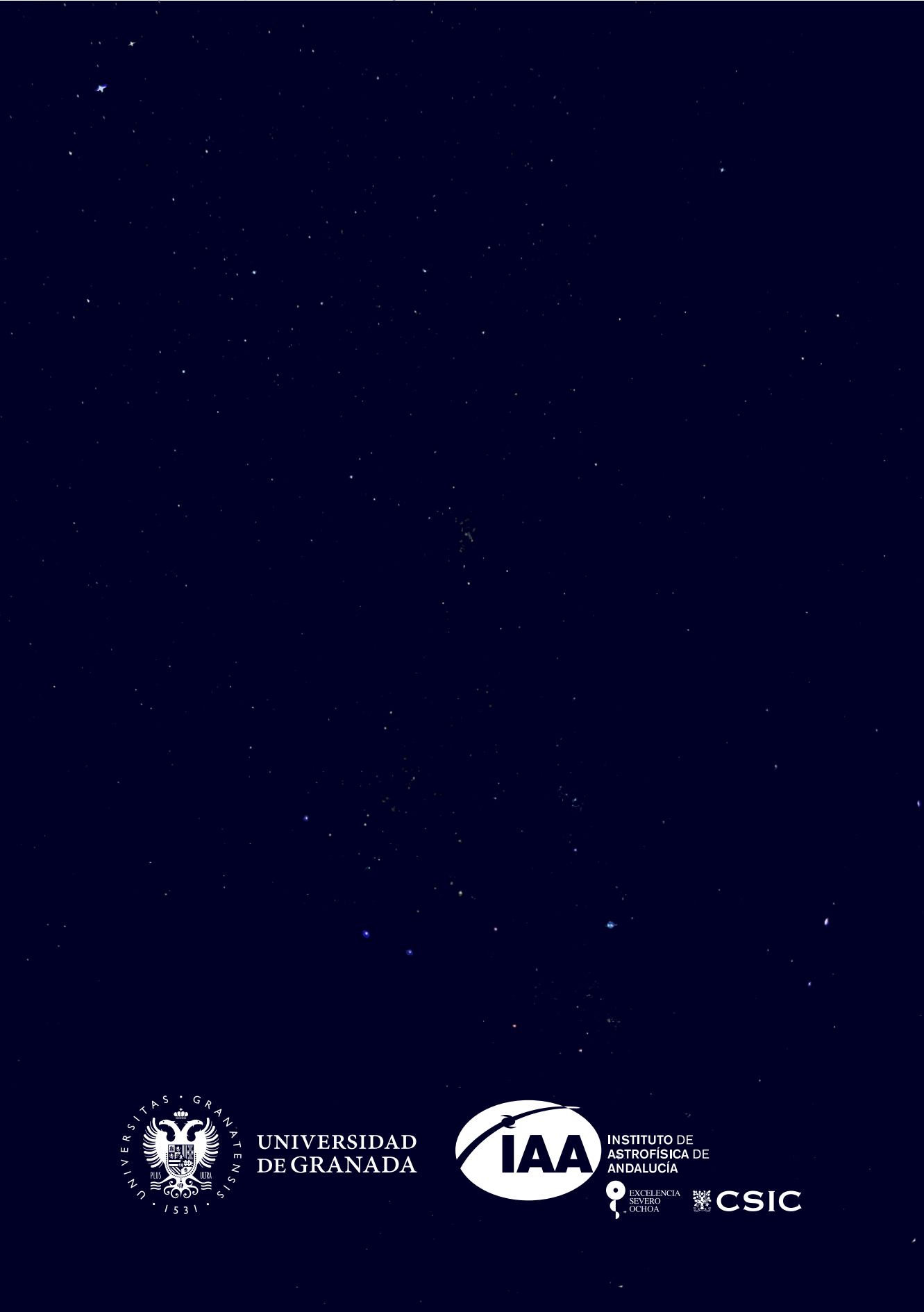
UNIVERSIDAD
DE GRANADA
IAA
INSTITUTO DE
ASTROFÍSICA DE
ANDALUCÍA
EXCELENCIA
SEVERO
OCHOA
CSIC